

PHYSICS-INFORMED DATA-DRIVEN MODELS FOR INELASTIC, AGING, FAILURE
BEHAVIOR OF CROSSLINKED POLYMERS

By

Aref Ghaderi

A DISSERTATION

Submitted to
Michigan State University
in partial fulfillment of the requirements
for the degree of

Civil Engineering - Doctor of Philosophy
Mechanical Engineering - Dual Major

2023

ABSTRACT

During cross-linked elastomers intended service-life, the material is supposed to sustain aggressive environmental damages induced by water infusion, temperature, and solar ultraviolet radiation (UV) during their operation, which affects their durability and properties.

A reliable design of rubber components to prevent early environmental degradation failure requires digital simulations using high-fidelity thermo-mechanical constitutive models that can simulate the adverse effects of aging on the mechanical, electrical, thermal, and failure properties of polymers. So far, most aging models have been developed by coupling hyperelastic constitutive models with single-kinetic degradation models to demonstrate the decay of materials during aging. However, a more detailed modeling approach can be achieved through modular continuum-based damage models that integrate the finite strain theory and thermo-mechanical degradation models.

Rubber elasticity theory is driven partly based on (i) statistical mechanics at the micro-scale, (ii) Phenomenological Modeling at the Meso-scale for modeling of the network (iii) Continuum Mechanics at the Macro-scale to model the material. Recently, the emergence of machine-learned (ML) models has attracted much attention. The first generation of "black-box" ML models, another type of phenomenological model, was proposed to model the mechanical behavior of rubbery media. In solid mechanics, stress-strain tensors are only partially observable in lower dimensions. Thus, obtaining data to feed a black-box ML model is exceptionally challenging. Thus, these approaches soon become obsolete due to the high demand for data for training and the lack of constraint on their output margins.

The issue can be resolved in a new generation of ML models inspired by physics-informed neural networks (PINN), which infuse physics-based Knowledge into the black-box models. Here, we modify PINN models to develop hybrid frameworks that can address the limitations of both phenomenological and micro-mechanical models by obtaining micro-structural behavior from the macroscopic experimental data set.

This dissertation aims to provide a new approach for reduced-order physics-based Data-driven modeling of multi-stressor damage in elastomers by infusing Knowledge into a neural network.

The following are the major thrusts of our research in the proposed dissertation:

- To design a systematic approach to reduce the order of the constitutive mapping and address the data volume problem for training.
- To incorporate background knowledge from polymer physics, continuum mechanics, and thermodynamics into the neural networks and constraint the solution space.
- To develop a neural network to predict various inelastic effects which is far less data-dependent, more interpretable than current PINN, and uses a knowledge-confined solution space.
- To validate our proposed hybrid framework based on limited data to describe the relationship between elastomeric network mechanics and environmental degradation.

To go into further detail, the model has been successfully developed and validated in five different damage scenarios, which describe the evolutionary process of developing the final platform. These steps are as follows, (I) Provide a model for polymers in non-extreme environments to capture the dependence of elastomer behavior on loading conditions such as strain rate and temperature, as well as compound morphology factors such as filler percentage and cross-link density, (II) developing a model for single mechanism aging, i.e., thermal aging, or hydrolytic aging, (III) developing a model to capture accumulation damages of fatigue and thermo-aging, (IV) introducing Physics informed neural networks (PINNs) to simulate multiple stiff and semi-stiff ODEs that govern Pyrolysis and Ablation, and (V) developing a Bayesian surrogate constitutive model to estimate the failure probability of elastomers. The models used in the proposed platform are the first hybrid models developed and validated for polymer components and, thus, bring great novelty and value to the industry. The model proposed in this work can significantly improve the design process of polymeric components by predicting the reliability, durability, and performance loss of materials based on the projected mechanical and environmental loading conditions. Such Knowledge can significantly reduce the design cost, the number of reliability tests needed, the maintenance costs and overhauls, and most importantly, prevent unexpected catastrophic failures.

Copyright by
AREF GHADERI
2023

"This dissertation is dedicated to my respectful parents, Zohreh and Abdolkarim for
always believing in me."

ACKNOWLEDGEMENTS

First of all, I want to thank my adviser, Dr. Roozbeh Dargazany. You helped me become an independent researcher. Thank you for taking a chance on me, I truly appreciate all your support.

Next, I would like to express my deepest appreciation to my committee members, Dr. Thomas Pence, Dr. Nizar Lajnef, Dr. Sara Roccabianca, and Dr. Hamidreza Modares. Being privileged to use their rich experiences through out these years on top of having the honor of sitting in their classes had a major influence on my intellectual development as a graduate student.

I gratefully acknowledge the assistance of my dear peers and friends in the High-Performance Materials (HPM) group, especially Vahid Morovati, Hamid Mohammadi, Amir Bahrololoumi, Yang Chen, Sharif Alazhary, Mamoon Shaafaey and for sharing ideas, and helping through experimental procedures.

TABLE OF CONTENTS

CHAPTER 1 INTRODUCTION	1
CHAPTER 2 PHYSICS-INFORMED MACHINE-LEARNED MODEL OF CONSTITUTIVE BEHAVIOR	15
CHAPTER 3 MACHINE-LEARNED CONSTITUTIVE MODEL FOR STRAIN RATE, TEMPERATURE, AND COMPOUND	38
CHAPTER 4 MACHINE-LEARNED MODEL FOR SINGLE-STRESSOR AGING	56
CHAPTER 5 FATIGUE AND AGING: REDUCED-ORDER KNOWLEDGE-DRIVEN MACHINE-LEARNED MODEL	86
CHAPTER 6 PHYSICS-INFORMED NEURAL NETWORK MODEL; PYROLYSIS AND ABLATION OF POLYMERS	109
CHAPTER 7 UNCERTAINTY QUANTIFICATION AND FAILURE PROBABILITY ESTIMATION	137
CHAPTER 8 SUMMARY AND FUTURE WORKS	163
BIBLIOGRAPHY	168

CHAPTER 1

INTRODUCTION

1.1 Motivation, Challenges and Objectives

Motivation: Cross-linked polymers, due to their superior extensibility, strength, and resistance to abrasion, chemicals, and wear, are globally prevalent. They find applications in sectors like automotive, aerospace, and power distribution. Given their rigorous applications, these polymers must endure numerous cyclic loads in harsh conditions. Yet, their reliability diminishes over time due to aging—a process that alters their material properties significantly. Estimating the lifespan of these polymers, especially when exposed to repetitive damages, is challenging. Factors like humidity, temperature, and radiation can expedite aging. Degradation can be attributed to major processes like hygrothermal effects, hydrolysis, and thermo-oxidation, or minor ones like chemical corrosion and ozone cracking. While the individual contributions of these processes have been extensively studied, comprehensive modeling of aging mechanisms remains elusive. Often, in situ testing of polymers is impractical due to costs and accessibility, necessitating predictive models to preempt structural failures from aging. Hence, there's a pressing need for a computational model that accurately predicts the mechanical behavior of aging cross-linked polymers. Existing efforts are bifurcated into phenomenological and micro-mechanical approaches. The former employs mathematical models grounded in thermodynamics, while the latter derives from the statistical mechanics of polymer structures and polymer chain physics.

Concurrently, the rise of machine learning (ML) models, especially the "black-box" ML models, has been notable in modeling the mechanical behavior of rubbery media. However, their high data requirement for training, given the partial observability of stress-strain tensors in lower

dimensions, renders them less practical. The next-gen physics-informed machine learning amalgamate the strengths of both phenomenological and micro-mechanical models, aiming to deduce micro-structural behavior from macroscopic experimental data.

Challenges: Phenomenological approaches are empirical, easy, and less interpretable; however, micromechanical approaches are highly interpretable but complex because they consider the readjustment of kinks, the rearrangement of convolutions, reorientation, and uncoiling of molecular chains. Meanwhile, the emergence of machine-learned (ML) models has attracted much attention as a way to address the mentioned challenges of the phenomenological and micromechanical approaches.

The primary innovations of our models include:

- Despite numerous studies on elastomer behavior during aging and the plethora of available data, there exists a dearth of physics-informed, data-driven models capable of accurately replicating experimental data beyond their training sets.
- Existing data-driven constitutive models for single-mechanism aging predominantly rely on a black-box approach. There has been no established methodology to incorporate foundational knowledge into the model, thereby reducing data dependency.
- Comprehensive data-driven models addressing aging issues have been largely restricted to a handful of rudimentary studies.

Objectives: Given these challenges, our aim is to formulate a hybrid, machine-learned, physics-informed model for reduced-order representation of aging in elastomers, integrating foundational knowledge with a data-driven methodology. The primary objectives of this study are:

1. Develop a systematic strategy to diminish the order of the constitutive mapping, addressing the data volume challenge for training.

2. Validate an innovative physics-informed hybrid framework delineating the interplay between elastomeric network mechanics and environmental degradation.
3. Forecast diverse inelastic effects using our model, which demands less data, offers greater interpretability, and operates within a knowledge-defined solution space.
4. Integrate foundational knowledge from polymer physics, continuum mechanics, and thermodynamics into the neural networks to constrain the solution space.

1.2 Physics-informed Machine-learned Models for Polymers

1.2.1 Fundamentals of Polymer Physics

Polymers exhibit mechanical properties that are intricately influenced by temperature and deformation time scales. Owing to their viscoelastic nature, polymers manifest traits reminiscent of both viscous fluids and elastic solids. At lower temperatures or higher frequencies, a polymer assumes a glassy state, becoming susceptible to fracture or yielding under strains exceeding a few percent. Conversely, rubbers, typically at elevated temperatures or diminished frequencies, demonstrate remarkable elasticity, enduring extensive expansions (exceeding 200%) without sustaining permanent deformation. At even higher temperatures, polymers may undergo irreversible deformation under stress, behaving akin to viscous fluids.

Phenomenological descriptions of material behavior offer a generalized perspective, sidestepping the intricacies of the underlying microstructure. These characterizations stem from (i) initiatives to infer plausible strain–energy functions and (ii) endeavors to extrapolate small-strain elastic behaviors to encompass large-strain conditions.

When addressing hyperelastic rubbers, it’s imperative to acknowledge the following assumptions: (i) In its pristine state, a rubber is inherently isotropic, denoting uniform properties across all directions, and (ii) deformation-induced volume changes are minimal, particularly when the rubber is considered incompressible. As such, only states of homogeneous pure strain—marked by consistent strain across the medium devoid of shear components—are taken into account for finite

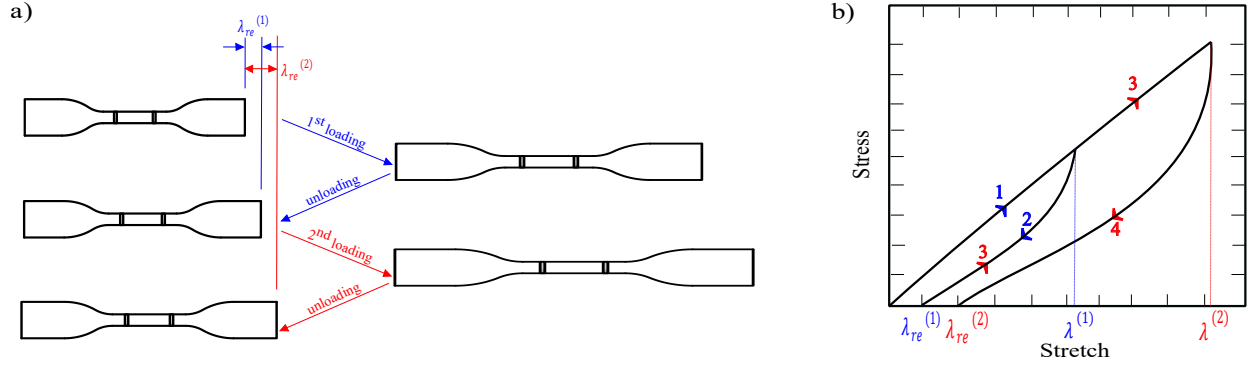


Figure 1.1. The Mullins effect schematic with a permanent set. a) Two uniaxial tensile cycles deformation b) the related stress-stretch curves

strain in isotropic substances.

The overall behavior of cross-linked polymers demonstrates significant non-linear elasticity combined with inelastic effects. Amorphous polymers exhibit rate-dependent finite elastic-plastic behavior, which stems from the inherent polymer micro-structure existing within the polymer matrix (see Fig.1.2). This behavior stems from the readjustment of kinks, rearrangement of convolutions, reorientation, and uncoiling of molecular chains while the load is accommodated through these mechanisms.

On the other hand, in these materials, temperature variation can affect the mechanical properties of these materials. They may be exposed to the surrounding environment or inherent heating due to energy dissipation. Most theoretical and experimental studies on this field have only been performed at room temperature [1]. However, the mechanical properties of these materials should be investigated at different temperatures other than room temperature. Also, variation of temperature affects the interaction between filler and polymer matrix.

So, filled polymers exhibit more complex non-linear behavior dependent on the temperature. Therefore, it is extremely important and challenging to develop a temperature-dependent and filler-dependent viscoelastic constitutive model, which predicts inelastic behavior of cross-linked polymers in different states of deformation for a wide range of strain, strain-rate, temperature, and filler concentration to be applicable for different types of operations.

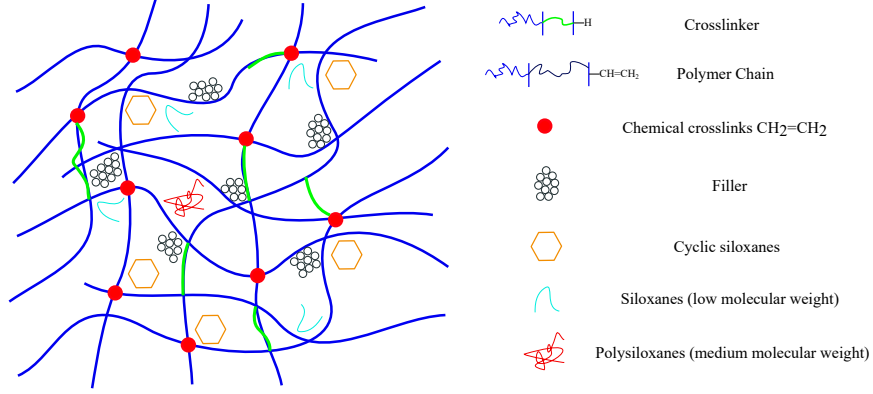


Figure 1.2. Schematic illustration for micro-structure of filled elastomers

Reducing Deformation History In microsphere concept, upon stretching of the matrix, some direction are extended and some will be contracted such that the total volume of the sphere to remain one. Accordingly, chains will be stretched or contracted based on their initial direction \mathbf{d} .

Macro-stretch $\chi^{\mathbf{d}}$: A major assumption in statistical mechanics of polymers is that the polymer chains will break under the stretch. When the matrix is deformed by \mathbf{F} , each direction of the micro-sphere will experience different stretch amplitude, further referred to as macro-stretch. The macro-stretch $\chi^{\mathbf{d}}$ defines the stretch applied to all chains in direction \mathbf{d} and is given by

$$\chi^{\mathbf{d}} = \mathbf{d}^T \mathbf{F} \mathbf{d}, \quad \Delta L^{\mathbf{d}} = \chi^{\mathbf{d}} R_0, \quad (1.1)$$

where $\Delta L^{\mathbf{d}}$ is the total extension that is applied to all chains in direction \mathbf{d} .

Micro-stretch $\lambda^{\mathbf{d}}$: Since all chains should sustain the extension of similar extension $\Delta L^{\mathbf{d}}$, the shorter chains may break due to the higher micro-stretch levels they need to sustain $\lambda^{\mathbf{d}} = 1 + \frac{\Delta L^{\mathbf{d}}}{L^{\mathbf{d}}}$ and the maximum micro-stretch a chain can sustain is limited by its geometry $\lambda_{limit}^{\mathbf{d}} = \frac{L_c}{\nu R_0}$, where L_c is the chain contour length, R_0 is its end-to-end distance and $\nu > 1$ is the mechanical breakage threshold [2]. Accordingly, the micro-stretch $\lambda^{\mathbf{d}}$ experienced **by each chain depends on the chain length, and a chain will break once the required stretch exceeds its stretch limit, namely $\lambda^{\mathbf{d}} > \lambda_{limit}^{\mathbf{d}}$** . Breakage of the chains often take place in various forms, i.e. polymer-polymer detachment, crosslink rupture, desorption of chains from particle surfaces, chain slippage

at entanglement junctions, and chain slippage over particle surfaces (see Fig. 1.3 for extended review).

Maximum micro-stretch in history λ_{max}^d : In the course of deformation, polymer chains begin to slide on or debond from the aggregates. This debonding starts with the shortest chain and gradually involves longer and longer chains. Under unloading, the debonded chains do not reattach back to the aggregate's active sites, and thus the maximal microstretch previously reached in the loading history,

$$\lambda_{max}^d = \max_{\tau \in (-\infty, t]} \lambda^d(\tau) \quad (1.2)$$

is crucial for the description of the polymer-filler debonding.

1.2.2 Fundamentals of Continuum Mechanics

This section gives a quick summary of the nonlinear continuum mechanics principles, which define the balancing rules for a solid body encountering large deformation.

Deformation

Assume a three-dimensional Euclidean space continuum body B at any time t_0 , as depicted in Fig. 1.4. Then, by using $\mathbf{X} \in \mathbb{E}^3$, one may address any point P_0 of the body B with regard to any basis. As the continuum body B travels across three-dimensional Euclidean space from time t_0 to time t , it occupies another geometrical area known as β 's configuration. Because the mapping of body B into β is one to one, the point P_0 in the body B is also mapped to point P .

We also refer to the areas of body B and β as reference and current configurations, respectively, to make the mapping method easier to understand. The position of point P and P_0 can be further represented by introducing a coordinate system $\theta^i (i = 1, 2, 3)$ by

$$\mathbf{x} = \hat{\mathbf{x}}(\theta^1, \theta^2, \theta^3, t), \quad \mathbf{X} = \hat{\mathbf{X}}(\theta^1, \theta^2, \theta^3) = \hat{\mathbf{x}}(\theta^1, \theta^2, \theta^3, t_0), \quad i = 1, 2, 3, \quad (1.3)$$

respectively. As a result, the displacement of point P may be calculated by

$$\mathbf{u} = \hat{\mathbf{u}}(\theta^1, \theta^2, \theta^3, t) = \mathbf{x} - \mathbf{X}, \quad (1.4)$$

where \mathbf{u} stands for displacement vector. When, the Euclidean space is introduced with a set of pairwise orthogonal unit vectors, say \mathbf{e}_i , one has

$$\begin{aligned} \mathbf{X} &= X^i \mathbf{e}_i, & X^j &= \mathbf{X} \cdot \mathbf{e}_j, & j &= 1, 2, 3, \\ \mathbf{u} &= u^i \mathbf{e}_i, & u^j &= \mathbf{u} \cdot \mathbf{e}_j, & j &= 1, 2, 3, \\ \mathbf{x} &= x^i \mathbf{e}_i, & x^j &= \mathbf{x} \cdot \mathbf{e}_j = X^j + u^j, & j &= 1, 2, 3, \end{aligned} \quad (1.5)$$

where the Einstein summation convention is used to repeated indices.

Deformations of a body can be readily characterized by vectors tangent to the coordinate lines in the reference and current configurations in the case of substantial deformations. The tangent vectors are defined as follows

$$\mathbf{G}_i = \frac{\partial \mathbf{X}}{\partial \theta^i}, \quad \mathbf{g}_i = \frac{\partial \mathbf{x}}{\partial \theta^i}, \quad i = 1, 2, 3 \quad (1.6)$$

Furthermore, \mathbf{G}_i and \mathbf{g}_i may be defined as the bases dual to \mathbf{G}_i and \mathbf{g}_i , implying that

$$\mathbf{G}_i \cdot \mathbf{G}^j = \delta_i^j, \quad \text{and} \quad \mathbf{g}_i \cdot \mathbf{g}^j = \delta_i^j \quad (1.7)$$

Also, the deformation gradient tensor \mathbf{F} can be represented by,

$$\mathbf{F} = \text{Grad} \mathbf{x}. \quad (1.8)$$

In deformation kinematics, the deformation gradient tensor is a fundamental second-order tensor that describes the changes in material constituents during deformation. To this goal, consider $d\mathbf{X}$ and $d\mathbf{x}$ in reference and current configurations as infinitesimal material components, respectively.

Then, one has

$$d\mathbf{x} = \mathbf{F}d\mathbf{X}, \quad d\mathbf{X} = \mathbf{F}^{-1}d\mathbf{x}. \quad (1.9)$$

Additionally, the changes in volume J may be derived by

$$J = \frac{dV}{dV_0} = \left| F_{\cdot j}^i \right| = \det \mathbf{F} > 0 \quad (1.10)$$

In the current setup, the lengths of the material components are provided by

$$\begin{aligned} \|d\mathbf{x}\|^2 &= d\mathbf{x} \cdot d\mathbf{x} = d\mathbf{X} \left(\mathbf{F}^T \mathbf{F} \right) d\mathbf{X} = d\mathbf{X} \mathbf{C} d\mathbf{X} \\ \|d\mathbf{X}\|^2 &= d\mathbf{X} \cdot d\mathbf{X} = d\mathbf{x} \left(\mathbf{F}^{-T} \mathbf{F}^{-1} \right) d\mathbf{x} = d\mathbf{x} \mathbf{b}^{-1} d\mathbf{x}, \end{aligned} \quad (1.11)$$

where

$$\mathbf{C} = \mathbf{F}^T \mathbf{F} = g_{ij} \mathbf{G}^i \otimes \mathbf{G}^j, \quad \mathbf{b} = \mathbf{F}^T = G^{ij} \mathbf{g}_i \otimes \mathbf{g}_j, \quad (1.12)$$

are referred to as the right and left Cauchy-Green tensor, respectively. To determine the stretch of a material element, divide the deformed length by the referenced length of the material element. To this aim, the stretch in the direction of \mathbf{N} is supplied by adding the unit vectors \mathbf{N} and \mathbf{N} along the material element $d\mathbf{X}$ and its counterpart $d\mathbf{x}$.

$$\lambda(\mathbf{N}) = \frac{dx}{dX} = \sqrt{\frac{\|d\mathbf{x}\|^2}{\|d\mathbf{X}\|^2}} = \sqrt{\frac{d\mathbf{X} \mathbf{N} \mathbf{C} \mathbf{N} d\mathbf{X}}{dX^2}} = (\mathbf{N} \mathbf{C} \mathbf{N})^{\frac{1}{2}}, \quad (1.13)$$

Thermo-elasticity

With the unit vectors \mathbf{N} and \mathbf{n} normal to the points P_0 and P , we may create infinitesimal areas dA_0 and dA around them. Furthermore, the infinitesimal force acting on the surface elements is denoted by $d\mathbf{F}$. As a result, one may write for any arbitrary point P

$$d\mathbf{F} = t dA = \mathbf{T} dA_0, \quad (1.14)$$

where the Cauchy and first Piola-Kirchhoff stress vectors, respectively, are the vector \mathbf{t} and its counterpart in reference configuration \mathbf{T} .

On the basis of Cauchy's stress theorem, second-order tensors σ and \mathbf{P} may be introduced, such that

$$\mathbf{t} = \sigma \mathbf{n} \quad \mathbf{T} = \mathbf{P} \mathbf{N}. \quad (1.15)$$

\mathbf{P} represents the first Piola-Kirchhoff stress tensor, and the tensor σ is known as the Cauchy stress tensor. Study of the thermoelastic features of rubber-like materials is necessary in order to establish the relations between force, internal energy and temperature. The changes in the internal energy of the system dU are equal to the heat absorbed by the system dQ and the work done on the system dW , according to the first law, and thus

$$dU = dW + dQ. \quad (1.16)$$

The second law defines a reversible process (elastic deformation) by

$$dQ = T ds. \quad (1.17)$$

where dS represents changes in entropy and T represents absolute temperature. Furthermore, the Helmholtz free energy Ψ is defined by

$$d\Psi = dU - SdT - TdS, \quad (1.18)$$

one can conclude that $dW = d\Psi$ at a constant temperature. The corresponding Helmholtz energy required to modify the entropy in the isothermal situation for non-energetic, purely entropic responses is

$$d\Psi = -TdS. \quad (1.19)$$

1.2.3 Fundamentals of Machine learning

Artificial intelligence is an interdisciplinary field aimed at developing machine intelligence, such as the capacity to interact with the environment, gather and analyze data, learn from it, and make context-adapted judgments. To process, analyze, interpret, summarize, and display data, *data scientists* employ mathematical and statistical approaches. *Big data* is a field of data science that deals with very big datasets and was inspired by the massive quantity of data acquired over the Internet, for example. Another major discipline of data science dedicated to knowledge discovery is *data mining*. To derive a prediction model from data, *machine learning* approaches integrate statistics and mathematical optimization.

Statistical learning is the process of utilizing data to calibrate the model's parameters using an optimization technique. Machine learning aims to use data-derived knowledge to produce predictions for fresh data that hasn't been seen before, whereas data mining focuses on knowledge extraction. As a result, there are two types of data: training data and test data. Training data is used to develop a predictive model, while test data is utilized in an exploitation phase for which the model will produce new predictions. Deep learning, which relies on the superposition of basic functionality in deep structures, has recently emerged as a key field of machine learning. Artificial neural networks, often known as deep neural networks, are models that have some similarities to neurons in the human brain.

Neural Network Architecture

Neural networks are well-known for their ability to represent information. Based on the universal approximation theorem, any continuous function can be arbitrarily estimated by a multi-layer perceptron containing one hidden layer and finite number of neurons. While neural networks can compactly express very complicated functions, obtaining the precise parameters (weights and biases) required to solve a particular PDE can be challenging.

The bulk of solutions has used feed-forward neural networks since Raissi et al. [4] original vanilla physics-informed machine learning. Some researchers, on the other hand, have tested with

several types of neural networks to investigate their effect on the overall physics-informed machine learning performance.

We start by building a simple D -layer multilayer feed-forward neural network comprising an input layer, $D - 1$ hidden layers, and an output layer. We suppose that the d^{th} hidden layer has N_d neurons. The previous layer's post-activation output $\mathbf{x}^{d-1} \in \mathbb{R}^{N_{d-1}}$ is then fed into the d^{th} hidden layer, and the specific affine transformation is of the form

$$\mathcal{H}_d(\mathbf{x}^{d-1}) \triangleq \mathbf{W}^d \mathbf{x}^{d-1} + \mathbf{b}^d, \quad (1.20)$$

where the network weight $\mathbf{W}^d \in \mathbb{R}^{N_d \times N_{d-1}}$ and the bias term $\mathbf{b}^d \in \mathbb{R}^{N_d}$ to be learned are both initialized using unique procedures like Xavier or He initialization.

The nonlinear activation function $\sigma(\cdot)$ is applied component-by-component to the current layer's affine output \mathcal{H}_d . Furthermore, for some regression issues, this nonlinear activation is not employed in the output layer. As a result, the neural network may be denoted as

$$\mathcal{N}(\mathbf{x}; \Theta) = (\mathcal{H}_D \circ \sigma \circ \mathcal{H}_{D-1} \circ \cdots \circ \sigma \circ \mathcal{H}_1)(\mathbf{x}), \quad (1.21)$$

where \circ denotes the composition operator, $\Theta = \{\mathbf{W}^d, \mathbf{b}^d\}_{d=1}^D \in \mathcal{P}$ denotes the learnable parameters to be optimized later in the network, and \mathcal{P} denotes the parameter space, and \mathcal{N} and $\mathbf{x}^0 = \mathbf{x}$ denote the network's output and input, respectively.

Shallow networks: Various scholars have tried to examine shallower network alternatives to address these difficulties: They can be sparse neural networks rather than fully linked designs, or more frequently single hidden layers like ELM (Extreme Learning Machine). More hidden layers help model complex nonlinear connections when compared to the shallow architecture; nevertheless, employing physics-informed machine learning for real applications might lead to deep networks with a large number of layers that can significantly influence training costs and efficiency. As a result, not only deep neural networks but also shallow ANNs have been reported in the literature for physics-informed machine learning.

Activation function The activation function of a node in artificial neural networks determines the output of that node given input or a set of inputs. This is similar to the linear perceptron's behavior in neural networks. However, only nonlinear activation functions allow such networks, using only a small number of nodes, to measure non-trivial problems, and such activation functions are called non-linearities. Choosing the activation function has a significant impact on the neural network's capacity and efficiency, and various activation functions can be used in different sections of the model. Based on the type of neural network architecture, the activation function used in hidden layers is usually chosen. If we are unsure which activation function to use for our network, we try and compare the results to find the best ones. We have done the same procedure in this study. Note that the choice of activation function in the hidden layer will control how well the network model learns the training dataset. Also, the effect of choosing different activation functions has not a significant effect on training time [5].

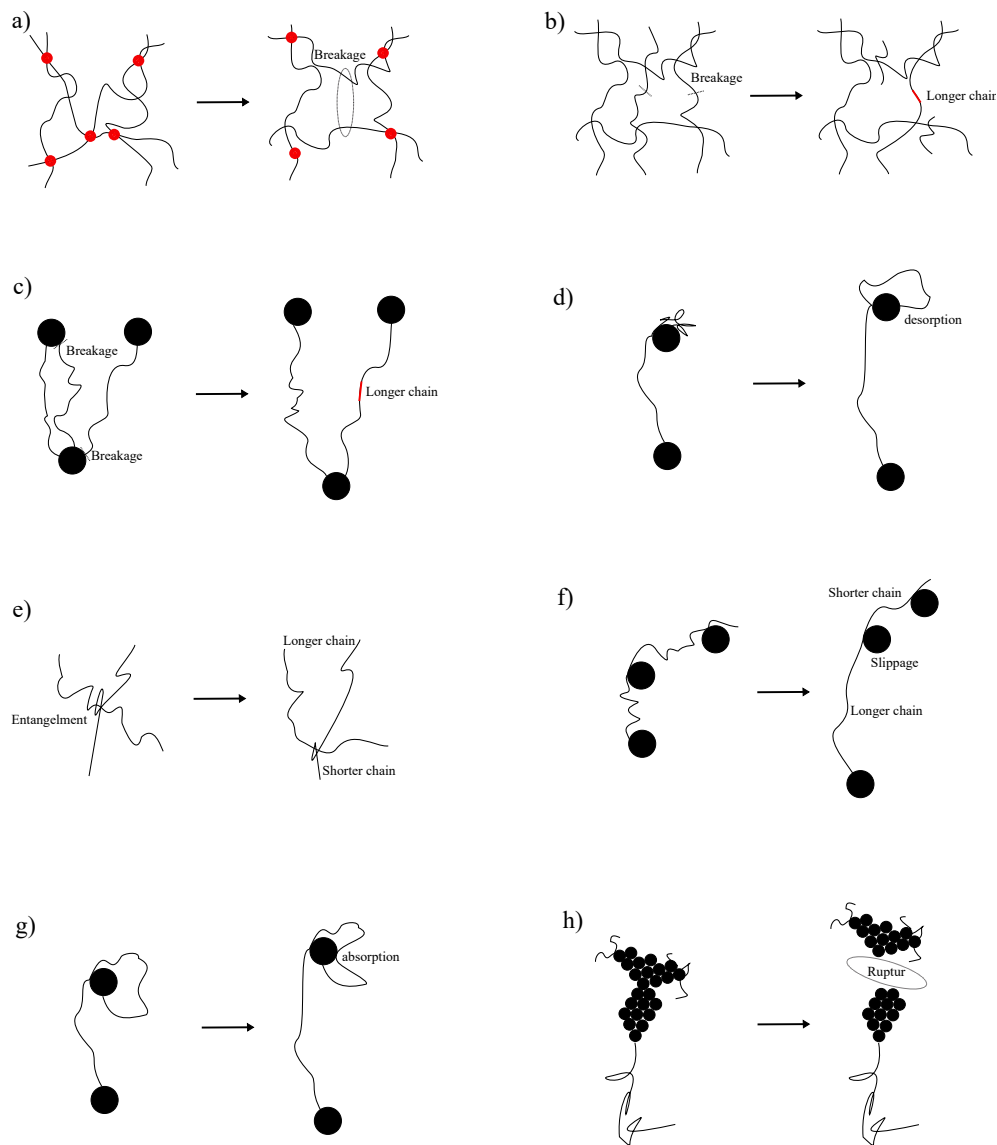


Figure 1.3. a) The breakage of chain crosslinks, b) Chain scission, c) The bond rupture of rubber-particle linkages, d) Desorption of chains from particle surfaces e) The slippage of chains at entanglement junctions, f) The slippage of chains over particle surfaces, g) Reforming absorption of chains to the particle surfaces, h) Filler rupture

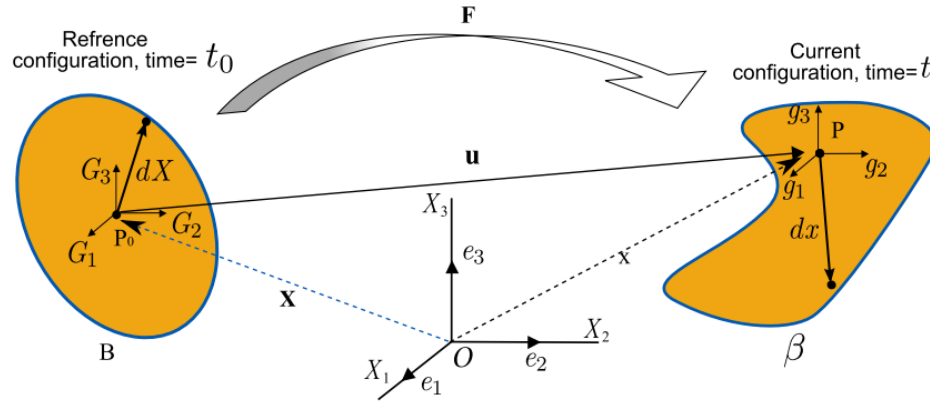


Figure 1.4. Description of body motion

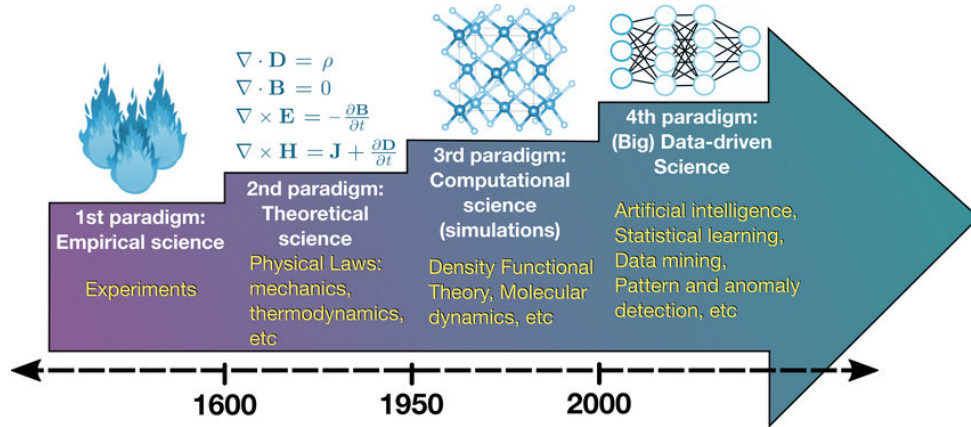


Figure 1.5. The four science paradigms: empirical, theoretical, computational, and data-driven [3]

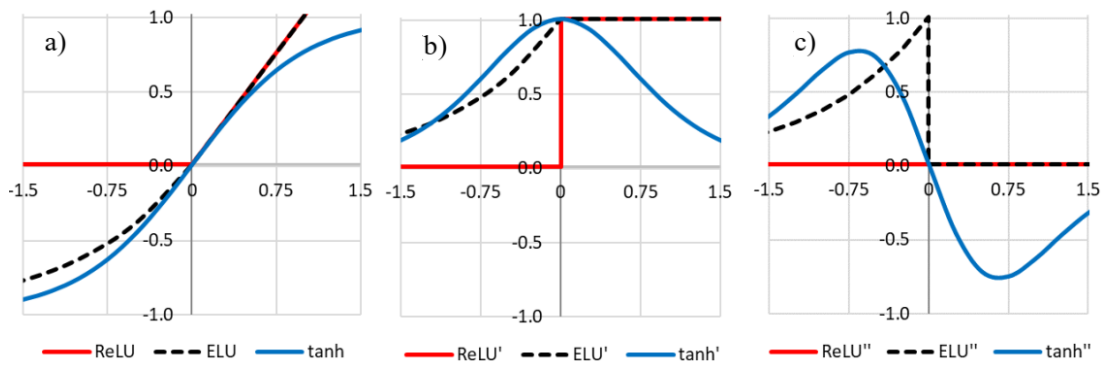


Figure 1.6. a) ReLU(Rectified Linear Unit), ELU(Exponential Linear Unit) and tanh activation functions, b) first derivatives of activation functions, and c) second derivatives of activation functions [6]

CHAPTER 2

PHYSICS-INFORMED MACHINE-LEARNED MODEL OF CONSTITUTIVE BEHAVIOR

2.1 Introduction

Cross-linked polymers, owing to their diverse applications in sectors like automotive, structural, and medical, have emerged as a focal point of research. Characterized by a 3D network of randomly oriented, elongated molecular chains that are cross-linked, spiraled, and entwined, these materials can be broadly categorized into filled and unfilled types. Fillers predominantly serve to reinforce polymers, as illustrated in Fig. 2.1. Given their multifaceted applications, accurately modeling the mechanical behavior of these materials across a spectrum of strains is paramount. Under quasi-static deformations, they exhibit hyper-elastic tendencies, predominantly steered by alterations in network entropy as chains reorient to macroscopic deformations. Farhangi et al. delved into the effects of fiber-reinforced polymer tubes infused with recycled materials [7, 8]. Similarly, Izadi et al. explored the impact of nanoparticles on polymer mechanical properties [9, 10, 11]. Numerous studies have probed this hyper-elastic behavior, leveraging either phenomenological or micromechanical methodologies rooted in molecular chain network statistics [12, 13]. Shojaeifar et al. [14, 15] proposed a model for the visco-hyperelasticity of materials. While phenomenological methods are empirical, straightforward, and less interpretative, micromechanical ones, though highly elucidative, are intricate, factoring in molecular chain adjustments like kink realignments, convolution rearrangements, reorientations, and uncoilings. Concurrently, the advent of machine-learned (ML) models offers a promising avenue to circumvent the inherent challenges of both the phenomenological and micromechanical methodologies.

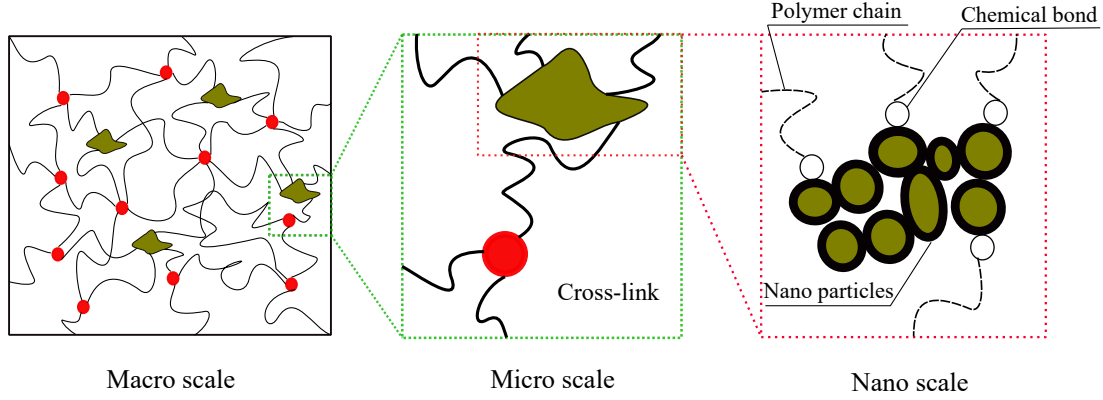


Figure 2.1. Schematic illustration for micro-structure of filled elastomers which is depicted micro scale and nano scale

The exponential growth of computational power over the last decade has enabled the first-generation of ML models to be used in computational mechanics and polymer physics [16, 17, 18, 19]. Current ML models were often developed based on "black box" approaches, which besides low interpretability, require a large volume of training data to prescribe a particular behavior [20, 21]. In solid mechanics, stress-strain tensors are only partially observable in lower-dimensions. Thus, obtaining data to feed the black-box ML model is exceptionally challenging. In general, one can classify current Data-driven efforts in computational mechanics into three categories with lots of approaches placed between two categories (see review [22]).

- **Model-free Distance-minimization Approaches** were developed to circumvent the need for constitutive models by directly finding stress-strain pairs with the least distance to experimental data, which also satisfy compatibility and equilibrium constraints. This approach was initially set for nonlinear truss and linear elastic materials [23] and later were expanded to include hyper-elastic materials [24]. While being superior to other models by being statistically independent of any prior knowledge of the materials, the method has few major limitations. It has a excessively high computational cost, has strong sensitivity to data scattering, and in high-dimensional problems suffers from lack of data [25]. This approach is further amended by studies on the combination of data-driven identification and computational mechanics [26]. To reformulate the heuristic optimization approach adopted by [23], mixed-integer programming was used for its implementation

[27]. Coelho and Breitenkopf [28] in their book investigated the main approaches for constitutive modeling using optimization methods.

- **Non-linear Dimensionality Reduction Approaches** seek to build a constitutive manifold from experimental data to describe an accurate approximation of the strain energy in different states of deformation. These approaches focus on describing the constitutive behavior through a set of shape functions, such as *B – spline* [29], with constants derived through the LSQ error minimization [30, 31, 32] or a ML approach [33]. Mainly derived from the WYPiWYG model [34], it focuses on solving the system of linear equations which consist coefficients of shape functions, rather than nonlinear fitting a predefined model. In elasticity, manifold learning is more efficient and more accurate than black-box ML models and it has already been generalized to cover damage [35]. In Matous’s study, a manifold-based reduced order model was proposed [36]. This model relies on non-linear dimensionality reduction and the connection of macroscopic loading parameters to reduced space using an artificial neural network (ANN). Fritzen et. al [37] proposed a data-driven homogenization method for hyper-elastic solids using the reduced order method. In their work, the surrogate model combines radial basis functions and piece-wise cubic polynomials. The main problem with these approaches is the large number of tests needed for validation and their dependency on the assumption of constitutive manifolds with a particular functional structure [32].

- **Autonomous Approaches** incorporate ML models as surrogate functions to capture the high-dimensional and non-smooth micro-scale behavior of material constituents, which has been shown to be a successful approach in Multi-scale analysis [38]. Several multi-scale methods of analysis have been proposed based on the implementation of micro-scale ML models into the reduced-order FE simulations of the macro-scale approach [18]. This coupling allows for the scalable utilization of ML surrogate models. However, the validity range of current ML models is extremely limited due a number of reasons:

- the unconstrained search space of optimization variables
- neglecting underlying physics

- difficulties in deriving parameter feasibility ranges
- lack of transition models to reduce the order of the problem

Recently by implementing the reinforcement learning concept, a new class of ML meta-models have been successfully developed based on (non)cooperative games, where the model trains a pair of L-agents to emulate a specific performance through turn-based trial and error [39]. This paradigm employs ML techniques to capture the behavior and interaction of microstructures as a surrogate model. In Stoffel’s study [40], they replaces the viscoplastic material law in finite element simulation with a feed-forward neural network to make an intelligent element. Another study [41] was conducted to predict the tension response of rubber by a feed-forward neural network. They used strain values and filler percentages as inputs generated from a regression model and stress as output.

Kaliske and Zopf [42] proposed an inelastic model-free approach represented by recurrent neural networks for uncured elastomers. For history-dependent functions, naturally, recurrent neural networks offer attractive alternatives, but require enormous amounts of training paths of standardized lengths, which are highly non-trivial. In 2019, Haghighat et al. [4] proposed a physics-informed neural network that solves any given law of physics described by non-linear partial differential equations. Another study [43] showed that the performance of this model for linear elasticity, and Xu et al. [44] modeled viscoelastic materials using physic constrained learning. Recently, we developed a a Bayesian surrogate constitutive model based on Bayesian regression and Gaussian process [45] to consider uncertainty of model [46]. A recent study [18] proposed a data-driven constitutive model by predicting a non-linear constitutive law using a neural network surrogate model constructed using a learning phase on a set of RVE non-linear computations. An investigation was conducted to formulate a constitutive model for rate-dependent materials by neural network and its implementation in finite element analysis. The challenge of sufficient data set for training, however, still remains [47].

Here, a cooperative multi-agent system $\mathcal{B}^{d_i} = \mathcal{A}_j^i$, $i \in \{1, n\}$, $j \in \{1, m\}$ is proposed to describe different features in material behavior by using $n \times m$ different machine-learned agents

(L-agents) which learn from experimental data sets. To reduce problem dimensionality, the 3D matrix is represented by m 1D directions, which allows researchers to replicate each L-agent m times to represent the 1D behavior of the material. The proposed model trains each agent to emulate a certain material behavior with the objective function being the error between the overall prediction of the system and the experimental data. Model fusion is used to integrate all L-agents back into a centralized system.

The main contributions of this work is to infuse knowledge of physics into the model through certain modeling constraints, namely (1) by providing a new data-driven model based on physics behind a machine learning process for predicting non-linear mechanical behavior of cross-linked polymers (2) the first data-driven model that captures inelastic behavior of cross-linked polymers such as Mullins effect and permanent set (3) a new paradigm with the upgrade-ability of model from hyper-elastic to damage behavior roots from easy transformation from the integration of micro-mechanics to the machine learning process (4) proposing a new model with better training speed and accuracy compared to several well-known models. There are two types of cross-linked polymers. One type shows hyper-elastic behavior; however, another type does not have hyper-elasticity at all. In this study, our focus is on cross-linked polymers which have hyper-elasticity such as rubbers and elastomers. This paper is organized as follows; in section 2.2, the main concepts of non-linear behavior and deformation-induced damage in cross-linked polymers are introduced and described in detail. Section 2.3 explains the idea and formulation of the proposed model in detail. Model verification with experimental data on rubber inelasticity is discussed in section 2.4. On resume, section 2.5 provides some concluding remarks and outlines some perspectives.

2.2 Non-linear Features in Cross-Linked Polymers

Hyper-elasticity in materials, particularly cross-linked polymers, is characterized by their nonlinear elastic response under extensive deformations. Notably, these polymers often manifest inelastic traits within their hyper-elastic behavior, such as the Mullins effect—a damage post initial elongation [48, 49]. This effect is observed in both filled and unfilled variants of cross-linked polymers.

For a deeper insight into the micro-structural origins of these inelasticities, Fig. 2.2 delineates physical sources in amorphous polymeric systems, including chain breakage [50], chain disentanglement [51], molecular slippage [52], and rupture within filler clusters [53]. Post initial loading, deformation-induced damages typically result in a residual strain termed as the permanent set. While unfilled rubbers exhibit a negligible permanent set, it becomes pronounced in most filled compounds, as illustrated in Fig. 2.2.e.

Historical attempts to model the inelastic characteristics inherent to the constitutive behavior of cross-linked polymers predominantly leaned on either phenomenological or physics-based analytical methodologies. The former, while simpler, often falter outside design conditions, whereas the latter, despite their accuracy, are overly intricate for real-time applications.

In this work, **by synergizing a physics-based methodology with machine-learned L-agents**, we introduce a knowledge-infused ML strategy to tackle the inelastic nuances in the hyper-elastic behavior of cross-linked polymers. To accurately capture the nonlinear behavior of these polymers, we employ a tailored neural network, optimizing activation functions, layer counts, and neuron numbers. Furthermore, to encapsulate damages, L-agent internal parameters are meticulously crafted, reflecting the material’s memory characteristics. For materials with a comprehensive memory, like rubbery substances exhibiting damage, the historical maximum state predominantly dictates subsequent sequences. Employing a micro-sphere as a directional model for the polymer matrix ensures the accurate representation of inelastic traits, including the permanent set. A detailed exposition of these steps is provided in the ensuing section.

2.3 Physics-based Constraining of the Solution Domain

To model the second order stress-strain fields required for characterisation of hyper-elastic material, current approaches ranging from phenomenological to data-driven, face one major challenge, namely lack of data on 3D stress-strain fields. There are no tools to measure stress field across a structure, and for strain we can only measure the strain field for relatively simple structures using digital image correlation (DIC) techniques [54].

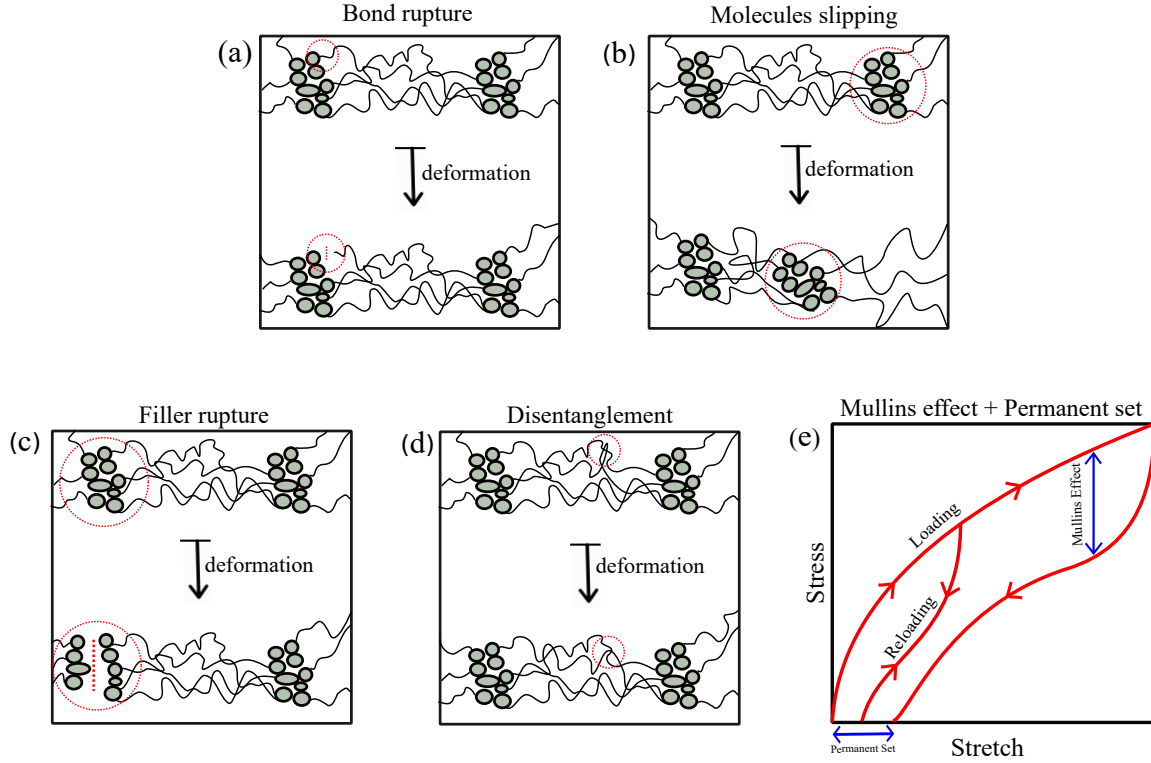


Figure 2.2. Schematic Physical explanation of Deformation Induced Damage

Helmholtz free energy Ψ is governed by deformation and temperature. Differentiating Ψ with respect to kinematic state variables at constant temperature yields internal forces (i.e. stresses) defined per unit mass. For the case in which Ψ is solely a function of deformation (i.e. isothermal processes), the Helmholtz free energy referred to as the strain energy function.

For hyper-elastic materials, strain energy is derived directly from Clausius-Planck form of second law of thermodynamics through different work conjugate pairs, such as two-point strain/stress tensors (\mathbf{F} /deformation gradient: \mathbf{P} /first-order Piola stress), material strain/stress tensors (\mathbf{E} /Lagrange strain: \mathbf{S} /second-order Piola stress), and spatial strain/stress tensors (\mathbf{L} /Hencky strain: $\boldsymbol{\tau}$ /Kirchhoff stress). Strain energy function must accompany conditions like normalization, growth conditions, isotropy, objectivity, and polyconvexity, which guarantees the uniqueness of the solution. In view of the lack of data on the stress fields, a proper modeling approach is expected to be able to only use the limited information obtained from the classical characterization tests on the collective sample behavior. In rare cases, a model can be provided by digital image correlation reconstruction of

2-D strain fields, which shall be used for model validation but should not become a necessary data for model fitting in view of the cost/complexity of the experiment. The challenge of significant missing data has been historically addressed by implementing knowledge of the material behaviour in the model and to constrain the model in advance before having the data. Such a solution is not relevant in data-driven approaches due to lack of infused knowledge of the material. Here, we propose to address the challenge of significant missing data in high-dimensional data-driven approaches through a physics-driven order-reduction approach by infusing knowledge through implementation of the concept of micro-sphere, network decomposition, continuum mechanics, and polymer physics. Accordingly, we developed a sufficiently constraint machine-learned model that can predict the material behavior solely based on the macro-scale collective behavior of the sample. Fig. 2.3 demonstrates a schematic of the proposed model simplification idea.

2.3.1 Constraining by Continuum Mechanic Laws

We introduce the first and the most important constraint from continuum mechanics understanding on 3D mapping of second order stress/strain tensors. While, $\mathbf{F} \rightarrow \mathbf{P}$ mapping generally needs a complicated fourth order tensor $\mathbf{C} = \frac{\mathbf{P}}{\mathbf{F}}$, in hyper-elastic materials, unlike hypo-elastic materials, the procedure can be simplified using an internal energy density function. Accordingly, we can use Finite strain theory to simplify $\mathbf{F} \rightarrow \mathbf{P}$ mapping by introduction of the strain energy Ψ_m as the middle agent in mapping, where $\mathbf{F} \rightarrow \Psi_m \rightarrow \mathbf{P}$. The strain energy is a non-negative scalar-valued function $\Psi_m(\mathbf{F})$ which can replace part of the process requires to derive tensor-valued stress function $\mathbf{P}(\mathbf{F})$. The increment of Ψ_m denotes the stress required to change the strain field, and thus Ψ_m can be described with respect to any stress-strain work conjugates such as (i) two-point tensors, (ii) material tensors, or (iii) spatial tensors, as shown below

$$\mathbf{P} = \frac{\partial \Psi_m}{\partial \mathbf{F}}, \quad \mathbf{S} = \frac{\partial \Psi_m}{\partial \mathbf{E}}, \quad \boldsymbol{\tau} = \frac{\partial \Psi_m}{\partial \mathbf{L}}. \quad (2.1)$$

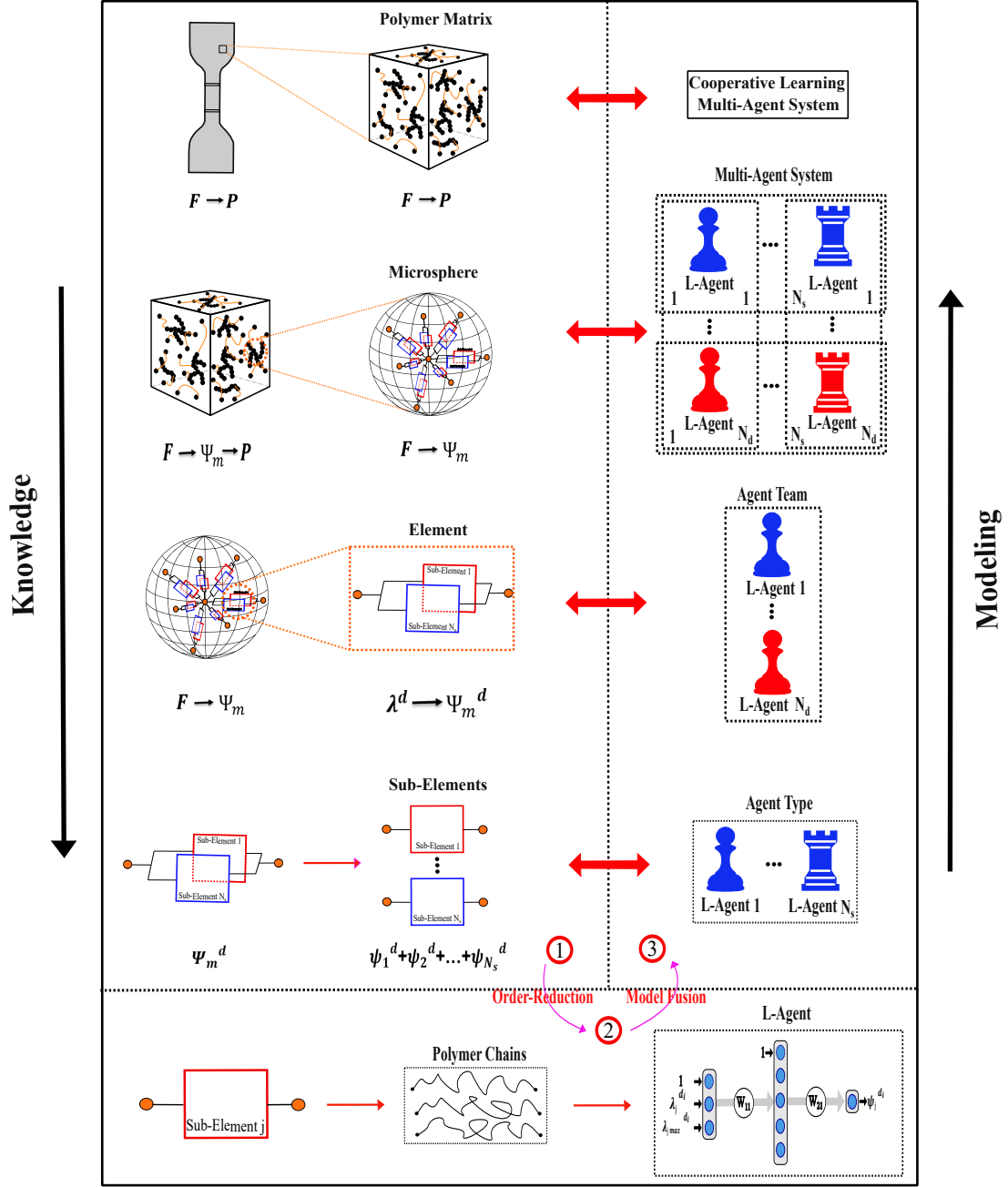


Figure 2.3. Schematic of proposed model from order-reduction to model fusion

One particular advantage of using Ψ_m as middle agent is that it ensures the material objectivity, and thermodynamic consistency on all the derived constitutive model (see Truesdell et al. [55]). Considering the physics of the problem, certain restrictions exist for strain energy which needs to be enforced further in the data-driven model, namely

$$\begin{aligned}
\Psi_m(\mathbf{F}) &\geq 0 \quad \text{when} \quad \mathbf{F} \neq \mathbf{0} && \text{Increase energy by deforming,} \\
\Psi_m(\mathbf{F}) &= 0 \quad \text{when} \quad \mathbf{F} = \mathbf{I} && \text{Normalization condition,} \\
\Psi_m(\mathbf{F}) &\rightarrow \infty \quad \text{when} \quad \det \mathbf{F} \rightarrow \infty/0 && \text{Growth condition.}
\end{aligned} \tag{2.2}$$

Further restrictions can be introduced by finite strain theory to ensure stability of Ψ_m in large deformations of certain materials. For hyper-elastic materials, ellipticity is a major concern which can be enforced by verifying the strain energy in the absence of traction forces in two arbitrary directions [56]. Verifying this condition is generally labor-intensive, so polyconvexity is introduced as a stronger condition that entails ellipticity. It is also simpler to verify [57]. *So, the first constraint that we enforce in our model, is enforcing agents to derive $\Psi_m(\mathbf{F})$ such that it satisfies Eq. 2.2 and polyconvexity condition.*

2.3.2 Constraining by Micro-Sphere Concept

Micro-sphere concept is developed for materials which are initially isotropic. Here, the second constraint that is implemented is based on Micro-sphere concept to include the initial isotropy of cross-linked amorphous network. Knowing amorphous systems are isotropic at virgin state, polymer chains are considered to be uniformly distributed in all spatial directions. Such homogenized spatial arrangement of polymer chains allow us to use the micro-sphere concept to represent the 3D matrix as a homogeneous assembly of similar 1D elements that are distributed in different spatial directions over a micro-sphere (see Fig. 2.3). This approach can transfer information from super-simplified 1D elements to generate complex 3D behavior of the matrix via homogenization over the unit-sphere. Furthermore by discretizing the sphere into finite sections, the integration can

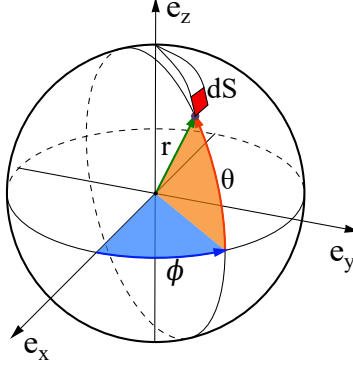


Figure 2.4. The unit micro-sphere and the orientation vector in terms of spherical coordinates

be taken out numerically over N_d integration directions $[\mathbf{d}_i]_{i=1\dots N_d}$ with different weight factors $[w_i]_{i=1\dots n}$ [58]. Accordingly, strain energy of the matrix Ψ_m with respect to its elements can be written as

$$\Psi_m = \frac{1}{4\pi} \int_S \Psi_m^{\mathbf{d}} dS^{\mathbf{d}} \cong \sum_{i=1}^{N_d} w_i \Psi_m^{\mathbf{d}_i}, \quad \text{where} \quad \Psi_m^{\mathbf{d}_i} = \mathcal{B}^{\mathbf{d}_i} \quad (2.3)$$

where $\Psi_m^{\mathbf{d}_i}$ is the energy of sub-matrix element in direction \mathbf{d}_i which will be represented by one team of L-agent $\mathcal{B}^{\mathbf{d}_i}$ which represents an additive cooperation between multiple L-agents \mathcal{A}_{\bullet}^i . Eq2.3 represents the integral $S(\theta, \phi) = \int_0^\theta \int_0^\phi \sin(\theta) d\theta d\phi$ over the unit-sphere with the unit vector $\mathbf{r} = \sin(\theta) \cos(\phi) \mathbf{e}_x + \sin(\theta) \sin(\phi) \mathbf{e}_y + \cos(\theta) \mathbf{e}_z$ (see Fig. 2.4). Assuming identical team in all directions in the virgin state, namely $\mathcal{B}^{\mathbf{d}_i} = \mathcal{B}^{\mathbf{d}_j}$, initial isotropy is assured, although the material can quickly become anisotropic due to different loading on different directions. Moreover, since L-agents react to varying loading in each direction, the model can consider the onset of damage, deterioration, and propagation of cascading failure in materials with directional response.

2.3.3 Problem Reduction using Network Decomposition Concept

The third constraint is derived from statistical mechanics, namely by infusing the concept of superposition, which allow us to predict complicated patterns by superposing simple patterns on top of each other. The concept, a.k.a network decomposition concept in constitutive modeling [59], will be carried out by representing the energy of an element, $\Psi_m^{\mathbf{d}_i}$ by superposing the energy of

multiple sub-elements, $\Psi_m^{d_i} = \sum_{j=1}^{N_s} \Psi_j^{d_i}$, where each sub-element is responsible for one simple inelastic feature. Representing each sub-elements by one L-agent, we can calculate the energy of one element by a team of cooperative L-agents $\mathcal{B}^{d_i} = [\mathcal{A}_j^i]$, and then replicating this cooperative team in different directions to provide us with the energy of the matrix.

To this end, by substituting Eq.(2.3), we can directly derive the energy of the matrix with respect to sub-elements and the L-agents which represent them as given here

$$\begin{aligned} \Psi_m &= \frac{1}{4\pi} \int_S \Psi_m^d dS^d \cong \sum_{i=1}^{N_d} \sum_{j=1}^{N_s} w_i \psi_j^{d_i} \\ \Psi_m &\approx \sum_{i=1}^{N_d} \sum_{j=1}^{N_s} w_i \mathcal{A}_j^i \quad \text{where} \quad \Psi_m^{d_i} = \sum_{j=1}^{N_s} \mathcal{A}_j^i. \end{aligned} \quad (2.4)$$

where N_s is the number of sub-elements considered for each element. Consequently, we derived super-simplified scalar-to-scalar mapping behaviour for each element which can be represented simplified 2-layer feed-forward neural network L-agent \mathcal{A}_j^i . While training data are only available on collective behaviour of the L-agents, the input parameters can be defined for each L-agent team individually. Each L-agent, $\mathcal{A}_j^i := \psi_j^i(\mathbf{E}^i, \mathbf{M}_j)$, will be trained based on a set of non-kinematic input \mathbf{E}^i and internal \mathbf{M}_j parameters, which depending on material memory (full or recent), can satisfy normalization, growth conditions, isotropy, objectivity, and polyconvexity.

The input vector is independent of the sub-element definition and should represent the problem setting, material or loading, e.g. stretch & time. Internal parameters are specifically hypothesized for the model to capture the evolution of damage and vary for each network. The behavior of all teams should be identical in the virgin state to represent initial isotropy, so one has $\mathcal{A}_j^i = \mathcal{A}_j^k \forall i \neq k$. Accordingly, we only assume different ANN types for L-agents associated to different sub-elements. All replicated agents associated to one sub-element are the same despite being distributed in different teams to represent different directions.

For the replicated agents, only the inputs are different depending on their direction (see

Fig.2.3). So the energy of one sub-element can be written as

$$\psi_j^{d_i} = \mathcal{A}_j^i = \text{ANN}_j(\mathbf{W}_j, \mathbf{E}^i, \mathbf{M}_j), \quad (2.5)$$

where \mathbf{W}_j is the weight vector associated to L-agent \mathcal{A}_j^\bullet , and $\mathbf{W} = [\mathbf{W}_1 \dots \mathbf{W}_{N_s}]$ is the weight matrix representing assembly of all \mathbf{W}_j . Consequently, based on Eqs. 2.1 and 2.4, the first Piola-Kirchhoff stress tensor \mathbf{P} can be derived as

$$\mathbf{P} = \frac{\partial \Psi_m}{\partial \mathbf{F}} - p \mathbf{F}^{-T} \mathbf{P} = \sum_{i=1}^{N_d} \sum_{j=1}^{N_s} w_i \frac{\partial \mathcal{A}_j^i}{\partial \mathbf{F}} - p \mathbf{F}^{-T}, \quad (2.6)$$

where p denotes the Lagrange multiplier to guarantee incompressibility of the material. To train the model, a cost function should be derived to quantify prediction error against experimental observations on collective sample behaviour, e.g. uni-axial tensile test provides 1D dataset $\mathcal{S} = [\tilde{P}, \tilde{\lambda}]$, with nominal stress \tilde{P} and stretch $\tilde{\lambda}$ in direction of principal stretch. Here, the error has been quantified using least-square method by writing

$$E(\mathbf{W}) = \frac{1}{2} \sum_{n=1} \left[\mathbf{g}_1 \left(\sum_{i=1}^{N_d} \sum_{j=1}^{N_s} w_i \frac{\partial \psi_j^{d_i}}{\partial \mathbf{F}} - p \mathbf{F}^{-T} \right) \mathbf{g}_1 - P_n \right]^2, \quad (2.7)$$

which $P_{(1,1)} := \mathbf{g}_1 \mathbf{P} \mathbf{g}_1$ is the first component of the experimental macro-scale stress tensor \mathbf{P} in loading direction \mathbf{g}_1 .

Neural-network L-agents: Artificial neurons, often termed as nodes, constitute the foundational units of the neural system. These nodes facilitate the reception and transmission of information to their counterparts via activation functions. The efficacy of an Artificial Neural Network (ANN) agent's "learning" capability hinges significantly on the judicious selection of the activation function for each node. Activation functions determine the activation state of a neuron, introducing non-linearity to its output. This non-linearity enables the model to adapt to diverse data sets and discern between outputs. The cost function aids in estimating \mathbf{W} , employing the gradient descent (GD) algorithm to iteratively refine the initial approximation towards target values.

Material With Full or Recent Memory: For materials exhibiting history-dependent properties, it's imperative to meticulously select parameters that encapsulate the material's memory. These parameters are subsequently integrated into the L-agents via internal parameters. The nature of these memory parameters varies based on the material in question. For instance, visco-elastic materials, which possess recent memory, necessitate internal parameters that relay information from one iteration to the subsequent one. Conversely, materials with comprehensive memory, like elastomers, allow for the definition of internal parameters that are decoupled from solution iterations. In such cases, these parameters act as precursors to external events, such as using the maximum stretch in rubber as an indicator of the historical peak loading in a given direction.

2.4 Implementation to Rubber Inelasticity

To show the performance of the proposed model, inelastic behavior of rubber has been studied. The number of teams and their associated agents can be chosen based on the trade-off between accuracy and computational cost. Here, we choose 21 teams, each with two agents which is a relatively small number [58] (21 integration-point). The inputs and internal parameters of L-agents are designed to capture the rubbers deformation with full memory through λ_{j-max} parameters. To enable teams to predict different states of deformation, each teams should be provided with the first and second invariants of deformation[60]. The condition is satisfied by providing input set $\mathbf{S}_1^{d_i} = [\lambda^{d_i}; \lambda_{max}^{d_i}]$ to L-agent 1 and $\mathbf{S}_2^{d_i} = [\nu^{d_i}; \nu_{max}^{d_i}]$ to L-agent 2

$$\lambda^{d_i} = \sqrt{\mathbf{d}_i \mathbf{C} \mathbf{d}_i}, \quad \nu^{d_i} = \sqrt{\mathbf{d}_i \mathbf{C}^{-1} \mathbf{d}_i}, \quad \mathbf{C} = \mathbf{F}^T \mathbf{F} \quad (2.8)$$

where λ^{d_i} and ν^{d_i} are designed that lead to first and second sub-elements represent the I_1 and I_2 , respectively. For the ANN structure of L-agents, we consider one input layer, one hidden layer with four neurons and three activation functions soft plus ($\psi(\bullet) = \ln(1 + e^\bullet)$), sinusoid ($\psi(\bullet) = \sin(\bullet)$) and hyperbolic tangent ($\psi(\bullet) = \tanh(\bullet)$). In summary, we represented the rubber matrix by the cooperative game of 21 teams of 2 agents through \mathcal{A}_j^i , $i \in \{1, 21\}$, $j \in \{1, 2\}$.

Final cost function after agents fusion is given by

$$E(\mathbf{W}_1, \mathbf{W}_2) = \frac{1}{2} \sum_{n=1}^{21} [\mathbf{g}_1 \left(\sum_{i=1}^{21} \sum_{j=1}^2 w_i \frac{\partial \mathcal{A}_j^i}{\partial \lambda_j^{d_i}} \frac{\partial \lambda_j^{d_i}}{\partial \mathbf{F}} - p \mathbf{F}^{-T} \right) \mathbf{g}_1 - P_n]^2, \quad (2.9)$$

subjected to weights related to λ_{max} and $\nu_{max} \leq 0$; and weights related to λ and $\nu \geq 0$ to satisfy thermodynamic consistency and polyconvexity respectively. Eq. 2.10 and Eq. 2.11 show the derivation of each sub-element's energy with respect to deformation gradient. Accordingly, Fig. 2.3 shows the schematic concept of the derived model.

$$\sum_{i=1}^{21} w_i \frac{\partial \mathcal{A}_1^i}{\partial \lambda^{d_i}} \frac{\partial \lambda^{d_i}}{\partial \mathbf{F}} = \sum_{i=1}^{21} w_i \frac{\partial \mathcal{A}_1^i}{\partial \lambda^{d_i}} \frac{1}{\lambda^{d_i}} \mathbf{F} (\mathbf{d}_i \otimes \mathbf{d}_i). \quad (2.10)$$

$$\sum_{i=1}^{21} w_i \frac{\partial \mathcal{A}_2^i}{\partial \nu^{d_i}} \frac{\partial \nu^{d_i}}{\partial \mathbf{F}} = - \sum_{i=1}^{21} w_i \frac{\partial \mathcal{A}_2^i}{\partial \nu^{d_i}} \frac{1}{\nu^{d_i}} \mathbf{F}^{-1} \mathbf{F}^{-T} \mathbf{F}^{-1} (\mathbf{d}_i \otimes \mathbf{d}_i). \quad (2.11)$$

2.4.1 Minimizing Data Requirement for Training

Data-set Minimization A critical step in the selection of the training dataset is to understand the role of the training points and assure their quality in the model predictions. Too little data may provide a false sense of confidence by preventing us to see the critical points, while low-quality data may provide faulty results which seems perfectly robust. For example, in the aforementioned model developed for rubber, we have introduced two L-agent types which represents two sub-elements using $\mathbf{S}_1^{d_i}$ and $\mathbf{S}_2^{d_i}$ input sets, respectively. In view of the definition of $\mathbf{S}_2^{d_i}$, we know that it has a limited variation in uni-axial tensile loading which makes the contribution of the second L-agent almost limited in such loading. However, $\mathbf{S}_2^{d_i}$ significantly varies in bi-axial loading, which makes the contribution of second L-agent quite considerable in this case. Therefore, training with uniaxial data cannot provide quality information needed for confident training of both agents since second-agent cannot be fully engaged.

In essence, we cannot train agents with the scenarios that they are not participating in or have minimal contribution. Thus, the confidence in training of agents is directly correlated to the quality

of the training data, and in contribution of agents in those scenarios. However, by defining the quality of data with respect to the input required by each agent, we can quantify the **confidence interval** in which an agent can be trained with high confidence with respect to the provided data.

The confidence interval of a system is equal to that of its agent with least confidence. The confidence of an agent can be calculated with respect to the deformation range used in each direction for training of that agent. Since the reliability of the predictions of each agent is related to its training, we can linearly correlate the agent's reliability to their training range. As an example, in case of uniaxial tension where the sample is stretched till χ_x , maximum first deformation state (axial) is χ_x which occurs in the loading direction, and minimum is $\frac{1}{\sqrt{\chi_x}}$, which occurs in the transverse directions. Similarly, the training domain for the second agent is $[\frac{1}{\chi_x}, \sqrt{\chi_x}]$. In case of bi-axial tension, range of agents deformations are $[\frac{1}{\chi_{bi.}^2}, \chi_{bi.}]$ and $[\frac{1}{\chi_{bi.}}, \chi_{bi.}^2]$.

If we train the model based on uniaxial tensile data till χ_x , the model can predict different states of deformation based the ranges that the model have calibrated based on that. In order to ensure accurate prediction of the model, the prediction ranges should be in the range that agent is trained. Thus, in the bi-axial prediction case, the model limits to

$$\begin{aligned} \text{Agent 1:} \quad & \left[\frac{1}{\chi_{bi.}^2}, \chi_{bi.} \right] \in \left[\frac{1}{\sqrt{\chi_x}}, \chi_x \right] \longrightarrow \chi_{bi.} \leq \sqrt[4]{\chi_x} \\ \text{Agent 2:} \quad & \left[\frac{1}{\chi_{bi.}}, \chi_{bi.}^2 \right] \in \left[\frac{1}{\chi_x}, \sqrt{\chi_x} \right] \longrightarrow \chi_{bi.} \leq \sqrt[4]{\chi_x}. \end{aligned} \quad (2.12)$$

As it can be in Eq. 2.12, these two ranges result into a same confidence interval for the agents. Accordingly, considering one of these agents confidence interval would be sufficient to calculate the network reliability. Likewise, these training/prediction domains can be calculated for different cases of traing and predictions with different states of deformation, see table 2.1. To show the confidence interval, we explore five different training data set and their resulting agents. Using two set of experiments for the training purpose can increase the predictability range of the model as each of the experiments can be activated in different ranges and agents. Note that the model may extrapolate and predict more than confidence interval but it is not necessarily accurate.

Table 2.1. Prediction domain for train till stretch χ

Prediction \ Training	Uni. ¹ Tensile	Bi. ²	Pure Shear	Uni. Comp. ³	Plane Strain Comp.
Uni. Tensile	χ	χ	χ	$\frac{1}{\sqrt{\chi}}$	$\frac{1}{\chi}$
Bi.	$\sqrt[3]{\chi}$	χ	$\sqrt[3]{\chi}$	$\frac{1}{\sqrt{\chi}}$	$\frac{1}{\chi}$
Pure Shear	χ	χ	χ	$\frac{1}{\sqrt{\chi}}$	$\frac{1}{\chi}$
Uni. Comp.	$\frac{1}{\sqrt{\chi}}$	$\frac{1}{\chi^2}$	$\frac{1}{\chi}$	χ	χ
Plane Strain Comp.	$\frac{1}{\sqrt{\chi}}$	$\frac{1}{\chi^2}$	$\frac{1}{\chi}$	χ	χ

1. **Training with uniaxial only vs biaxial only** Mars dataset which has three modes of pure shear, uni-axial and bi-axial tensile tests have been used [61]. In first case, the model is trained by bi-axial data only till $\chi = 1.65$ and validated against other modes (see Fig. 2.5.a). Confidence interval in uniaxial and pure shear predictions is also limited to $\chi = 1.65$.

In second case, the model is trained by uniaxial data only till $\chi = 2.18$ and validated against other modes (see Fig. 2.5.b). Confidence interval in shear will be limited to $\chi = 2.18$ but in bi-axial will be dramatically reduced to $\chi = 1.21$ due to the uncertainty in training L-agent 2.
2. **Training with uniaxial only over a long range** Here, we showed that we can improve the confidence interval of one agent not only by choosing the games in which it has high contribution, but also by increasing the length of the game in which one agent has small contribution. *In essence, we can have a short game with high contribution, or long game with low contribution.* In case of rubber, uniaxial tension is a game in which 2nd L-agent has low contribution. So, here we show that for a sufficiently long game (uni-axial till $\chi = 7.7$), we can increase the confidence interval for the second L-agent (bi-axial till $\chi = 1.66$), see Fig. 2.5.c Treloar dataset which has three modes of pure shear, uni-axial and bi-axial tensile tests have been used [62].
3. **Training with uni-axial Tension and Compression** Here, we showed that we can improve the confidence interval by using multiple games to train the agents. So, here model is trained by uniaxial tensile (till $\chi = 3.7$) and compression data (till $\chi = 0.4$). The confidence in

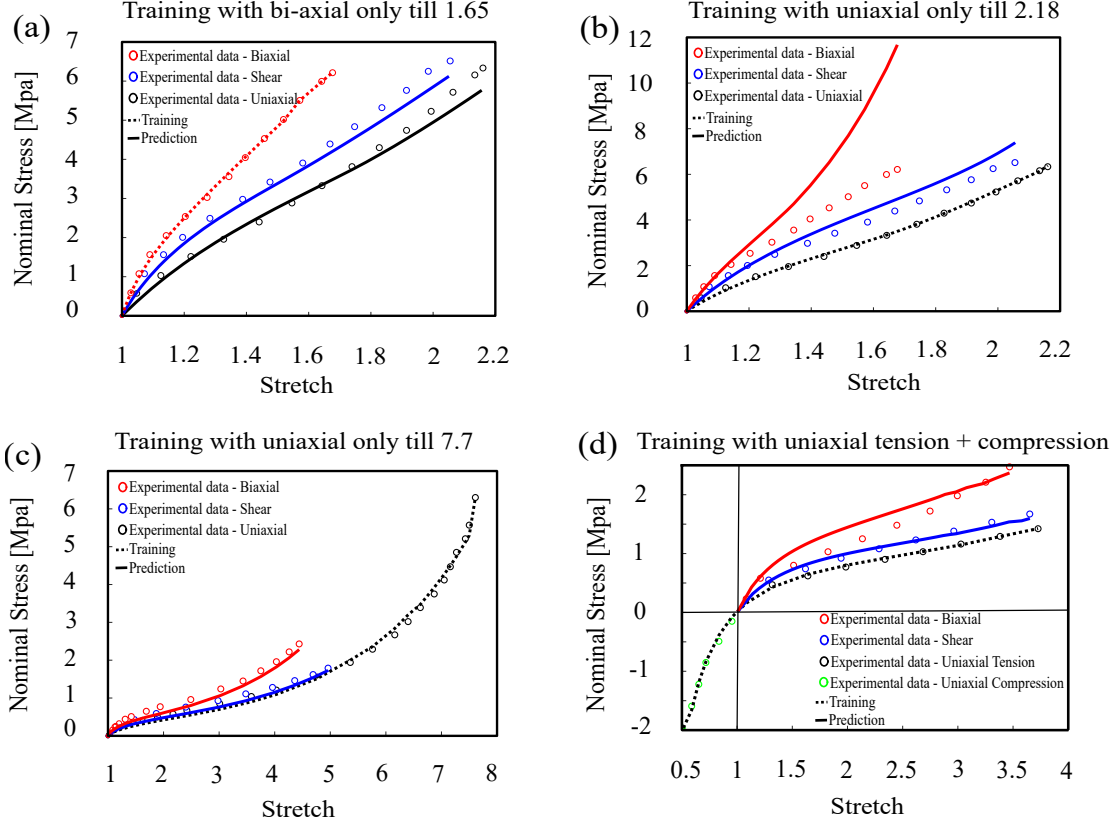


Figure 2.5. Model training and prediction with a) bi-axial tension training (filled natural rubber) b) uniaxial tension training (data set [61]) c) uniaxial tension training (Treloar's data set [62]) d) uniaxial tension and compression training (data set [63])

training of the 1st L-agent is mainly defined by the uni-axial tensile test while that of the 2nd L-agent is formed by compression test. The predictions of the trained agents were validated against other modes (see Fig. 2.5.d), and as expected confidence interval in bi-axial till $\chi = 1.58$ and pure shear predictions is also limited to $\chi = 3.7$. Heuillet data-set with three modes of pure shear, uniaxial and bi-axial tensile tests have been used for training/validation.

Accuracy within Confidence Interval The proposed engine shows exceptional accuracy within the confidence interval which is comparable to some of the most comprehensive and most expensive knowledge-based models. We have shown the predictions of the models against different sets of data provided by Uramaya[64] and Mars [61], where the model were trained using bi-axial tests only, see Fig. 2.6. Bi-axial tests were chosen to provide the longest confidence interval for other

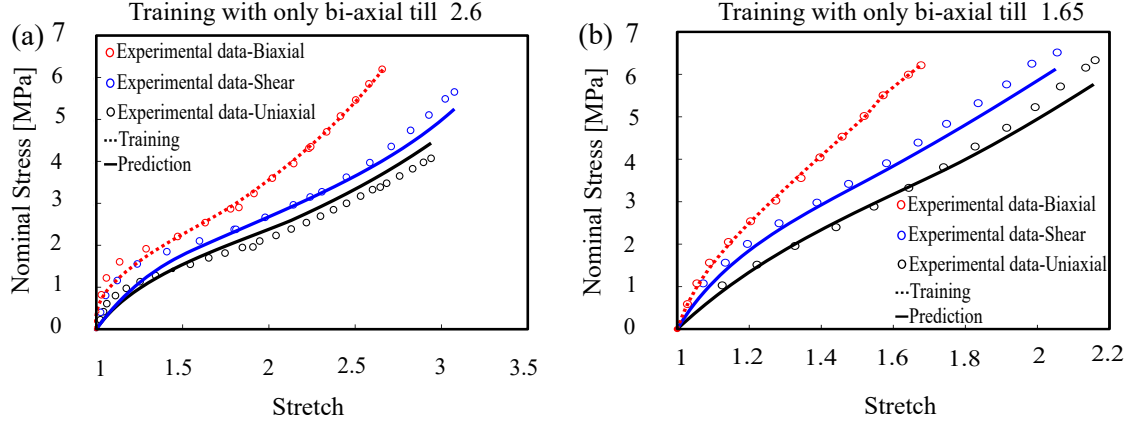


Figure 2.6. Model training and prediction of uniaxial, bi-axial and pure shear a) Urayama's data set [64] b) Mars's data set [61]

Table 2.2. Relative error for several well-known models for Treloar's data set

Model Type	AI	Phenomenological	Micro-Mechanical	
	Proposed model	WYPiWYG model [29]	Non-affine micro-sphere model [65]	Network averaging tube model [66]
Error(%)	1.12	5.26	0.93	2.11
Training Set	Uniaxial	Uniaxial	Uniaxial + Pure shear + Bi-axial	Uniaxial + Pure shear + Bi-axial

modes (see table 2.1).

To show the performance of the proposed model, we compared the relative error of our model in fitting and prediction of Treloar's data set with the non-affine micro-sphere model [65], WYPiWYG model [29], and network averaging tube model [66]. Note that the error reported for the non-affine micro-sphere model and network averaging tube models **is fitting error not prediction error**, since they have used all three uniaxial, bi-axial, and pure shear at the same time in their published results.

Although the proposed model and WYPiWYG model use uniaxial data for training and predict other states of deformation. Thus, results show the excellent performance of our model; however, the proposed model is not complicated and data-dependent as much as other physics-based models (see table 2.2).

The compression behavior of rubber-like material is another aspect that plays an essential role in industrial application. We trained the model with the data set of uniaxial compression experiments

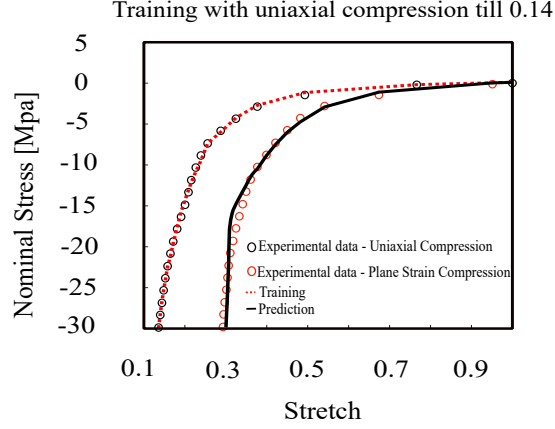


Figure 2.7. Model training with uniaxial compression and prediction of plane strain compression (Arruda-Boyce’s data set [67])

and predicted the behavior of plane strain compression. Fig. 2.7 shows the performance of the proposed model for compression tests. The error in training and prediction of the proposed model for Arruda-Boyce data is 0.73%, which compared to the non-affine micro-sphere model, which has 1.29% error, shows a significant performance of our less complicated model.

Damage Prediction and Deformation History To further investigate the performance of the proposed model in material with full memory, we predicted the inelastic features in the behaviour of filled elastomer, namely Mullins effect and permanent set. Fig. 2.8 shows that stress-stretch curves for this cross-linked polymer with experimental data of [64]. We used one set of bi-axial loading-unloading till $\chi = 2.7$ for training and predict inelastic effects in different states of deformation e.g. uniaxial and pure pure shear at increasing stretch amplitudes which constitutes deformation histories.

Convergency outside of the confidence interval To investigate the convergency of the proposed model outside of the confidence, prediction of the inelastic behaviour on stretch amplitudes larger than the confidence interval were illustrated on two different sets of experimental data on rubber, Itskov’s [68] and Zhong’s [69] dataset. While we strongly recommend the users to stay within confidence interval, the model prediction accuracy outside of the confidence interval shows the

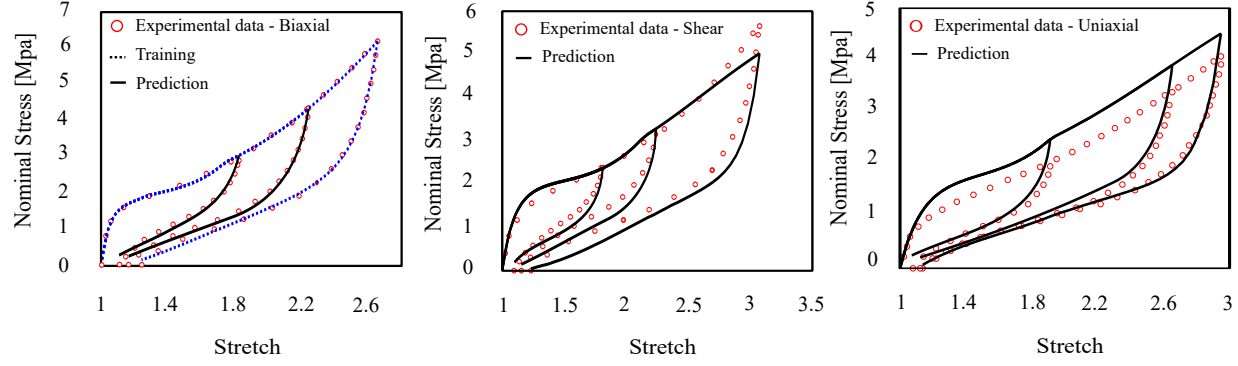


Figure 2.8. Model training and prediction of uniaxial, bi-axial and pure shear (Urayama's data set [64])

relevance and reliability of the model in extreme cases which is mainly resulted from the constraints induced by knowledge infused into the model. Results indicated that the trend and proposed model performance (Fig. 2.9 and Fig. 2.10). Here, we gradually reduce the confidence interval by using smaller range of training data to see the drop in quality of predictions. As expected, despite accuracy reduction, there is no significant change in the model predictions profile which is not usually the case for extrapolation methods. In Fig. 2.9.a, we trained the model with the largest amplitude. As we expected, the error in training and prediction is 4.6%. As we reduce the amplitude of training in Fig. 2.9, we see that the error has increased generally. There is an instability in the errors and overestimating in Fig. 2.9.b and Fig. 2.9.c which root from numerical simplification and choosing same neural network structures and activation functions for different sets of data for training. The important point is that we want to show that the model is accurate for different modes of training. To ensure our result is general for different elastomers, we did the same training procedure for another dataset (Fig. 2.10). The result shows the same results as the last dataset.

2.5 Conclusion

A physics-informed data-driven constitutive model for cross-linked polymers is developed by embedding Neural networks into a multi-scale model. We propose a systematic approach to reduce the order of the constitutive mapping by leveraging existing knowledge of polymer science, continuum physics, and statistical mechanics. We use our model to predict the mechanical behavior

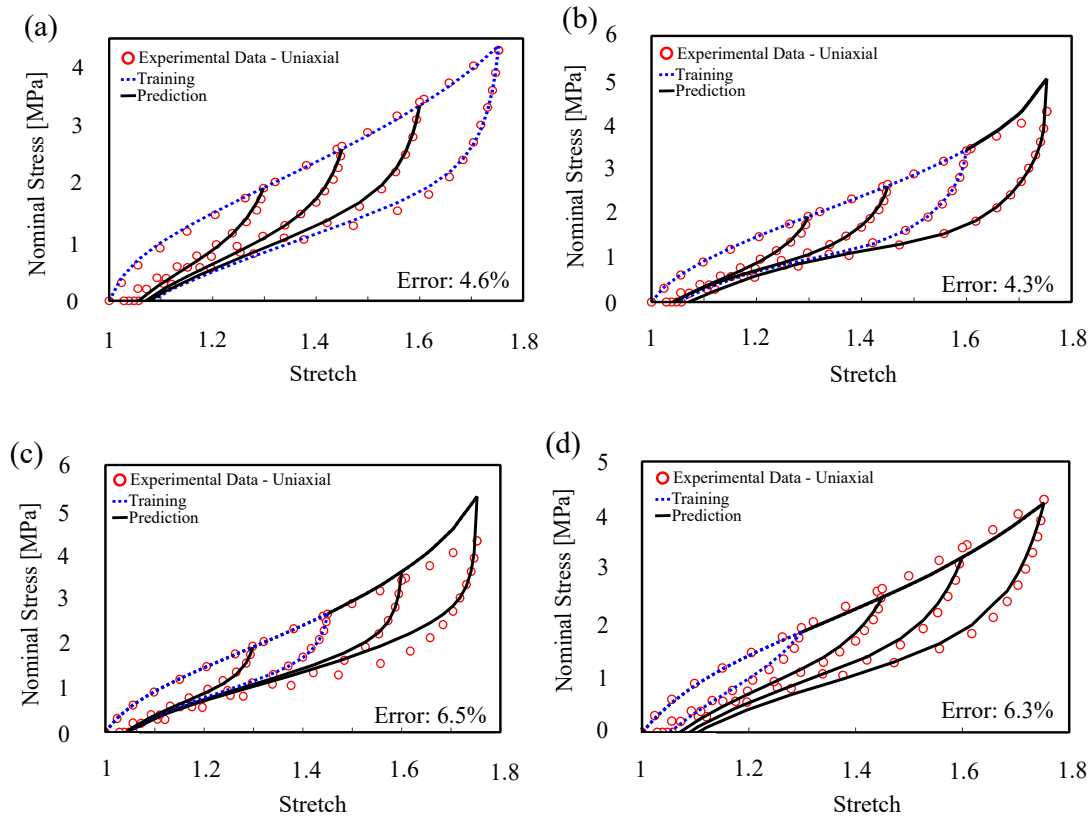


Figure 2.9. Model training and prediction of cyclic uniaxial tension with step-wise increasing of amplitude (Itskov's data set [68])

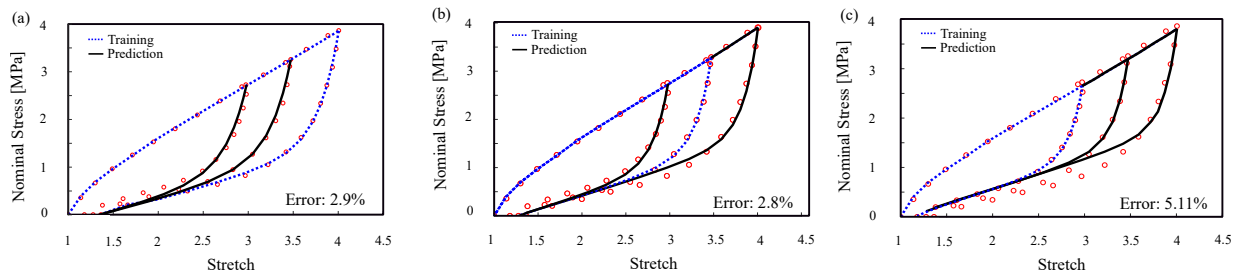


Figure 2.10. Model training and prediction of cyclic uniaxial tension with step-wise increasing of amplitude (data set [69])

of filled elastomers. The results indicate that our model can easily capture multiple inelastic effects in the behavior of the materials, is significantly less data-dependent, has lower dimensionality, and is interpretable. To illustrate the superior performance of knowledge-driven models developed by this approach, its predictions are bench-marked against several experimental data sets. We compare the stress responses from Treloar's data set in our model with several well-known models to show the accuracy and simplicity of our model. In summary, our model provides a hyper-elastic constitutive model which captures damage of polymer chains for cross-linked elastomers for quasi-static loading. In the future, the proposed model can be further extended to include the effect of the deformation rate. The modular platform nature of the proposed model allows the addition of such effects.

CHAPTER 3

MACHINE-LEARNED CONSTITUTIVE MODEL FOR STRAIN RATE, TEMPERATURE, AND COMPOUND

3.1 Introduction

Classification of Cross-Linked Polymers Response Fig. 3.1 illustrates two loading cycles of a uniaxial tensile test, elucidating this phenomenon. A pristine particle-filled rubber specimen, when loaded to stretch $\lambda^{(1)}$ via Path 1 and subsequently unloaded to a stress-free state through Path 2, exhibits an intersection with the positive λ – axis at stretch $\lambda_{re}^{(1)}$, denoting the specimen’s residual extension. Reloading the specimen to a stretch $\lambda^{(2)}$ exceeding $\lambda^{(1)}$ traces Path 3, followed by unloading along Path 4, resulting in an expanded residual stretch $\lambda_{re}^{(2)}$. Due to the stress-softening effect, the stress at identical stretch levels along Path 2 (Path 4) is considerably diminished compared to Path 1 (Path 3). The permanent set, representing the residual stretch post complete unloading, may undergo a gradual reduction over time. Empirical observations [70] indicate that post-loading, the reloading curve is subdued compared to the virgin material’s initial loading curve but elevated relative to the unloading curve. The disparity between unloading and reloading trajectories epitomizes the hysteresis phenomenon, predominantly attributed to strain rate effects [71, 72].

Cross-linked polymers have strong non-linear elasticity associated with inelastic effects in their overall behavior. Because of the underlying polymer micro-structure inside the polymer matrix, amorphous polymers display rate-dependent finite elastic-plastic behavior. The realignment of kinks, rearrangement of convolutions, reorientation, and uncoiling of molecular chains as the load is accommodated results in this behavior. Temperature fluctuation, on the other hand, can have an impact on the mechanical characteristics of these materials. They may be exposed to the outdoors or

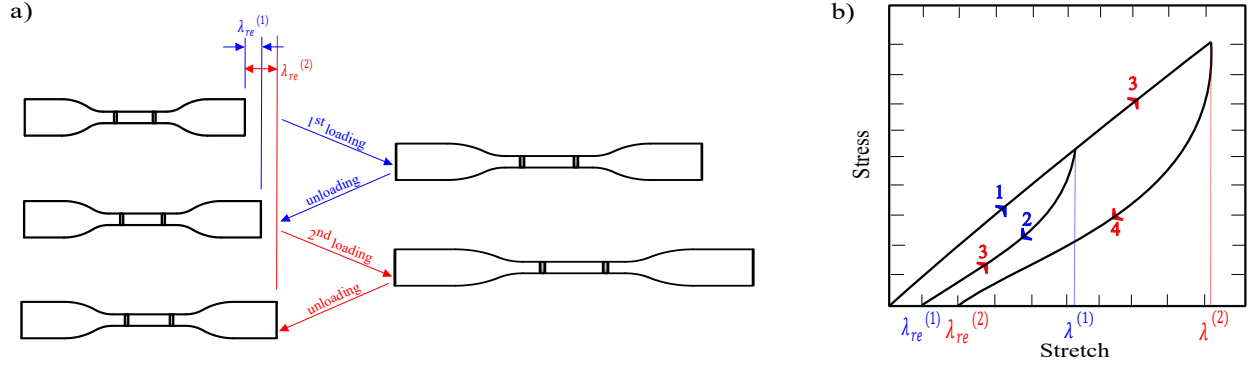


Figure 3.1. The Mullins effect schematic with a permanent set. a) Two uniaxial tensile cycles deformation based on ASTM D412-C [73], and b) the related stress-stretch curves

have internal heating as a result of energy dissipation. The majority of theoretical and experimental research on this topic has been done at room temperature [1]. However, these materials' mechanical characteristics should be explored at temperatures other than room temperature. The interaction between the filler and the polymer matrix is also affected by temperature changes. As a result, filled polymers display more complicated non-linear behavior that is temperature-dependent. As a result, developing a temperature-dependent and filler-dependent, strain rate constitutive model that predicts the inelastic behavior of cross-linked polymers in various states of deformation for a wide range of strain, strain rate, temperature, and filler concentration to be applicable for various types of operations is extremely important and challenging.

Constitutive Approaches to Model Strain rate of Soft Materials Phenomenological models, which are based on a collection of material properties, do not take into account the microphysics of materials [70, 74]. Micro-mechanical analysis, on the other hand, is based on the statistical mechanics of polymer structure and uses physical meaning in its analysis. Micromechanical models that include functions and material factors linked to microstructure take into account microstructural data; however, their practical applicability is restricted owing to their high computing costs and lengthy training procedure.

With the increase of the computational capacity, Data-driven approaches can address the limits of the analytical models derived based on continuum mechanics. Recently, increasing attention has

been given to developing data-driven approaches that are directly derived based on material data. Tang et al. [75, 76] proposed a mechanistic-based, data-driven approach for numerical analysis, and they demonstrated that this mechanistic-based approach could exploit the deep physical insights obtained from well-established finite strain theory and experimental evidence. At the same time, this approach can circumvent issues in establishing explicit functions to characterize material behaviors [77].

In this chapter, a physics-informed data-driven strain rate model was developed to predict the constitutive and failure behavior of the cross-linked polymers that integrates conditional artificial neural networks (CNN) into continuum reconfiguration. The data-driven constitutive model developed in this study can consider the synergistic effect of strain rate, temperature, polymer type, and filler ratio. A practical two-step method is proposed in the data training stage, enabling highly effective training using only a small amount of experimental data. To validate the approach, the proposed method was applied to investigate the mechanical behaviors of NR and SBR under various loading conditions. Our proposed network architecture has several advantages compared to other researches. Firstly, it is able to integrate strain rate, temperature and filler percentage together with physics to accurately predict the behavior of elastomers, allowing for more accurate predictions. Secondly, it uses a deep learning approach that enables the model to learn the complex interactions between the different parameters, allowing it to make more accurate predictions than traditional approaches. Finally, by incorporating physics into the model, it provides a more comprehensive understanding of how the elastomer behaves, allowing for more accurate predictions.

In this chapter, a physics-informed data-driven nonlinear rate-dependent constitutive model is proposed based on our recent work on implementing knowledge into NN models, which captures not only compounding ratios but also temperature and strain rate effects.

3.1.1 Mechanical Damage: Cooperative Multi-Agents System

Through the hard implementation of the physical laws into the neural network, we already discussed how the mechanical damage in constitutive behavior of polymer matrix could be represented by

cooperative multi-agents system \mathcal{A}_j^i , $i \in \{1, n\}$, $j \in \{1, m\}$, based on our last study [78]. The model can explain different features in the material behavior with $n \times m$ different learning agents. The objective is to minimize the collective error between the predicted system performance and the experimental data. Each agent is trained to provide a specific material behavior that minimizes the total error. To bring all of the agents back into a centralized system, model fusion is employed. Our model represents each agent by a simple deep-learned neural network (NN) constrained by the hard implementation of physical laws into a neural network.

Constitutive behaviour of the virgin material is modeled based on our recent paper [78] using a set of collaborative shallow neural network agents.

In our recent paper, we suggested a framework to use ideas from continuum mechanics, statistical physics, and polymer science to create super-constrained reduced-order machine learning algorithms, which could partially solve the present challenges. We have simplified the 3D stress-strain tensor mapping problem into a small set of super-constrained 1D mapping problems via sequential order reduction. Then, we added a collection of numerous replicated neural network learning agents (L-agents) to categorize those mapping issues into a select few groups, each of which was described by a different sort of agent. Accordingly, the polymer matrix continuum has been represented by a microsphere constructed by polymer chains that are uniformly and equally dispersed in all spatial directions. Micro-sphere concept is valid for materials that are initially isotropic and incompressible. The volumetric strain energy of the microsphere was then expressed by integrating the energy of chains in all directions as $[\mathbf{d}_i]_{i=1 \dots N_d}$. Assuming the 3D polymer matrix to be a homogeneous super-assembly of various 1D polymer bundles dispersed in all spatial directions, the energy of the sphere, Ψ_m , may be easily calculated by integrating the energies of all the components, as

$$\Psi_m = \frac{1}{4\pi} \int_S \Psi_m^d dS^d. \quad (3.1)$$

Using this approach, the behaviour of the polymer matrix can be modeled by having the

behaviour of basic 1D components. To calculate the energy of all 1D components, a surface integration may be carried out numerically across N_d integration directions $[\mathbf{d}_i]_{i=1\dots N_d}$ with different weight factors $[w_i]_{i=1\dots n}$. Such integration can be performed by discretizing the sphere into finite sections. Therefore, it is possible to express the strain energy of the polymer matrix Ψ_m in terms of its constituents as

$$\Psi(\mathbf{F}) = \frac{1}{4\pi} \int_S \psi^d dS^d \cong \sum_{i=1}^{N_d} w_i \psi^{d_i}, \quad \text{where} \quad \psi^{d_i} = \mathcal{B}^{d_i} \quad (3.2)$$

where \mathbf{F} stands for macro-scale deformation gradient, $\Psi_m^{d_i}$ is the element's energy in direction \mathbf{d}_i and is represented by a group of L-agents \mathcal{B}^{d_i} that, using the microsphere idea, represents the cooperative addition of many L-agents $\mathcal{B}^{d_i} = \sum_{j=1}^{N_s} \mathcal{A}_j^{(i)} = \sum_{j=1}^{N_s} \mathcal{N}_j^{(i)}(\mathbf{x}_e, \Theta_e)$. We assume that, in the virgin state, $\mathcal{B}^{d_i} = \mathcal{B}^{d_j}$, all multi-agents are identical in order to meet initial isotropy. It is crucial to reformat the energy of a single polymer chain with respect to $\lambda^d = \sqrt{\mathbf{d}^T \mathbf{F}^T \mathbf{F} \mathbf{d}}$ as follows because chains in different orientations are subject to multiple micro-stretches. As a result, we may directly extract the matrix's energy in terms of sub-elements and L-agents.

$$\Psi_m = \frac{1}{4\pi} \int_S \Psi_m^d dS^d \cong \sum_{i=1}^{N_d} \sum_{j=1}^{N_s} w_i \psi_j^{d_i} := \sum_{i=1}^{N_d} \sum_{j=1}^{N_s} w_i \mathcal{A}_j^i. \quad (3.3)$$

If each sub-element is characterized by an L-agent, a simplified feed-forward neural network will represent the super-simplified scalar-to-scalar mapping behavior of the sub-element.

The first Piola—Kirchhoff stress tensor \mathbf{P} may be calculated using Eqs. 3.1 and 3.3 to summarize the enforced restrictions.

$$\mathbf{P} = \frac{\partial \Psi_m}{\partial \mathbf{F}} - p \mathbf{F}^{-T} := \sum_{i=1}^{N_d} \sum_{j=1}^{N_s} w_i \frac{\partial \mathcal{A}_j^i}{\partial \mathbf{F}} - p \mathbf{F}^{-T}, \quad (3.4)$$

where p is the Lagrange multiplier used to assure the material's incompressibility.

\mathbf{P} may therefore be written as

$$\mathbf{P} = \frac{\partial \Psi_M(\mathbf{F})}{\partial \mathbf{F}} - p \mathbf{F}^{-T}, \quad \frac{\partial \Psi_M(\mathbf{F})}{\partial \mathbf{F}} = \sum_{i=1}^k w_i \frac{\partial \mathcal{B}^{d_i}}{\partial \lambda^{d_i}} \frac{1}{2\lambda^{d_i}} \frac{\partial d_i \bar{\mathbf{C}} d_i}{\partial \bar{\mathbf{F}}} : \frac{\partial \bar{\mathbf{F}}}{\partial \mathbf{F}}, \quad \text{while } \psi^{d_i} = \mathcal{B}^{d_i}, \quad (3.5)$$

where \mathbf{C} is the right Cauchy–Green tensor, $\bar{\mathbf{F}} = \mathbf{J}^{-1/3} \mathbf{F}$, and $\bar{\mathbf{C}} = \mathbf{J}^{-2/3} \mathbf{C}$. Additionally, by applying the following identities, Eq. 3.5 might be made even simpler as follow

$$\frac{\partial d \bar{\mathbf{C}} d}{\partial \bar{\mathbf{F}}} : \frac{\partial \bar{\mathbf{F}}}{\partial \mathbf{F}} = 2 \bar{\mathbf{F}} (d \otimes d) : \mathbf{J}^{-\frac{1}{3}} \mathbb{I} = 2 \mathbf{J}^{-\frac{1}{3}} \bar{\mathbf{F}} (d \otimes d). \quad (3.6)$$

Normalization, conditions of growth, isotropy, objectivity, and poly-convexity are already satisfied in the proposed equation in our recent paper [78].

Maximum micro-stretch in history λ_{max}^d : In the course of deformation, polymer chains begin to slide on or debond from the aggregates. This debonding starts with the shortest chain and gradually involves longer and longer chains. Under unloading, the debonded chains do not reattach back to the aggregate's active sites, and thus the maximal microstretch previously reached in the loading history,

$$\lambda_{max}^d = \max_{\tau \in (-\infty, t]} \lambda^d(\tau) \quad (3.7)$$

is crucial for the description of the polymer-filler debonding.

3.2 Strain Energy of the damage matrix

Given the multiple multiplicative elements involved in deriving the strain energy of the damaged matrix, we proposed using a Conditional Neural Network (CondNN) to represent the energy of each L-agent. The reason for the importance of this is having a model to predict superficial damage in non-aged material and also predict hardening in virgin but aged material.

3.2.1 Conditional Neural Network (CondNN) L-Agent

A simple N -layer multilayer feed-forward neural network comprising an input layer, $N - 1$ hidden layers, and an output layer. We suppose that the n^{th} hidden layer has N_n neurons. The previous layer's post-activation output $\mathbf{x}^{n-1} \in \mathbb{R}^{N_{n-1}}$ is then fed into the n^{th} hidden layer, and the specific affine transformation is of the form

$$\mathcal{H}_n(\mathbf{x}^{n-1}) \triangleq \mathbf{W}^{(n)}\mathbf{x}^{n-1} + \mathbf{b}^{(n)}, \quad (3.8)$$

where the network weight $\mathbf{W}^{(n)} \in \mathbb{R}^{N_n \times N_{n-1}}$ and the bias term $\mathbf{b}^{(n)} \in \mathbb{R}^{N_n}$ to be learned are both initialized using unique procedures like Xavier or He initialization [79, 80].

The nonlinear activation function $\sigma(\cdot)$ is applied component-by-component to the current layer's affine output \mathcal{H}_n . Furthermore, for some regression issues, this nonlinear activation is not employed in the output layer. As a result, the neural network may be denoted as

$$\mathcal{N}(\mathbf{x}; \Theta) = (\mathcal{H}_N \circ \sigma \circ \mathcal{H}_{N-1} \circ \cdots \circ \sigma \circ \mathcal{H}_1)(\mathbf{x}), \quad (3.9)$$

where \circ denotes the composition operator, $\Theta = \left\{ \mathbf{W}^{(n)}, \mathbf{b}^{(n)} \right\}_{n=1}^N \in \mathcal{P}$ denotes the learnable parameters to be optimized later in the network, and \mathcal{P} denotes the parameter space, and \mathcal{N} and $\mathbf{x}^0 = \mathbf{x}$ denote the network's output and input, respectively.

Conditional Neural Networks (CondNN) are a continuum of machine-learned models which are hybrids of two extreme machine-learning algorithms, computationally efficient trees, and super-accurate Neural Networks (see [81, 82]). CondNNs lie in between the two extremes, and we can tune the hyper-parameters to generate CondNNs with different efficiency/accuracy trade-offs. By using the routing feature from the decision tree, CondNNs can use conditional routing to confine computation to only a small region of the network rather than involving all nodes. Such capability makes CondNNs particularly relevant for complex problems where the outputs are not only dependent on past events, such as deformation-induced matrix damages, but also on external data, which can be loading conditions or compound properties.

Routed behavior, in which data is transmitted to one or more children depending on a learned routing function, is a characteristic of decision trees. In other words, CondNNs are decision trees with the difference that instead of nodes, shallow NNs are being used (see Fig. 3.2). Note that we can use routing conditions to derive physical or chemical evolution parameters or a combination thereof. Also, such architecture can be scaled to include other external effects such as aging, creep, swelling, or plasticity.

Conditional neural networks are advantageous in comparison to simple neural networks because they can be used to provide chances for more efficient and effective learning. These networks allow for the learning process to be tailored to specific conditions, meaning that the network can better adjust to the data it is given and can better predict future outcomes. This allows for more accurate and detailed predictions, as the network can adjust itself to the conditions that are being presented to it. Additionally, conditional neural networks allow for more efficient and effective learning as they can better identify patterns and make better predictions, leading to faster and more accurate results.

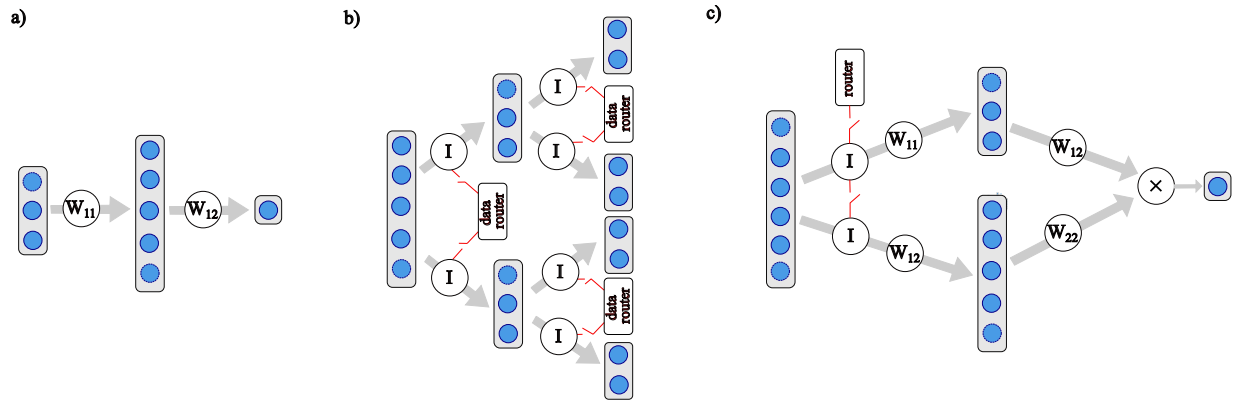


Figure 3.2. Schematic figures for a) a compact graphical notation for neural networks, b) a representing decision trees, and c) a generic conditional network

- Engine Setup with multiple CondNNs The hyper-parameters summary and inputs determine the design of the neural network: (i) the number of hidden layers, n_l (network depth), (ii) the number of neurons per hidden layer, n_n (network width), and (iii) the activation function.

So, we can write

$$\mathcal{E}_p = \mathcal{N}_p(\mathbf{x}_p, \Theta_p^{(i)}), \quad \mathcal{E}_c = \mathcal{N}_c(\mathbf{x}_c, \Theta_c^{(i)}), \quad \psi_{0:j}^{d_i} = \mathcal{N}_e(\mathbf{x}_e, \Theta_e^{(i)}), \quad (3.10)$$

Next, we define the loss function \mathcal{L} Mean Squared Error (MSE) for a total of n_{tot} data points as

$$\mathcal{L}(\mathbf{x}, \Theta) = \frac{1}{2} \sum_{n=1}^{n_{tot}} \left[\mathbf{g}_1 \left(\sum_{i=1}^{N_d} \sum_{j=1}^{N_s} w_i \frac{\partial(\mathcal{E}_p \mathcal{E}_c \psi_{0:j}^{d_i})}{\partial \mathbf{F}} - p \mathbf{F}^{-T} \right) \mathbf{g}_1 - P_n^{11} \right]^2, \quad (3.11)$$

where $P_n^{11} := \mathbf{g}_1 \mathbf{P}_n \mathbf{g}_1$ is the first component of the experimental macro-scale stress tensor \mathbf{P}_n in loading direction \mathbf{g}_1 for point n .

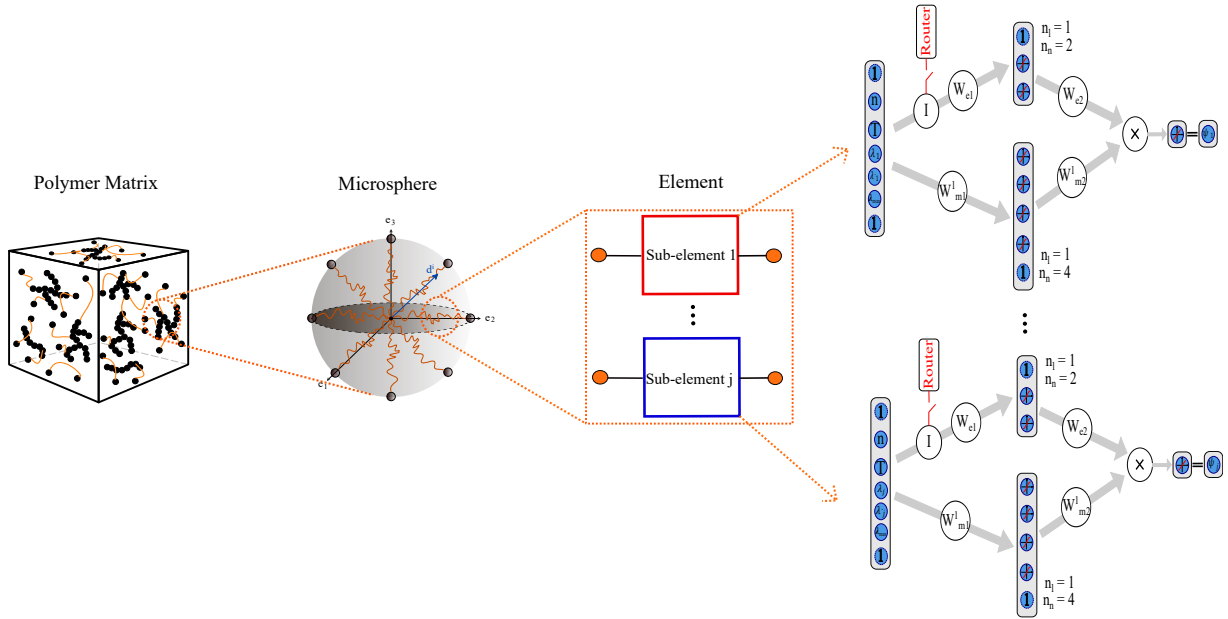


Figure 3.3. Illustration of the suggested model, which includes order-reduction and model fusion. It demonstrates how we propose a knowledge-based platform using ideas from continuum mechanics, polymer sciences, physics, and machine learning

3.3 Experimental Validation

For benchmarking, the proposed engine has been trained and validated in four different loading scenarios

1. Digital materials that promote relaxation

2. modeling strain rate effects on uni-axial tension and compression
3. modeling individual and combination of the temperature and filler-ratio effects on constitutive behavior
4. modeling coupled effects of the temperature and strain rate on constitutive behavior

To evaluate engine's prediction at different stages of deformation, the predictions were benchmarked against experimental data in all scenarios.

3.3.1 Engine Architecture

We employed an identical engine to mimic both loading scenarios, and the engine is made by $N_d = 21$ teams, each with $N_s = 2$ L-agents [83]. It is worth noting that the number of teams and associated L-agents were determined based on the accuracy/efficacy trade-off. We evaluated one input layer, one hidden layer with four neurons, and three activation functions soft plus $\psi(\bullet) = \ln(1+e^\bullet)$, sinusoid $\psi(\bullet) = \sin(\bullet)$, and hyperbolic tangent $\psi(\bullet) = \tanh(\bullet)$ for the CondNNs structure of L-agents. We are employing a shallow network to guarantee the convergence of FEM analysis.

To capture the deformation of the rubbers with complete memory, the internal parameters of L-agents were developed using λ_{j-max} parameters. The first and second deformation invariants were provided to each team in order to allow them to anticipate possible deformation states [60]. The requirement was met by feeding input sets to the first and second L-agents in the following order

$$\mathbf{x}_p^{(i)} = [\lambda^{d_i}, \dot{\lambda}^{d_i}, \lambda_{max}^{d_i}], \quad \mathbf{x}_c^{(i)} = [T], \quad \mathbf{x}_e^{(i)} = [n, \dot{\lambda}^{d_i}, \lambda_{max}^{d_i}], \quad (3.12)$$

while

$$\lambda^{d_i} = \sqrt{\mathbf{d}_i \mathbf{C} \mathbf{d}_i}, \quad \mathbf{C} = \mathbf{F}^T \mathbf{F} \quad (3.13)$$

where λ^{d_i} is connected to I_1 , as the first invariants of \mathbf{C} .

In conclusion, the rubber matrix was represented as a cooperative game with 21 teams of two agents through \mathcal{A}_j^i , $i \in \{1, 21\}$, $j \in \{1, 2\}$. The ultimate cost function of the engine after agent fusion is given as

$$\mathcal{L}(\mathbf{x}, \Theta) = \frac{1}{2} \sum_{n=1}^{n_{tot}} \left[\mathbf{g}_1 \left(\sum_{i=1}^{21} \sum_{j=1}^2 w_i \frac{\partial \mathcal{A}_j^i}{\partial \lambda_j^{d_i}} \frac{\partial \lambda_j^{d_i}}{\partial \mathbf{F}} - p \mathbf{F}^{-T} \right) \mathbf{g}_1 - P_n^{11} \right]^2, \quad (3.14)$$

assuming $\lambda_{max} \leq 0$, and weights related to λ , and $\dot{\lambda} \geq 0$ to satisfy thermodynamic consistency and poly-convexity, respectively.

Grid search is a powerful tool for hyperparameter selection and can help to identify the optimal set of hyperparameters for a given model. Based on that, we tuned the model's hyperparameter such that a range of hyperparameters and their respective values are identified, and the performance of each set of hyperparameters is evaluated. The set of hyperparameters that yields the best performance is then selected as the optimal set of hyperparameters that should be used. Also, the model training time is less than a few minutes due to the simplicity of the model. However, the time can be reduced by using more powerful hardware, such as GPUs or multiple CPUs, in order to speed up the training process.

Results for Elastomers We assess the performance of the suggested model in this part using experimental data from multiple elastomers in various rate ranges. First, we look at uniaxial deformations since evaluating the effectiveness of suggested models in simple deformations, which are easier to test, is a standard method (actually, most available data in the literature are for uniaxial tension or uniaxial compression). The following set of data was used for benchmarking (see Table 2).

- **HDR compression experiment** Our engine was validated against monotonic HDR compression experiments at low to moderate strain rates [84]. To eliminate the Mullins effect, each virgin specimen was exposed to five pre-loading cycles before the actual test, as described in [84]. Our engine predictions and the experimental data are in strong agreement, as shown in Fig.3.4(a). HDR's behavior did not show a significant shift at rates higher than 0.88/s,

Table 3.1. The summary of the experimental datasets used for benchmark

Material	Loading Type	Feature	Reference
HDR	compression	strain rate	[84]
Black filled rubber	uniaxial	strain rate	[85]
Polyurea	uniaxial	high strain rate	[86]
Rubber	uniaxial	temperature	[87]
SBR	uniaxial	filler ratio	[88]
PVA	uniaxial	temperature and strain rate	[89]

according to [84]. Note that dot lines have been used for training and the solid lines show the performance of the model in prediction after the training.

- **Tensile tests on carbon black filled rubber** [85] After removing the Mullins effect, the experiments were carried out on five different specimens using monotonic strain-controlled tension. The tests were performed at low to moderate strain rates, and the data is recorded as nominal stress vs. stretch. When compared to the experimental data, the performance is illustrated in Fig.3.4(b). Note that dot lines have been used for training and the solid lines show the performance of the model in prediction after the training.
- **Polyurea behavior at high strain rates** using a drop weight tensile testing device[86]. In view of the high flexibility and economic feasibility of polyurea, the high rate-dependent deformation behavior of polyurea was used for benchmarking. The comparison against experiments is shown in Fig.3.4(c). Experiments show that at rates exceeding 400/s, the material's behavior becomes nearly rate-independent, which is exactly what the model predicts.
- **Uniaxial Tensile Test at Different Temperatures** Seasonal temperature changes can cause significant variations in the mechanical properties of rubber. Therefore, the impact of temperature on the mechanical properties of rubber must be considered. Although the mechanical responses of filled and unfilled rubber have been characterized at room temperature, the effects of temperature on the mechanical response of rubber materials in a certain deformation range have rarely been studied [87]. Four types of rubber materials filled with different

contents of carbon black were used in this study[87]. The rubber matrix was natural rubber, and the filled carbon black was N234. The proposed model has been benchmarked against these results to show the performance of the model in predicting the effects of temperature on the mechanical response of rubber materials (see Fig.3.5).

- **Uniaxial tensile tests on SBR with different filler ratio** The data of four styrene-butadiene rubbers filled with 30, 40, 50, or 60 phr carbon-black N347 and constructed of the identical gum composition were used to validate our engine's predictive capabilities [88]. Each material softens to some extent when loaded to maximum strain, and this is reflected in a gentler reaction when unloaded. The comparison against experiments is shown in Fig.3.6. Note that dot lines have been used for training and the solid lines show the performance of the model in prediction after the training.

Results for PVA We have previously shown that our constitutive model can properly predict uniaxial tension test data for elastomers. Uni-axial tension tests for dual-crosslink PVA [89] at various temperatures, and strain rates may also be accurately predicted, as shown below. We forecast the stress-stretch curve for uni-axial constant stretch rate tension tests using weights gained during model training and compare these predictions to test outcomes. Model predictions are compared to three temperature and two loading rate tests in Fig. 3.7. There is a high agreement between model predictions and experimental evidence. Fitting is shown by dashed lines, whereas prediction is represented by solid lines.

Results for Digital Materials In this paragraph, we use the weights derived from VHB 4910's stress relaxation training to demonstrate the model's relaxation capture ability. The VHB was loaded at a stretch rate of $\dot{\lambda} = 0.1613/s$, as shown in Fig.3.8(b). This sample is stretched at a set pace, and once it reaches $\lambda = 2, 4, 6$, it is held in that stretch for 900s before being loaded again. When it hits the $\lambda_{max} = 7$ maximum stretch, it is emptied at the same pace. Please read this article [91] for more information. The experiment's outcome is depicted in Fig.3.8(a). Our strain

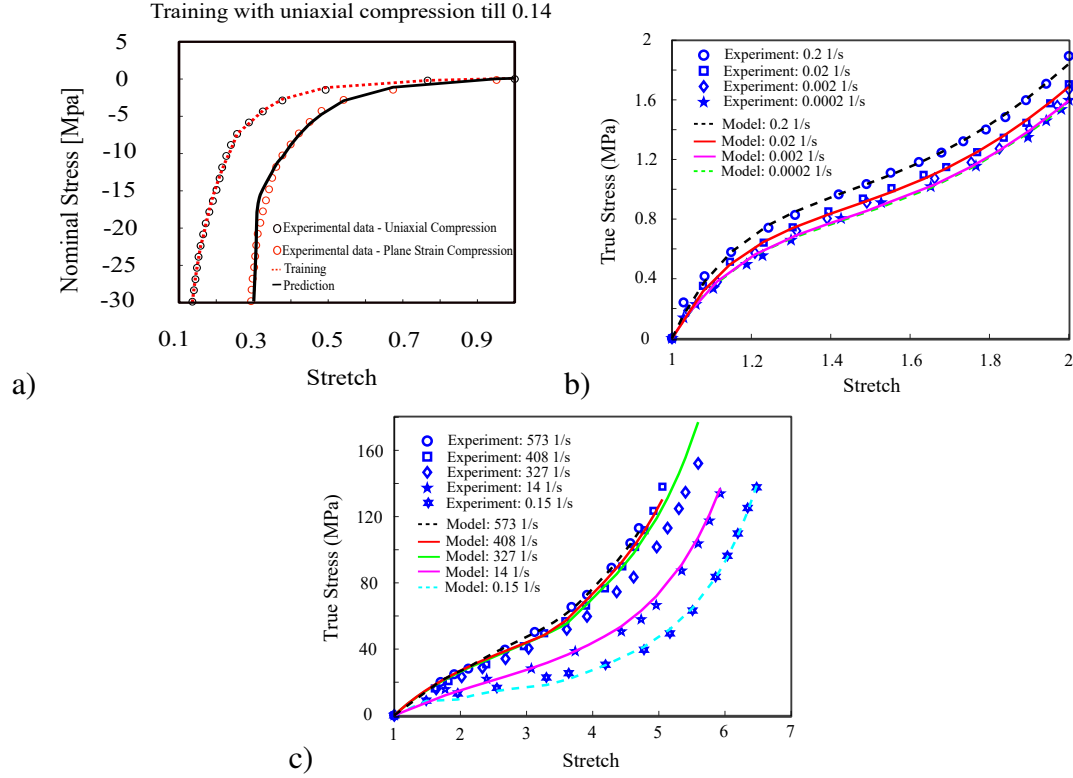


Figure 3.4. a) Comparison of the proposed model results with [84] nonlinear's uniaxial compression test data for high damping rubber, b) Comparison of the proposed model results with [85] uniaxial extension test data for carbon black filled rubber, and c) Comparison of the proposed model results with [86] uniaxial extension test data for polyurea. Fitting is shown by dashed lines, whereas prediction is represented by solid lines

rate model can well capture the relaxation behavior of VHB in loading, relaxing, and unloading operations, as illustrated in Fig.3.8. Note that due to the lack of using convolution integral in our model, it is not able to predict behavior that has a different situation from the training dataset.

3.4 Summary

The purpose of this study was to expand our most recent model, [78], to include the impacts of strain rate, temperature, and percentage of filler without sacrificing the accuracy of the prior model in order to make the previous model more complete. To anticipate the inelastic hyperelastic behavior of soft materials, a large strain three-dimensional physics-informed data-driven model was developed. Despite significant attempts to predict hyperelasticity and its influence on the

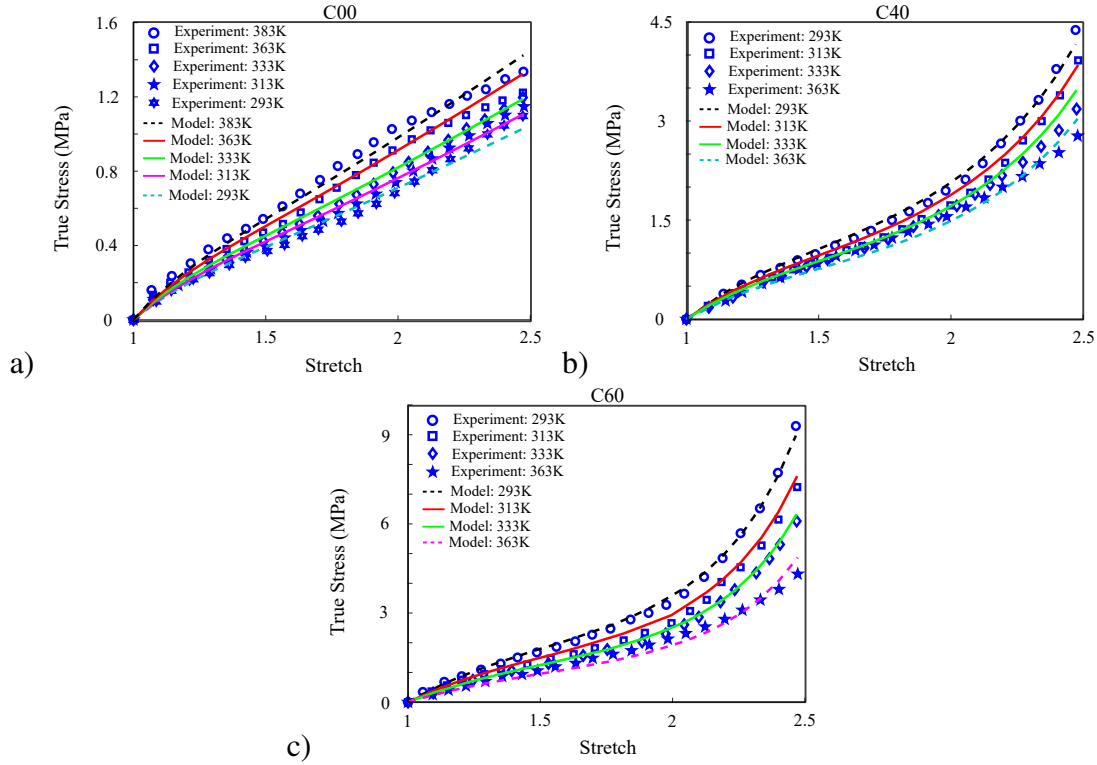


Figure 3.5. Based on the suggested model and the uniaxial extension test results provided by [87], stress-strain curves of three types of carbon black filled vulcanized rubber compounds a) C00, b) C40, c) C60 at different temperatures. Fitting is shown by dashed lines, whereas prediction is represented by solid lines

mechanical performance of soft materials, there have been few models that can concurrently account for strain rate, temperature, and filler percentage with acceptable computational resources. By order-reduction into a 1D mapping issue, we used polymer science, statistical physics, machine learning, and continuum mechanics techniques to simplify 3D stress-strain tensor mapping. The mechanical behavior of VHB 4910, elastomers, and hydrogel was predicted using our model. The results reveal that our model accurately describes the hyperelastic behaviors of soft materials. Based on the findings of the proposed model on various datasets, the following conclusions may be drawn. (1) The suggested model has predicted rubber stress-strain curves at various strain rates that were in good agreement with the experimental data. The developed model may, therefore, properly represent the hyperelastic mechanical behavior of soft materials over a specified deformation range. (2) The devised approach was evaluated for its ability to represent the temperature dependency of elastomer mechanical performance. (3) The suggested model was used to create a filler-dependent

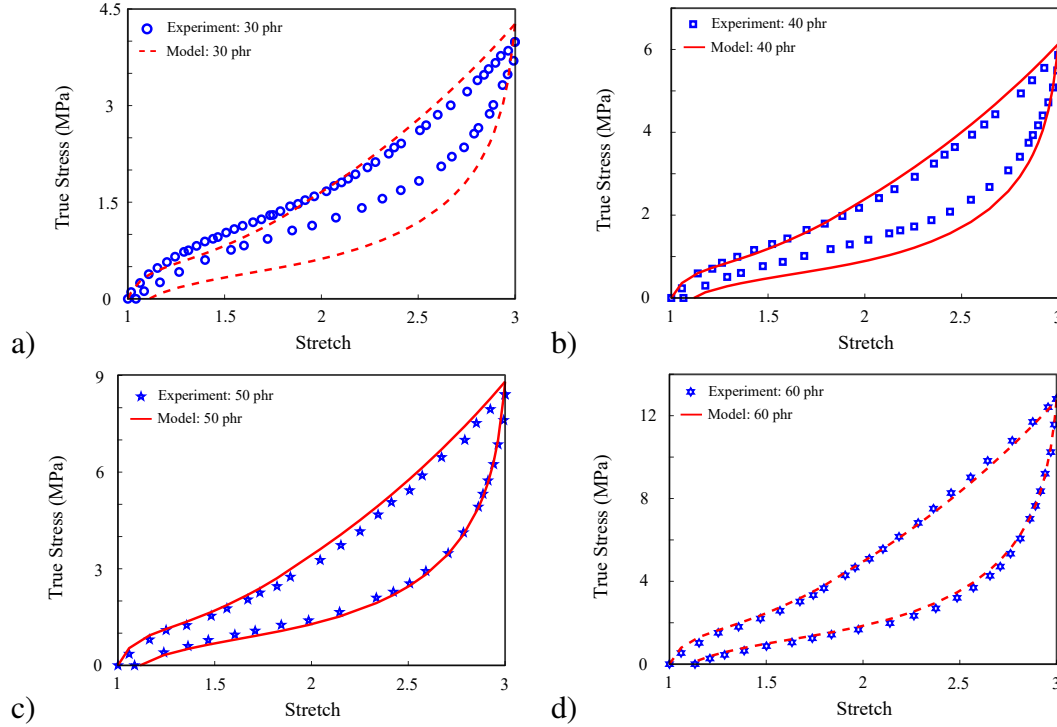


Figure 3.6. The suggested model was used to compare the outcomes of four rubbers manufactured of the same SBR gum and filled with either 30, 40, 50, or 60 phr of N347 carbon-black when they were subjected to cyclic uniaxial loading-unloadings, as described by [88]. Fitting is shown by dashed lines, whereas prediction is represented by solid lines

model with specific filler-quantity parameters. At various filler quantities, the explicit filler quantity model may adequately explain the hyperelastic mechanical behavior of rubber. Because of its computing speed, simplicity, correctness, and interpretability programs for FE, the model is an excellent choice for advanced implementations.

Note that Hybrid methods combine data-driven and physics-based approaches to tackle complex problems. While these methods often have the advantage of combining the best of both worlds, they also present certain limitations. Data-driven methods rely on large amounts of training data to approximate a solution. This reliance on data means that these methods are limited by the quality and quantity of the data available. If the data is incomplete or noisy, the resulting solution may be inaccurate. Additionally, data-driven methods do not take into account any physical or theoretical constraints. On the other hand, physics-based methods rely on theoretical models to approximate a solution. These models are often complex and require a great deal of knowledge to

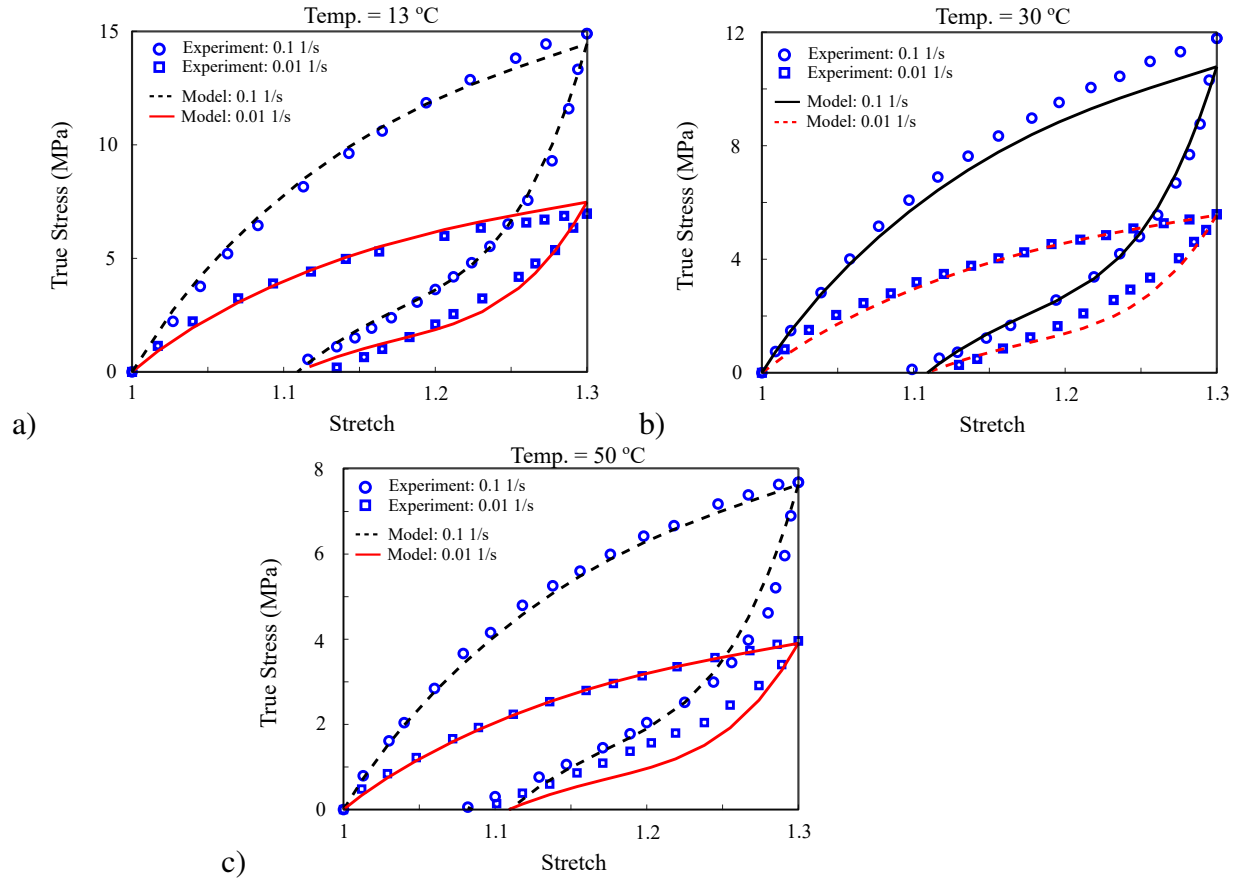


Figure 3.7. [90] provided a comparison of model and experimental testing at two distinct stretch rates and temperatures of (a) 13°C, (b) 30°C, and (c) 50°C. Fitting is shown by dashed lines, whereas prediction is represented by solid lines

implement correctly. Additionally, physical laws are often too restrictive and may not capture all of the complexity of a problem. The limitations of hybrid methods arise from the limitations of both data-driven and physics-based methods. Hybrid methods combine the best of both approaches, but they are still limited by the availability of data and the complexity of the physical models. Hybrid methods are also limited by the time and effort required to develop and implement them. Finally, hybrid methods tend to be more difficult to interpret, as they combine the complexity of both data-driven and physics.

Also, the shape and size of the sample in tensile testing have a direct effect on the output of the test. The shape of the sample affects the stress-strain curve, which is the output of the test. The size of the sample affects the maximum load that can be applied before the sample fails. In general,

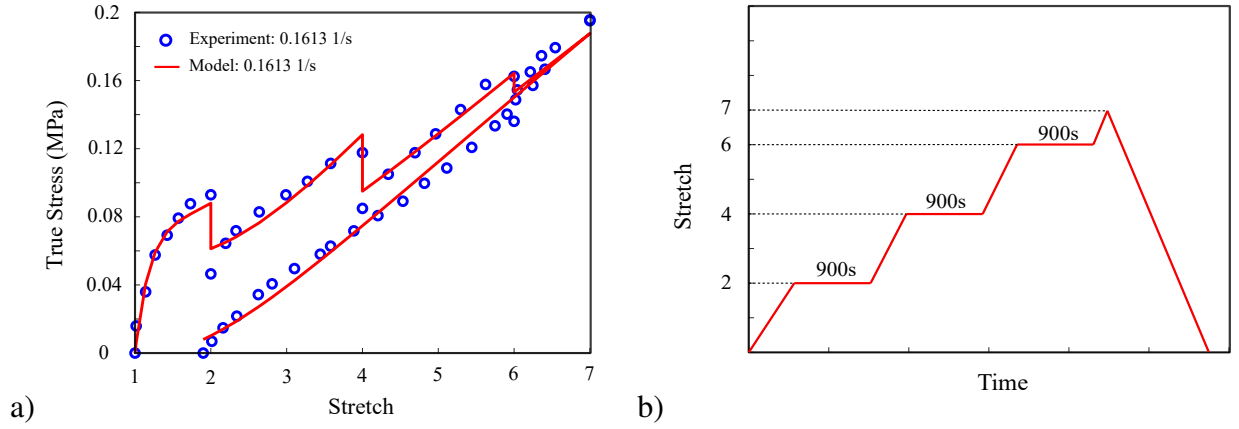


Figure 3.8. a) Comparison of the model results and experimental data of stress-stretch relations for VHB 4910 at loading rate $\dot{\lambda} = 0.1613/s$, b) Experimental method of sequential relaxation experiment [91]

larger specimens have higher ultimate tensile strengths than smaller specimens because they are able to resist larger loads. The shape of the sample also affects the stress-strain curve because different shapes will have different stress-strain curves. For example, a round sample will have a different stress-strain curve than a rectangular sample. However, the model works as long as the stress-strain curves are based on the same standards.

CHAPTER 4

MACHINE-LEARNED MODEL FOR SINGLE-STRESSOR AGING

Overview This chapter presents a new model that is the extended of the first chapter (mechanical damage) to describe the accumulated effects of the mechanical and environmental damage on elastomer Matrix. The model describes the matrix through a cooperative multi-agents framework where each agent has been defined by a simple conditional neural network (CondNN) which is super-constrained by equations derived from physics, thermodynamics, and continuum mechanics.

4.1 State of The Art

Nowadays, cross-linked elastomers play a significant role in several industries such as aerospace, structure, transportation, shipbuilding, and automotive due to excellent flexibility, toughness, formability, and versatility, [92, 93]. These materials encounter aggressive environmental conditions such as water, temperature, and solar ultraviolet radiation (UV) during their operation, which affects their durability and properties. Fig. 4.1 shows common forms of aging.

Over the last four decades, many degradation studies have dealt with the complexity of polymer lifetime prediction and extrapolations, either by measuring mechanical or similar degradation indicators over a large temperature range, thereby establishing the basis for predictions, or by focusing on limitations in straight line Arrhenius extrapolations. It is interesting to note how trends in these studies over the years reflect on the evolution of more sensitive analytical techniques, better stabilization of materials, and an overall improved understanding of polymer aging phenomena [94, 95, 96, 97].

The reliable design of rubbery structures, which prevents failure due to environmental degra-

dition, requires the development of constitutive models considering the high stretching capacity in different states of deformation. This can be achieved through continuum-based models integrating the relationship between the large-strain macro-response and the degradation processes, all of which are of crucial importance. In this regard, it is the main goal of this study to propose a practical and simple description of the environmental aging of rubbery media through a novel constitutive model using physically realistic approaches. In this study, we try to use machine learning algorithms that need the minimum possible dataset for training. It is axiomatic that the predictability of the model is related to the dataset size that we are using for training.

Polymer aging can take form in either physical or chemical changes or both. Notable examples of chemical changes that occur due to weathering are chain scission during the curing of polymers, thermal conditioning at elevated temperatures, and photo-chemical aging. In polymeric systems, physical aging refers to the structural relaxation of the glassy state toward the meta-stable equilibrium amorphous state and it is accompanied by changes in almost all physical properties. Specifically, physical aging occurs when the material is in a non-equilibrium state, and gradually tends towards an equilibrium due to the macromolecular relaxation; Note that the proposed model in this chapter does not consider high-temperature aging and is just valid for a small range around glass transition temperature (T_g). Temperature elevation can often accelerate physical aging and is often used for this purpose since real-time physical aging is super-slow, which makes it often infeasible for most studies.

Higher temperatures can also accelerate chemical reactions of the matrix in the presence of oxidizing agents like oxygen, which causes chemical aging of the system. The collection of the physical and chemical changes induced by time at high temperatures is often known as thermal-induced oxidative aging. The polymer matrix changes during thermal-induced aging as the polymer backbone interacts with oxygen. There are two main consequences of chemical reactions at the macromolecular scale: (i) polymer chain scission and (ii) cross-link formation. The contribution of those two mechanisms to the behavior of the aged material will increase along the aging period; the resulting state of the material can be considered a product of the competition between

these reactions. The change can be dominated by either reaction depending on the polymer matrix type, cross-linking agents, and the aging temperature. Generally, the increase of cross-link density significantly increases the matrix stiffness, increases T_g , and reduces its stretchability. Both reactions have a substantial effect on the polymer chain length distribution within the matrix as well. Additionally, aging alters the arrangement of molecules in the polymer matrix. [98, 99].

In the presence of water, such as in the case of submerging polymer samples in water, hydrolytic aging can take place. The interaction of the elastomer matrix with the hydroxyl or hydrogen ions in water causes hydrolytic aging. Chain scission and chain detachment may occur as a result of water molecules attacking the polymer matrix hydrolytically. Hydrolytic attacks, on the other hand, reduce the molecular weight of the matrix, which also affects the mechanical behavior [49]. Generally, short-term aging is attributed to the materials that need curing, such as adhesives. This phenomenon is also referred to as over curing as well [100]. In this respect, here we used cured specimens to avoid over-curing in our aging setup. During thermo-oxidative aging, two simultaneous phenomena will occur, which are namely chain scission and cross-link formation. In most of the cross-linked polymers such as SBR, crosslink formation is dominant, which made the material tougher. On the other hand, during hydrolytic aging, chain scission is dominant, and as a result, water acts as a plasticizer, and as a result, makes the material softer. From the constitutive modeling point of view, constitutive behavior is mainly getting harder by thermo-oxidative aging while hydrolytic aging makes it softer [101].

There are other types of aging, such as (i) hygrothermal aging, which is a coupled concurrent effect of thermal-induced and hydrolysis aging, and (ii) photo-oxidative aging, which is accelerated thermal-induced aging with UV (see Fig. 4.1). Many experimental and theoretical models have been proposed in order to show the effect of thermal-induced and hydrothermal aging on the mechanical behavior of cross-linked elastomers.

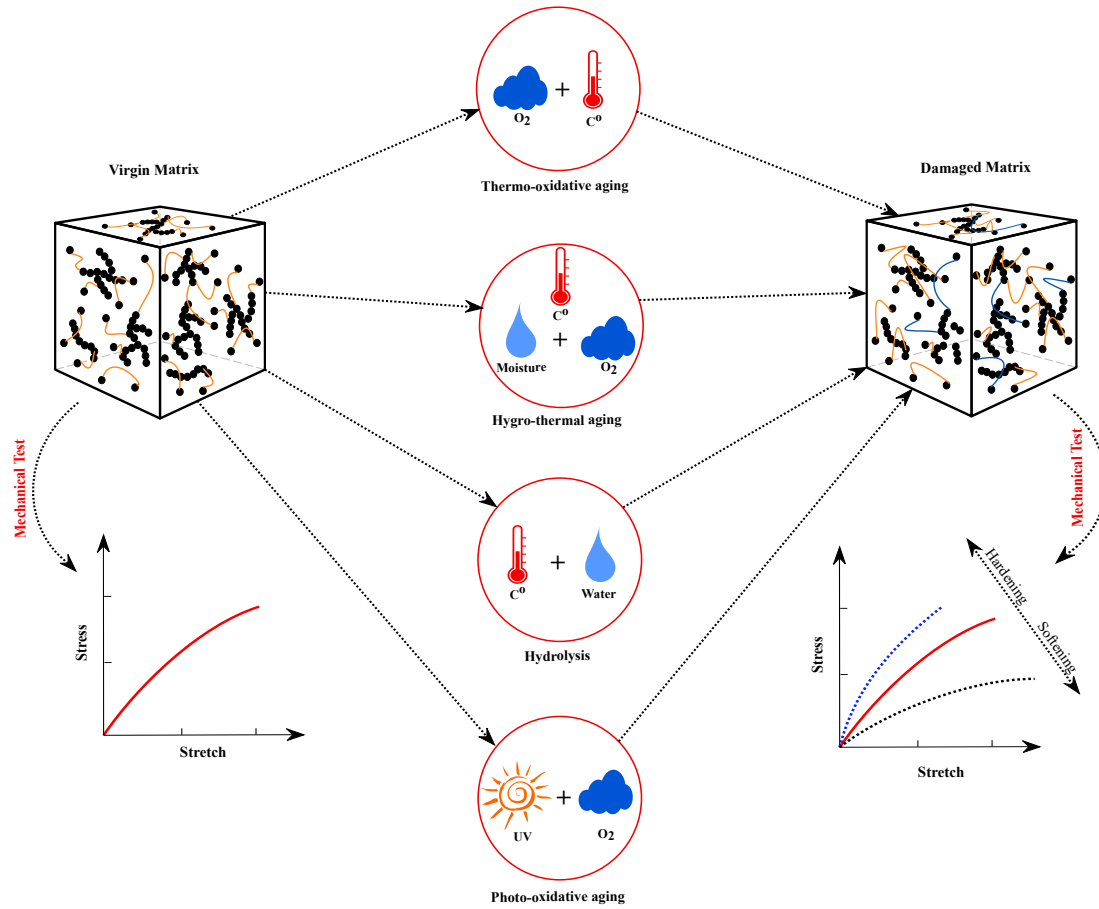


Figure 4.1. Schematic of common types of aging including thermo-oxidative, hygrothermal, hydrolysis, and photo-oxidative agings

In experimental approaches, three types of tests are used to characterize the mechanical behavior of elastomers during "single-stressor chemical" aging;

(i) **Relaxation test**, where the temperature and strain of samples are held constant during the aging, and the stress drop is studied over time (Fig. 4.2.a).

(ii) **Permanent set test**, which is similar to the relaxation test, but after relaxation, the specimen is unloaded, and the final length is measured and investigated with initial length (Fig. 4.2.b).

(iii) **Intermittent test**, where the sample is aged at stress-free state first and then characterized [102] (Fig. 4.2.c).

Several studies have investigated thermal-induced aging through those tests for different types of materials, such as natural rubber [103, 104, 105, 106, 107, 108], and composites [109, 110, 111].

Similarly for hydrolysis, those tests were used to characterize aging in rubbers, [112, 113, 114], composites [115, 116], and biodegradable materials [117, 118].

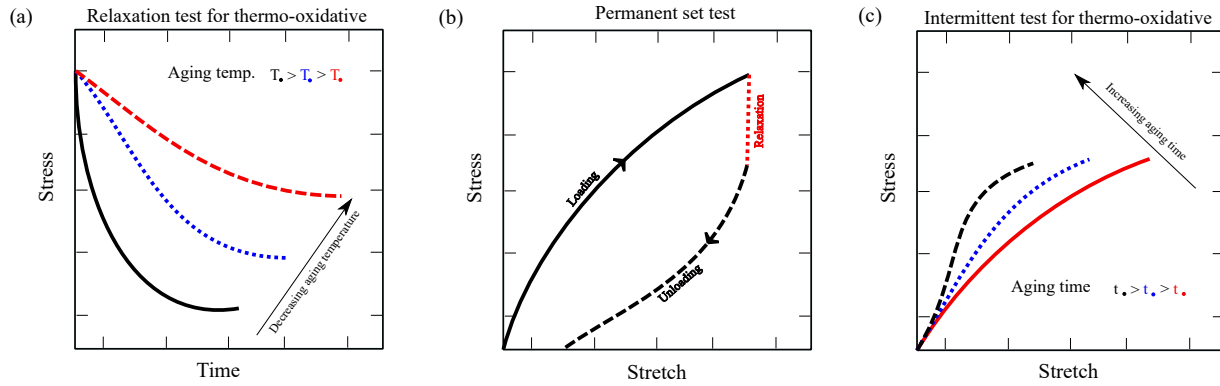


Figure 4.2. Schematic illustration of a) intermittent test b) relaxation test c) permanent set test for thermo-oxidative aging [119]

In recent decades, reliability and material performance through degradation has attracted wide attention; Scholars have proposed different mathematical degradation models based on their applications. The Arrhenius along with the [120] Archard [121] and Paris models, [122] fall in single stressor degradation, which is continuous and without any fluctuation. Several models have been proposed from a combination of constitutive models and degradation models. Ha-Anh and Vu-Khanh [123] employed an Arrhenius function and combined it with the Mooney-Rivlin model to predict the hyperelastic behavior of aged polychloroprene. Lion et al. [102] proposed a phenomenological model by splitting Helmholtz free energy into three parts. In 2013, Johlitz [124] proposed a phenomenological model that considers both mechanical and chemical degradation. Meanwhile, in the micro-mechanics category, Mohammadi et al. [125, 98] proposed a model for thermal-induced aging that combined the Author's network evolution model with the Arrhenius function and different decay rates. This study [126] investigated the geometry dependency of aging between substrate and adhesive by employing finite element simulation based on chemo-mechanical modelling. There are a few models that theoretically investigate hydrolysis [127]. Viera et al. [128] proposed a model for hydrolysis using Bergstrom and Boyce's constitutive model by decomposing mechanical behavior into time-dependent and time-independent parts. In another study, the Author

investigated the mechanical behavior of biodegradable materials during hydrolysis aging by employing a quasi-linear viscoelastic model [129]. In another micromechanical study, Bahrololoumi et al. [101] proposed a model for hydrolysis that combined Author's network evolution model and Arrhenius decay function. All the mentioned models have several advantages and disadvantages.

The three key novelties of the proposed methodology are:

- Despite wide range of studies on behaviour of elastomers behavior during aging and abundance of data, there has been very few physics-informed data-driven models that can successfully reproduce the experimental data other than those used for training.
- So far, data-driven constitutive model for single-stressor aging are mostly based on black-box approach and there has been no methodology to infuse background knowledge into the modeling to reduce the dependency on data.
- A comprehensive data-driven model for aging problems are strictly limited to few simple studies.

In view of those challenges, we proposed a new approach for reduced order modeling single-stressor aging in elastomers by infusing Knowledge into a data-driven approach. The following are the major novelties of the proposed method:

(i) Developed a systematic approach to reduce order of the constitutive mapping and address data volume problem for training.

(ii) Validated a novel physics-informed hybrid framework to describe the relationship between elastomeric network mechanics and environmental degradation.

(iii) Predicted various inelastic effects through our model which is also less data-dependent, has higher interpretability, and uses a knowledge confined solution space.

(iv) Incorporating background knowledge from polymer physics, continuum mechanics, and thermodynamics into the neural networks and constraint the solution space.

Therefore, in this chapter, we develop a hybrid physics induced data-driven framework that is constrained and simplified by applying rules and concepts from polymer physics, continuum

mechanics, and thermodynamics to predict the effects of a single mechanisms environmental aging such as thermal-induced aging or hydrolysis on constitutive behaviour of the material. The proposed model is based on the concept of a cooperative multi-agent system \mathcal{A}_j^i , $i \in \{1, n\}$, $j \in \{1, m\}$ to describe different features in the material behaviour with $n \times m$ different neural network learning agents (L-agents), which are responsible for learning from experimental data sets. We have simplified the 3D stress-strain tensor mapping problem into a small number of super-constrained 1D mapping problems by means of a sequential order reduction. We assume that during aging, the polymer matrix is changed by degradation, and due to the lack of exact knowledge on behavior and interaction of polymer microstructures, we model it using an L-agent system. The model is validated by our set of experimental data. In addition, relaxation and intermittent experimental data available in the literature are used to show the proposed model's accuracy in different conditions. The hybrid NN model can predict aging behavior between the lowest and highest temperature. Although in NNs, we can control it, so it is only valid in the domain it is trained. The reason is that we have not implemented physical equations in the proposed hybrid model. It is our outlook for future study.

4.2 Mechanical and Environmental Damages in Polymers

Cross-linked elastomers are created by mass cross-linkage of polymer macro-molecules to each other within a confined space. Modeling the constitutive behaviour and damage mechanisms in cross-linked polymers has been the subject of interest for the past 50 years, and a general description of the micro-processes has been formulated. In general, elastomer degradation is caused by two types of stresses: mechanical, such as deformation, vibration, and relaxation, and environmental, such as thermal aging, hydrolysis, and photo-oxidation.

Deformation-induced damage: One good example of mechanical damages is the Mullins effect, where the matrix softens after the first stretch [130, 69, 131]. This phenomenon happens in filled rubber polymers, not all polymers. There are multiple sub-structural changes in the matrix

that are formed due to mechanical damages, such as chain breakage in the filler interface, chain disentanglement, molecules slipping, and rupture in the cluster of fillers [50, 51].

Environmental Damage: Multiplicative Decomposition of Strain Energy *Environmental damage* occurs mostly due to changes in the chemical micro-structure of the matrix, which occurs due to competition or collaboration of multiple sub-mechanisms. For example, thermal aging is widely considered as the competition between cross-link formation mechanism and chain scission mechanisms, where the former makes the matrix stiffer by inducing new bonds. In contrast, the latter makes it softer by debonding polymer chains from the system. The rate of polymer chain scission and cross-links formation defines that the material should become brittle or ductile, although in both cases, the matrix experiences damage[132]. The effects of loading scenarios, material morphology, and environmental conditions on rubber behavior are generally considered inelastic. From a modeling aspect, inelastic effects can be described through a collection of chemical and physical events within the matrix. However, establishing the relationship between the chemical/physical evolution of the matrix and the changes in macro-performance remains a significant challenge in physics-based modeling. On the contrary, the data-driven models do not need to establish this relationship explicitly and thus can directly describe the strain energy of the matrix through multiplicative decomposition to describe the effects of physical \mathcal{E}_p and chemical \mathcal{E}_c evolutions on the strain energy of a sub-element as

$$\psi_j^{d_i} = \mathcal{E}_p \mathcal{E}_c \psi_{0;j}^{d_i}, \quad (4.1)$$

where $\psi_j^{d_i}$, and $\psi_{0;j}^{d_i}$ denote the updated and reference energy of a sub-element in the network j and direction d_i damaged portion.

Almost all external inelastic effects can be described using multiplicative chemical and physical evolution parameters, ranging from aging and degradation to hyperelasticity and creep.

- **Reversible Physical changes** \mathcal{E}_p mainly involves deformation-induced changes in the material and often heals over time. Thus, \mathcal{E}_p gradually tends toward 1 with time. It is mainly

induced by the breakage of ionic bonds, the recoverable hyperelastic motion of free chains, and the slippage of elastically active crosslinked chains. In filled elastomers, physical evolution can be further induced by the sliding between fillers and filler-rubber matrix, the breakage and reformation of agglomerates, and the deformation of elastic aggregates. These mechanisms also induce physical stress relaxation, cyclic hysteresis, and often healing. Within the context of this paper, deformation-induced mechanical damages are mainly described by Maximum micro-stretch in history λ_{max}^d and classified as physical changes. One can approximate \mathcal{E}_p as a DNN with following parameters

$$\mathcal{E}_p = \mathcal{N}_p(\mathbf{x}_p, \Theta_p^{(i)}), \quad \{\lambda^d \in \mathbf{x}_p, \dot{\lambda}^d, \lambda_{max}^d\} \quad (4.2)$$

- **Irreversible Chemical changes** \mathcal{E}_c mainly involves the **unrecoverable** inelastic events, and thus \mathcal{E}_c remains constant or go toward 0 over time. Unrecoverable molecular changes in the crosslinked network are often manifested by the breakage of covalent bonds and the formation of a "plastic-like" behavior upon complete unloading, i.e., permanent set. The chemical evolution can lead to competing mechanisms such as scission or formation of chemical bonds and crosslink formation, which are also influenced by rubber compounds such as the ratio of antioxidants, fillers, etc. Within the context of this paper, the effects of the aging condition, compounding ratios, and external temperatures are mainly described by chemical evolution. One can approximate \mathcal{E}_c as a DNN with following parameters

$$\mathcal{E}_c = \mathcal{N}_c(\mathbf{x}_c, \Theta_c^{(i)}), \quad \{n, T\} \in \mathbf{x}_c \quad (4.3)$$

In general, we outline two key requirements that \mathcal{E}_p and \mathcal{E}_c must meet

1. \mathcal{E}_p should always move toward 1 with time ,
2. depends on the situation \mathcal{E}_c will stay the same or go toward 0 over time.

Thermo-oxidative kinetics: During thermo-oxidative aging, the rate of chemical oxidation

can be characterized as

$$-\frac{d[P]}{dt} = k[P]^q, \quad (4.4)$$

$[P]$ is the chemical compound concentration of P , k is the reaction rate coefficient, and q is the reaction order. The chemical reaction governing a degradation process is commonly described using first-order kinetic equations ($q = 1$). Furthermore, k is just a function of temperature in the presence of homogenous conditions, low stretches during aging, and no diffusion-limited oxidation. The major cause of alterations in the polymer matrix is chemical interactions between the polymer backbone and oxygen during thermal-induced aging [133, 134, 135].

Hydrolysis kinetics: Hydrolysis is commonly described using first-order kinetics equations, similar to thermal-induced aging, but with respect to the production rate of carboxylic end groups.

$$\frac{d[C]}{dt} = \zeta[C], \quad (4.5)$$

where $[C]$ is the carboxyl end group content in the polymer matrix. The parameter ζ is the hydrolytic degradation rate, which determines the rate at which the material ages. Mechanical stress, ester group condensation, polymer structure, water diffusion, temperature, and the pH of the degradation environment are all elements that influence the rate of degradation. As a result, applying mechanical stress during hydrolytic degradation might increase the likelihood of chain cleavage and, as a result, the hydrolysis rate constant. Similarly, the pH of the degrading environment can influence the hydrolysis rate constant via catalysis. Due to the absence of mechanical force, constant temperature, and constant pH in the domain, the hydrolysis rate remains constant through the degradation process in this investigation. Furthermore, as compared to hydrolytic aging, the time spent diffusing water into the sample volume is insignificant. In fact, the water was evenly distributed across the sample volume. As a result, during the course of the degradation process, the concentration of water molecules is considered to remain constant. To make the formulation easier, the deterioration rate is assumed to remain constant throughout the aging process at a given

temperature θ [136, 137].

4.3 Physics-Constrained Data-driven Modeling: Multi-Agents Model

Overview This work presents a new generation of *super-constrained deep-learned hybrid constitutive models* that can describe the accumulated effects of the mechanical and environmental damage on elastomer Matrix. The model describes the matrix through a cooperative multi-agents framework where each agent has been defined by a simple deep-learned neural network (NN) which is super-constrained by equations derived from physics, thermodynamics, and continuum mechanics. The use of NN agents within the micro-mechanical models, as opposed to traditional physics-driven modeling methods, provides a new generation of hybrid models that use the interpretability/simplicity of micro-mechanical models plus the computational speed and adaptability of machine-learned algorithms. While the accuracy of the predictions of the proposed hybrid model still relies heavily on the quality of the data used for training, the model output is already constrained within the region that satisfies our existing knowledge of the matrix behaviour.

The model has been constrained at multiple steps; (1) model defined based on strain energy; (2) hiring micro-sphere for 3D to 1D order reduction; (3) using network decomposition to separate different inelastic effects; (4) defining learning agents to represent each 1D subnetwork. Those steps which are required to build a cooperative multi-agents hybrid model and their formulation are outlined in the following.

4.3.1 Cooperative Multi-Agents System

In finite deformation regimes, strain-energy based constitutive functions are extremely advantageous over classical stress-strain equations by satisfying multiple conditions at once, such as normalization, growth conditions, isotropy, objectivity, and poly-convexity to ensure the solution's uniqueness. Moreover, strain energy based formulations can be easily verified against the 2nd law of thermodynamics and consequently Clausius-Planck inequality by being formulated with respect to different work conjugate pairs such as

$$\begin{aligned}
\text{Two-point strain/stress tensors } (\mathbf{F} : \mathbf{P}) &\rightarrow \mathbf{F}:\text{deformation gradient}, \quad \mathbf{P}:\text{first stress}, \\
\text{Material strain/stress tensors } (\mathbf{E} : \mathbf{S}) &\rightarrow \mathbf{E}:\text{Lagrange strain}, \quad \mathbf{S}:\text{second stress}, \\
\text{Spatial strain/stress tensors } (\mathbf{L} : \boldsymbol{\tau}) &\rightarrow \mathbf{L}:\text{Hencky strain}, \quad \boldsymbol{\tau}:\text{Kirchhoff stress}.
\end{aligned}
\tag{4.6}$$

To model the second-order stress–strain fields required for characterization of hyperelastic material, current approaches ranging from phenomenological to data-driven, face one major challenge, namely lack of data on 3D structures. There are no tools to measure stress field across a structure, and for strain, we can only measure the strain field for relatively simple structures using digital image correlation (DIC) techniques. The problem of considerable missing data has traditionally been solved by incorporating material behavior information into the model and constraining the model in advance of obtaining the data. Due to the lack of infused knowledge of the material, such a solution is irrelevant in data-driven approaches.

We propose to resolve the problem of significant missing data in finite deformation constitutive behaviour through a physics-driven order-reduction approach by implementing the micro-sphere concept, network decomposition theory, continuum mechanics compatibility equations, and general rules provided by polymer physics on matrix behaviour. Therefore, we will create a micro-mechanical model with super-constrained deep-learned agents serving as the constitutive models at 1D to predict the matrix behavior solely based on the macro-scale collective behavior of the sample. We have previously discussed [78, 138] the formation of such algorithm for mechanical induced deformation as shown in Fig. 4.3. In other words, we will use exactly the same procedure of knowledge implementation into the model from our recent work, and the only difference is the network architecture used to define L-agents which is based on a new generation of machine learning algorithms known as conditional neural networks (CondNNs).

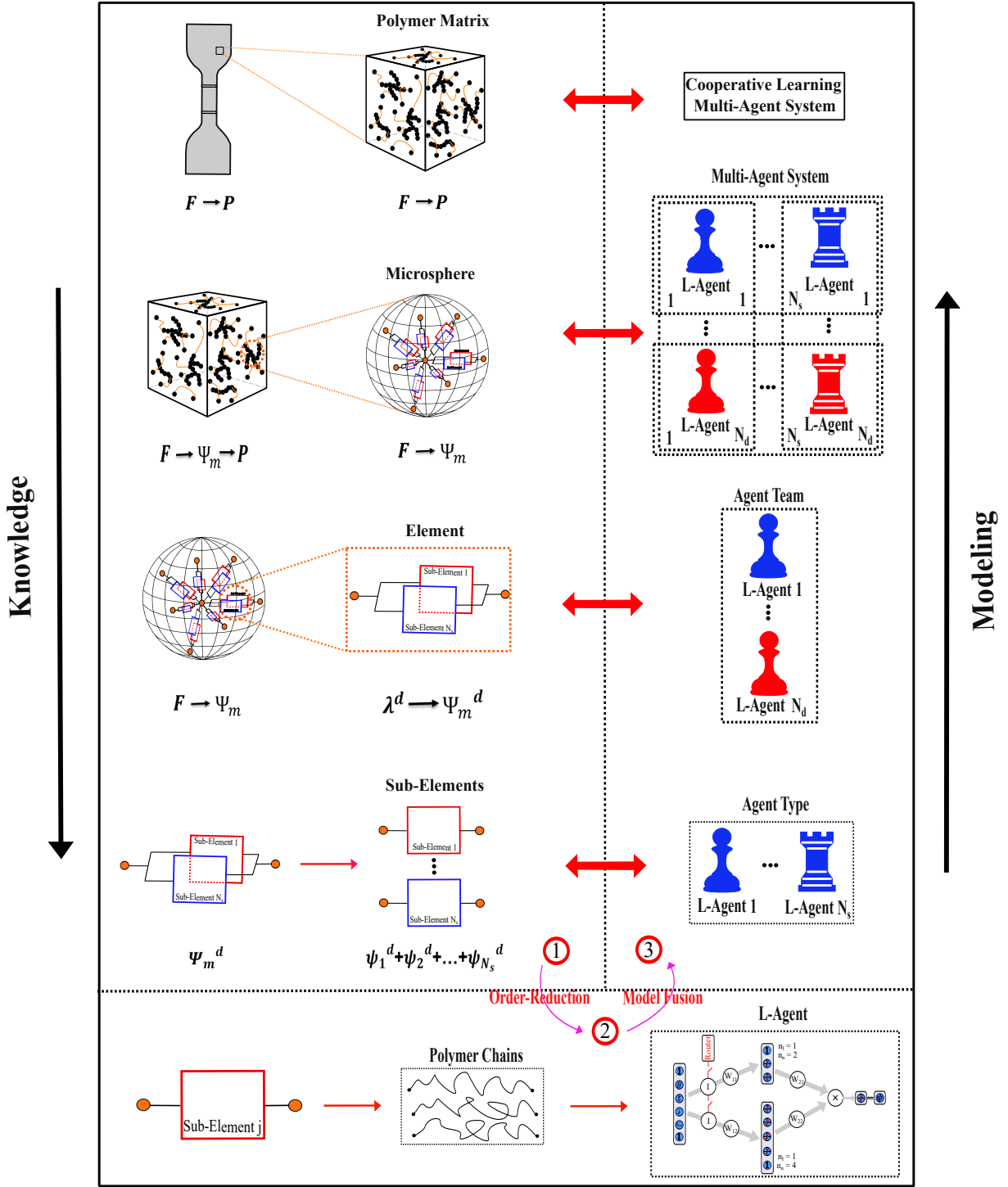


Figure 4.3. Schematic of the proposed model from order-reduction to model fusion. It shows how we use the concepts from continuum mechanics, polymer sciences, physics, and machine learning to reduce the order of problem

- **Network Decomposition** Network decomposition constraint is derived from statistical mechanics, namely by infusing the concept of superposition, which allows us to predict complicated patterns by superposing simple patterns on top of each other. To account for damage accumulation, the cross-linked matrix is hypothetically divided into a number of parallel networks, where each network represents one damage model. Accordingly, the entropic energy of the polymer matrix is the summation of the energies of the parallel networks. The platform is defined as a generalized set of assumptions to describe the micro-structure evolution through the mechanics of a single chain. The quasi-static deformation in polymeric joints are often induced by manufacturing process, thermal expansion and/or the coefficient of thermal expansion (CTE) mismatch between adhesive and adhered. The energy of the polymer matrix in the quasi-static deformation can be given as the superposition of the energy of two parallel networks, which consist of polymers between crosslinks or between particles, respectively. Motivated by breakage of shorter chains during elongation and its consequent network rearrangement, *directional pre-stretch* will be used as a history variable to describe permanent damages, i.e., stress softening and permanent set.

Networks and Subnetworks Each network is considered to have a unique composition and describes a different energy-dissipating damage mechanism. Using the concept of micro-sphere, each network is considered as a 3D composition of infinite 1D subnetworks that are distributed in all spatial directions. Subnetworks can only be subjected to uniaxial deformation and thus will experience different deformations based on their directions. To develop a model for the subnetwork in direction, only a simplified form of entropic energy is needed with respect to uniaxial deformation. Integrating a subnetwork in all directions, the consequent network is a representation of that concept in a 3D configuration. The similar concept will be used for training of the neural network.

As a result, network decomposition helps us describing the complex behaviour of a 1D element as the super-position of the simple behaviour of N_s sub-elements, where $\Psi_m^{d_i} = \sum_{j=1}^{N_s} \Psi_j^{d_i}$. Here, each sub-element is responsible for one or no inelastic behaviour. Assigning L-agent to each sub-element, $\mathcal{A}_j^i := \Psi_j^{d_i}$, an element behaviour is described by a team of cooperative L-agents

$\mathcal{B}^{d_i} = \sum_{j=1}^{N_s} \mathcal{A}_j^i$. Consequently, we can extract the energy of the matrix directly with regard to sub-elements and the L-agents as

$$\Psi_m = \frac{1}{4\pi} \int_S \Psi_m^d dS^d \cong \sum_{i=1}^{N_d} \sum_{j=1}^{N_s} w_i \psi_j^{d_i} := \sum_{i=1}^{N_d} \sum_{j=1}^{N_s} w_i \mathcal{A}_j^i. \quad (4.7)$$

Considering each sub-element is represented by an L-agent, the super-simplified scalar-to-scalar mapping behavior of a sub-element can be modeled by a simplified feed-forward neural network. Summarizing the implemented constraints, the first Piola—Kirchhoff stress tensor \mathbf{P} can be derived, as

$$\mathbf{P} = \frac{\partial \Psi_m}{\partial \mathbf{F}} - p \mathbf{F}^{-T} := \sum_{i=1}^{N_d} \sum_{j=1}^{N_s} w_i \frac{\partial \mathcal{A}_j^i}{\partial \mathbf{F}} - p \mathbf{F}^{-T}, \quad (4.8)$$

where p signifies the Lagrange multiplier to ensure incompressibility of the material.

4.3.2 Conditional Neural Network (CondNN) L-Agent

There is a new family of hybrid machine learning algorithms known as conditional neural networks (CondNNs) for problems in which the outputs are not only dependent on past occurrences, e.g., deformation effects on the matrix, but also on external actions, e.g., temperature and time of aging effects on the polymer matrix. This new algorithm has been derived by the combination of general neural network and decision tree concepts (see [81, 82]). A routed behavior is a feature of decision trees; the data is sent to one or more children based on some learned routing function. This conditional computation means that we can infuse the knowledge in the model. Meanwhile, throughout many tasks, NNs achieve industry-leading precision for learning, but decision trees have the ability to infuse the knowledge into NNs. In other words, CondNNs are decision trees with the exception that instead of moving the data as is, each node applies a non-linear transformation to it. We can also forward the data to one or more of its children using routers.

In order to design an L-agent which can model mechanical and environmental damage in the polymer matrix, we use CondNNs as a new hybrid framework. The feed-forward L-agents consist

of NNs followed by a fully connected layers, which the first branch represents the mechanical damage in the polymer matrix. The resulting features are then combined multiplicatively with the second branch of NN followed by fully connected layer that represents environmental damage in the matrix. (see Fig. 4.4)

- Neural Network Architecture The architecture of the neural network (Fig. 4.4) is determined via the hyper-parameters summary: (i) number of hidden layers, n_l (network depth), (ii) number of neurons per hidden layers, n_n (network width), (iii) activation function.

The L-agent response is computed using a feed -forward algorithm for a given set of hyper-parameters (n_l, n_n) . Each L-agent can be represented by a CondNNs as

$$\mathcal{A}_j^i := \mathcal{D}^{d_i}(E^i) \psi_j^{d_i}(\mathbf{M}_j^i, \mathbf{S}_j^i) \quad \mathcal{D}^{d_i} = CNN_e(\mathbf{W}_e, E^i), \quad \psi_j^{d_i} = CNN_m(\mathbf{W}_m^j, \mathbf{M}_j^i, \mathbf{S}_j^i), \quad (4.9)$$

where $\psi_j^{d_i}$ represents the energy of deformation-induced damage part and \mathcal{D}^{d_i} is related to environmental damage of one sub-element. Similarly, two weight matrices $\mathbf{W}_m^j = [\mathbf{W}_{m1}^j \dots \mathbf{W}_{m_{n_l+1}}^j]$ and $\mathbf{W}_e = [\mathbf{W}_{e1} \dots \mathbf{W}_{e_{n_l+1}}]$ are related to weight matrices of mechanical and environmental damage CondNNs, respectively. Here, $\psi_j^i(\mathbf{M}_j^i, \mathbf{S}_j^i)$ is trained on the basis of a non-kinematic input sets \mathbf{M}_j^i and internal parameters \mathbf{S}_j^i for the mechanical damage CondNN. Selection of internal parameters depend on (full or recent) material memory. Also, the input vector E^i should represent the setting of the problem related to environmental damage such as temperature and time of degradation.

Normalization, conditions of growth, isotropy, objectivity, and poly-convexity are already satisfied in the proposed equation.

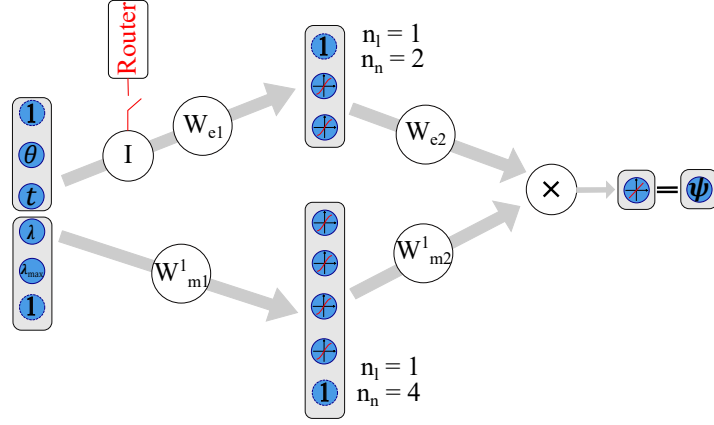


Figure 4.4. Schematic of a neural network with physics-informed engineered features to learn the effect of environmental aging on the mechanical Behaviour. This is referred to as CNN in this study

- **Model parameter identification** The parameters of the CondNN model are identified using a Gradient descent algorithm. A data collection consisting of n data points is the basis for model recognition. Loss function was defined with respect to the difference between target values, AKA experimental data, and approximated value, AKA CondNN output. Here, we define the loss function \mathcal{L} Mean Squared Error (MSE) for a total of n_{tot} data points as

$$\mathcal{L}(\mathbf{W}_m^1, \dots, \mathbf{W}_m^j, \mathbf{W}_e) = \frac{1}{2} \sum_{n=1}^{n_{tot}} \left[\mathbf{g}_1 \left(\sum_{i=1}^{N_d} \sum_{j=1}^{N_s} w_i \frac{\partial \mathcal{A}_j^i}{\partial \mathbf{F}} - p \mathbf{F}^{-T} \right) \mathbf{g}_1 - P_n^{11} \right]^2, \quad (4.10)$$

where $P_n^{11} := \mathbf{g}_1 \mathbf{P}_n \mathbf{g}_1$ is the first component of the experimental macro-scale stress tensor \mathbf{P}_n in loading direction \mathbf{g}_1 for point n .

4.4 Validation: Environmental + Mechanical Damages in Rubber

Here, the proposed hybrid model is developed and validated for two different loading scenarios

1. Thermal-induced aging + Mechanical deformation (Mullins effect)
2. Hydrolysis (desalinated water) + Mechanical deformation (Mullins effect)

In both cases, the model was benchmarked against experimental data to predict the inelastic behavior of cross-linked elastomers for different states of deformation at different stages of aging. We also

validated the model predictions for different coupling scenarios for mechanical and environmental damages, namely

- **Intermittent test** where the sample has been aged first with no stress, and then the mechanical behaviour is characterized

- **Relaxation test** where the samples were loaded and aged at constant deformation and the drop in the stress has been recorded.

In both cases, the predictions were validated against four main variables the effect of (i) deformation, (ii) deformation history, (iii) aging time (t), and (iv) aging temperature (θ).

4.4.1 Network Architecture

For modeling both loading scenarios, we used identical engines; a relatively simple engine built by $N_d = 21$ teams, where each team had $N_s = 2$ agents [83]. Note that the number of teams and their related agents can be chosen based on the trade-off between accuracy and computational cost. In other words, we consider 21 teams because it is a small number for estimation of the integral with a summation. As a result, it guarantees that the proposed model error in prediction is excellent even in a small number of teams. To capture all deformation states, we used only two agents, each of which is representative of the first and second invariants of the Green-Cauchy deformation tensor. For the CondNNs structure of L-agents, we considered one input layer, one hidden layer with four neurons and three activation functions soft plus $\psi(\bullet) = \ln(1 + e^\bullet)$, sinusoid $\psi(\bullet) = \sin(\bullet)$ and hyperbolic tangent $\psi(\bullet) = \tanh(\bullet)$.

The internal parameters of L-agents were built via λ_{j-max} parameters to capture the deformation of the rubbers with full memory. In order to allow teams to predict various deformation states, the first and second deformation invariants were supplied to each team [139, 60].

The condition was satisfied by providing input sets into the first and second L-agents as

$$\mathbf{M}_1^{d_i} = [\lambda^{d_i}], \quad \mathbf{S}_1^{d_i} = [\lambda_{max}^{d_i}], \quad \mathbf{E}^{d_i} = [t, \theta], \quad \mathbf{M}_2^{d_i} = [\nu^{d_i}], \quad \mathbf{S}_2^{d_i} = [\nu_{max}^{d_i}], \quad \mathbf{E}^{d_i} = [t, \theta], \quad (4.11)$$

while

$$\lambda^{d_i} = \sqrt{\mathbf{d}_i \mathbf{C} \mathbf{d}_i}, \quad \nu^{d_i} = \sqrt{\mathbf{d}_i \mathbf{C}^{-1} \mathbf{d}_i}, \quad \mathbf{C} = \mathbf{F}^T \mathbf{F} \quad (4.12)$$

where $[\mathbf{d}_i]_{i=1 \dots N_d}$ is integration directions in micro-sphere, λ^{d_i} and ν^{d_i} are related to I_1 and I_2 , as the first and second invariants of \mathbf{C} , respectively.

In summary, the rubber matrix was represented by a cooperative game of 21 teams of 2 agents through \mathcal{A}_j^i , $i \in \{1, 21\}$, $j \in \{1, 2\}$. After agent fusion, the final cost function is given by

$$\mathcal{L}(\mathbf{W}_m^1, \mathbf{W}_m^2, \mathbf{W}_e) = \frac{1}{2} \sum_{n=1}^{21} [\mathbf{g}_1 \left(\sum_{i=1}^{21} \sum_{j=1}^2 w_i \frac{\partial \mathcal{A}_j^i}{\partial \lambda_j^{d_i}} \frac{\partial \lambda_j^{d_i}}{\partial \mathbf{F}} - p \mathbf{F}^{-T} \right) \mathbf{g}_1 - P_n^{11}]^2, \quad (4.13)$$

subjected to weights related to λ_{max} and $\nu_{max} \leq 0$, and weights related to λ and $\nu \geq 0$ to satisfy thermodynamic consistency and poly-convexity, respectively. Accordingly, the energy of each sub-element can be written with respect to the deformation gradient \mathbf{F} as follows

$$\sum_{i=1}^{21} w_i \frac{\partial \mathcal{A}_1^i}{\partial \lambda^{d_i}} \frac{\partial \lambda^{d_i}}{\partial \mathbf{F}} = \sum_{i=1}^{21} w_i \frac{\partial \mathcal{A}_1^i}{\partial \lambda^{d_i}} \frac{1}{\lambda^{d_i}} \mathbf{F} (\mathbf{d}_i \otimes \mathbf{d}_i). \quad (4.14)$$

$$\sum_{i=1}^{21} w_i \frac{\partial \mathcal{A}_2^i}{\partial \nu^{d_i}} \frac{\partial \nu^{d_i}}{\partial \mathbf{F}} = - \sum_{i=1}^{21} w_i \frac{\partial \mathcal{A}_2^i}{\partial \nu^{d_i}} \frac{1}{\nu^{d_i}} \mathbf{F}^{-1} \mathbf{F}^{-T} \mathbf{F}^{-1} (\mathbf{d}_i \otimes \mathbf{d}_i). \quad (4.15)$$

Minimizing Data Requirement for Training For history-dependent materials, parameters should be specifically chosen to represent material's damage and then fed into the L-agents through internal parameters. However, different types of damage parameters may be required for describing different materials, e.g., for materials with recent memory such as visco-elastic materials, internal parameters should transfer information from each iteration to the next. In contrast, for materials with full memory such as elastomers, the internal parameters can be defined independently of

the solution iterations as a damage-precursor of the external events; for example, the maximum stretch and aging time/temperature in rubber material can be used as a damage precursor to show the history of damage in each direction. So, each L-agents in all directions consists of damage parameters.

The reason for training with biaxial datasets roots from the point that we cannot train agents with scenarios in which they aren't involved or have a minor role to play. As a result, the quality of the training data and the contribution of agents in those situations are strongly proportional to the confidence in agent training. We can measure the confidence interval in which an agent may be trained with high confidence with regard to the provided data by describing the quality of data with respect to the input required by each agent. Too little data can give us a false sense of safety because it prevents us from seeing the crucial points, while low-quality data can lead to incorrect conclusions that appear to be completely reliable. We added two L-agent types in the aforementioned rubber model, which represent two sub-elements using $M_1^{d_i}$ and $M_2^{d_i}$ input sets, respectively. We know from the definition of $M_2^{d_i}$ that it has a restricted variation in uni-axial tensile stress; therefore, the contribution of the second L-agent in such loading is essentially non-existent. However, because $M_2^{d_i}$ changes greatly in bi-axial stress, the contribution of the second L-agent is fairly important in this instance. Because the second agent cannot be completely engaged, training using uniaxial data cannot give the quality information required for reliable training of both agents (please see our recent paper [78]). The reason for training with different states of deformation is that we want to show the performance of the model by choosing different datasets. If we train the model based on uniaxial tensile data till stretch χ_x , the model can predict different states of deformation based on the ranges that the model has calibrated based on that. In order to ensure accurate prediction of the model, the prediction ranges should be in the range that the agent is trained. Thus, in the bi-axial

prediction case, the model is limited to

$$\begin{aligned}
 \text{Agent 1:} \quad & \left[\frac{1}{\chi_{bi.}^2}, \chi_{bi.} \right] \in \left[\frac{1}{\sqrt{\chi_x}}, \chi_x \right] \longrightarrow \chi_{bi.} \leq \sqrt[4]{\chi_x} \\
 \text{Agent 2:} \quad & \left[\frac{1}{\chi_{bi.}}, \chi_{bi.}^2 \right] \in \left[\frac{1}{\chi_x}, \sqrt{\chi_x} \right] \longrightarrow \chi_{bi.} \leq \sqrt[4]{\chi_x}.
 \end{aligned} \tag{4.16}$$

4.4.2 Step 1: CondNN Training in the absence of aging

To investigate the performance of the proposed model in the material in the absence of aging, we benchmarked the inelastic features in the behavior of natural rubber, namely Mullins effect and permanent set. Figure 4.5 shows stress-stretch curves for this cross-linked polymer with experimental data of [64]. We used one set of bi-axial loading-unloading until $\lambda = 2.7$ for training and predicting inelastic effects in different states of deformation, e.g., uniaxial and pure shear at increasing stretch amplitudes which constitutes deformation histories.

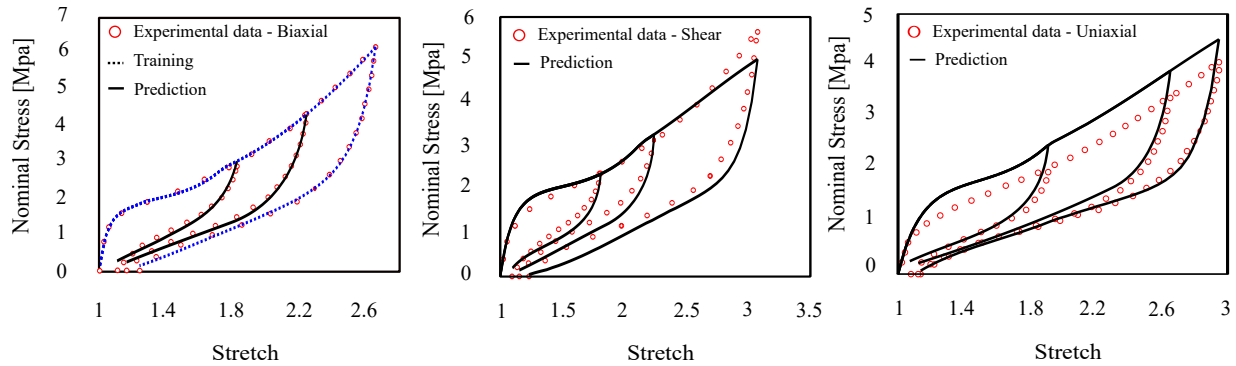


Figure 4.5. Model training and prediction of bi-axial, pure shear, and uni-axial(Urayama's dataset [64]). Dash lines stand for fitting and solid lines stand for prediction. The biaxial dataset which have been showed with the blue line used for training and of the model. The black lines in bi-axial, shear, and uni-axial datasets show the performance of the model in prediction after training

4.4.3 Case Study 1: Thermo-Oxidation + Mechanical Damage

Natural Rubber Prediction of aging was validated against experiments for samples aged at various times and temperatures. Firstly, experimental data from natural rubber relaxation test filled with 60 phr carbon-black was used to demonstrate model results (see Fig. 4.6). Intermittent test

results were also used to verify the model's functionality to predict the impact of various degrees of aging alongside various strains (see Fig. 4.7). The training dataset is chosen to cover different relaxation stretches and the highest and lowest effect of temperature and time in order to increase the predictability of the model for different temperatures and times. Note that the model is just able to capture the relation effect of aging, not the relaxation effect of viscosity.

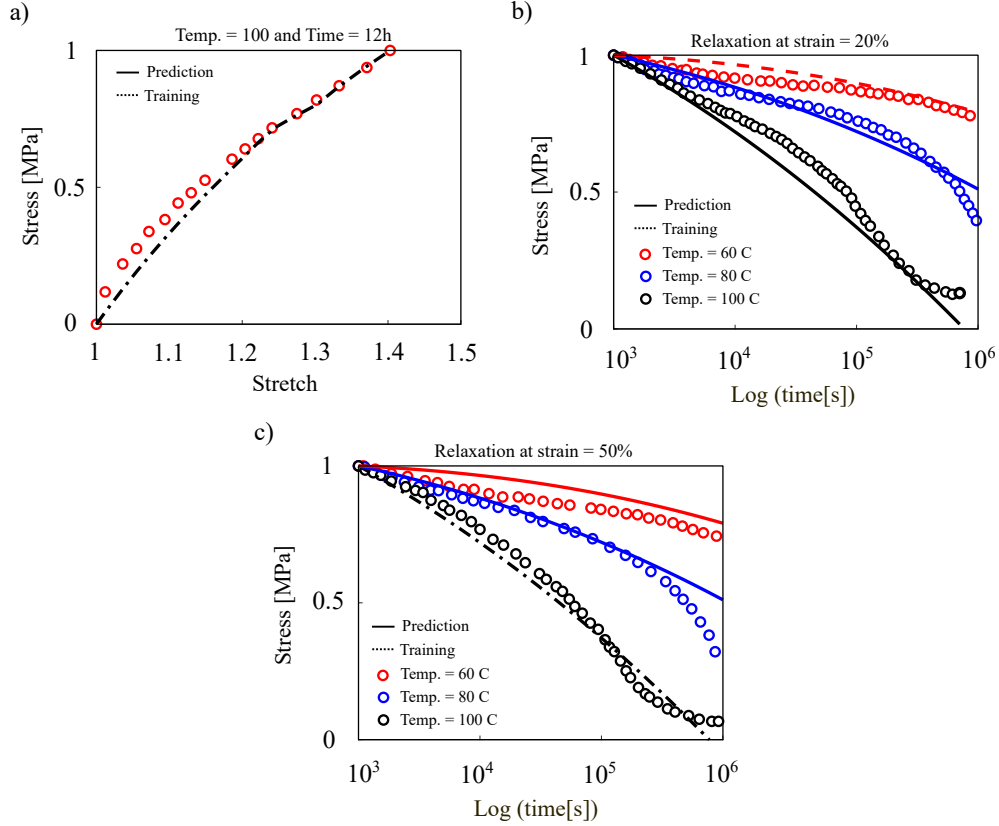


Figure 4.6. Training and model predictions for NR against; (a) intermittent test, (b) relaxation test at $\varepsilon = 20\%$, (c) relaxation test at $\varepsilon = 50\%$. Dash lines stand for fitting and solid lines stand for prediction. The red points in figure a) and b), and the black points in the figure c) have been used for training of the model. The solid lines show the performance of the model in prediction after training

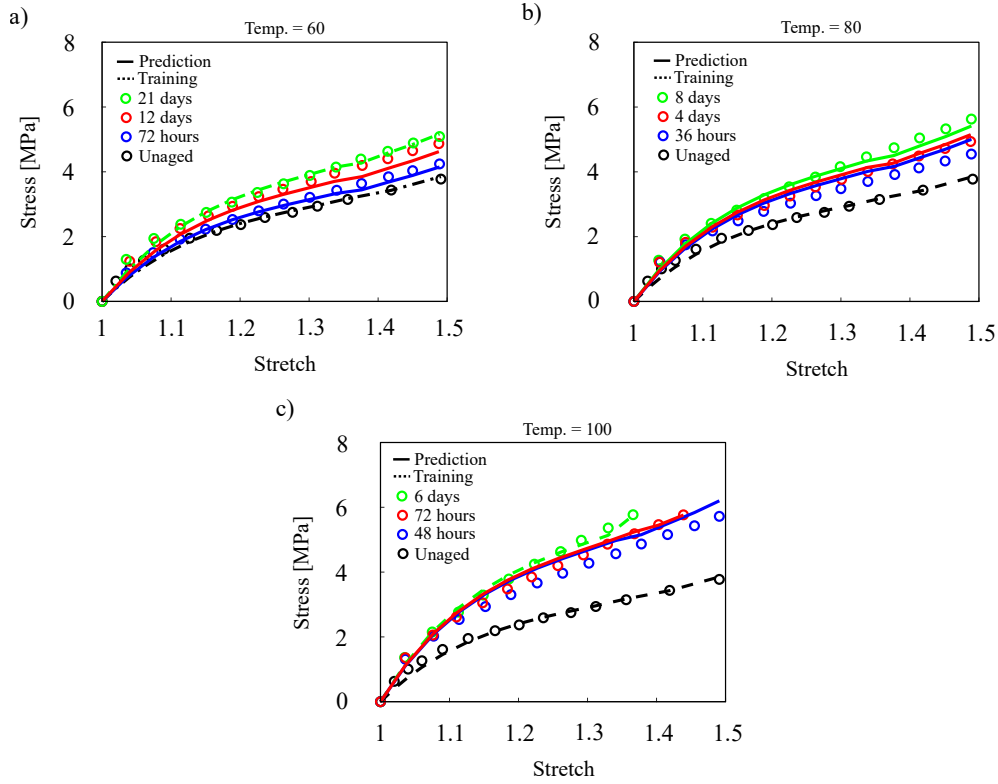


Figure 4.7. Training and model predictions for NR against intermittent test; (a) at 60°C , (b) at 80°C , (c) at 100°C . Dash lines stand for fitting and solid lines stand for prediction. The black(unaged) and green points in the figure a) and c), and just the black(unaged) points in figure b) have been used for training. The solid lines show the performance of model in prediction after the training

Polyurethane A bone form punch was used to punch dumbbell samples in compliance with ASTM D412 standards. The reason that we are using dog-bone samples is that in this shape, when we put the extensometer in a specific location of that sample, we are sure that it gives us one component of the deformation matrix, for example, x-x direction. But in complex shapes, several components of stress tensor participate; so, it is not possible to see the effect of each component with an external extensometer. Three different temperatures, 60°C , 80°C , and 95°C , in zero humidity level, were used to age the samples. The performance of the invented model was determined using the results of the uni-axial tensile failure tests. Fig. 4.8 depicts the evaluation's related findings.

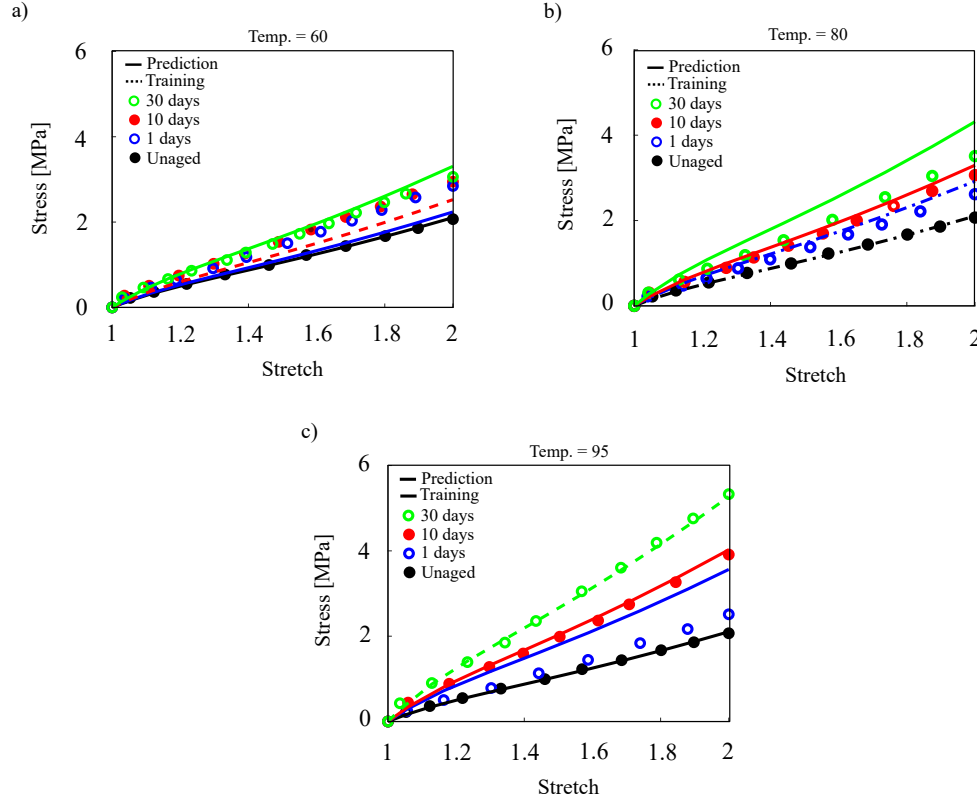


Figure 4.8. Training and model predictions for polyurethane against intermittent test; (a) at 60°C , (b) at 80°C , (c) at 95°C . Dash lines stand for fitting and solid lines stand for prediction. The black(unaged) and red points in the figure a), the black(unaged) and blue points in figure b), and the black(unaged) and green points in the figure c) have been used for training. The solid lines show the performance of model in prediction after the training

Silicon Adhesive To assess the model's capabilities, we compared its predictions to our experimental results, which were specifically developed to demonstrate the effect of chemical aging on the constitutive response of silicone adhesive. In this case, samples were placed in ovens at temperatures 60°C , 80°C , and 100°C with a relative humidity of zero (i.e. $\text{RH} = 0\%$). All of the specimens were aged under constant pressure, and after a set amount of time, they were removed from the containers and dried with tissue paper. The predictions of the proposed model against the experimental data for different types of aging and different amount of aging times, temperatures, and deformations are plotted in figure 4.9.

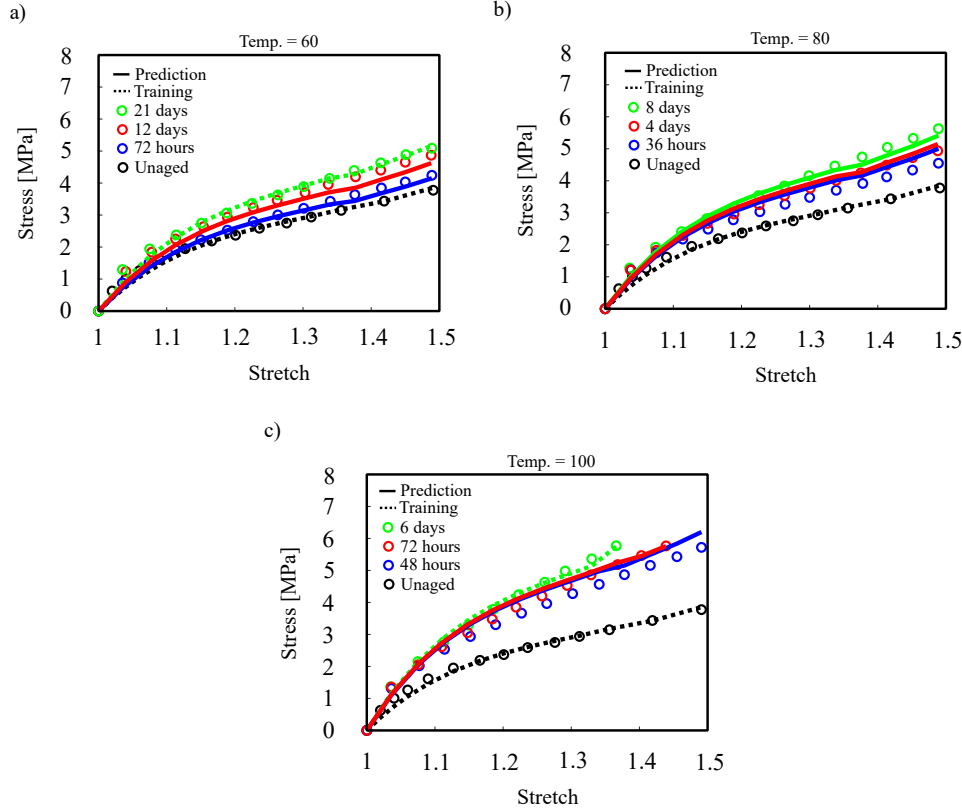


Figure 4.9. Training and model predictions for silicone adhesive against intermittent test; (a) at 60°C , (b) at 80°C , (c) at 100°C . Dash lines stand for fitting and solid lines stand for prediction. The black(unaged) and green points in the figure a), the black(unaged) points in figure b), and the black(unaged) and green points in the figure c) have been used for training. The solid lines show the performance of model in prediction after the training

Note that the model is able to predict the behavior of elastomers even in the stretch greater than 4. Thermo-oxidative aging makes the samples brittle. As a result, the failure point for samples happens on the less stretch. So, because the focus of the proposed model is on the behavior of aged materials we showed the performance of the model till stretch less than 4. In addition, the kernel of model is the same even for higher stretches. So, the model works for higher stretch as well.

4.4.4 Case Study 2: Hydrolysis + Mechanical Damage

Styrene-butadiene rubber (SBR) samples were placed at temperatures of 60°C and 80°C at 1bar pressure in sealed containers filled with distilled water. After aging, samples were removed and dried at room temperature for ten days. We used an SFM-20 united testing machine with a 1000

lb load cell for quasi-static tensile tests. A strain rate of $43.29 \frac{\%}{min}$ was used at room temperature for extension. The samples were subjected to uni-axial tensile test to failure in monotonic failure experiments, but the samples were expanded to preset amplitudes of 1.3, 1.6, 1.9, and 2.1 in the cyclic test. The central zone extension was measured using an external extensometer. Fig. 4.10 shows the effect of time and temperature on damages induced by deformation.

Silicon Adhesive In sealed containers filled with distilled water, samples were held at $60^{\circ}C$, $80^{\circ}C$, $95^{\circ}C$, and 1 bar pressure. After aging, samples were removed and dried for 1, 10, and 30 days at room temperature. For quasi-static tensile tests, we used an SFM-20 united testing system with a 1000 lb load cell. Fig. 4.11 depicts the influence of time and temperature on deformation-induced damage.

Other Compounds with behaviour reported in the literature were also used for validation of the proposed model to predict behaviour with complex patterns of inelasticity, such as hardening and curvature alteration. Here, we have been generalizing the experimental data available in the literature to form a model for predicting the hydrolytic aging activity of three other compounds. Fig. 4.12 shows the excellent performance of the devised model in prediction of mechanical behavior of Poly-Urethane submerged at $100^{\circ}C$ in seawater [140], PLA–PCL fiber at $37^{\circ}C$ submerged in phosphate buffer solution [128], Natural rubber (vulcanized A) submerged in seawater at $40^{\circ}C$ [141].

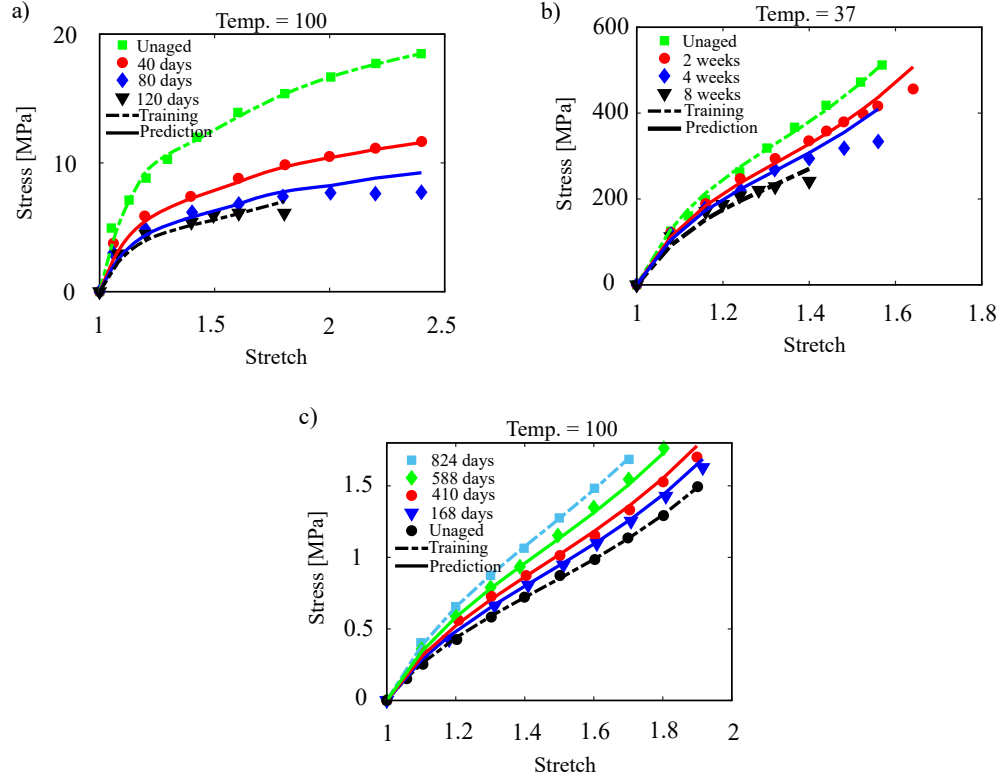


Figure 4.12. Training and model predictions of three different materials against aging; (a) PolyUrethane (PU) submerged at 100°C in seawater [140], (b) PLA-PCL fiber at 37°C submerged in phosphate buffer solution [128], (c) Natural rubber (vulcanized A) submerged in seawater at 40°C [141]. Dash lines stand for fitting and solid lines stand for prediction

4.5 Conclusion

The aim of this chapter was to propose a novel physics-informed hybrid framework to capture the relation between elastomeric network mechanics and environmental damage. The proposed model is used to describe the effect of single-stressor aging, such as thermal-induced or hydrolytic aging, on the behavior of the material in this hybrid system. Huge chain scission, cross-link reduction, chain formations, and changes in polymer morphology are all examples of environmental single-stressor damages that alter the polymer matrix over time. In other words, this model is a predictive model and not a descriptive model. As a result, it can provide prediction in a fraction of time and cost to the end-users for the reliable design of components. Although, The model cannot be used to understand or explore kinetics. By extracting micro-structural activity from macroscopic experimental data,

the data-driven approach aims to overcome the shortcomings of both phenomenological and micro-mechanical models.

The model arises from polymer physics and an order reduction strategy ending to the constrained L-agents training. The polymer matrix was described by a cooperative multi-agents system, in which each agent is represented by a simple deep-learned CondNN that is super-constrained by laws derived from physics, thermodynamics, and continuum mechanics. While satisfying the continuum mechanics and thermodynamics rules, the proposed hybrid model is quite simple for the most rubbery media in the extreme environment.

The excellent performance of the proposed method was proven by validating against different experimental data on different materials that are particularly selected to reveal the evolution of inelastic behaviour during single stressor agings. The efficiency of the model was found satisfactory, and in some cases, excellent when compared with the experimental data. "In general, the error of our model in training and prediction is less than 10%." Accuracy and simplicity of the model make it a proper choice for commercial and industrial application because we do not need to know the exact behavior and interaction of micro-structures; however, in the future, the model can be extended to consider viscoelasticity and non-isotropic formation for better precision due to platform of the model. Besides, note that the proposed model focus is on the mechanical behavior of the material during degradation, not lifetime prediction. Also, the performance of the proposed model is completely dependent on the dataset that we choose for training. It is axiomatic that if we increase the available dataset for training, the predictionability of the model is more accurate.

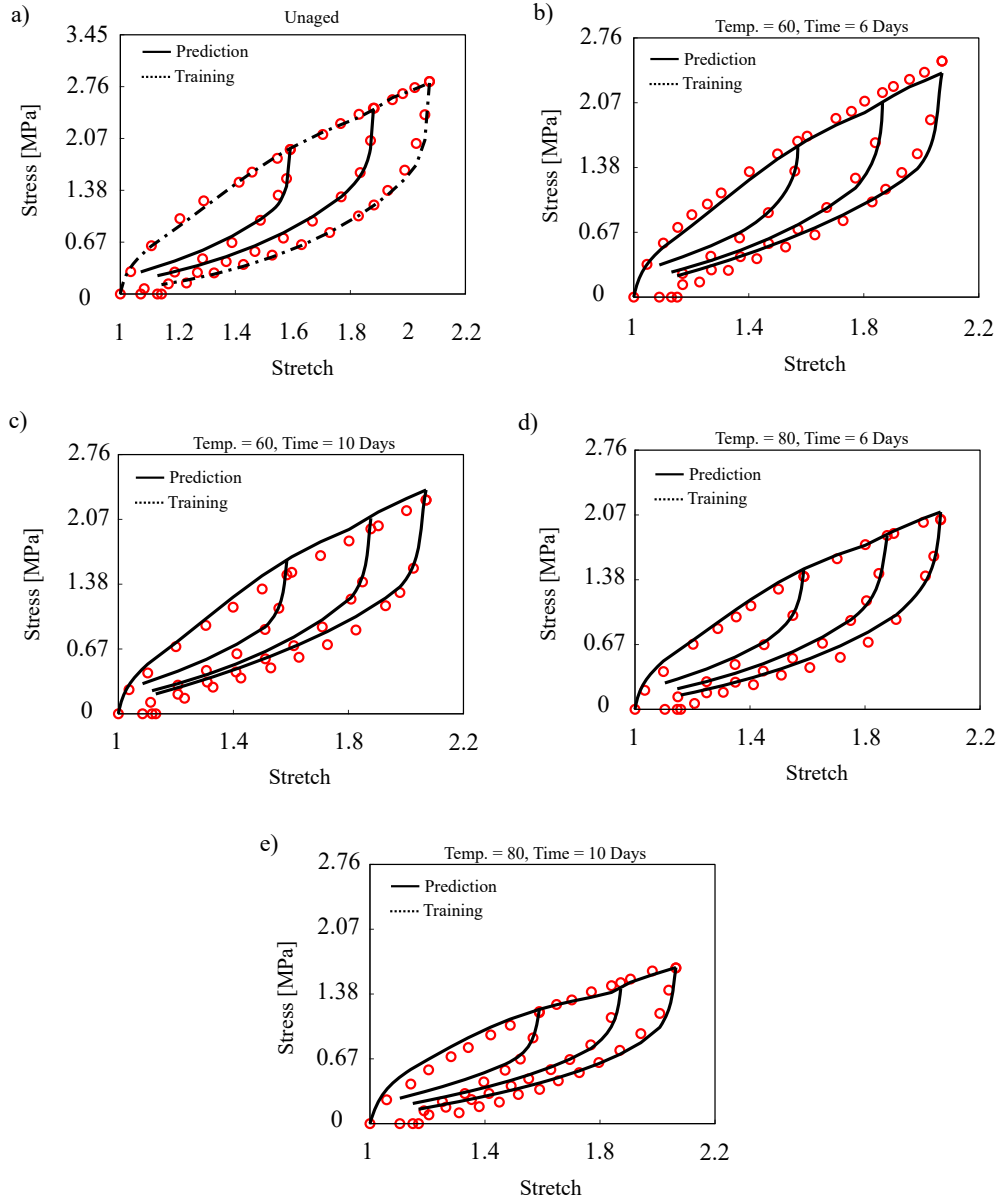


Figure 4.10. Multiple SBR training and model predictions; (a) unaged, (b) constitutive behavior for 6 days of age at temperature study of 60°C, (c) constitutive behavior for 10 days of age at temperature study of 60°C, (d) constitutive behavior for 6 days of age at temperature study of 80°C, (e) constitutive behavior for 10 days of age at temperature study of 80°C. Dash lines stand for fitting and solid lines stand for prediction

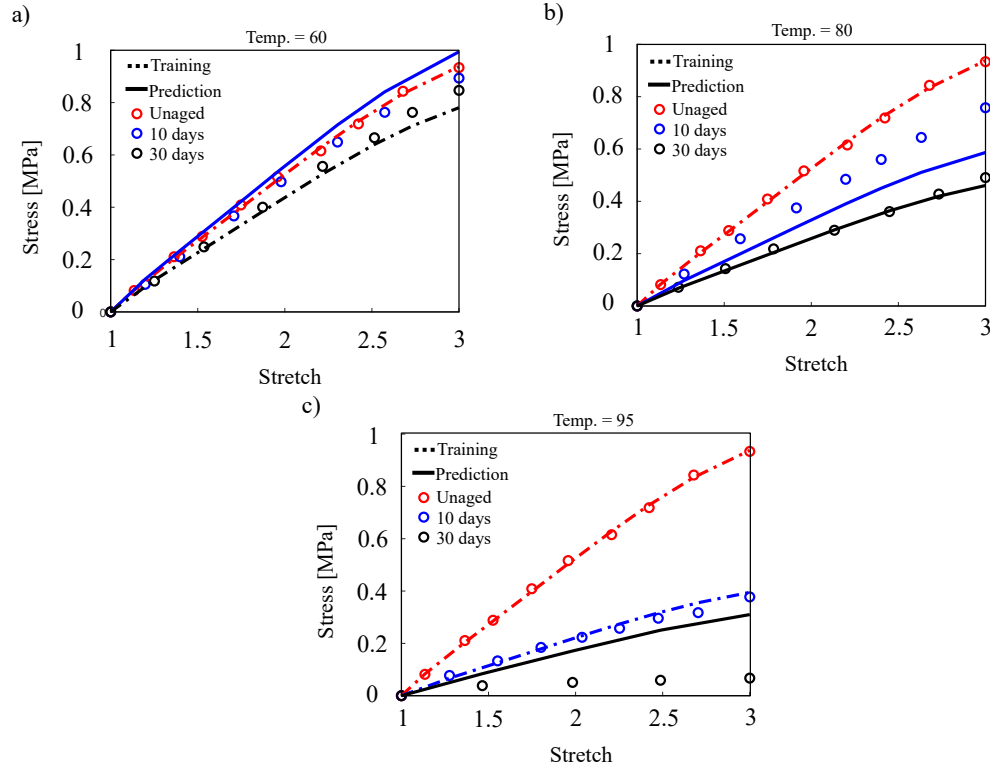


Figure 4.11. Training and model predictions for silicon adhesive against intermittent test; (a) at 60°C, (b) at 80°C, (c) at 95°C. Dash lines stand for fitting and solid lines stand for prediction. The red(unaged) and black points in the figure a), the red(unaged) points in figure b), and the red(unaged) and blue points in the figure c) have been used for training. The solid lines show the performance of model in prediction after the training

CHAPTER 5

FATIGUE AND AGING: REDUCED-ORDER KNOWLEDGE-DRIVEN MACHINE-LEARNED MODEL

Elastomeric materials are widely used in numerous automotive and aeronautic applications as critical components that must reliably operate for an extended time. To assure the reliability of elastomer components, it is crucial to predict their end-of-life for any given load condition [142]. There is growing evidence that elastomers' fatigue is a function of both environmental and mechanical loads, which may alter components' properties, appearance, and performance before visible cracks form and spread. The fatigue of elastomers due to coupled environmental and mechanical loads is the subject of this work. We will mainly focus on the nature of fatigue—mechanisms and possible experiments that can correlate fatigue damage to the matrix changes. End-of-life prediction requires an accurate model of three items (1) constitutive and failure behavior, (2) fatigue behavior, (3) aging behavior.

Constitutive and Failure Behaviour

Constitutive Behaviour: The constitutive models of elastomeric components, which are often described by explicit functions within the context of continuum mechanics, are generally very important for their design and optimization [143, 144]. Numerous studies have been conducted on and applications made to conventional continuum mechanics-based constitutive models for the numerical analysis of engineering structures. These models, however, are only as precise as their underlying assumptions [145, 146].

Failure Behaviour: When exposed to moderate or large strains, crosslinked polymers are vulnerable to failure and fracture. Failure often represents the beginning of damage, whereas fracture represents damage localization into cracks for subsequent propagation. While there are numerous methods to model failure and fracture based on continuum damage mechanics (CDM) was developed [147, 148, 149]. predicting failure and fracture along with the constitutive behavior remains a primary challenge. The core idea in most models is to describe the gradual accumulation of damage via an additional variable called the internal variable, which often has no physical meaning. If the damage is abrupt rather than gradual, then there is no need for internal variables, and it is only necessary to bound the strain-energy function[150], which is the core concept of our data-driven approach here.

Fatigue Modeling

Fracture-based methods: The fatigue life of rubbers may be predicted using fracture mechanics techniques. There are two steps to fatigue failure prediction. The first stage is predicting the location of the fracture nucleation using continuum mechanics, and the second one involves estimating the crack evolution using geometrical factors and energy release rates [151].

To simulate crack initiation and propagation in elastic substances, linear elastic fracture mechanics (LEFM) was introduced. This approach has been widely utilized to forecast fracture behavior in a variety of fields, including soft matter domain and geology [152].

Continuum-based methods: Another option is to use the continuum damage mechanics (CDM) idea in conjunction with a fatigue predictor to compute damage accumulation cycle by cycle. The beginning and spread of microcracks occur throughout the fatigue process due to a continuous evolution of the damage. The basic assumption in the CDM technique is that the net section contributing to load transmission in a specimen or structure decreases with damage owing to these microcracks.

Ayoub et al. [153] used a continuum damage mechanics technique to estimate the fatigue life of

rubber-like materials and expanded a model published by Wang et al. [154] for uniaxial loadings. In order to calculate the evolution of damage, a scalar damage variable D is introduced which defines the continuum damage mechanics method. The evolution of D is computed by a history-dependent evolution equation or a simpler algebraic model, for example by a Miner rule.

Data-driven Models: When (1) there is a significant amount of data available, (2) a precise solution using physics-based mathematical techniques is not feasible, and (3) the data are noisy and/or complicated, machine learning models are appropriate. Fatigue meets the criteria for the machine learning analysis since it exhibits all of those attributes. The neural network (NN) is the most popular machine learning model utilized in the subject of fatigue.

Traditional NN models are only data-driven methods. It is impossible to directly transfer the impact of many factors on the performance of the material under fatigue. Without taking into account any previous physics knowledge, the data treatment alone takes time. On the other hand, over the years, a lot of knowledge regarding the physical mechanism of fatigue phenomena has been gathered. Therefore, a good direction for fatigue research is the physics-informed NN method [4].

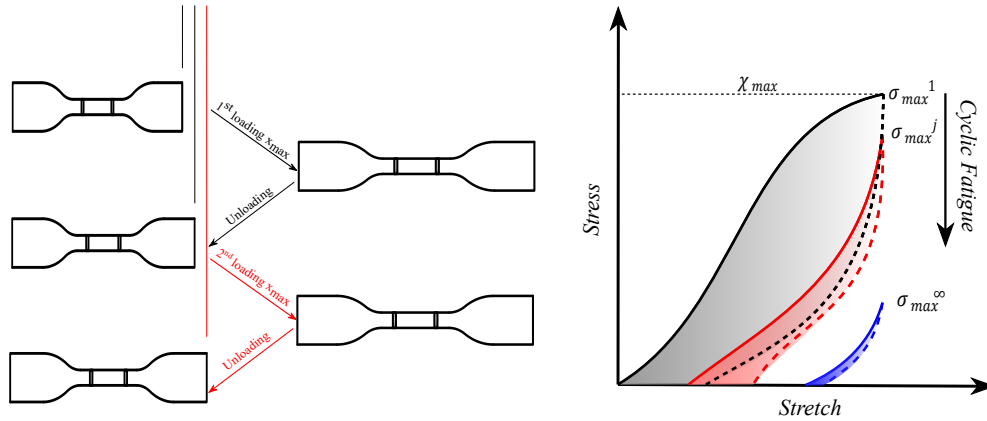


Figure 5.1. The crosslinked elastomer specimen's constitutive response to cyclic loading contains three defining characteristics of inelasticity: stress softening, growing permanent stretch, and stiffness degradation

Aging Modeling

Chemo-physical deterioration brought on by mechanical loads and environmental variables will eventually lead to material failure. Understanding the relationship between chemical decay and mechanical performance deterioration is crucial to foreseeing the breakdown of elastomers in demanding applications like offshore platforms. Different degradation processes functioning alone or in combination might be the cause of this breakdown. These processes may be divided into two categories: those having significant impacts, such as thermo-oxidation, hydrolysis, and hygro-thermal aging, and those with minor effects, such as chemical corrosion and ozone cracking [155, 156, 157, 95, 158, 159, 160].

In the presence of oxidizing substances like oxygen, higher temperatures can also intensify the matrix's chemical processes, leading to the chemical aging of the system. Thermal-induced oxidative aging is a term used to describe a group of physical and chemical alterations brought on by prolonged exposure to high temperatures as the polymer backbone interacts with oxygen during thermally induced aging, the polymer matrix alterations. The production of crosslinks and polymer chain scission are the two fundamental effects of chemical reactions at the macromolecular scale [161, 162].

Along the ageing process, both crosslinking and chain scission contribute to the behaviour of the material. Its current state is the outcome of the competition between both mechanisms. Depending on the kind of polymer matrix, crosslinking agents, and aging temperature, either reaction may predominate the change. In general, an increase in crosslink density increases the matrix's stiffness, T_g , and stretchability to all rise dramatically 5.2. The distribution of polymer chain lengths inside the matrix is significantly influenced by both processes as well [163, 164, 165, 166].

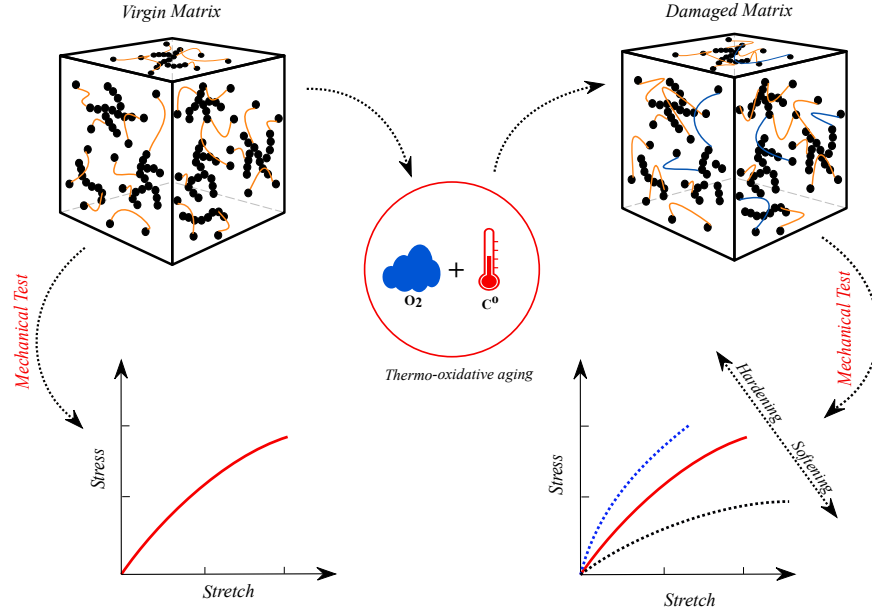


Figure 5.2. Schematic representations of the constitutive response of elastomers during the process of thermal aging

Most research on rubber's simultaneous exposure (synergistic fatigue) to static (environmental) and dynamic (mechanical) fatigue has been experimental. Only a few micro-mechanical and phenomenological models are currently available. In the meanwhile, the development of machine-learned (ML) models has received a lot of attention as a solution to the problems with phenomenological and micromechanical techniques [167, 125, 168, 169, 170, 171].

The three main contribution of the suggested methodology to fill the gap in the modelling of concurrent fatigue and aging, are as follows:

- There have been very few physics-informed data-driven models that can accurately recreate the experimental data other than those utilized for training, despite the large range of research on the behavior of elastomers during synergistic fatigue and the amount of data.
- Black-box approaches have dominated data-driven constitutive models up to this point, and there is no way to incorporate prior information into the modeling to lessen its reliance on data.

- There are just a few straightforward research that can provide a complete data-driven model for synergistic fatigue problems.

In consideration of these obstacles, we developed a novel method for knowledge infusion into a data-driven methodology for reduced order modeling of synergistic fatigue in elastomers. The suggested method's main innovations include the following:

- Developed a methodical strategy to handle the training data volume issue and lower the order of the constitutive mapping.
- Proven an innovative hybrid framework based on physics to explain the connection between elastomeric network mechanics and environmental deterioration.
- Our model, which is also less data-dependent, more interpretable, and employs a solution space with less knowledge, predicted a variety of inelastic effects.
- Constricting the solution space and incorporating background information from thermodynamics, continuum mechanics, and polymer physics into the neural networks.

5.1 Experimental observations

SBR sheets that were sulfur-vulcanized and provided by a local merchant were utilized for this investigation. The ASTM D412-C size die was used to cut the SBR specimens into dog-bone pieces, and its shape is shown in Fig. 1a. Here, a quick summary of the experimental characterizations is provided. In this regard, quasi-static tensile tests were conducted using uni-axial universal testing equipment (Test Resources 311 series frame). The extensometer grips holding each specimen were 25.4mm apart, and all tests were displacement-controlled. All experiments were carried out at standard room temperature T_0 .

Induce thermal aging damage: Thermal aging gradually modifies the chemical composition of rubber materials, which in turn influences the structure of their macro-molecular network. Numerous studies conducted over the past ten years have attempted to pinpoint the various aging

Table 5.1. The results of coupled fatigue and thermal aging experiments conducted on SBR specimens are summarized

Strain (%)	Number of cycles (j)	Aging time (days)	Aging temperature ($^{\circ}C$)
10 %	5, 50, 100, 500	Unaged, 10, 20	60, 80
20 %	5, 50, 100, 500	Unaged, 10, 20	60, 80

pathways brought on by thermo-oxidation. Thermal aging includes the production of free radicals P_0 , in contrast to thermal treatment, which is often best done in an oxygen-free environment. Because the free radicals P_0 are so reactive with oxygen, they stimulate a series of chemical reactions in the polymer known as propagation [172, 173, 96, 174, 161].

For several weeks or months, material samples are stored in an air convection oven with ambient oxygen and a constant temperature as part of intermittent testing for thermal aging. At regular intervals, the aged samples are taken out of the medium and put to a quick test at room temperature. The intermittent test was applied in this case. As a result, the aged samples are taken out of the medium at set intervals and put through a quick examination at room temperature. The samples were kept in a stress-free environment at $60^{\circ}C$ or $80^{\circ}C$ with 0% RH for 10 or 20 days.

To cause cyclic fatigue damage, aged and virgin samples were subjected to various amplitudes of uni-axial tensile cycles under displacement control conditions. In this regard, non-relaxing cyclic loads with amplitudes ranging from 10% to 20% and a cross-head speed of $50mm/min$ cause cyclic fatigue. Here, we measured the changes in constitutive behavior under uni-axial stress to describe cumulative damage after 5, 50, 100, and 500 cycles (see Figs. 4.2). The overview of all test conditions is shown in Table 1.

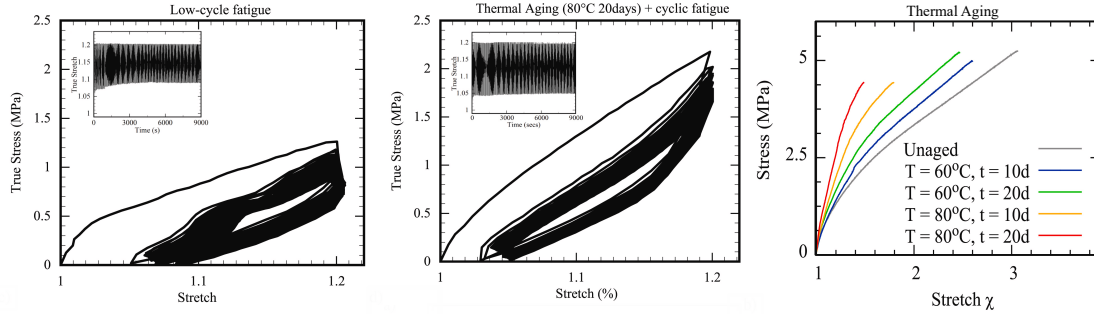


Figure 5.3. Cyclic fatigue of unaged material (left), fatigue-induced damage of aged material (middle), and thermo-oxidation aging of material(right)

5.1.1 Effects of Concurrent Aging and Fatigue

Here, our objective is to model the changes in the constitutive behavior of materials concurrently exposed to Fatigue and aging.

Aging damage is mainly governed by two sub-structural mechanisms, namely (1) crosslink formation and (2) chain scission. The former can make the material more brittle, while the latter makes it softer. Those phenomena can be conveniently described through first-order kinetics for most elastomers, and the well-known Arrhenius function can best approximate it (see Figure 4.2(right)).

Fatigue damage, on the other hand, softens the stress-stretch curves of elastomers in each cycle due to the loss of physical bonds until the material reaches a steady behavior known as the fatigue limit. The peak stress level at each cycle, σ_{max}^j , is maximum in the first cycle and then gradually decreases as the number of cycles increases until it reaches a steady state (see Figure 4.2(left)).

Accordingly, when the material is exposed to concurrent aging and fatigue, the material response is defined through a competition between aging-induced hardening and fatigue-induced softening. In other words, the hardening induced by thermal aging due to the creation of crosslinks can be neutralized by stress softening of cyclic fatigue due to bond breakage, molecules sliding, filler rupture, and disentanglement. According to concept shown in Fig. 5.1, the evolution of σ_{max}^j during quasi-static cyclic testing mostly depends on the number of cycles j and the degree of thermal damage (aging time and temperature). Normalizing the peak stress value to the first cycle

maximum for each aging state shows that thermal and fatigue damage may be separated and that fatigue damage can be represented as a function of the number of cycles.

5.2 Knowledge-Informed Data-Driven Model

The experimental results show that an elastomeric sample exposed to parallel damage behaves in a mode that may be characterized as hyperelastic with accumulated mechanical (\mathcal{D}_{me}) and environmental damages (\mathcal{D}_{ev}). Accordingly, two phenomena (i) environmental degradation and (ii) mechanical damage brought on by fatigue—contribute to the damaging buildup in the elastomers. The major objective of this part is to define a suitable expression for the strain energy of the matrix taking the damage variable \mathcal{D} into account. We define $0 < \mathcal{D} < 1$ as a general non-kinematic scalar parameter, taking into account effective factors for damage accumulation, to describe the overall state of damage in relation to the damages brought on by mechanical and environmental forces.

The strain energy of the damaged polymer matrix Ψ_D can be correlated to the strain energy of the virgin matrix $\Psi_D = (1 - \mathcal{D})\Psi_0$ by using nonlinear damage variable \mathcal{D} . The strain energy function may be hypothesized by constructing a constitutive equation for an incompressible polymer matrix (i.e., $J = \det \mathbf{F} = 1$) as follow

$$\Psi_M = \Psi_D - p(J - 1), \quad (5.1)$$

where the scalar p is an indeterminate Lagrange multiplier, often known as hydrostatic pressure, and may be derived from boundary conditions (a comprehensive discussion of p 's derivation for the planar stress condition appears in [175]).

Let us define the damage variable $\mathcal{D} = \mathcal{F}(\mathcal{D}_{me}, \mathcal{D}_{ev})$ of the matrix as a function of \mathcal{D}_{me} , and \mathcal{D}_{ev} , which can represent accumulative damage during concurrent mechanical and environmental loading. Based on this definition, one can say material fails ($\mathcal{D} = 1$) if mechanical damage ($\mathcal{D}_{me} = 0$) or environmental damage reaches the failure limits ($\mathcal{D}_{me} = 0$). Moreover, one can say

material is virgin ($\mathcal{D} = 0$) if no mechanical or environmental damage is present ($\mathcal{D}_{me} = \mathcal{D}_{ev} = 0$). Therefore, the mathematical expression that describes the damage \mathcal{D} in dependence on \mathcal{D}_{me} and \mathcal{D}_{ev} must comply with the following conditions

$$\begin{aligned} \mathcal{D} &= 0 & \forall & \quad \mathcal{D}_{me} = 0 \cap \mathcal{D}_{ev} = 0, \\ \mathcal{D} &= 1 & \forall & \quad \mathcal{D}_{me} = 1, \\ \mathcal{D} &= 1 & \forall & \quad \mathcal{D}_{ev} = 1. \end{aligned} \tag{5.2}$$

In view of those boundary conditions, one can represent failure conditions or $\mathcal{D} = 0$ through a 3D curved surface with fixed corner lines and edges. The exact composition of $\mathcal{F}(\mathcal{D}_{me}, \mathcal{D}_{ev})$ can first be calculated by having multiple failure points obtained from deformed and aged materials. In general, we outline three key requirements that \mathcal{F} must meet

1. Regardless of the circumstances involving mechanical and environmental loads, damage should always range between 0 and 1,
2. As long as the events are controlled by the same kinetic, the damage function and its first derivative should be continuous, and
3. Damage accumulation is an irreversible process which yields $\nabla \mathcal{F} > 0$.

When all of the aforementioned requirements are met, the damage function \mathcal{F} can be approximated by using other failure points. As there is no specific function for cumulative damage, any function that can meet the aforementioned requirements and can be used. Within consideration of this (see Fig. 5.4), a phenomenological damage model is developed that may be divided into mechanical and environmental damages and is expressed as

$$\mathcal{D} = \text{sigmoid}(a\mathcal{D}_{me} + b\mathcal{D}_{ev}) \quad \Rightarrow \quad \mathcal{D} = \text{sigmoid}(a\mathcal{E}_{me}(\mathbf{x}_{me}) + b\mathcal{E}_{ev}(\mathbf{x}_{ev})), \tag{5.3}$$

where vector \mathbf{x}_{ev} represents the environmental aging conditions, such as aging time t , temperature T , humidity RH , and \mathbf{x}_{me} shows mechanical damage conditions.

The behavior of the damage function is designed based on the resistance of the material to crack nucleation. For high-resistant rubbers to crack nucleation, we choose a convex function for damage modeling, and for low-resistant rubbers to crack nucleation, concave functions are the best options.

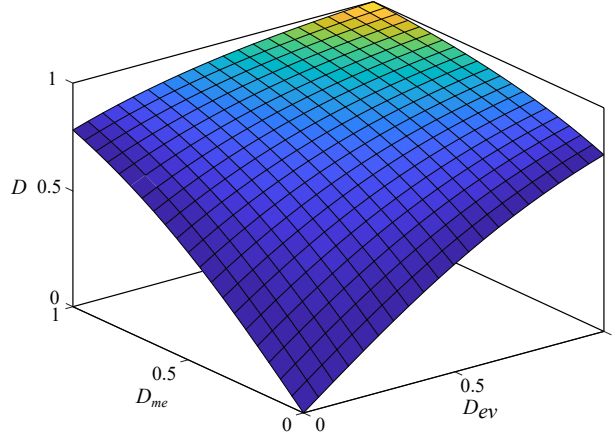


Figure 5.4. Diagram showing the accumulation of damage during mechanical and environmental aging as a family of concave functions

Environmental Damage Add-on

The contribution of environmental damage, such as thermal oxidation, on the mechanical behaviour of polymeric materials, will be modeled based on our recent paper [176] using an Add-on correction function that is derived by conditional Neural Network (CondNN). This approach is appropriate for issues where the outputs depend on both past events such as the effect of deformation history on the matrix and current events such as the effects of temperature and aging on the polymer matrix. Combining ideas from decision trees and deep neural networks led to the development of this novel method. We first independently formulate the impact of environmental damage on a multiplicative damage parameter \mathcal{D}_{ev} , which is directly correlated to material loss of toughness during aging. For example, in thermal-oxidative aging, loss of toughness is directly proportional to the irreversible damage generated by aging kinetics, although the material becomes stiffer.

Using the concept of CondNN [82], we describe \mathcal{D}_{ev} as

$$\psi_{aged} = (1 - \mathcal{D}_{ev})\psi_{virgin} \quad \text{where} \quad \mathcal{D}_{ev} = \mathcal{E}_{ev}(\mathbf{x}_{ev}) \quad \text{and} \quad \mathbf{x}_{ev} = \{t, T, RH, \dots\} \quad (5.4)$$

Fatigue Damage Add-on

he contribution of fatigue damage under cyclic loads to the mechanical behaviour of polymeric materials, will be modeled based on our recent paper [177] by proposing an Add-on correction function. Most cross-linked materials, e.g., hydrogels and elastomers, soften by each cycle of tensile loading due to the damage evolution in the matrix induced by deformation. In the case of high cycle numbers, the material responds and eventually reaches a stable curve known as the fatigue limit. This behaviour has been illustrated in Fig. 5.1 where the peak stress σ_{\max}^1 reaches its maximum value in the first cycle and then gradually decreases as the number of cycles increases until it reaches a steady-state value of σ_{\max}^{∞} . Interestingly, experimental results demonstrate that $\hat{\sigma}^j$ is an ever-decreasing function that depends solely on j and is independent of the stretch amplitudes (see [178] for more discussion).

It should be noted that the distance between this zone and the fracture affects how much normalized softening occurs (from the start of the softening to reaching the stable zone). The three-zone normalized softening charts till fracture reflect this [179]. (i) A stress softening takes place in the first zone, starting with the second cycle and continuing until the stable zone is reached. (ii) To reach the critical damage level, there is a slight variation in the normalized maximum stress laying up in the second zone. (iii) The normalized maximum stress rapidly decreases in the third and final zone, which lasts until the sample fails. Consequently, one can describe the mechanical damage \mathcal{D}_{me} as

$$\mathcal{D}_{me} = \mathcal{E}_{me}(\mathbf{x}_{me}^{(i)}) \quad \text{where} \quad j \in \mathbf{x}_{me} \quad (5.5)$$

Constitutive Model

The constitutive behaviour of the material is modeled based on our recent paper [78] using a set of collaborative shallow neural network agents. In our recent paper, we suggested a framework to use ideas from continuum mechanics, statistical physics, and polymer science to create super-constrained reduced-order machine learning algorithms, which could help to partially solve the challenges now present. We have simplified the 3D stress-strain tensor mapping problem into a small set of super-constrained 1D mapping problems via sequential order reduction. Then, we added a collection of numerous replicated neural network learning agents (L-agents) to categorize those mapping issues into a select few groups, each of which was described by a different sort of agent. Accordingly, the polymer matrix continuum has been represented by a microsphere constructed by polymer chains that are uniformly and equally dispersed in all spatial directions. Micro-sphere concept is valid for materials that are initially isotropic and incompressible. The volumetric strain energy of the microsphere was then expressed by integrating the energy of chains in all directions as $[\mathbf{d}_i]_{i=1\dots N_d}$. Assuming the 3D polymer matrix to be a homogenous super-assembly of various 1D polymer bundles dispersed in all spatial directions, the energy of the sphere, Ψ_0 , may be easily calculated by integrating the energies of all the components, as

$$\Psi_0 = \frac{1}{4\pi} \int_S \psi^{\mathbf{d}} dS^{\mathbf{d}}. \quad (5.6)$$

Using this approach, the behaviour of the polymer matrix can be modeled by having the behaviour of basic 1D components. To calculate the energy of all 1D components, a surface integration may be carried out numerically across N_d integration directions $[\mathbf{d}_i]_{i=1\dots N_d}$ with different weight factors $[w_i]_{i=1\dots n}$. Such integration can be performed by discretizing the sphere into finite sections. Therefore, it is possible to express the strain energy of the polymer matrix Ψ_D in terms of its constituents as

$$\Psi_D(\mathbf{F}) = (1 - \mathcal{D}) \frac{1}{4\pi} \int_S \psi^{\mathbf{d}} dS^{\mathbf{d}} \cong (1 - \mathcal{D}) \sum_{i=1}^{N_d} w_i \psi^{\mathbf{d}_i}, \quad \text{where} \quad \psi^{\mathbf{d}_i} = \mathcal{B}^{\mathbf{d}_i} \quad (5.7)$$

where \mathbf{F} stands for macro-scale deformation gradient, $\Psi_m^{d_i}$ is the element's energy in direction \mathbf{d}_i and is represented by a group of L-agents \mathcal{B}^{d_i} that, using the microsphere idea, represents the cooperative addition of many L-agents $\mathcal{B}^{d_i} = \sum_{j=1}^{N_s} \mathcal{A}_j^{(i)}$. We assume that, in the virgin state, $\mathcal{B}^{d_i} = \mathcal{B}^{d_j}$, all multi-agents are identical in order to meet initial isotropy. It is crucial to reformat the energy of a single polymer chain with respect to $\lambda^d = \sqrt{\mathbf{d}^T \mathbf{F}^T \mathbf{F} \mathbf{d}}$ as follows because chains in different orientations are subject to multiple micro-stretches.

Constitutive formulation By differentiating Eq. 5.1 with respect to the deformation gradient \mathbf{F} and using the formula $\frac{\partial J}{\partial \mathbf{F}} = J\mathbf{F}^{-T}$, the first Piola-Kirchhoff tensor \mathbf{P} may be obtained. \mathbf{P} may therefore be written as

$$\mathbf{P} = \frac{\partial \Psi_M(\mathbf{F})}{\partial \mathbf{F}} - p\mathbf{F}^{-T}, \quad \frac{\partial \Psi_M(\mathbf{F})}{\partial \mathbf{F}} = \sum_{i=1}^k w_i \frac{\partial \mathcal{B}^{d_i}}{\partial \lambda^{d_i}} \frac{1}{2\lambda^{d_i}} \frac{\partial d_i \bar{\mathbf{C}} d_i}{\partial \bar{\mathbf{F}}} : \frac{\partial \bar{\mathbf{F}}}{\partial \mathbf{F}}, \quad \text{while } \psi^{d_i} = \mathcal{B}^{d_i}, \quad (5.8)$$

where \mathbf{C} is the right Cauchy–Green tensor, $\bar{\mathbf{F}} = \mathbf{J}^{-1/3}\mathbf{F}$, and $\bar{\mathbf{C}} = \mathbf{J}^{-2/3}\mathbf{C}$. Additionally, by applying the following identities, the equation might be made even simpler as follow

$$\frac{\partial d \bar{\mathbf{C}} d}{\partial \bar{\mathbf{F}}} : \frac{\partial \bar{\mathbf{F}}}{\partial \mathbf{F}} = 2\bar{\mathbf{F}}(\mathbf{d} \otimes \mathbf{d}) : \mathbf{J}^{-\frac{1}{3}}\mathbb{I} = 2\mathbf{J}^{-\frac{1}{3}}\bar{\mathbf{F}}(\mathbf{d} \otimes \mathbf{d}). \quad (5.9)$$

Normalization, conditions of growth, isotropy, objectivity, and poly-convexity are already satisfied in the proposed equation.

A simple N -layer multilayer feed-forward neural network comprising an input layer, $N - 1$ hidden layers, and an output layer. We suppose that the n^{th} hidden layer has N_n neurons. The previous layer's post-activation output $\mathbf{x}^{n-1} \in \mathbb{R}^{N_{n-1}}$ is then fed into the n^{th} hidden layer, and the specific affine transformation is of the form

$$\mathcal{H}_n(\mathbf{x}^{n-1}) \triangleq \mathbf{W}^{(n)}\mathbf{x}^{n-1} + \mathbf{b}^{(n)}, \quad (5.10)$$

where the network weight $\mathbf{W}^{(n)} \in \mathbb{R}^{N_n \times N_{n-1}}$ and the bias term $\mathbf{b}^{(n)} \in \mathbb{R}^{N_n}$ to be learned are both initialized using unique procedures like Xavier or He initialization [79, 80].

The nonlinear activation function $\sigma(\cdot)$ is applied component-by-component to the current layer's affine output \mathcal{H}_n . Furthermore, for some regression issues, this nonlinear activation is not employed in the output layer.

As a result, the neural network may be denoted as

$$\mathcal{N}(\mathbf{x}; \Theta) = (\mathcal{H}_N \circ \sigma \circ \mathcal{H}_{N-1} \circ \cdots \circ \sigma \circ \mathcal{H}_1)(\mathbf{x}), \quad (5.11)$$

where \circ denotes the composition operator, $\Theta = \left\{ \mathbf{W}^{(n)}, \mathbf{b}^{(n)} \right\}_{n=1}^N \in \mathcal{P}$ denotes the learnable parameters to be optimized later in the network, and \mathcal{P} denotes the parameter space, and \mathcal{N} and $\mathbf{x}^0 = \mathbf{x}$ denote the network's output and input, respectively. Each L-agent can be represented by a neural network as follow

$$\mathcal{A}_j^{(i)} := \psi_j^{d_i}(\mathbf{x}_e^{(i)}; \Theta_e^{(i)}), \quad (5.12)$$

where $\psi_j^{d_i}$ represents the energy of deformation-induced damage part.

Physics-informed Neural Network Here, we define the loss function \mathcal{L} Mean Squared Error (MSE) for a total of n_{tot} data points as

$$\mathcal{L}(\mathbf{x}, \Theta) = \frac{1}{2} \sum_{n=1}^{n_{tot}} \left[\mathbf{g}_1 \left(\sum_{i=1}^{N_d} \sum_{j=1}^{N_s} w_i \frac{\partial(\text{sig}(a\mathcal{D}_{me} + b\mathcal{D}_{ev})\psi_j^{d_i})}{\partial \mathbf{F}} - p\mathbf{F}^{-T} \right) \mathbf{g}_1 - P_n^{11} \right]^2, \quad (5.13)$$

where $P_n^{11} := \mathbf{g}_1 \mathbf{P}_n \mathbf{g}_1$ is the first component of the experimental macro-scale stress tensor \mathbf{P}_n in loading direction \mathbf{g}_1 for point n , while

$$\mathcal{D}_{me} = \mathcal{N}_{me}(\mathbf{x}_{me}, \Theta_{me}), \quad \mathcal{D}_{ev} = \mathcal{N}_{ev}(\mathbf{x}_{ev}, \Theta_{ev}), \quad \psi_j^{d_i} = \mathcal{N}_e(\mathbf{x}_e^{(i)}, \Theta_e^{(i)}). \quad (5.14)$$

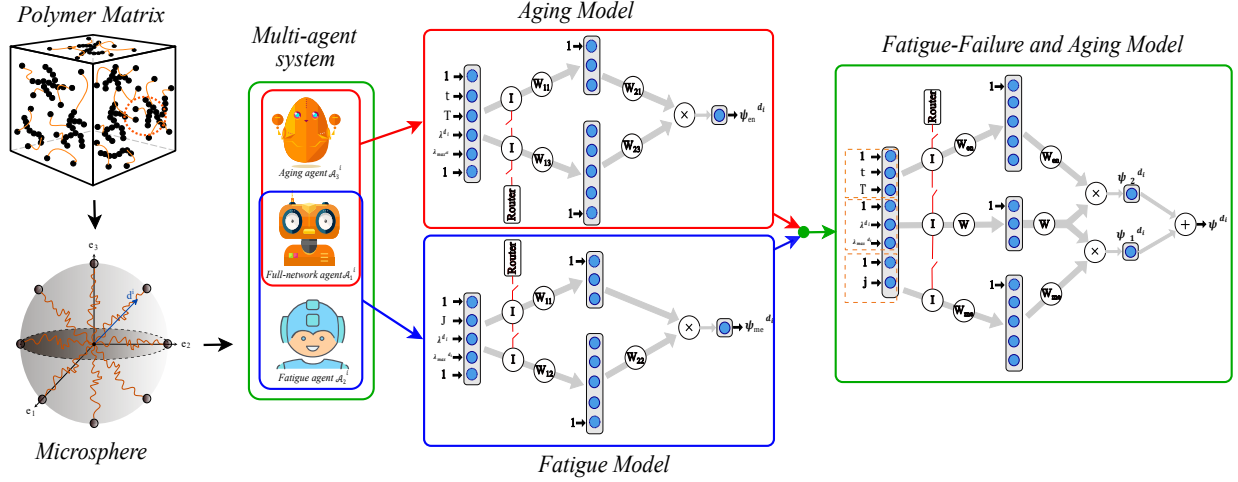


Figure 5.5. Illustration of the suggested model, which includes order-reduction and model fusion. It demonstrates how we propose a knowledge-based platform using ideas from continuum mechanics, polymer sciences, physics, and machine learning

5.2.1 Failure model

The failure point in a continuum body is then captured using an extension of our methods. Typically, when the strain increase, hyper-elastic material models permit an unlimited growth in strain energy.

$$\|\mathbf{F}\| \rightarrow \infty \Rightarrow \Psi_D(\mathbf{F}) \rightarrow \infty \quad (5.15)$$

where $\|\dots\|$ is a tensorial norm. Obviously, no natural substance stores more and more strain energy when its deformation becomes larger and larger. Here, a strain energy limiter known as the critical failure energy is shown.

$$\|\mathbf{F}\| \rightarrow \infty \Rightarrow \Psi_D(\mathbf{F}) = \mathcal{E}(t, T, j) \quad (5.16)$$

where $\mathcal{E}(t, T, j)$ may be thought of as the energy of material failure, which depends on the aging period (t), temperature (T), and the number of cycles (j). We assume that $E(t, T, j)$ is the single constant explaining the characteristics of material failure, similar to how classical fracture mechanics introduces only one constant of material toughness (or the critical energy release rate) to characterize failure. In fact, this may be seen as a failure criterion that describes how a material's

"toughness" changes with time and is defined in the previous step. In other words, we assume that the evolution of toughness of intact material over aging is equivalent to the change in strain energy of a polymer matrix during aging $\Psi_D(\mathbf{F}_f^a)$. The damage function D , which may take into account the interaction of thermal aging and fatigue, models the evolution of toughness. Accordingly, the breakdown point of the material during aging may be determined by equating the strain energy of the damaged matrix Ψ_D and the virgin state Ψ_{unaged} .

$$\|F\| \rightarrow \infty \quad \Rightarrow \quad \Psi_D(\mathbf{F}_f^a) = \mathcal{E}(t, T, j) = (1 - \mathcal{D})\Psi_0(\mathbf{F}_f^0) \quad (5.17)$$

where the failure points of aged and new materials, respectively, are \mathbf{F}_f^a and \mathbf{F}_f^0 . It should be emphasized that as a result of the polymer matrix's changing shape during aging, free radical P° production occurs. The propagation of chemical processes in the polymer is favored by the unique reactivity of the free radicals P° with oxygen. As a result, a chain's starting entropy in the material's aged state c_0^a , as opposed to its virgin state c_0^0 , is different. As a result, in order to compare the elongation at break for aged and virgin materials, one must first normalize the polymer matrix's strain energy with regard to its starting value. Note that we are using stress-strain point of unaged (\mathbf{F}_f^0) and several aged (\mathbf{F}_f^a) conditions for training. Next, by an inverse problem, we can find tensile strength and elongation at break for various aged conditions using Eq. 5.17.

Algorithm 1 The algorithm for thermo-vibration and failure modeling

```
1:  $\mathbf{F}, \mathbf{t}, \mathbf{T}, \mathbf{j} \leftarrow$  Import defromation, time, temperature, and number of cycles as NN inputs.
2:  $l, n \leftarrow$  Initialize NN hyperparameters.
3:  $\mathbf{W} \leftarrow$  Initialize NN parameters.
4:  $\mathbf{d}, \mathbf{w} \leftarrow$  Initialize set of directions and their weights.
5:  $\Psi_D(\mathbf{F}_f^a) = (1 - \mathcal{D})\Psi_0(\mathbf{F}_f^0) \leftarrow$  define constraints for failure point.
6: while  $err > TOL$  do
7:   while  $i < k$  do
8:      $\lambda^{d_i}, \lambda_{max}^{d_i} \leftarrow$  Calculate stretch and hisory of that.
9:      $\psi^{d_i} \leftarrow$  Calculate the strain energy based on NN.
10:   end while
11:    $\Psi_D(\mathbf{F}_f^a) \leftarrow$  Calculate matrix energy using 21 integration points.
12:    $\mathcal{L} \leftarrow$  define cost function based on NN and experimental data.
13:    $\mathbf{W} \leftarrow$  Constraint optimization of  $\mathcal{L}$  for  $\mathbf{W}$ .
14: end while
```

5.3 Validation and results

We compared the proposed model's predictions to the outcomes of our experiments, which were conducted with the explicit goal of revealing the detrimental effects of chemical and mechanical aging on the constitutive response and energy absorption of the polymer matrix.

We employed identical engines, a rather straightforward engine created by $N_d = 21$ multi-agents with $N_s = 3$ agents each, as described in [83]. It should be noted that the decision about the number of multi-agents and the associated agents might depend on the trade-off between accuracy and computational expense. In other words, since 21 multi-agents is a modest number for an integral estimate with a summation, we take it into consideration. As a result, it ensures that even in a limited number of multi-agents, the suggested model error in prediction is negligible . Only two agents, one of which is a representation of the first and second invariants of the Green-Cauchy deformation

tensor, were utilized to capture all deformation states. For the NNs structure of L-agents, we considered one input layer, one hidden layer with four neurons, and three activation functions soft plus $\psi(\bullet) = \ln(1 + e^\bullet)$, sinusoid $\psi(\bullet) = \sin(\bullet)$ and hyperbolic tangent $\psi(\bullet) = \tanh(\bullet)$.

To capture the deformation of the rubbers with full memory, the internal parameters of L-agents were developed using λ_{j-max} parameters. The first and second deformation invariants were provided to each multi-agents in order to enable them to forecast different deformation states [139, 60]. By feeding input sets to the first and second L-agents as needed, the requirement was met as

$$\mathbf{x}_e^{(i)} = [\lambda^{d_i}, \lambda_{max}^{d_i}, \nu^{d_i}, \nu_{max}^{d_i}], \quad \mathbf{x}_{ev}^{(i)} = [T, t], \quad \mathbf{x}_{me}^{(i)} = [j], \quad (5.18)$$

while

$$\lambda^{d_i} = \sqrt{\mathbf{d}_i \mathbf{C} \mathbf{d}_i}, \quad \nu^{d_i} = \sqrt{\mathbf{d}_i \mathbf{C}^{-1} \mathbf{d}_i}, \quad \mathbf{C} = \mathbf{F}^T \mathbf{F} \quad (5.19)$$

where $[\mathbf{d}_i]_{i=1\dots N_d}$ is integration directions in micro-sphere, λ^{d_i} and ν^{d_i} are related to I_1 and I_2 , as the first and second invariants of \mathbf{C} , respectively.

In summary, the rubber matrix was represented by a cooperative game of 21 multi-agents of 3 agents through $\mathcal{A}_j^{(i)}$, $i \in \{1, 21\}$, $j \in \{1, 2\}$. After agent fusion, the final cost function is given by

$$\mathcal{L}(\Theta_e, \Theta_{ev}, \Theta_{me}) = \frac{1}{2} \sum_{n=1} [\mathbf{g}_1 \left(\sum_{i=1}^{21} \sum_{j=1}^2 w_i \frac{\partial \mathcal{A}_j^{(i)}}{\partial \lambda_j^{d_i}} \frac{\partial \lambda_j^{d_i}}{\partial \mathbf{F}} - p \mathbf{F}^{-T} \right) \mathbf{g}_1 - P_n^{11}]^2, \quad \text{while} \quad \mathcal{A}_j^{(i)} := \mathcal{D}^{d_i} \psi_j^{d_i}(\mathbf{x}^{(i)}; \Theta^{(i)}), \quad (5.20)$$

subjected to weights related to λ_{max} and $\nu_{max} \leq 0$, as well as λ and $\nu \geq 0$, to fulfill poly-convexity and thermodynamic consistency, respectively.

As a result, each sub-energy element can be expressed in terms of the deformation gradient \mathbf{F} as follows

$$\sum_{i=1}^{21} w_i \frac{\partial \mathcal{A}_1^{(i)}}{\partial \lambda^{d_i}} \frac{\partial \lambda^{d_i}}{\partial \mathbf{F}} = \sum_{i=1}^{21} w_i \frac{\partial \mathcal{A}_1^{(i)}}{\partial \lambda^{d_i}} \frac{1}{\lambda^{d_i}} \mathbf{F} (\mathbf{d}_i \otimes \mathbf{d}_i). \quad (5.21)$$

$$\sum_{i=1}^{21} w_i \frac{\partial \mathcal{A}_2^{(i)}}{\partial \nu^{d_i}} \frac{\partial \nu^{d_i}}{\partial \mathbf{F}} = - \sum_{i=1}^{21} w_i \frac{\partial \mathcal{A}_2^{(i)}}{\partial \nu^{d_i}} \frac{1}{\nu^{d_i}} \mathbf{F}^{-1} \mathbf{F}^{-T} \mathbf{F}^{-1} (\mathbf{d}_i \otimes \mathbf{d}_i). \quad (5.22)$$

The predictions of the developed model versus experimental findings for various aging durations and the number of cycles at temperatures of 60 and 80°C, respectively, are shown in Figs. 5.6 and 5.7. The created model is able to forecast both the material's reaction to softening brought on by fatigue damage and hardening brought on by thermal aging. Additionally, it can forecast how both damage processes would behave when added together.

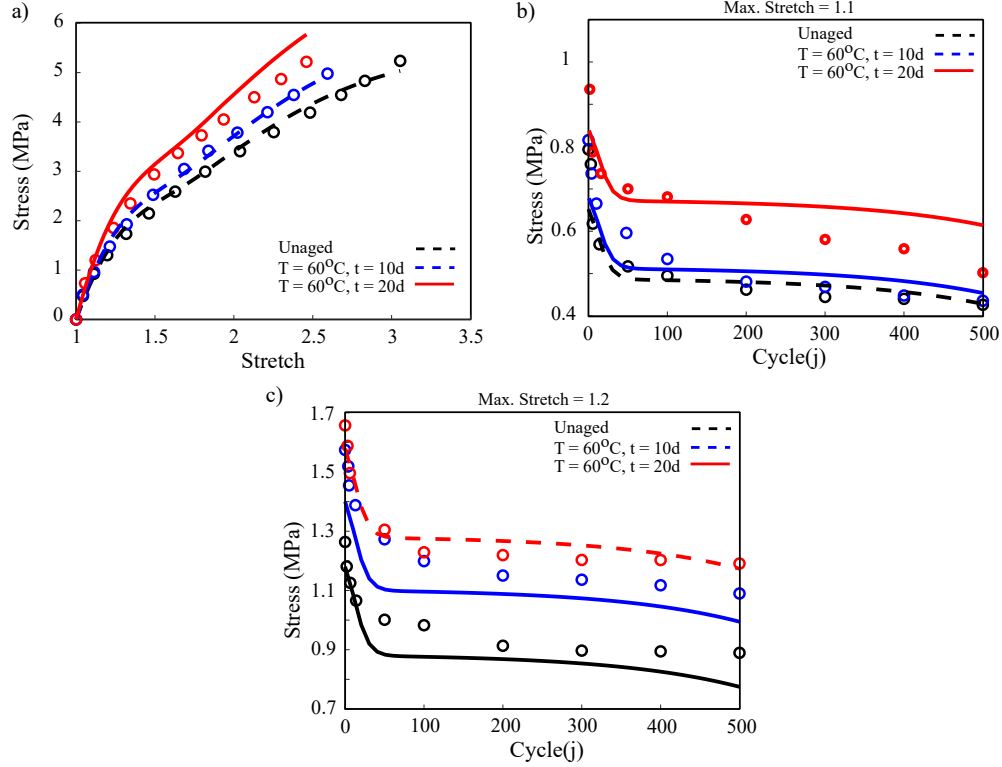


Figure 5.6. Validation of the model predictions for SBR for unaged, and aged material for 10 and 20 days in at 60°C; a) the samples' constitutive behavior, including their respective failure endpoints, b) maximum stress versus the number of cycles with maximum stretch of $stretch_{max} = 1.1$, and c) maximum stress versus the number of cycles with maximum stretch of $stretch_{max} = 1.2$. The solid lines show the performance of model in prediction after the training

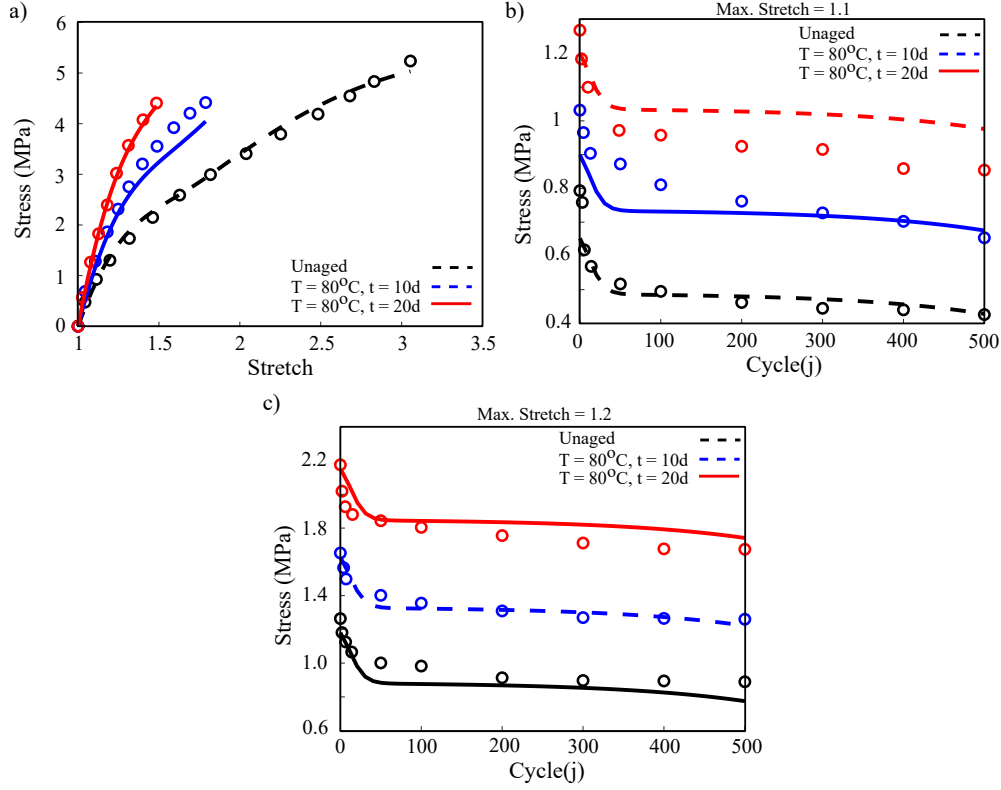


Figure 5.7. Validation of the model predictions for SBR for unaged, and aged materials for 10 and 20 days in at 80°C ; a) the samples' constitutive behavior, including their respective failure endpoints, b) maximum stress versus the number of cycles with maximum stretch of $stretch_{max} = 1.1$, and c) maximum stress versus the number of cycles with maximum stretch of $stretch_{max} = 1.2$. The solid lines show the performance of model in prediction after the training

The model has a reasonable accuracy and can predict both constitutive behavior and the failure point (see Fig. 5.8).

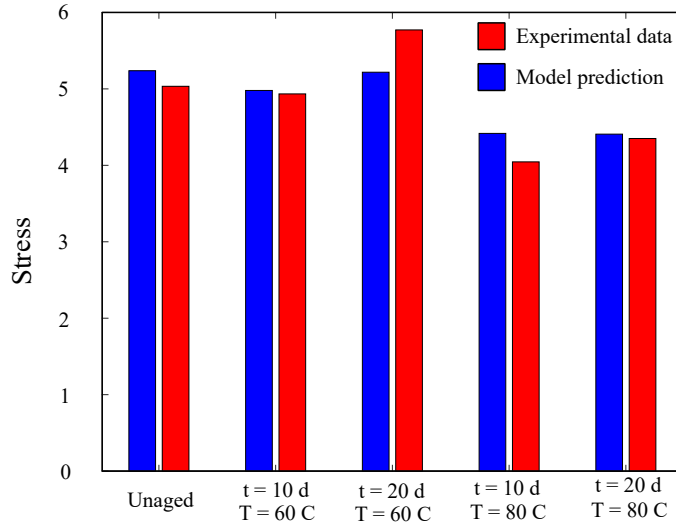


Figure 5.8. Prediction of the failure points due to degradation effect

The aging experiments were carried out separately since we lacked the experimental capacity to perform thermal and mechanical aging simultaneously (i.e., intermittent approach). Therefore, the goal of this research is to comprehend how the damage caused by mechanical and thermal aging builds up over time. Mechanical aging and thermal aging both cause various damage pathways. Therefore, in order to expand the research to simultaneous damage accumulation, it is crucial to comprehend how sequential damage accumulation affects the evolution of mechanical characteristics. The present model, it should be highlighted, links damage to the buildup of thermal aging and fatigue as well as to their combined impact.

5.4 Conclusion

The purpose of this research was to put out a unique, physics-based framework to describe how elastomeric network mechanics and environmental degradation are related. The proposed model is utilized to explain how thermal aging and cyclic fatigue affect the material's behavior. Massive chain scission, cross-link reduction, chain forms, and modifications in polymer morphology are a few examples of mechanical and environmental damages that, over time, influence the polymer matrix. To put it another way, this model is predictive rather than descriptive. As a result, it can

give end customers a prediction for the trustworthy design of components at a fraction of the time and expense. The model, however, cannot be utilized to comprehend or research kinetics. The data-driven approach seeks to overcome the limitations of both phenomenological and micro-mechanical models by deriving micro-structural activity from macroscopic experimental data.

Additionally, we hypothesize that the development of strain energy and the loss of toughness during aging are related, which enables us to predict the breakdown point along the aging trajectory.

By validating against various experimental data chosen to illustrate the evolution of inelastic behavior during parallel damage accumulation, the good performance of the proposed scheme was demonstrated. Comparing the model's efficiency to the experimental data revealed that it was generally acceptable and, in some circumstances, great. Because we do not need to know the precise behavior and interaction of microstructures, the model's accuracy and simplicity make it a good choice for commercial and industrial applications. However, in the future, the model can be expanded to consider viscoelasticity and non-isotropic formation for greater precision due to the model's platform. Additionally, the dataset we select for training fully determines how well the suggested model performs. It follows logically that expanding the training dataset will improve the model's ability to predict results.

CHAPTER 6

PHYSICS-INFORMED NEURAL NETWORK MODEL; PYROLYSIS AND ABLATION OF POLYMERS

6.1 Introduction

Heat causes both physical and chemical changes in solid polymeric materials. Thermal decomposition and thermal degradation need to be distinguished clearly from one another. The process of considerable chemical species change brought on by heat is known as thermal decomposition. Thermal degradation is the loss of physical, mechanical, or electrical qualities as a result of the effect of heat or excessive temperature on material, product, or assembly. Thermal decomposition is the main alteration in burning.

Pyrolysis is one of the many different types of chemical decomposition processes that take place at higher temperatures. It differs from other processes like combustion and hydrolysis in that it seldom requires the addition of additional reagents such as oxygen (O_2) or water (in hydrolysis). Pyrolysis results in solids (char), condensable liquids (tar), and non-condensing/permanent gases [180, 181, 182]. Pyrolysis is widely used in the chemical industry to make ethylene, various kinds of carbon, and other compounds from petroleum, coal, and even wood, as well as to make coal coke. It has also been utilized lately on an industrial scale to convert natural gas (mainly methane) into non-polluting hydrogen gas and non-polluting solid carbon char. Pyrolysis might be used to turn biomass into syngas and charcoal, waste plastics back into useful oil, or trash into securely disposable substances, among other things [183, 184].

The combined impacts of thermal, chemical and physical processes play a significant role in the pyrolysis problems in polymeric materials [185, 186]. Table 6.1 summarizes the different thermal,

chemical, and physical processes that may be investigated in burning.

Table 6.1. A summary of processes that can be anticipated in burning analysis

Heat conduction/temperature	[187], [188], [189]
Pyrolysis	[190], [191], [192]
Volatile convective flow	[193], [194], [195]
Char formation/mass loss	[193], [194], [195]
Internal pressure	[190], [191], [192]
Thermal expansion	[192], [194], [195]
Thermal stresses	[196], [197], [198]

Before getting into the details of the models, it is crucial to understand what happens when the polymer is exposed to a high-temperature heat source.

Chemical Processes: Polymers can decompose thermally by oxidative reactions or just by being exposed to heat. Several main groups of chemical processes play significant roles in the heat decomposition of polymers, including (1) Chain-stripping, in which atoms or groups not a part of the polymer chain (or backbone) are cleaved; (2) cross-linking, in which bonds are formed between polymer chains. (3) Random-chain scission, in which chain scissions occur at seemingly random locations in the polymer chain; (4) End-chain scission, in which individual monomer units are successively removed at the chain end; It suffices to state here that heat decomposition of a polymer often involves many reactions from each of these kinds. However, these broad categories offer a conceptual framework that is helpful for comprehending and categorizing polymer decomposing behavior (see Fig. 6.1).

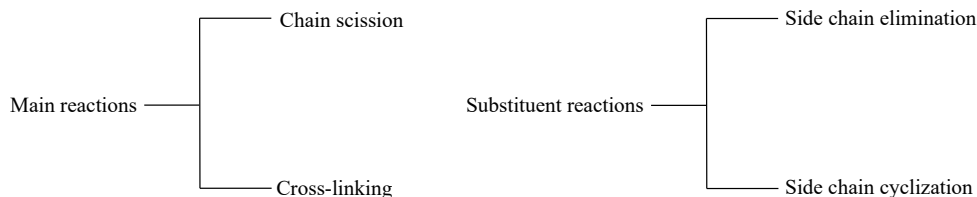


Figure 6.1. General decomposition mechanisms

Physical Processes: The nature of the material may have an impact on the many physical processes that take place during heat decomposition. For instance, simple phase transitions upon heating are not achievable for thermosetting polymeric materials because they are infusible and insoluble after they have been synthesized. On the other hand, if heating does not go over the minimum thermal breakdown temperature, thermoplastics can be softened by heating without the material undergoing irreversible alterations. This gives thermoplastic materials a significant edge in terms of how simple it is to mold or thermoform items. Carbonaceous chars are created during the thermal decomposition of several materials, including cellulosic, thermosetting, and thermoplastic ones. The ongoing thermal decomposition process will be significantly impacted by the physical makeup of these chars. The pace of heat decomposition of the remaining polymer is frequently determined by the physical properties of the char. Even though char production is a chemical process, its relevance is mostly because of its physical characteristics.

The polymer continues to decompose endothermically until the reaction zone reaches the material's back-face when the rest of the polymer is degraded to volatiles and char.

The physics of this thermo-chemical reaction is well understood, and it is described by a collection of coupled nonlinear partial differential equations (PDEs) that describe heat conduction and burning kinetics [200, 201]. These PDEs (see section 6.2), however, do not have a closed-form solution; computational approximation is necessary.

Traditional solvers vs. Data-driven methods. The finite element method (FEM) is a common approach that (1) uses a set of basis functions within discretized sub-domains of the geometry to approximate the solution to the PDE at each time point and (2) iteratively simulates the evolution of the basis function coefficients forward in time [202, 203]. Comes with a restrictive computational cost in the case of repetitive simulations, such as optimization, control, real-time monitoring, probabilistic modeling, and uncertainty quantification. This is due to the fact that forward simulations require solving large non-linear equations repeatedly.

In general engineering applications, the advent of Machine Learning (ML) and AI in recent years has provided an opportunity to construct quick surrogate ML models to replace classical FEM.

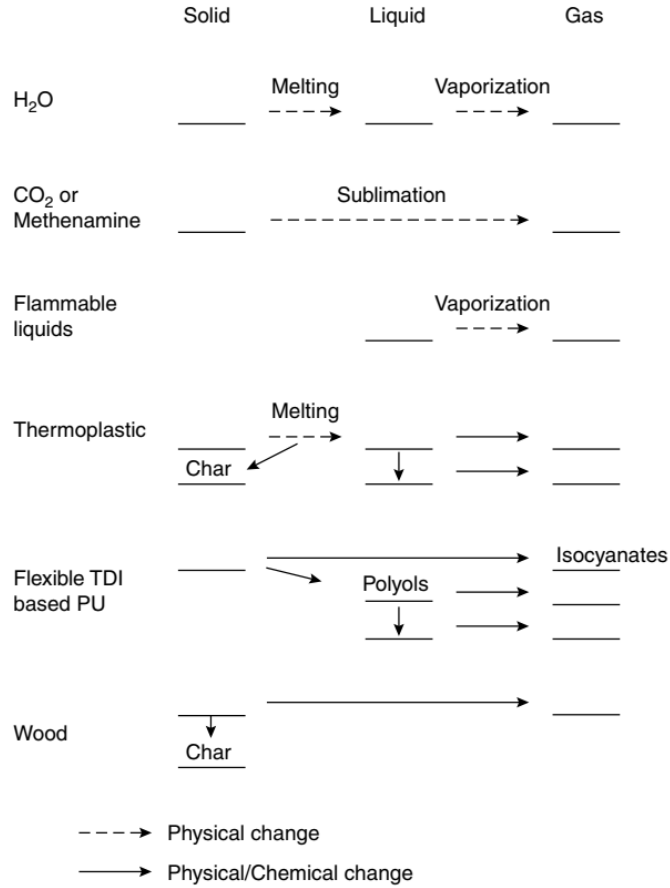


Figure 6.2. Physical and chemical changes during thermal decomposition [199]

Classic neural networks, on the other hand, map across finite-dimensional spaces and can thus only learn discretization-specific solutions. This is frequently a constraint in actual applications, necessitating the creation of mesh-invariant neural networks. The finite-dimensional operators and Neural-FEM are two popular neural network-based techniques for solving multiple PDEs [204]

Finite-dimensional operators. A new line of research has suggested using neural networks to learn mesh-free, infinite-dimensional operators [6, 205]. Only a forward pass of the network is required to provide a solution for a new instance of the parameter, avoiding the significant computational difficulties that plague Neural-FEM approaches. The neural operator just requires data, not knowledge of the underlying PDE. Due to the difficulty of evaluating integral operators, neural operators have not provided effective numerical techniques that can match the success of convolutional or recurrent neural networks in the finite-dimensional scenario.

Neural-FEM. The third method is known as the physics-informed neural network (PINN). PINN differs from other machine learning paradigms widely employed for mechanics and physics challenges in terms of how data is needed and employed. Unlike supervised learning, which is often used for materials laws and requires artificial intelligence to be trained with labels in order to generate forecasts, the search for the solution in PINN does not require any data other than the ones required to form the loss function [206, 207, 208, 209].

PINN challenges. The training of PINN, however, is far from simple, especially for nonlinear systems of equations. To construct the multi-layer perceptron, non-linearities should be applied to each element of the output of the linear transformation. This is unlike the finite element method, which is a more entrenched framework with clear strategies and established mathematical analysis that guarantees convergence and stability for both the solution and weighting functions in pre-determined finite-dimensional spaces. Furthermore, for both forward and inverse problems, the physical constraints or controlling equations could be expressed in several ways; for instance, the collocation-based loss function, which evaluates the solution at specific collocation points, or the energy-based method that can reduce the order of the derivatives in governing equations despite requiring numerical integrations. A large number of tunable hyperparameters, such as the configurations of the neural network, the types of activation functions, and the neuron weight initialization, as well as different techniques to impose boundary conditions while providing significant flexibility, may bewilder researchers who are unacquainted with neural networks [210, 211, 212].

Goals. The training element of the physics-informed neural network for high nonlinear PDEs like Burning is the core of this article. Our goal is to find techniques to make PINN training less costly, lower the amount of trial-and-error necessary to appropriately tune the hyper-parameters, and at the very least, empirically increase the training process's robustness. Although the strategies given in this research may be relevant to other versions, we confined the scope of this study to the collocation physics-informed neural network. Our current attempt is to present a synthesis that incorporates: (i) employing non-dimensionalization and normalization of the physical parameter to address the problem of complex equations, (ii) infusing a broad understanding of the solution field

with imprecise knowledge, (iii) using a weighted-sum scheme to enhance optimization algorithms in the context of multi-objective optimization, (IV) exploiting different approaches for weight initialization due to unbalanced gradients causes inaccuracy in optimization.

6.2 Exothermic Heat Transfer

When charring polymers are subjected to high temperatures, thermal energy is transferred into the polymer via thermal convection. Pyrolytic gases and solid residues will arise from the material's decomposition. According to the degree of pyrolysis, the polymer may be divided into three zones, as indicated in Figure 6.2: The polymer decomposes into three zones: charring, pyrolysis, and virgin material. [213].

In the thermal study of heat transfer in polymers, three main types of thermal energy transmission are often considered: conduction, convection, and radiation. However, for the sake of simplicity, all mathematical models for polymers cover the effect of heat conduction in the case of one-sided heating only. The effect of external convection on heat transfer is rarely explored. Similarly, heat radiation from a polymer is rarely taken into account.

So, the following PDE governs heat transfer in polymers, i.e., heat transfer with internal heat generation is expressed as [214, 215, 216].

$$\frac{\partial}{\partial t} (\rho C_p T) = \frac{\partial}{\partial x} \left(k_{xx} \frac{\partial T}{\partial x} \right) + \frac{\partial}{\partial y} \left(k_{yy} \frac{\partial T}{\partial y} \right) + \frac{\partial}{\partial z} \left(k_{zz} \frac{\partial T}{\partial z} \right) + \dot{Q}, \quad (6.1)$$

where T is the temperature, $C_p(T, \alpha)$, $k(T, \alpha)$, and $\rho(T, \alpha)$ are the solid's specific heat capacity, conductivity, and density which are a function of temperature and degree of burning, and \dot{Q} is the rate of internal heat consumption. The change in thermal energy per unit volume is represented on the left-hand side of the equation, while the energy flux owing to conduction is represented on the right-hand side. The through-thickness direction is defined by the x-direction, whereas the planar directions are defined by the y- and z-directions.

Internal heat consumption in polymeric material is expressed as a function of the degree of

burning $\alpha \in (0, 1)$, which is a measure of the conversion achieved during the polymeric material's burning reactions. The relationship between \dot{Q} and α , in particular, can be expressed as [217, 218]

$$\dot{Q} = -Q_r \frac{d\alpha}{dt}, \quad (6.2)$$

where Q_r is the heat of reaction generated per unit mass of polymer during burning [188]. The evolving degree of burning in polymeric materials is usually controlled by an ordinary differential equation that indicates the rate of burning as a function of immediate temperature and degree of burning [187, 219, 220].

$$\frac{d\alpha}{dt} = g(\alpha, T) > 0. \quad (6.3)$$

Assumptions: Energy transfer via convection is considered to be insignificant in this study, and the volatile gases created by the pyrolysis reaction are expected to be evacuated from the material promptly and hence have no effect on the temperature. Temperature and the stage of the breakdown reaction influence thermal conductivity, density, and heat capacity. However, because the change in thermal conductivity with temperature cannot be calculated theoretically, this term must be determined experimentally throughout the temperature range of interest.

In the space-time domain (\mathbf{x}, t) , this results in a coupled system of differential equations for temperature and degree of burning. The temperature $T(\mathbf{x}, t)$ and degree of burning $\alpha(\mathbf{x}, t)$ in the polymeric material are predicted by solving this system of differential equations with initial and boundary conditions. This work aims to solve the system of differential equations for the polymeric system burning shown in Fig. 6.3.

The boundary conditions at both ends can be set to a specific temperature by using the following equations

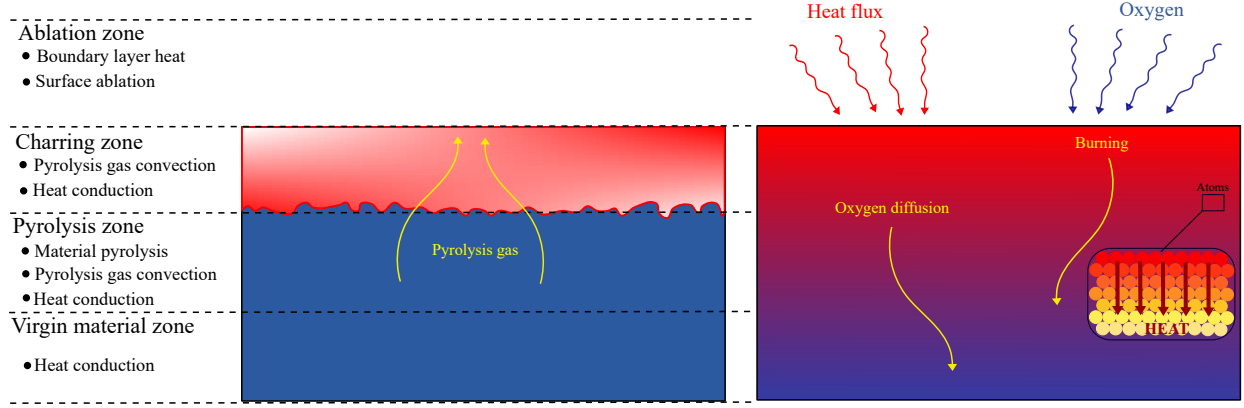


Figure 6.3. A schematic of polymeric materials during burning

$$\begin{aligned}
 T|_{x=0,y,z} &= T_{bx}(t), & T|_{x=L,y,z} &= T_{tx}(t), & T|_{x,y=0,z} &= T_{by}(t), \\
 T|_{x,y=L,z} &= T_{ty}(t), & T|_{x,y,z=0} &= T_{bz}(t), & T|_{x,y,z=L} &= T_{tz}(t),
 \end{aligned} \tag{6.4}$$

where the subscripts b and t represents the coordinates of the bottom and top surfaces of the material, respectively. The initial conditions are written as follows

$$T|_{t=0} = T_0(x) \quad \text{and} \quad \alpha|_{t=0} = \alpha_0(x), \tag{6.5}$$

where T_0 is the system's initial temperature, which is normally assumed to be constant in the geometry, and α_0 is the polymer's initial degree of burning, which is assumed to be zero for unburned materials in the entire spatial domain.

6.3 Physics-Informed Neural Network

6.3.1 Neural Network Architecture

Neural networks are well-known for their ability to represent information. Based on the universal approximation theorem, any continuous function can be arbitrarily estimated by a multi-layer perceptron containing one hidden layer and a finite number of neurons [221, 222]. While neural

networks can compactly express very complicated functions, obtaining the precise parameters (weights and biases) required to solve a particular PDE can be challenging [223].

The bulk of solutions has used feed-forward neural networks since Raissi et al. [4, 224] original vanilla PINN. Some researchers, on the other hand, have tested with several types of neural networks to investigate their effect on the overall PINN performance.

We start by building a simple D -layer multilayer feed-forward neural network comprising an input layer, $D - 1$ hidden layers, and an output layer. We suppose that the d^{th} hidden layer has N_d neurons. The previous layer's post-activation output $\mathbf{x}^{d-1} \in \mathbb{R}^{N_{d-1}}$ is then fed into the d^{th} hidden layer, and the specific affine transformation is of the form

$$\mathcal{H}_d(\mathbf{x}^{d-1}) \triangleq \mathbf{W}^d \mathbf{x}^{d-1} + \mathbf{b}^d, \quad (6.6)$$

where the network weight $\mathbf{W}^d \in \mathbb{R}^{N_d \times N_{d-1}}$ and the bias term $\mathbf{b}^d \in \mathbb{R}^{N_d}$ to be learned are both initialized using unique procedures like Xavier or He initialization [79, 80].

The nonlinear activation function $\sigma(\cdot)$ is applied component-by-component to the current layer's affine output \mathcal{H}_d . Furthermore, for some regression issues, this nonlinear activation is not employed in the output layer. As a result, the neural network may be denoted as

$$\mathcal{N}(\mathbf{x}; \Theta) = (\mathcal{H}_D \circ \sigma \circ \mathcal{H}_{D-1} \circ \cdots \circ \sigma \circ \mathcal{H}_1)(\mathbf{x}), \quad (6.7)$$

where \circ denotes the composition operator, $\Theta = \{\mathbf{W}^d, \mathbf{b}^d\}_{d=1}^D \in \mathcal{P}$ denotes the learnable parameters to be optimized later in the network, and \mathcal{P} denotes the parameter space, and \mathcal{N} and $\mathbf{x}^0 = \mathbf{x}$ denote the network's output and input, respectively.

Activation function DNN training performance is influenced by the activation function. Activations like as ReLU, Sigmoid, and Tanh are frequently utilized [225, 226]. Because the activation function in a PINN framework is evaluated using the second-order derivative, it is critical to choose it carefully. Because most activation functions (such as Sigmoid, Tanh, and Swish) are nonlinear around 0, it is preferable to pick a range of $[0, 1]$ rather than a wider domain when rescaling the

PDE to a dimensionless form. Furthermore, smooth activation functions such as the sigmoid and hyperbolic tangent can be used to ensure the regularity of PINNs, allowing for accurate calculations of PINN generalization error[227, 228].

6.3.2 Automatic Differentiation

In order to solve a PDE in PINNs, it is necessary to take derivatives of the network's output with respect to the input. The function u can be differentiated since it is approximated by a NN with smooth activation function \hat{u}_Θ . Calculating derivatives can be done in four ways: manually, symbolically, numerically, or automatically. When applied to complex functions, symbolic and numerical methods such as finite differentiation perform poorly; on the other hand, automatic differentiation (AD) conquers many limitations such as floating-point precision errors, numerical differentiation, and memory-intensive symbolic approaches [229, 230].

Nondimensionalization & Normalization of Equations Nondimensionalization $\bar{X} = \frac{X}{X_0}$ will be used to remove of physical dimensions of the governing parameters X to describe the physical process as the deviation of the parameters from their reference point X_0 which is used for normalization. This procedure allows us to simplify the loss function and prevent the effects of measured units in dimensional analysis. Further scaling of the non-dimensionless parameters is also used to prevent the effects of massive fluctuation of certain quantities that are less important relative to some appropriate unit. These units refer to quantities intrinsic to the physics of the process rather than measured units. Consider the dimensionless variables (denoted by $\bar{\circ}$) as follows:

$$\bar{t} = \frac{t}{t^*}, \quad \bar{x} = \frac{x}{x^*}, \quad \bar{y} = \frac{y}{y^*}, \quad \bar{T} = \frac{T}{T^*}, \quad \bar{\alpha} = \frac{\alpha}{\alpha^*}, \quad (6.8)$$

$t^*, x^*, y^*, T^*, \alpha^*$ are dimensionless variables that written as

$$x^* = L_x, \quad y^* = L_y, \quad t^* = \frac{\rho C_p L_x^2 L_y^2}{k_{xx} L_y^2 + k_{yy} L_x^2}, \quad T^* = T_t - T_0, \quad \alpha^* = 1. \quad (6.9)$$

As a result, the partial derivatives and the divergence operator are likewise stated in this manner [231].

$$\frac{\partial \circ}{\partial t} = \frac{1}{t^*} \frac{\partial \circ}{\partial \bar{t}}, \quad \nabla \cdot \circ = \frac{1}{x^*} \bar{\nabla} \cdot \circ, \quad \nabla \cdot \circ = \frac{1}{y^*} \bar{\nabla} \cdot \circ. \quad (6.10)$$

The degree of burning relations and the heat equation are written in a dimensionless form as

$$\frac{1}{t^*} \frac{\partial}{\partial \bar{t}} (\rho C_p \bar{T}) = \frac{1}{x^*} \frac{\partial}{\partial \bar{x}} \left(k_{xx} \frac{1}{x^*} \frac{\partial \bar{T}}{\partial \bar{x}} \right) + \frac{1}{y^*} \frac{\partial}{\partial \bar{y}} \left(k_{yy} \frac{1}{y^*} \frac{\partial \bar{T}}{\partial \bar{y}} \right) + \frac{1}{z^*} \frac{\partial}{\partial \bar{z}} \left(k_{zz} \frac{1}{z^*} \frac{\partial \bar{T}}{\partial \bar{z}} \right) + \dot{Q}, \quad \text{while} \quad \dot{Q} = -Q_r \frac{1}{t^*} \frac{\partial \bar{\alpha}}{\partial \bar{t}}. \quad (6.11)$$

6.3.3 Model Estimation by Learning

In the PINN methodology, network training takes place by minimizing the total loss of the network parameters Θ ,

$$\Theta^* = \underset{\Theta \in \mathbb{R}^D}{\operatorname{argmin}} \mathcal{L}_{\mathcal{T}}(\mathbf{X}; \Theta). \quad (6.12)$$

An error or loss function is defined in PINNs utilizing the network's processed outputs and derivatives based on the equations guiding the problem's physics. As a result, the network's total loss, $\mathcal{L}_{\mathcal{T}}$, is made up of the sum of loss terms for the PDE ($\mathcal{L}_{\mathcal{F}}$) and the initial and boundary conditions ($\mathcal{L}_{\mathcal{B}}$). Also, let us assume that we have some imprecise knowledge which can provide a general idea of the solution field.

By updating the loss function, the imprecise knowledge can be easily included in the total loss function to guide the training process as

$$\mathcal{L}_{\mathcal{T}}(\Theta) = \mathcal{L}_{\mathcal{F}}(\Theta) + \mathcal{L}_{\mathcal{B}}(\Theta) + \sum_{i=1}^{N_{back}} \eta_i \mathcal{L}_i, \quad (6.13)$$

where \mathcal{L}_i is the loss term for the i_{th} background knowledge, and η_i is the control term for each knowledge's contribution. Since the imprecise knowledge is not exact, the minimizer is far away from any true optimal point. As a result, we are interested in an adaptive optimization problem in which imprecise knowledge is originally integrated into a supervised learning assignment. Setting $\eta_i = 0$ turns off the associated objective once the solution is close enough to finish the supervised learning work.. $\mathcal{L}_{\mathcal{F}}$ represents due to error in satisfying the governing differential equations \mathcal{F} . It imposes the differential equation \mathcal{F} at collocation points over the domain, Ω , which can be chosen uniformly or unevenly. The other term, $\mathcal{B}(\hat{u}_{\Theta}) = \mathbf{g}$, represents due to the error in satisfying of the boundary or initial conditions. A mean square error formulation is used in a common implementation of the loss, where

$$\mathcal{L}_{\mathcal{F}}(\Theta) = MSE_{\mathcal{F}} = \frac{1}{N_c} \sum_{i=1}^{N_c} \|\mathcal{F}(\hat{u}_{\Theta}(z_i)) - \mathbf{f}(z_i)\|^2 = \frac{1}{N_c} \sum_{i=1}^{N_c} \|r_{\Theta}(\mathbf{u}_i) - \mathbf{r}_i\|^2, \quad (6.14)$$

and

$$\mathcal{L}_{\mathcal{B}}(\Theta) = MSE_{\mathcal{B}} = \frac{1}{N_B} \sum_{i=1}^{N_B} \|\mathcal{B}(\hat{u}_{\Theta}(z)) - \mathbf{g}(z_i)\|^2. \quad (6.15)$$

Optimization is used to minimize the loss function. Based on the literature, optimization of loss functions is performed using minibatch sampling with the Adam and LBFGS method, which is a quasi-Newton optimization procedure in most of the PINN literature. The gradient-based optimizer will almost likely become stuck in one of the local minima for the loss function [232, 233]. Because stochastic gradient descent (SGD) struggles with random collocation points, especially in 3D setups, the Adam approach, which combines adaptive learning rate and momentum approaches, is used to

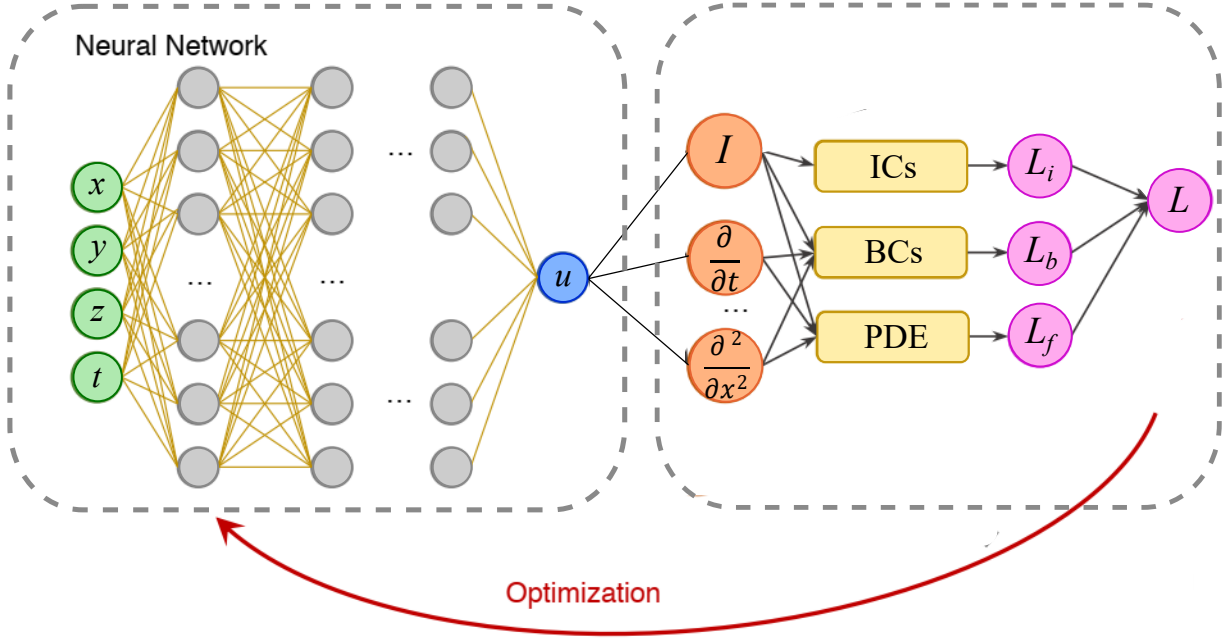


Figure 6.4. A schematic of PINN blocks. Differential equation residual (loss) terms, as well as initial and boundary conditions, make up PINNs

speed up convergence [234, 235].

Note that because it may incorporate numerous different objectives for separate tasks, the PINN problem might be regarded as a multi-objective multi-task problem. This view of modeling has several advantages. It lowers the order of regularity, which is advantageous for problems involving discontinuities. Additionally, because the order of partial derivatives increases exponentially in terms of time complexity in the automated differentiation technique, it may lower the total computing cost [236]. Multiple objectives used to assess the correctness of the solution may result in gradients that are conflicting. As a result of the opposing gradient, a compromised solution that is not always Pareto optimal may emerge. We use the gradient surgery technique [237] for the PINN framework to address the conflicting gradient and the challenge of balancing different objectives. We have the following update rule in the most common form of GD-based methods,

$$\Theta_n = \Theta_{n-1} - \alpha_n \nabla_{\Theta} \mathcal{L}_{\mathcal{T}_{n-1}}, \quad (6.16)$$

where Θ_n is the updated unknown vector at iteration n^{th} , $\nabla_{\Theta} \mathcal{L}_{\mathcal{T}_{n-1}}$ is the gradient of the total

loss function with respect to the unknown vector at iteration $n - 1$, and α_n is the learning rate that regulates the solution's stability during iterations.

Let's call each objective's gradient vector $\mathbf{g}_i = \nabla_{\Theta} \mathcal{L}_i(\Theta)$ in gradient surgery, and the total gradient is $\mathbf{g} = \nabla_{\Theta} \mathcal{L}_T(\Theta) = \sum_{i=1}^{N_{obj}} \mathbf{g}_i$. You can find the concept in Fig. 6.5. For further information, we direct interested readers to [237].

Algorithm 2 Algorithm of gradient surgery

```

1:  $\Theta \leftarrow$  Initialize random weights and biases.
2:  $n, i \leftarrow 1$ 
3: for  $n$  to  $N_{itr}$  do
4:   for  $i$  to  $N_{obj}$  do
5:      $\mathcal{L}_i(\Theta_n), \mathbf{g}_i = \nabla \mathcal{L}_i \leftarrow$  compute objectives and gradients.
6:     if  $\mathbf{g}_i \cdot \mathbf{g}_j < 0$  then
7:        $\mathbf{g}_i = \mathbf{g}_i - \frac{\mathbf{g}_i \cdot \mathbf{g}_j}{\|\mathbf{g}_i\|^2} \mathbf{g}_j \leftarrow$  modified gradient.
8:     end if
9:      $\mathbf{g} = \sum_{i=1}^{N_{obj}} \mathbf{g}_i \leftarrow$  Aggregate gradient vectors.
10:  end for
11:   $\Theta_{n+1} \leftarrow GD(\Theta_n, \mathbf{g})$ 
12: end for

```

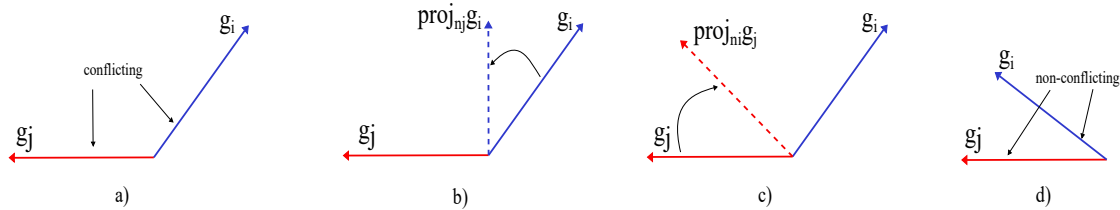


Figure 6.5. Gradient surgery idea [237, 238]

Weight initialization Because training deep models is such a challenging operation, the choice of initialization has a significant impact on most algorithms. The beginning point can decide whether or not the method converges at all, with certain initial points being so insecure that the algorithm

runs into arithmetic issues and fails. Over the previous decade, more customized techniques have been the de facto norm, as they may result in a slightly more successful optimization process. Pang et al. [232] describe a method for picking the most appropriate one.

For initialization, Glorot and Bengio [79] advocated using a correctly scaled uniform distribution. This is referred to as the "Xavier" initialization. The assumption that the activations are linear is used to derive it. This approach is computed as a random number with a uniform probability distribution (\mathcal{U}) as " $weight = \mathcal{U}[-\frac{1}{\sqrt{n}}, \frac{1}{\sqrt{n}}]$ ", where n is the number of node inputs. When used to initialize networks that employ the rectified linear (ReLU) activation function, the "Xavier" weight initialization was discovered to have issues.

The "He" initialization method is the current standard for initializing the weights of neural network layers and nodes that employ the rectified linear (ReLU) activation function [80]. The he initialization technique is computed as a random number with a Gaussian probability distribution (\mathcal{G}) as $weight = \mathcal{G}(0, \sqrt{\frac{2}{n}})$, where n is the number of node inputs.

Adaptive weights Training multi-objective total loss functions pose challenges for optimization techniques, as others have pointed out [4]. The unique solution to the governing equations is obtained once initial and boundary conditions are imposed strongly, especially in the case of boundary value problems. It is common to use a weighted-sum scheme to enhance optimization algorithms in the context of multi-objective optimization [239]. Wang et al. [240] showed that unbalanced gradients cause inaccuracy in optimization and developed an adaptive loss weight approach where gradients of individual terms in the loss function are normalized in order to decrease the stiffness of the gradient dynamics in PINNs. As a result, the total loss term $\mathcal{L}_{\mathcal{T}\cup}$ is changed to

$$\mathcal{L}_{\mathcal{T}\cup} = \omega_{\mathcal{F}} \mathcal{L}_{\mathcal{F}} + \omega_{\mathcal{B}} \mathcal{L}_{\mathcal{B}}, \quad (6.17)$$

where ω represents the weight loss associated with each loss term.

Based on the parameter values $(\Theta)^e$ at epoch e , the updated scaling weight ω^{e+1} for each loss term is calculated as

$$\omega^{e+1} = \beta\omega^e + (1 - \beta)\hat{\omega}^{e+1}, \quad (6.18)$$

where $\beta = 0.9$ based on [240] and

$$\hat{\omega}_i^{e+1} = \frac{1}{\omega_i^e} \frac{\max(|\nabla \mathcal{L}_T(\Theta^e)|)}{\text{mean}(|\nabla \mathcal{L}_i(\Theta^e)|)} \quad (6.19)$$

Such an adaptive strategy for loss weights improves the system's robustness and improves the model's prediction accuracy.

Algorithm 3 PINN Algorithm for Burning Problem

- 1: $\mathbf{X}, \mathbf{t} \leftarrow$ Sample uniformly spatial and temporal domains.
 - 2: $\Theta_n \leftarrow$ Initialize randomly using Xavier scheme.
 - 3: $n \leftarrow 1$
 - 4: **while** $err > TOL$ **do**
 - 5: $\Theta_n \leftarrow$ Optimize \mathcal{L}_T for Θ .
 - 6: $T_n, \alpha_n \leftarrow$ Evaluate temperature and degree of burning using Θ .
 - 7: $err \leftarrow \|\Theta_n - \Theta_{n-1}\| / \|\Theta_n\|$ with $\|o\|$ as the L^2 norm.
 - 8: $n \leftarrow n + 1$
 - 9: **end while**
-

6.4 Case Study 1: 1D Burning Problem of Polymer

To evaluate the performance of the proposed PINN, the heat transfer PDEs in a polymeric material are trained in Python (V3.6.8), using Tensorflow and Keras libraries (V2.10).

We can define the PINN solution approach for the 1D pyrolysis problem now that we have covered the method of Physics-Informed Neural Networks (PINNs) and heat equations.

$$\frac{1}{t^*} \frac{\partial}{\partial \bar{t}} (\rho C_p \bar{T}) = \frac{1}{x^*} \frac{\partial}{\partial \bar{x}} \left(k_{xx} \frac{1}{x^*} \frac{\partial \bar{T}}{\partial \bar{x}} \right) + \dot{Q}, \quad \text{while} \quad \dot{Q} = -Q_r \frac{1}{t^*} \frac{\partial \bar{\alpha}}{\partial \bar{t}}. \quad (6.20)$$

T and α are the unknown solution variables in the case of 1D burning. For the dimensionless version of these variables, neural networks are,

$$\bar{T} : (\bar{x}, \bar{t}) \mapsto \mathcal{N}_{\bar{T}}(\bar{x}, \bar{t}; \Theta_{\bar{T}}), \quad \text{and} \quad \bar{\alpha} : (\bar{x}, \bar{t}) \mapsto \mathcal{N}_{\bar{\alpha}}(\bar{x}, \bar{t}; \Theta_{\bar{\alpha}}), \quad (6.21)$$

where Θ_o denotes that these networks have their own set of parameters. After that, the total coupled loss function is written as,

$$\mathcal{L}_{Tot} = \omega_1 \mathcal{L}_T + \omega_2 \mathcal{L}_\alpha + \omega_3 \mathcal{L}_{\alpha_0} + \omega_4 \mathcal{L}_{T_0} + \omega_5 \mathcal{L}_{T_{BC1}} + \omega_6 \mathcal{L}_{T_{BC2}} + \sum_{i=1}^{N_{back}} \eta_i \mathcal{L}_i, \quad (6.22)$$

while

$$\begin{aligned} \mathcal{L}_T &= \frac{1}{N_c} \sum_{i=1}^{N_c} \left\| \frac{1}{t^*} \frac{\partial}{\partial \bar{t}} (\rho C_p \bar{T}) - \frac{1}{x^*} \frac{\partial}{\partial \bar{x}} \left(k_{xx} \frac{1}{x^*} \frac{\partial \bar{T}}{\partial \bar{x}} \right) + Q_r \frac{1}{t^*} \frac{\partial \bar{\alpha}}{\partial \bar{t}} \right\|^2, \\ \mathcal{L}_\alpha &= \frac{1}{N_c} \sum_{i=1}^{N_c} \left\| \frac{1}{t^*} \frac{\partial \bar{\alpha}}{\partial \bar{t}} - g(\bar{\alpha}, \bar{T}) \right\|^2, \quad \text{loss of burning degree} \\ \mathcal{L}_{T_0} &= \frac{1}{N_B} \sum_{i=1}^{N_B} \|\bar{T} - \bar{T}_0(x)\|^2, \quad \text{loss of initial condition of temperature} \\ \mathcal{L}_{T_{bc1}} &= \frac{1}{N_B} \sum_{i=1}^{N_B} \|\bar{T} - \bar{T}_b(t)\|^2, \quad \text{loss of boundary condition at bottom} \\ \mathcal{L}_{T_{bc2}} &= \frac{1}{N_B} \sum_{i=1}^{N_B} \|\bar{T} - \bar{T}_t(t)\|^2, \quad \text{loss of boundary condition at top} \\ \mathcal{L}_{\alpha_0} &= \frac{1}{N_B} \sum_{i=1}^{N_B} \|\bar{\alpha} - \bar{\alpha}_0(x)\|^2 \quad \text{loss of initial condition of burning degree,} \end{aligned} \quad (6.23)$$

Training and Hyperparameter Searches It is hardly surprising that network size, architecture, and optimizer hyperparameters like learning rate can significantly impact PINN solution quality. We used the hyperbolic-tangent and sigmoid activation functions to create neural networks with four hidden layers and 20 neurons in each layer for all of the examples in this paper. We used the Adam optimizer with an initial learning rate of $2 * 10^{-3}$ and an exponential learning decay to 10^{-5} at the end of training. We have also explored a range of hyperparameters, but we have not noticed any substantial improvements in terms of improving the pyrolysis problem studied here. Fig. 6.6 shows the training history for various hidden layers and neurons.

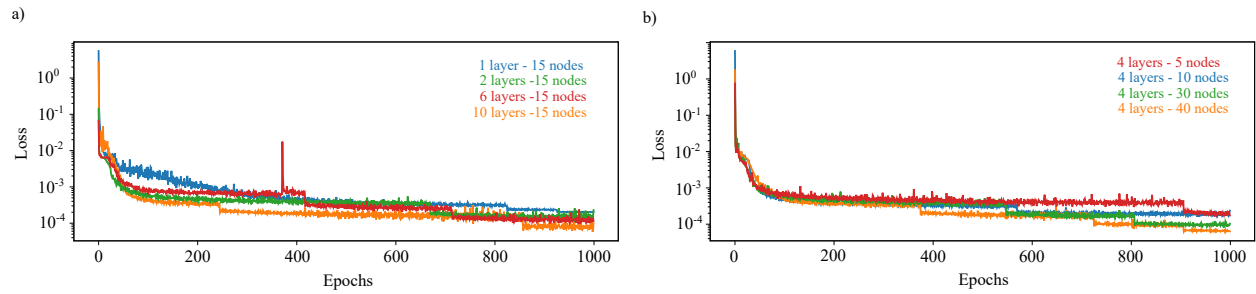


Figure 6.6. Losses for a variety of hidden layer (left) and neuron numbers (right)

Comparison with Numerical Results The reference numerical model results will be compared to the above-mentioned best-performing PINN model outputs in this part. Fig. 6.7 shows the PINN, numerical solution, and errors. As you can see, the PINN solution has a high level of agreement with the expected solution when compared to the findings of numerical analysis. The upper face is given a temperature of $T_t = 700$, while the bottom face is given a temperature of $T_t = 700\sin(\frac{\pi}{20}t)$. $T_0 = 700x^3$ is the initial temperature.

Role of Weight Initialization Because training deep models is such a tough operation, the choice of initialization has a significant impact on most algorithms. So, we trained the model with Xavier and He initialization for tanh and ReLU activation functions hereunder. Fig. 6.8 shows the results for Xavier and He initialization.

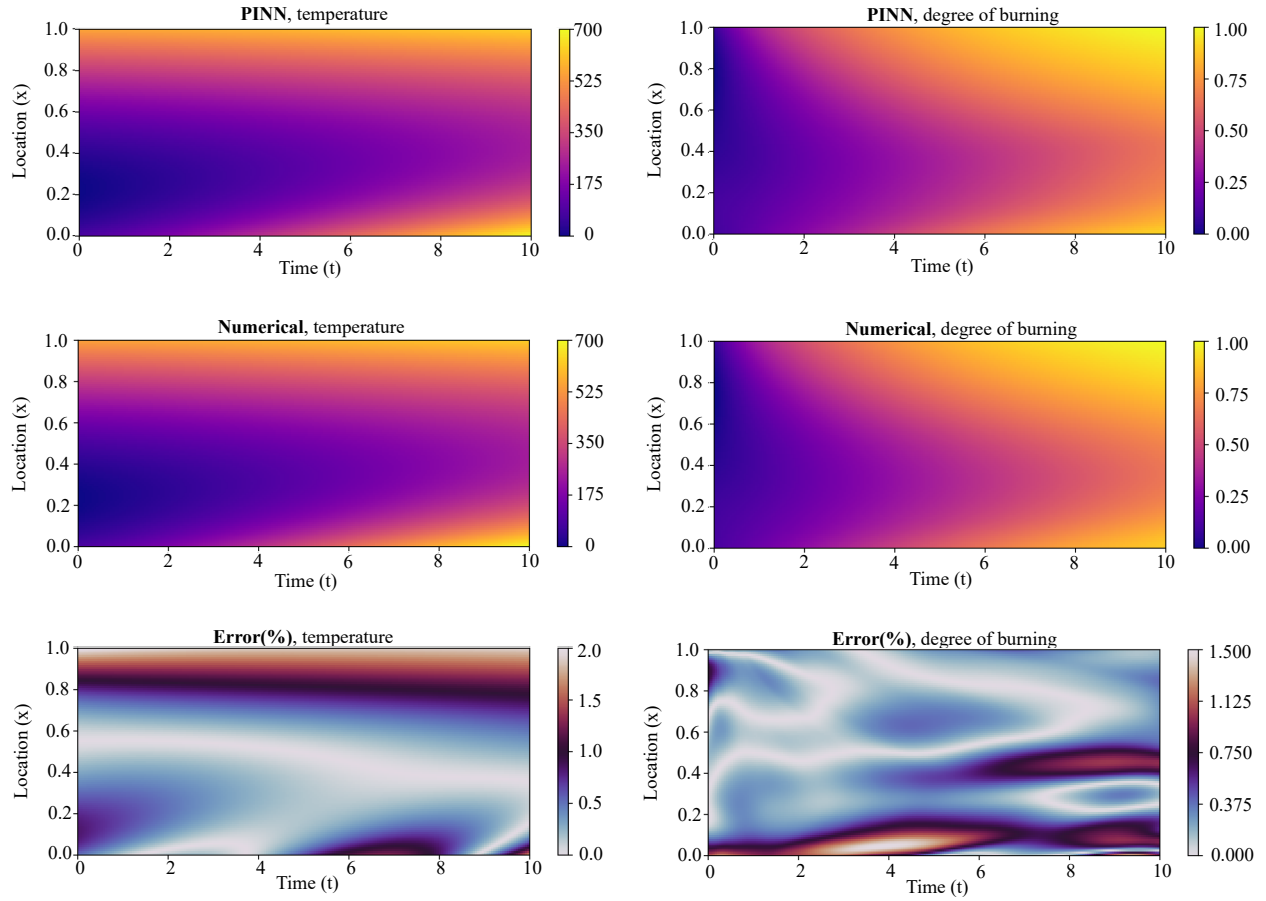


Figure 6.7. PINN and numerical predictions for full cycle of burning for temperature (left), and degree of burning (right)

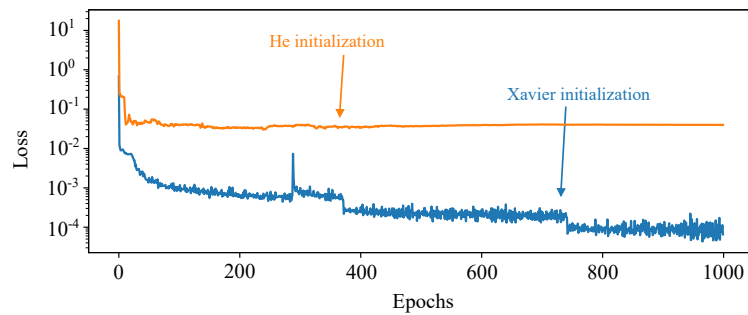


Figure 6.8. Evolution of loss term for Xavier weight initialization and He weight initialization

Training with and without Adaptive Weights. The performance of the suggested PINN with and without loss weights is shown in Fig. 6.9 to emphasize the need to use loss weights.

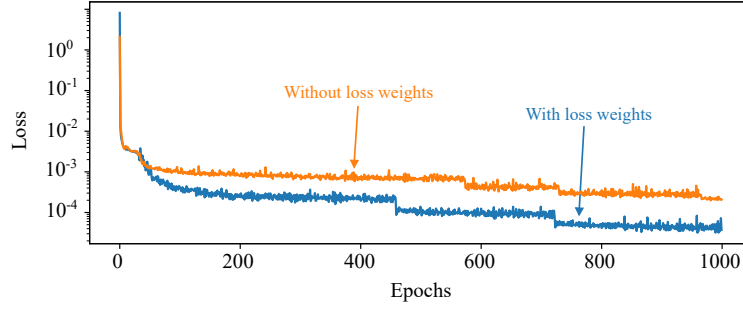


Figure 6.9. Evolution of loss term for optimization with and without loss weights

Training with and without Background Knowledge. To show the ability of background knowledge, we compare two case studies with and without background knowledge. We consider that the top of the geometry of polymer has a higher temperature and degree of burning always compared to the bottom of that. We considered it as the background knowledge and added it to the total loss. Fig. 6.10 shows the result for comparing of this factor.

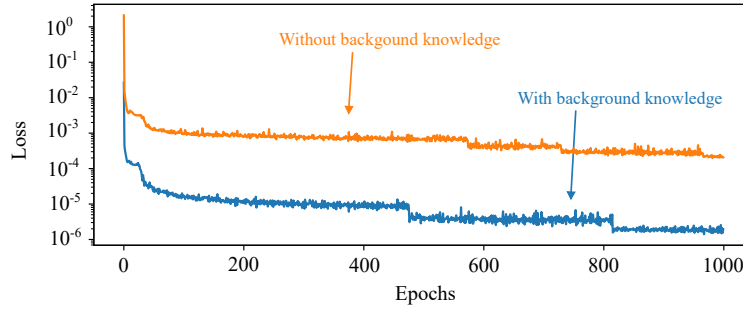


Figure 6.10. Evolution of loss term for optimization with and without background knowledge

6.5 Case Study 2: 2D Burning Problem of Matrix Cube

For the second example, we modeled the pyrolysis of ethylene propylene diene monomer (EPDM) composites at the high temperature and pressure of solid rocket motors (SRMs), which results in a char layer with a non-uniform distribution pattern. Interestingly, the compact structure of the char can increase the ablation resistance of the composites. To better understand the ablation mechanism and inform the design of EPDM composites for SRMs, it is crucial to understand and describe the char formation pattern throughout the life of the material and also understand the material behaviour at the interface. We used our H-PINN to predict the spatial evolution of

chemical processes (pyrolysis and charring) before validating them against mesoscale finite element results. It is of great theoretical and practical significance to study the formation mechanism of the compact structure of the char layer for further studying the ablation mechanism and guiding the development of EPDM composites. To date, the char formation pattern in polymeric materials cannot be predicted with reduced order models, such as machine-learned approaches. In this work, the hybrid PINN for 2D pyrolysis of EPDM composites are designed from the basic 2D heat equation, namely

$$\frac{1}{t^*} \frac{\partial}{\partial \bar{t}} (\rho C_p \bar{T}) = \frac{1}{x^*} \frac{\partial}{\partial \bar{x}} \left(k_{xx} \frac{1}{x^*} \frac{\partial \bar{T}}{\partial \bar{x}} \right) + \frac{1}{y^*} \frac{\partial}{\partial \bar{y}} \left(k_{yy} \frac{1}{y^*} \frac{\partial \bar{T}}{\partial \bar{y}} \right) + \dot{Q}, \quad \text{while} \quad \dot{Q} = -Q_r \frac{1}{t^*} \frac{\partial \bar{\alpha}}{\partial \bar{t}}. \quad (6.24)$$

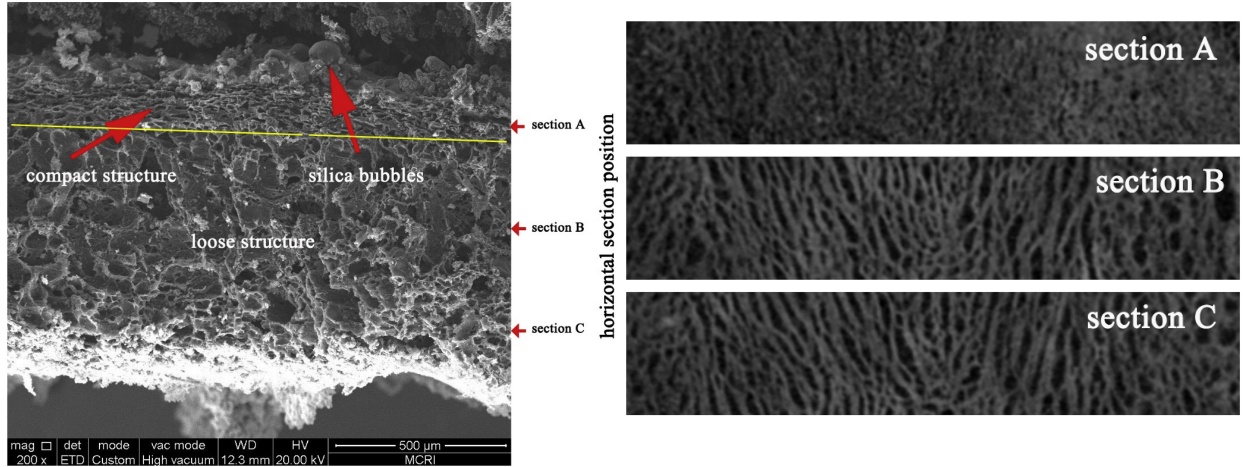


Figure 6.11. SEM image of vertical-section of the char layer (left) and Micro-CT images of horizontal-section of the char layer (right) [241]

The following steps were required to expand the PINN to 2D: adding one input (y dimension) and providing a pre-layer for the y input, adjusting error calculation to include a term for the second derivative of the PINN prediction with respect to y, and modifying the error calculation for the heat transfer boundary conditions. The total loss function's many terms, as well as their complexity, present huge complications in network training. The only way to get meaningful results from the Adam optimizer was to utilize scored-adaptive weights; however, we have found that the process

has a high computational cost and lacks robustness. We offer a unique strategy, inspired by [242], to overcome the limitations of standard network training methods for multiphysics issues.

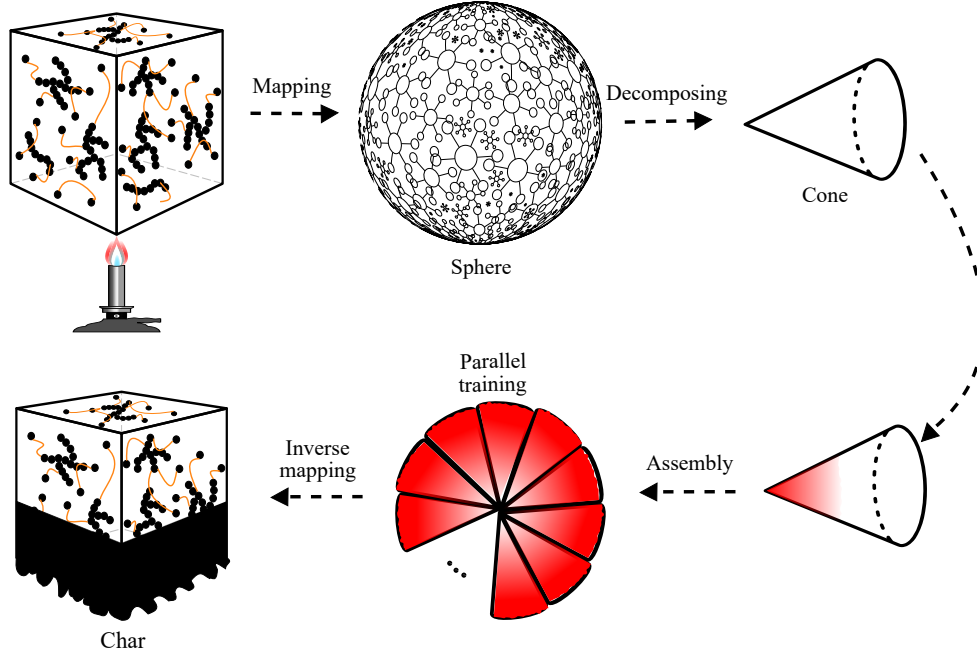


Figure 6.12. A mesh is used to discretize the material (left), the pyrolyzing front proceeds towards the last spot of burning as pyrolysis progresses (right)

The pyrolyzing front is shown as a two-dimensional triangle element. It means that we reduce the order of 2D problems by decomposing them into many 1D problems and training them as a collection of learning. In this concept, we need to assume the last point of burning in the material. Next, we decompose 2D geometry into many 1D elements, which the last point of burning is shared among all 1D elements. Fig. 6.13 and Fig. 6.14 show the PINN solution for temperature and degree of burning for different time steps, respectively. The domain is subjected to a constant temperature $300 + 700e^{-15x^2}$ at the top and bottom faces and a constant temperature $300 + 600e^{-15y^2}$ at the right and left faces.

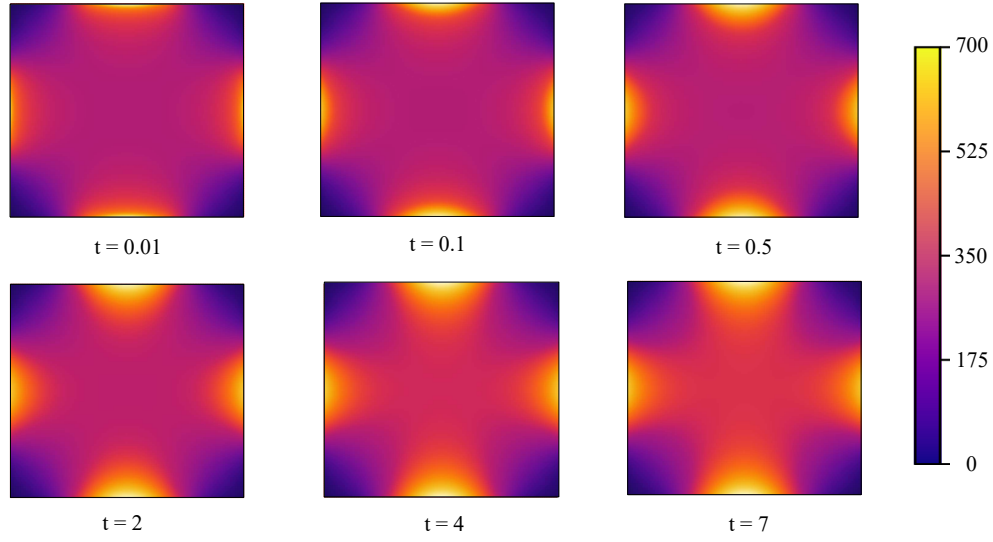


Figure 6.13. Temperature predictions using PINN for various time steps in burning $t = 0.01, 0.1, 0.5, 2, 4, 7$

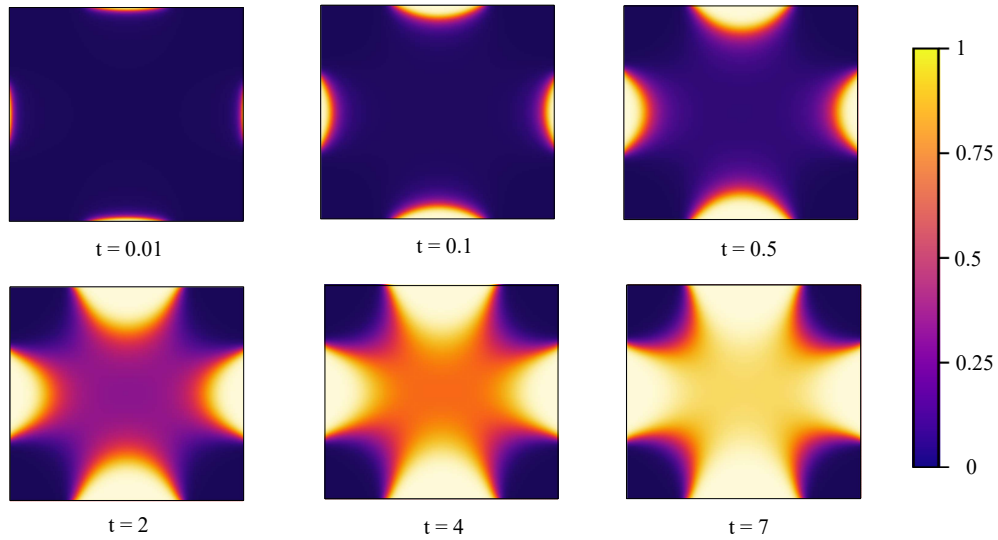


Figure 6.14. Degree of burning predictions using PINN for various time steps in burning $t = 0.01, 0.1, 0.5, 2, 4, 7$

6.6 Case Study 3: Shen's Model for Burning

The second category of burning, which considers that the specific heat remains constant, with only thermal conductivity and material density being temperature dependent, is presented in this section [243].

The heat transfer PDE in a polymeric material is presented as

$$\frac{\partial}{\partial t} (\rho_s C_s T + \rho_c C_c T) = \frac{\partial}{\partial x} \left(k_{xx} \frac{\partial T}{\partial x} \right) + \dot{Q}, \quad \text{while} \quad \dot{Q} = K \rho_s (C_s - C_c)(T). \quad (6.25)$$

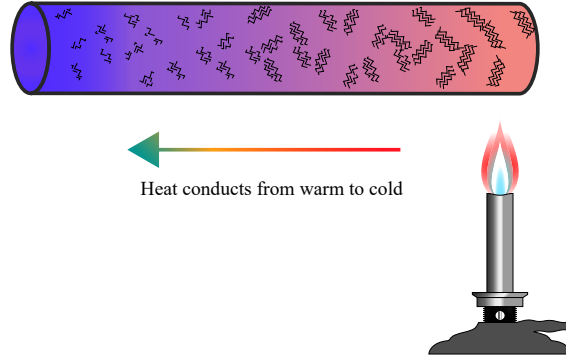


Figure 6.15. Schematic of 1D burning and char formation

Results are presented for boundary and initial conditions such that $L = 1mm$, $T_0 = 700x^3$, $T_b = 0$ and $T_t = 700$ for duration of 10 seconds. The training is conducted on 500 uniformly distributed points in (x, t) .

Thermal characteristic values of polymers

The thermal conductivity and density of the polymer, as well as char, have temperature-dependent properties, as shown in Fig. 6.16. The thermal conductivity of the material is shown in Fig. 6.16.a. When the temperature rises above $250F^\circ$, the sample's exposure time to heat flux increases, and the material's thermal conductivity rapidly decreases as a result of the temperature rise. The material's thermal conductivity before this temperature is around $10W/mK$. The thermal conductivity of the solid stabilizes at $0.3W/mK$ at temperatures up to $550F^\circ$. Beyond 250 degrees Fahrenheit, the density of the polymer rapidly declines until it reaches zero at 550 degrees Fahrenheit. The density of the char, on the other hand, rapidly increases to $800kg/m^3$ at temperature 700 (see Fig. 6.16.b).

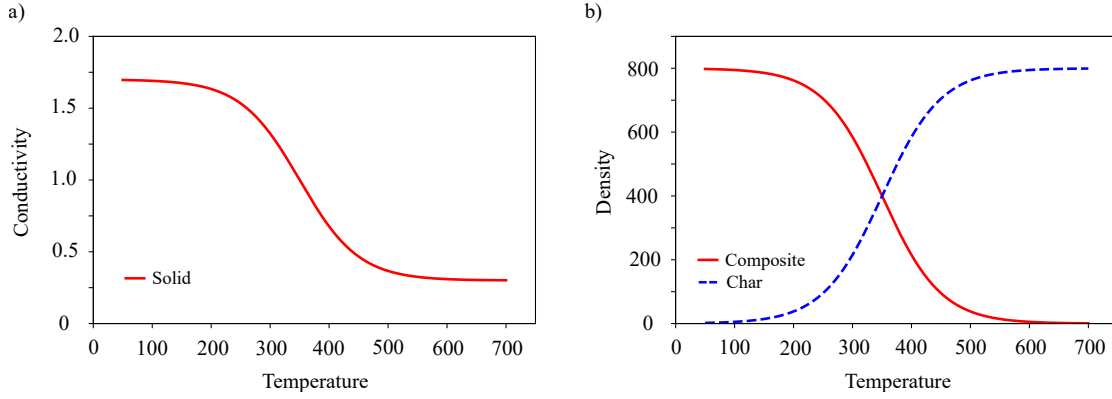


Figure 6.16. Thermo-physical properties of polymer

Comparison between numerical and predicted temperature profiles

To assess the accuracy of the PINN in terms of predicting T , results are compared to numerical predictions from MATLAB. Fig. 6.17 shows the temperature prediction for the case study. The obtained relative error of the predicted temperature when comparing PINN and numerical methods is below 1%.

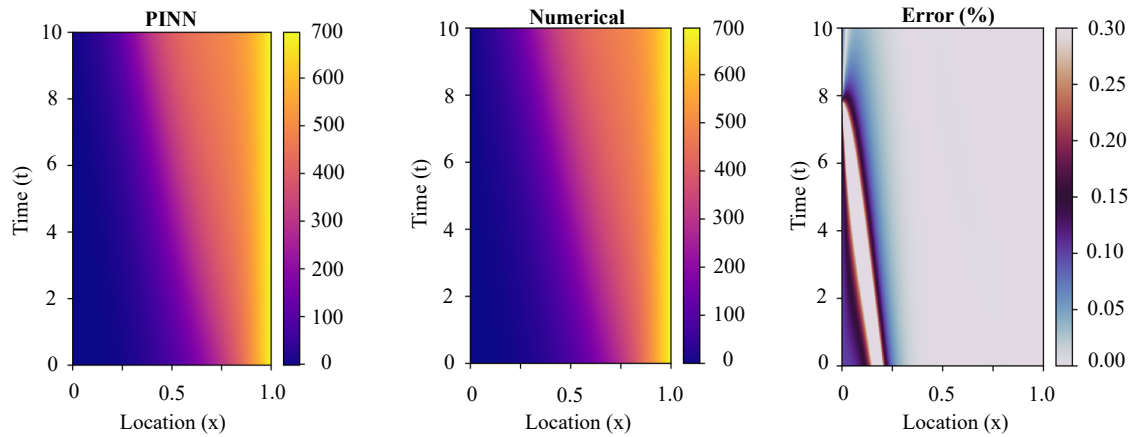


Figure 6.17. PINN and numerical temperature predictions for full cycle of burning

The temperature evolution at the left side of the polymeric material, middle of the polymeric material, and right side of the polymer are shown for the full burning cycle in Fig. 6.18. Also, The mean square error of the loss function is reported in Fig. 6.19.

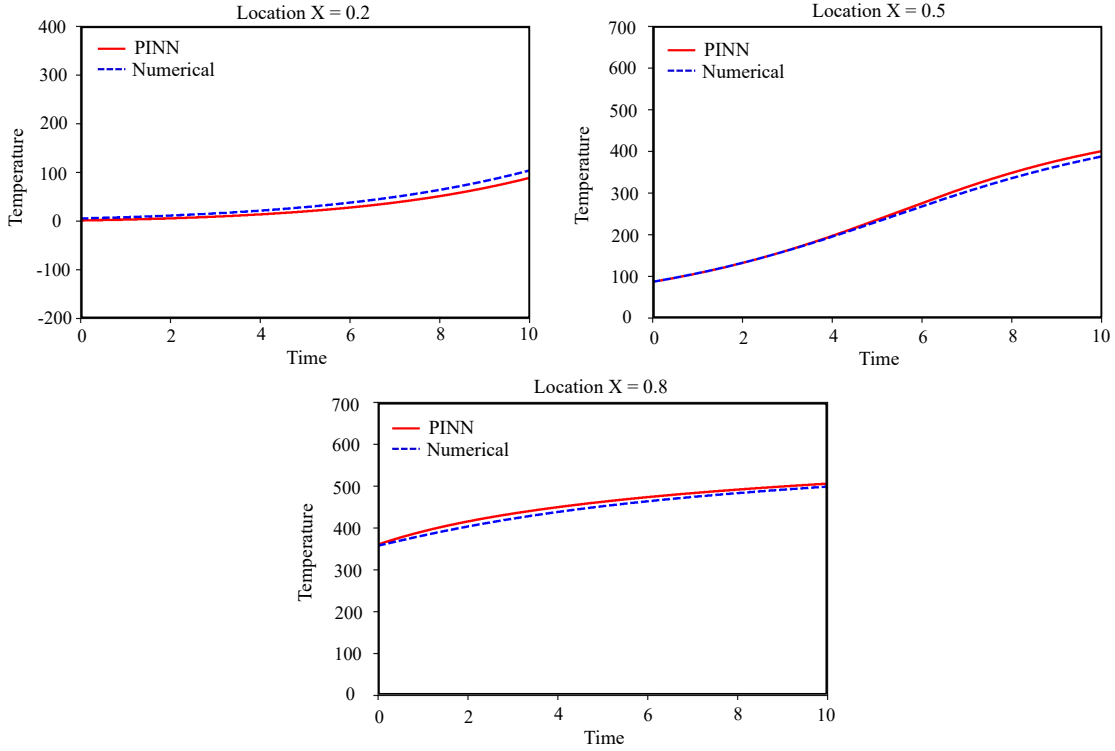


Figure 6.18. Temperature history for ($x = 0.2$), middle of polymer ($x = 0.5$), and for boundary ($x = 0.8$)

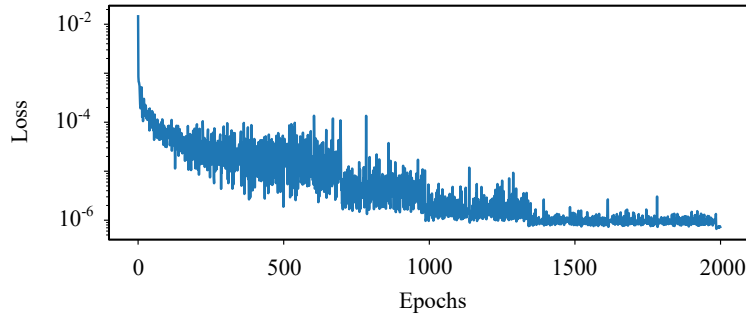


Figure 6.19. Evolution of loss term in the training of the network

It is somewhat remarkable that a neural network with hundreds of parameters cannot approximate the analytical solution of the 1D hyperbolic PDE with a non-convex flux function with any degree of accuracy. This is particularly striking because, in theory, there should exist a network that can offer a near approximation of the continuous solution for any arbitrarily chosen PDE. However, this is not what is seen. As a result, this leads us to conclude that the issue is not with the solution in nature but with the methodology we employ to obtain it, i.e., the optimization procedure or the

loss function.

6.7 Discussion and Concluding Remarks

In this paper, we studied a comprehensive study on Physics-Informed Neural Networks (PINNs) for the forward solution of pyrolysis problems by making the training more straightforward. We explored how Physics-Informed Neural Networks (PINNs) can be employed to solve pyrolysis problems in the forward phase. Our research is the first to explore fully coupled temperature-degree-of-burning relationships in pyrolysis problems. We presented a dimensionless version of these relations that leads to the optimizer's stable and convergent behavior.

While the achieved results are close to our expectations, it should be noted that training PINNs is time-consuming. We relate the training challenge to the multi-objective optimization issue and the application of a first-order optimization algorithm, as reported by others. Given the difficulties encountered and overcome in this work for the forward problem, the next step is to use PINNs to inverse burning situations.

A multi-task learning approach has emerged in which a NN must fit observed data while decreasing a PDE residual. This article introduces single- and separated-network PINN architectures to forecast temperature distributions and the degree of burning of a pyrolysis problem in a one-dimensional (1D) and two-dimensional (2D) rectangular domain for the first time to model through collocation training.

The complex and non-convex multi-objective loss function presents substantial obstacles for forward problems in training PINNs. We discovered that adding several differential relations to the loss function causes an unstable optimization issue, which may lead to convergence to the trivial null solution or significant deviation of the solution. The dimensionless form of the coupled governing equations that we find most beneficial to the optimizer is used to address this problem. The numerical results are compared with results obtained from PINN to show the performance of the solution. Our research is the first to explore fully coupled temperature-degree-of-burning relationships in pyrolysis problems. Unlike classical numerical methods, the proposed PINN

does not depend on domain discretization. In addition to these characteristics, the proposed PINN achieves good accuracy in predicting solution variables, which makes it a candidate to be utilized for surrogate modeling of pyrolysis problems. While the achieved results are close to our expectations, it should be noted that training PINNs is time-consuming.

CHAPTER 7

UNCERTAINTY QUANTIFICATION AND FAILURE PROBABILITY ESTIMATION

Overview A qualitative breakdown of total uncertainty describing the contributions from data (noisy, gappy); physical models (misspecification, stochasticity); neural networks (architecture, hyperparameters, overparametrization); and posterior inference. Aleatoric uncertainty is due to noisy data and cannot be reduced. Epistemic uncertainty is due to noisy and limited data, as well as neural network overparametrization. The aim of this chapter is that to model the uncertainty of a constitutive model for various materials and estimate the probability of failure in them.

7.1 Introduction

Elastomers, primarily composed of cross-linked polymer matrices, exhibit non-linear behavior during extensive deformation. This behavior, especially evident before failure, has been a focal point of research due to its application significance. The hyperelastic behavior of isotropic incompressible rubbers has been analyzed to derive strain energy functions [244, 245, 67]. However, the development of constitutive models is constrained by theoretical and experimental limitations.

Historically, deterministic models, which describe average material responses, have been predominant [13]. These models, while useful, overlook inherent uncertainties in elastomer behavior. This oversight challenges the computation of confidence intervals and model accuracy. The variability in failure stretch/stress across samples further complicates deterministic descriptions. This study aims to address these challenges by viewing the failure state as a Fuzzy variable.

Uncertainty Quantification (UQ) focuses on characterizing and mitigating uncertainties in both computational and real-world scenarios. UQ provides error bounds, setting the validity range for

model predictions. While most models are deterministic, real-world polymeric system behaviors often follow probabilistic patterns, limiting deterministic models' relevance [246, 247].

UQ's strength lies in its ability to offer probabilistic models that present a range of material parameter values. This range allows for the analysis of system behavior under unforeseen conditions. In deterministic models, failure is defined when the nominal stress σ exceeds a threshold σ_f . In probabilistic models, both σ and σ_f are probabilistic, meaning stress increase only heightens failure probability without specifying an exact failure point.

Failure in materials can be better understood as a probabilistic event rather than a binary outcome. The inherent uncertainty can be decomposed into two primary sources: (i) "epistemic errors", which arise from knowledge gaps and can be mitigated with additional resources, and (ii) "aleatory errors", representing the system's intrinsic variability that remains constant across parameters. The primary objective of Uncertainty Quantification (UQ) in computational modeling is to ascertain and predict these uncertainties [248, 249].

Two prevailing statistical paradigms for UQ are the frequentist and Bayesian views. The former defines probability based on long-term occurrence rates, while the latter integrates prior knowledge with new data to determine probability. In the frequentist approach, parameters are treated as *fixed random variables*. Conversely, the Bayesian perspective sees parameters as *random variables contingent on available data*. While misguided prior knowledge can skew Bayesian models, accurate priors enhance statistical inference [250, 251]. Thus, UQ serves as the foundation for computing failure probabilities.

Several deterministic models have been proposed during past decades. In 1948, Rivlin [252] investigated fundamental concepts of large elastic deformation of isotropic materials. In 2020, we proposed a physics-based data-driven constitutive model for cross-linked polymers by embedding neural networks in micro-sphere [78].

In recent years, several studies have been conducted on the stochastic modeling of constitutive models of soft materials [253, 254, 255]. In 2015, a Bayesian parametric approach was employed for calibration of the constitutive model for soft tissue based on Bayes factors [253]. Brewick and

Teferra [254] derived a parametric UQ model of Ogden model for brain tissue. They calculated posterior distribution of the constitutive parameters by employing Markov Chain Monte Carlo. Kaminski and Lauke [256], derived parametric UQ models of multiple constitutive models ranging from Neo-Hookean to Arruda-Boyce, and showed probabilistic characteristics, such as expectation, variance, skewness, and kurtosis. Recently, Mihai et al. [255] published their study on the uncertainty quantification of elastic materials by using Bayes' theorem to select the model. Another parametric study has been used as a Bayesian calibration framework to determine the posterior parameter distributions of a hyper-viscoelastic constitutive model using mechanical testing data of brain tissue [257].

While several studies were conducted on predicting the failure probability of materials and structures, [258, 259, 260, 261] the failure of rubber-like materials remains a challenging issue. Here, our goal is to advance a parametric UQ approach to predict failure probability from the Carroll constitutive model. The model is then compared with predictions of a non-parametric UQ approach which comes at considerably higher computational cost. Note that we selected the Carroll model because compared to other complex model such as microsphere model and tube model it is simpler with equal accuracy for both Treloar's and Kawataba's dataset [145]. Carroll model not only has just three parameters but also it can capture the behavior of elastomers in different states of deformation such as biaxial, and shear because it is function of first and second invariants of deformation tensor.

In this chapter, we delineate a comprehensive probabilistic modeling approach for elastomers, encompassing three pivotal facets: (i) Bayesian calibration of the Carroll model's [262] parameters for hyperelastic behavior using two distinct datasets, (ii) formulating confidence intervals for stress-strain curves via conjugate priors, and (iii) computing failure probability using the First Order Reliability Method (FORM) and contrasting it with Crude Monte Carlo (CMC) simulations to discern parameter sensitivities.

Our methodology unfolds as follows:

Step 1: Introduction of a Bayesian-calibrated **parametric** stochastic model tailored *for smooth*

data based on the Carroll model [262].

Step 2: Formulation of a **non-parametric** stochastic constitutive model *for noisy data* leveraging Gaussian Process (GP).

Step 3: Calibration of both models using silicon- and polyurethane-based adhesive data, demonstrating their efficacy in predicting behaviors in rubber-like materials.

Step 4: Construction of a probabilistic failure model from the parametric stochastic model using a limit state function. This approach can be adapted for non-parametric models, albeit with increased computational demands and an altered implementation strategy.

Step 5: Failure prediction via the FORM method, incorporating a sensitivity analysis to gauge the impact of each constitutive model parameter on failure probability, and juxtaposing the outcomes with CMC-based predictions.

Here, we first developed a parametric stochastic constitutive model based on Bayesian model calibration is mentioned for both cases of maximum prior estimation and maximum likelihood estimation, see section 7.2. Next, we discuss GP as a non-parametric model in detail for finding hyper-parameters of the kernel-based on the limited-memory Broyden–Fletcher–Goldfarb–Shanno (L-BFGS) method in section 7.3. Moreover, the probability of failure analysis based on FORM and CMC simulations are explained in section 7.4. Finally, the results are presented in section 7.5 for two compounds tested in our facility as are described in details.

7.2 Parametric Approach

The foundational step in parametric failure probability estimation involves constructing a stochastic surrogate model to encapsulate the material behavior, necessitating a probabilistic constitutive model to account for inherent uncertainties.

Uncertainty Quantification (UQ) typically discerns several uncertainty sources:

(1) *Parameter Uncertainty*: Originating from model input parameters with indeterminate values, either due to experimental constraints or statistical inference limitations.

(2) *Structural Uncertainty*: Often termed model inadequacy or bias, it arises from incomplete

understanding of the underlying physics.

(3) *Algorithmic Uncertainty*: Attributed to numerical errors and approximations in model implementation.

(4) *Experimental Uncertainty*: Stemming from variability in experimental measurements.

(5) *Interpolation Uncertainty*: Resulting from gaps in data from model simulations or experimental observations.

For the Parametric Stochastic Constitutive model, the Carroll model [262] delineates the hyper-elastic response. The associated strain energy function, Ψ , and the uni-axial stress, P^{UT} , are defined as:

$$\Psi = W_1 I_1 + W_2 I_1^4 + W_3 \sqrt{I_2}, \quad (7.1)$$

$$P^{UT} = \left(2W_1 + 8W_2 \left(2\lambda^{-1} + \lambda^2 \right)^3 + W_3 \left(1 + 2\lambda^3 \right)^{-\frac{1}{2}} \right) \left(\lambda - \lambda^{-2} \right), \quad (7.2)$$

where λ is the principal stretch in the uni-axial tensile loading, I_1 and I_2 are the second invariant of Green-Cauchy tensor, and $W_i |_{i=1..3}$ are model parameters.

Let us first describe the steps required for the calibration of a constitutive model as a stochastic model. A constitutive model should be able to connect deformation input λ to stress output P through certain internal parameters \mathbf{W} such that

$$\mathbf{P} = f(\boldsymbol{\lambda}; \mathbf{W}) + \epsilon, \quad \text{with} \quad f(\boldsymbol{\lambda}; \mathbf{W}) = \sum_{j=1}^m W_j \phi_j(\lambda), \quad \text{and} \quad \mathcal{P}(\epsilon) = N(\epsilon|0, \sigma^2), \quad (7.3)$$

where ϕ_j are the basis functions, m is the number of basis functions, and W_j are the weight parameters gathered in vector \mathbf{W} . Here, $N(\epsilon|0, \sigma^2)$ represents the Gaussian distribution of noise around zero with variance σ^2 which is assumed to represent $\mathcal{P}(\epsilon)$. Inserting Carroll model [262] in Eq. 7.2, $f(\boldsymbol{\lambda}; \mathbf{W})$ will be represented by three weight parameters and three basis functions, where $m = 3$. As a representative constitutive models, the Carroll model [262] is chosen due to its performance in predicting different states of deformation, which has a rational error. In a stochastic calibration problem [263], we optimize function $f(\boldsymbol{\lambda}; \mathbf{W})$ by fitting \mathbf{W} with a dataset \mathbf{D}

of n observations of λ , and P as summarized below

$$\mathbf{D} = \{[\lambda_1, P_1] \dots [\lambda_n, P_n]\} = \{\mathbf{P}, \boldsymbol{\lambda}\}. \quad (7.4)$$

Bayesian Methodology is used to calculate the joint probability distribution of model parameters and accordingly to derive uncertainty associated with experimental data [264]. In comparison to the least square method (LSM), the Bayesian approach can show the model uncertainty with stochastic parameters, while LSM mainly search for the best parameters for fitting without providing any information regarding parameters' probability. Bayesian method is based on the Bayes conditional rule of probability where

$$\mathcal{P}(\mathbf{W}|\mathbf{D}, M) = \frac{\mathcal{P}(\mathbf{D}|\mathbf{W}, M) \mathcal{P}(\mathbf{W}|M)}{\mathcal{P}(\mathbf{D})}, \quad (7.5)$$

which \mathbf{W} is the vector of unknown model parameters, and M is the chosen model, namely, the Carroll model [262]. $\mathcal{P}(\mathbf{W}|M)$ is the prior joint distribution and shows the degree of belief to the parameters before we know the data. $\mathcal{P}(\mathbf{D}|\mathbf{W}, M)$ is the likelihood joint distribution which describes the observation probability of what we have observed, and $\mathcal{P}(\mathbf{W}|\mathbf{D}, M)$ is the posterior distribution. Here, $\mathcal{P}(\mathbf{D})$ is a normalizer, given as follow

$$\mathcal{P}(\mathbf{D}) = \int_{\mathbf{W}} \mathcal{P}(\mathbf{D}|\mathbf{W}, M) \mathcal{P}(\mathbf{W}|M) d\mathbf{W}. \quad (7.6)$$

For parameter estimation, the marginal likelihood $\mathcal{P}(\mathbf{D})$ does not affect the value of the weight parameters \mathbf{W} , so it is often considered as a normalization constant. In the absence of any information, the prior probability of the parameters can be assumed to be a Gaussian distribution on the parameter space. It is one way to illustrate our prior ignorance about the weight parameters \mathbf{W} .

Prior Selection is pivotal in the Bayesian framework. Various strategies exist, including right Haar measure, Jeffreys prior [265], reference priors [266], Maxent priors [267], and conjugate priors

[268]. Notably, conjugate priors yield specific posterior distribution families. For computational simplicity in this study, we adopt a Gaussian prior, sidestepping challenges inherent to other methods. This choice remains robust, as subsequent observations iteratively refine the prior distribution.

Bayesian model selection offers multiple methodologies. Among them, the Bayes factor, frequentist methods, and the Bayesian Information Criterion stand out. The Bayesian approach holds advantages, notably its interpretability in terms of model posterior probabilities and the Bayes factor. It also ensures, under mild conditions, the selection of the true model if it exists within the candidate set [269, 270].

Our chosen prior is expressed as:

$$\mathcal{P}(\mathbf{W}; \alpha) = \mathcal{N}\left(\mathbf{W} | \mathbf{0}, \frac{1}{\alpha} \mathbf{I}\right), \quad (7.7)$$

where the initial assumption centers the weights around zero, $\mathcal{N}(\mathbf{W} | \mathbf{0}, \alpha^{-1} \mathbf{I})$. The precision parameter, α , acts as a regularization index in MAP to counteract overfitting, and is set to 1 for MLE. This parameter quantifies the uncertainty surrounding \mathbf{W} values [271, 272].

Model Calibration is executed via two distinct methods for cross-validation: (i) Maximum Likelihood Estimation (MLE) and (ii) Maximum a Posteriori (MAP) estimation [273].

7.2.1 Maximum Likelihood Estimation (MLE)

MLE aims to identify a probability distribution that best replicates observed data. Specifically, it determines the weight parameter vector, \mathbf{W}_{MLE} , that maximizes the likelihood function $\mathcal{P}(\mathbf{W} | \mathbf{D}, M)$. However, \mathbf{W}_{MLE} might not always be unique or even existent. To enhance computational efficiency, the log of the likelihood function, $\ln \mathcal{P}(\mathbf{W} | \mathbf{D}, M)$, is often maximized due to its slower growth rate. Since the likelihood function and its logarithm are monotonically related, maximizing one implies

maximizing the other. Given a differentiable log-likelihood, the MLE criteria can be expressed as:

$$\left. \frac{\partial \ln \mathcal{P}(\mathbf{W}|\mathbf{D}, M)}{\partial \mathbf{W}} \right|_{\mathbf{W}=\mathbf{W}_{MLE}} = 0, \quad \left. \frac{\partial^2 \ln \mathcal{P}(\mathbf{W}|\mathbf{D}, M)}{\partial \mathbf{W}^2} \right|_{\mathbf{W}=\mathbf{W}_{MLE}} < 0, \quad (7.8)$$

where the latter condition ensures the function's convexity at the optimal \mathbf{W}_{MLE} . Considering Eq. 7.5 in terms of stress and deformation, the posterior encapsulates our knowledge post-data observation, given known noise variance σ^2 .

Based on Eq. 7.5, the posterior can be expressed as

$$\mathcal{P}(\mathbf{W}|\boldsymbol{\lambda}, \mathbf{P}; \sigma^2) = \frac{\mathcal{P}(\mathbf{P}|\boldsymbol{\lambda}, \mathbf{W}; \sigma^2) \mathcal{P}(\mathbf{W})}{\mathcal{P}(\mathbf{P}|\boldsymbol{\lambda})}, \quad \mathcal{P}(\mathbf{P}|\boldsymbol{\lambda}) = \int \mathcal{P}(\mathbf{P}|\boldsymbol{\lambda}, \mathbf{W}; \sigma^2) \mathcal{P}(\mathbf{W}) d\mathbf{W}, \quad (7.9)$$

where $\mathcal{P}(\mathbf{P}|\boldsymbol{\lambda})$ is the marginal likelihood of producing the experimental dataset \mathbf{D} . Assuming likelihood and prior to be Gaussian, we can write the likelihood function with respect to Eq. (7.8) as

$$\mathcal{P}(\mathbf{P}|\boldsymbol{\lambda}, \mathbf{W}; \sigma^2) = \exp\left(-\frac{1}{2\sigma^2} \|\boldsymbol{\Phi}\mathbf{W} - \mathbf{P}\|^2\right) \quad (7.10)$$

where $\boldsymbol{\Phi} \in \mathbb{R}^{n \times m}$ is a matrix with values of basis functions distributed over observation points \mathbf{D} such that $\Phi_{i,j} = \phi_j(\lambda_i)$. In MLE approach, one can find the weight parameters, \mathbf{W}_{MLE} , by derivation from Eq. 7.10

$$\nabla \mathcal{P}(\mathbf{P}|\boldsymbol{\lambda}, \mathbf{W}; \sigma^2) = 0 \quad \Rightarrow \quad \mathbf{W}_{MLE} = \left(\boldsymbol{\Phi}^T \boldsymbol{\Phi}\right)^{-1} \boldsymbol{\Phi}^T \mathbf{P}, \quad \sigma_{MLE}^2 = \frac{\|\boldsymbol{\Phi}\mathbf{W}_{MLE} - \mathbf{P}\|^2}{n}. \quad (7.11)$$

The posterior function is consequently derived as a PDF function of multivariate distribution \mathcal{N} as

$$\mathcal{P}(\mathbf{P}|\boldsymbol{\lambda}, \mathbf{W}; \sigma^2) = \mathcal{N}\left(\mathbf{P}|\mathbf{W}_{MLE}^T \boldsymbol{\Phi}(\boldsymbol{\lambda}); \sigma_{MLE}^2\right). \quad (7.12)$$

The posterior function allows us to make a probability distribution for a new target constitutive

values λ^* , and σ^* based on the optimized weight parameters \mathbf{W}_{MLE} using $\mathcal{P}(\mathbf{P}^*|\boldsymbol{\lambda}^*, \mathbf{W}_{MLE}; \sigma)$, where the median $m(\lambda)$, lower bound $l(\lambda)$, and upper bound $u(\lambda)$, for any new target deformation can be calculated as

$$m(\lambda) = \sum_{j=1}^m W_{MLE:j} \phi_j(\lambda), \quad l(\lambda) \approx m(\lambda) - 2\sigma_{MLE}, \quad u(\lambda) \approx m(\lambda) + 2\sigma_{MLE}. \quad (7.13)$$

7.2.2 Maximum A Posteriori (MAP) Estimation

In this method, in order to find parameters, the measurement process is modeled using the posterior. We believe that our measurement is around the model prediction, but it is contaminated by Gaussian noise. So, we have the same likelihood here Eq. 7.10. The difference between this method with the last method is, here, we maximize posterior. This method is very similar to MLE, with the addition of the prior probability over the distribution and parameters. In fact, if we assume that all values of weights are equally likely because we do not have any prior information, then both calculations are equivalent. Thus, both MLE and MAP often converge to the same optimization problem for many machine learning algorithms because of this equivalence. This is not always the case. If the calculation of the MLE and MAP optimization problem differ, the MLE and MAP solution found for an algorithm may also differ. We model the uncertainty in model parameters using a prior. In the MAP approach, the likelihood function in Eq. (7.9) will be calculated differently based on conjugate prior and given as

$$\mathcal{P}(\mathbf{P}|\boldsymbol{\lambda}, \mathbf{W}; \sigma) = \exp\left(-\frac{1}{2\sigma^2}\|\boldsymbol{\Phi}\mathbf{W} - \mathbf{P}\|^2 - \frac{\alpha}{2}\|\mathbf{W}\|^2\right), \quad (7.14)$$

where one can find the optimized weight parameters that are gathered in \mathbf{W}_{MAP} , by derivation from Eq. 7.14

$$\nabla \mathcal{P}(\mathbf{P}|\boldsymbol{\lambda}, \mathbf{W}; \sigma^2) = 0 \quad \Rightarrow \quad \mathbf{W}_{MAP} = \log \mathcal{P}(\mathbf{P} | \boldsymbol{\lambda}, \mathbf{W}; \sigma) = \mathbf{S}_M \boldsymbol{\Phi}^T \mathbf{P}, \quad \mathbf{S}_M = \left(\alpha \mathbf{I} + \frac{1}{\sigma^2} \boldsymbol{\Phi}^T \boldsymbol{\Phi}\right)^{-1}. \quad (7.15)$$

The posterior function is consequently derived as

$$\mathcal{P}(\mathbf{W}|\boldsymbol{\lambda}, \mathbf{P}) = \mathcal{N}(\mathbf{W}|\mathbf{W}_N, \mathbf{S}_N) = \det(2\pi\mathbf{S}_N)^{-\frac{1}{2}} \exp\left(-\frac{1}{2}(\mathbf{W} - \mathbf{W}_N)^T \mathbf{S}_N^{-1}(\mathbf{W} - \mathbf{W}_N)\right), \quad (7.16)$$

where \mathbf{W}_N is the mean vector, \mathbf{S}_N is covariance matrix, and for a Gaussian posterior, $\mathbf{W}_{MAP} = \mathbf{W}_N$, and $\mathbf{S}_M = \mathbf{S}_N$. The posterior function allows us to make a probability distribution for a new target deformation values λ^* based on the optimized weight parameters \mathbf{W}_{MAP} as

$$\mathcal{P}(\mathbf{P}^*|\boldsymbol{\lambda}^*, \mathbf{W}_N, \mathbf{S}_N) = \mathcal{N}(\mathbf{P}^*|\mathbf{W}_N^T \phi(\boldsymbol{\lambda}^*), \mathbf{S}_N), \quad (7.17)$$

where the median $m(\lambda)$, lower bound $l(\lambda)$, and upper bound $u(\lambda)$, for any new target deformation can be calculated as

$$m(\lambda) = \sum_{j=1}^m W_{MAP:j} \phi_j(\lambda), \quad l(\lambda) \approx m(\lambda) - 2\sigma, \quad u(\lambda) \approx m(\lambda) + 2\sigma. \quad (7.18)$$

7.3 Non-parametric Approach

A Non-parametric Stochastic Constitutive Model is proposed to describe the constitutive behavior of elastomers and its associated uncertainty. Unlike parametric method, this method is generic and can be applied to any mapping ranging simple to complex, although at significantly higher computational cost. Gaussian processes (GP) take a non-parametric approach to model selection. Compared to Bayesian linear regression, GP is more general because the form of the classifier is not limited by a parametric form. GP can also handle the case in which data is available in different forms, as long as we can define an appropriate covariance function for each data type. Bessa et al. [274] employed Gaussian processes and neural networks to create a constitutive model for hyperelastic materials, and also to predict plastic properties.

Gaussian Process (GP) represents the probability of function outputs by providing a joint Gaussian distribution of the output for any set of input points [275]. This property, and the fact that the distribution of a subset conditioned on the rest is also Gaussian for any set of observations with a joint Gaussian distribution, allows predictions to be made at an unknown point (λ^*) based on previous observations \mathbf{D} . A GP on a model can be written as

$$\mathcal{P}(\mathbf{P}) = \mathcal{G}_{\mathcal{P}} \{ \mathbf{P} | \mu; \mathbf{K}(\lambda, \lambda) \} \quad (7.19)$$

where μ is the mean function which indicates the central tendency of the $\mathcal{G}_{\mathcal{P}}$. Assuming no particular knowledge about the trend of the function, we pick a zero mean function. $\mathcal{P}(\mathbf{P})$ denotes our beliefs about \mathbf{P} . Tensor \mathbf{K} is symmetric matrix (kernel) that describes the covariance between every pair of components in the input vector λ and depends on a set of hyperparameters θ . There is a one-to-one correspondence between the differentiability of the covariance function and samples from the GP probability measurement of the GP probability measurement when selecting the covariance function model [276]. Describing \mathbf{K} using the squared exponential covariance function, we can write the components as

$$K_{ij} = k(\lambda_i, \lambda_j) = \nu_0 \exp \left(-\frac{1}{2} \sum_{n=1} \frac{(\lambda_i^n - \lambda_j^n)^2}{l_n} \right), \quad (7.20)$$

where $\theta \in \{\nu_0, l_1, l_2, \dots, l_n\}$, and λ_i^n is n-th element of λ_i from data set. Hyperparameters l_n and ν_0 represent the length-scale and output-scale, respectively. Consider that a GP prior $\mathcal{G}_{\mathcal{P}}(\mathbf{P} | \mu; \mathbf{K})$ is chosen for the constitutive model M , and our experimental data set is $D = [(\lambda_i, P_i)]$, where $P_i = M(\lambda_i) + \epsilon_i$ and $\mathcal{P}(\epsilon | \lambda) = \mathcal{N}(\epsilon, 0; \sigma^2)$; we can write GP prior as

$$\mathcal{P}(\mathbf{P} | \theta) = \mathcal{N}(\mathbf{P} | \mu(\lambda | \theta); \mathbf{K}(\lambda, \lambda | \theta)), \quad (7.21)$$

To fit the hyperparameters, we look for the θ that maximizes the log-likelihood [277].

Based on Eq. 7.16 for a Gaussian distribution, log-likelihood can be written as

$$\log \mathcal{P}(\mathbf{P}|\boldsymbol{\lambda}, \boldsymbol{\theta}) = -\frac{(\mathbf{P} - \boldsymbol{\mu})^T \mathbf{V}^{-1} (\mathbf{P} - \boldsymbol{\mu})}{2} - \frac{\log \det \mathbf{V}}{2} - \frac{n \log 2\pi}{2}, \quad \text{with} \quad \mathbf{V} = \mathbf{K}(\boldsymbol{\lambda}, \boldsymbol{\lambda}|\boldsymbol{\theta}) + \sigma^2 \mathbf{I} \quad (7.22)$$

Marginal likelihood indicates the quality of the fitting of the model to our training data. To optimise the training and maximize the log-likelihood, the best hyperparameters should be located and used for fitting. In this study, we used L-BFGS method to maximize log-likelihood. Our goal is prediction of function $M(\boldsymbol{\lambda}^*)$ at some test locations $\boldsymbol{\lambda}^*$. Now, we can calculate mean and covariance functions at $\boldsymbol{\lambda}$ and evaluate multivariate Gaussian distribution. So, we can write joint distribution between the training function $M(\boldsymbol{\lambda}) = \mathbf{P}$ and the prediction function values $M(\boldsymbol{\lambda}^*) = \mathbf{P}^*$.

Using Bayes' rule

$$\mathcal{P}(\mathbf{P}^*|\boldsymbol{\lambda}^*, D) = \mathcal{N}(\mathbf{P}^*|\boldsymbol{\mu}_{M|D}(\boldsymbol{\lambda}^*); \mathbf{K}_{M|D}(\boldsymbol{\lambda}^*, \boldsymbol{\lambda}^*)), \quad (7.23)$$

where

$$\boldsymbol{\mu}_{M|D}(\boldsymbol{\lambda}^*) = \boldsymbol{\mu}(\boldsymbol{\lambda}^*) + \mathbf{K}(\boldsymbol{\lambda}^*, \boldsymbol{\lambda}) \left(\mathbf{K}(\boldsymbol{\lambda}, \boldsymbol{\lambda}) + \sigma^2 \mathbf{I} \right)^{-1} (\mathbf{P} - \boldsymbol{\mu}(\boldsymbol{\lambda})), \quad (7.24)$$

and

$$\mathbf{K}_{M|D}(\boldsymbol{\lambda}^*, \boldsymbol{\lambda}^*) = \mathbf{K}(\boldsymbol{\lambda}^*, \boldsymbol{\lambda}^*) - \mathbf{K}(\boldsymbol{\lambda}^*, \boldsymbol{\lambda}) \left(\mathbf{K}(\boldsymbol{\lambda}, \boldsymbol{\lambda}) + \sigma^2 \mathbf{I} \right)^{-1} \mathbf{K}(\boldsymbol{\lambda}, \boldsymbol{\lambda}^*). \quad (7.25)$$

where $\mathbf{K}(\boldsymbol{\lambda}, \boldsymbol{\lambda}^*)$ is the cross covariance between $\boldsymbol{\lambda}$ and $\boldsymbol{\lambda}^*$.

7.4 Probability Failure Calculation of Hyperelastic Materials

In the previous section, we discussed the incorporation of uncertainties from various sources into constitutive models. This section delves into the utilization of the probabilistic model, derived from the previous section, as an input for calculating failure probability.

For hyperelastic materials, uncertainties stemming from the material matrix (both parameter and model uncertainties), compounding processes (experimental uncertainty), geometry (struc-

tural uncertainty), and loading conditions (both experimental and interpolation uncertainties) can significantly influence prediction accuracy. A primary challenge in developing failure prediction mechanisms is the absence of a definitive failure threshold, making it difficult to categorize events as binary (either failure or non-failure). In real-world scenarios, samples exhibit failure across a broad spectrum of stress or strain levels, leading to significant errors in deterministic failure models. To address this, we require probabilistic models that can accurately depict the probability of failure.

Consider the failure stress criteria, denoted by σ_U . This can be viewed either as a deterministic value or as a probabilistic distribution (as illustrated in Fig. 7.2). Given the probabilistic constitutive behavior of the material, represented by $P(\mathbf{W})$, we can determine the failure profile p_f in relation to σ_U .

This is achieved using a limit state function (LSF) $g(\mathbf{W})$, which is given as

$$g(\mathbf{W}) = \sigma_U - P(\mathbf{W}), \quad \Rightarrow \quad g(\mathbf{W}) : \begin{cases} > 0 & \text{Safe region} \\ = 0 & \text{Limit state} \\ < 0 & \text{Failure region: } p_f \end{cases} \quad (7.26)$$

where $P(\mathbf{W})$ is a constitutive equation of the variables W_1, W_2, \dots, W_n which is estimated from the Bayesian surrogate constitutive model procedure which can be derived through aforementioned parametric or non-parametric procedures (see Eq. 7.3). The distribution $P(\mathbf{W})$ can be derived based on the experimental data on stress-strain behaviour of materials.

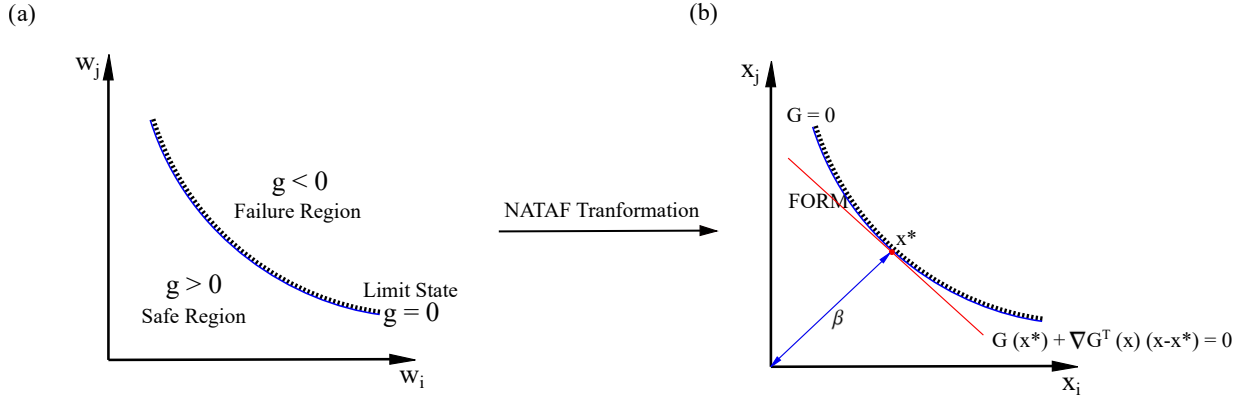


Figure 7.2. Concept of β index with respect to LSF in a) the physical space b) the standard normal space

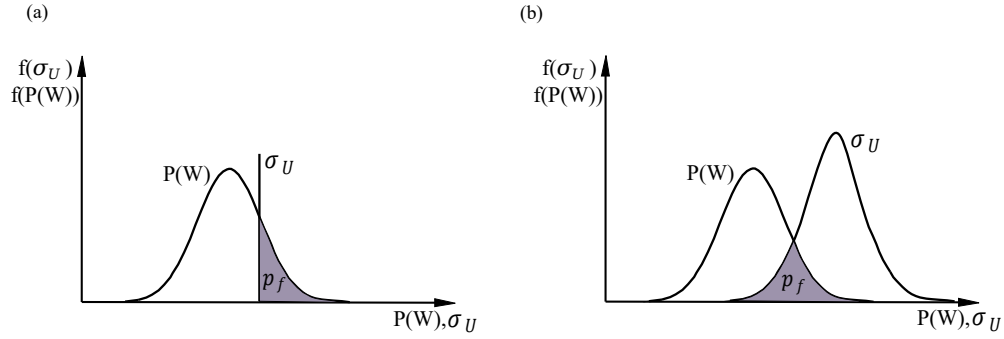


Figure 7.1. Concept of failure probability in an specific stretch and formation of failure region p_f with a) a deterministic criterion for ultimate stress b) a probabilistic criterion for ultimate stress

NATAF transformation will be used to map the distributions of random constitutive variables, (\mathbf{W}), within their standard normal space (for computational purposes [278]). Next, a first-order Taylor expansion at the most probable point is sufficient to locate the maximum failure probability of $g(\mathbf{W})$ [279] (see Fig. 7.2.b). The failure probability P_f integral over the failure region $g < 0$ is written as

$$P_f = \mathcal{P}(g < 0) = \int_{g < 0} \dots \int f(W_1, W_2, \dots, W_n) dW_1 \dots dW_n, \quad (7.27)$$

where f is the probability density function, and n is the size of the input vector \mathbf{W} . In Eq. 7.27, the integral should be taken over p_f where $g < 0$. To simplify the integration, it would be sufficient to rewrite the integration with respect to a normal standard space with $\mu = 0$ and $\sigma = 1$. Accordingly,

one can introduce a new limit state function G on a normal standard space which represents the former $g(\mathbf{W})$ over the current space. To convert the problem from current space to the normal standard space, NATAF transformation [280] will be used, which introduce new input parameters x_i based on \mathbf{W} as

$$x_i = \Phi^{-1}(f(W_i)), \quad (7.28)$$

where f and Φ^{-1} represents the cumulative distribution functions (CDF) of \mathbf{W} and the inverse CDF of x_i , respectively. Accordingly, P_f is estimated as given below [281]

$$P_f = \Phi(-\beta), \quad \beta = \frac{\mu_G}{\sigma_G}, \quad \mu_G \cong G(\mu_{x_1}, \mu_{x_2}, \dots, \mu_{x_n}), \quad \sigma_G^2 \cong \sum_{i=1}^n \sum_{j=1}^n \frac{\partial G}{\partial x_i} \frac{\partial G}{\partial x_j} \text{cov}(x_i, x_j), \quad (7.29)$$

where β is the reliability index, and represents the shortest distance from the origin in standardized normal space to the hyperplane (deterministic) or paraboloid (probabilistic) formed by $G = 0$. β can be calculated by solving an optimization problem. Let us introduce \mathbf{x}^* to represent the point along the paraboloid, which has the least distance to the origin, further referred to as the design point. Here, μ_G and σ_G are the mean and standard deviation of the $G(\mathbf{x})$ in the standard normal space. In the FORM analysis, the paraboloid $G(\mathbf{x}) = 0$ can be represented by a linear smooth surface which passes through the design point, \mathbf{x}^* , designated by position vector \mathbf{x}^* .

Accordingly, we have $G(\mathbf{x}) \approx 0$ while $G(\mathbf{x}^*) = 0$, and thus the surface can be represented by

$$G(\mathbf{x}) = G(\mathbf{x}^*) + \nabla G^T(\mathbf{x}^*)(\mathbf{x} - \mathbf{x}^*), \quad \mathbf{x}^* = \arg \min \{\|\mathbf{x}\| \mid G(\mathbf{x}) = 0\}, \quad (7.30)$$

where $\beta = \|\mathbf{x}^*\|$. The improved Hasofer-Lind-Rackwitz-Fiessler (iHLRF) method is used [282] to find the design point. Furthermore, having an arbitrary point (\mathbf{x}_m) as the design point candidate in the iteration m , the new candidate design point (\mathbf{x}_{m+1}) can be obtained by

$$\mathbf{x}_{m+1} = \mathbf{x}_m + \delta_m \cdot d_m, \quad (7.31)$$

where δ_m , and d_m are the step search and the search direction at the m th iteration, respectively. Here, $\delta_m = a^k$ can be determined by Armijo rule which considers a to be a positive value (usually $a = 0.5$), and k to be an integer that is iteratively increased from zero [283]. The proper search direction (d_m) and the step search (δ_m) for carrying out the search algorithms to find the design point are presented as follows

$$d_m = \left(\frac{G(\mathbf{x}_m)}{\|G(\mathbf{x}_m)\|} + \alpha^T \mathbf{x}_m \right) \alpha - \mathbf{x}_m, \quad \alpha = \frac{\nabla G(\mathbf{x}_m)}{\|\nabla G(\mathbf{x}_m)\|}. \quad (7.32)$$

A convergence criteria is required to stop the search algorithm for finding \mathbf{x}_m which is considered as follows

(1) By assuming \mathbf{x}_m to be **almost** on the surface of the limit state function, we have $G(\mathbf{x}_m) \approx 0$ which yields

$$\frac{G(\mathbf{x}_{m+1}) - G(\mathbf{x}_m)}{G(\mathbf{x}_m)} < e_1, \quad (7.33)$$

where $e_1 \approx 0.001$ is the convergence parameter that defines the stop criteria.

(2) The surface gradient of the limit state function passes through the coordinate reference point at the last point, which shows that the current point is the closest point to the origin

$$\left| \frac{\mathbf{x}_m}{\|\mathbf{x}_m\|} - \left(\alpha_m^T \frac{\mathbf{x}_m}{\|\mathbf{x}_m\|} \right) \alpha_m \right| < e_2, \quad (7.34)$$

where e_2 is convergence parameter as a criteria to stop iteration. It is 0.001 based on literature. After finding the design point (\mathbf{x}^*), probability of failure is equal to $P_f = \Phi(-\|\mathbf{x}^*\|)$.

Crude Monte Carlo (CMC) Simulation is used to provide benchmark for validating the predictions obtained by FORM. CMC simulation is also used concurrently to estimate the limit state probabilities. The results show the accuracy of the first-order approximation of LSF. CMC is a popular method among the methods of sampling which generates random numbers for random variables \mathbf{W} , based on their distribution. Each time a random vector is generated, $g(\mathbf{W})$ will be

validated and consequently, we assume sample failure if $g(\mathbf{W}) < 0$ (see Fig. 7.3). Integral of failure probability can be written as

$$P_f = \mathcal{P}(g < 0) = \int_{g < 0} \dots \int f(\mathbf{W}) d\mathbf{W} = \int_{-\infty}^{+\infty} \dots \int_{-\infty}^{+\infty} I(\mathbf{W}) f(\mathbf{W}) d\mathbf{W} = \frac{1}{N} \sum_{i=1}^N I(W_i), \quad (7.35)$$

where $N = \frac{1}{\delta_{P_f}^2} \left(\frac{1-P_f}{P_f} \right)$ is the number of simulation, and $\delta_{P_f} = 0.05$ is a common value in the literature [281, 284].

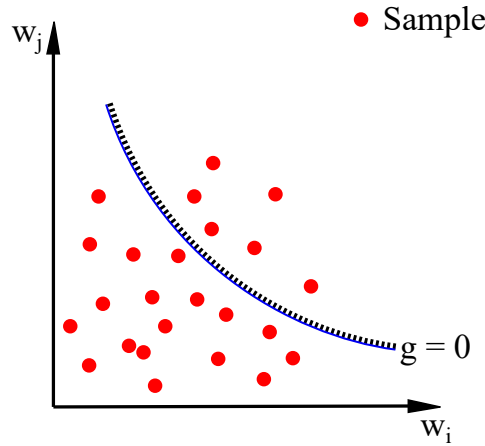


Figure 7.3. Monte Carlo simulation

Note that Monte Carlo simulations constitute an integration method which, with respect to numerical integration, represents an economical means of choosing only some points by chance in the integration domain instead of systematically scanning in all directions. The value of the integration is thus deduced from the mathematical expectations of the sampling. On the other hand, FORM is a method which includes an integration method by estimation of LSF with Taylor expansion. The reason that we represent and compare these methods is that we want to show with CMC that first-order estimation of LSF in FORM is correct or not. So, if their results are in a good agreement, it means that the estimation is correct.

For understanding the procedure of this research, the below flowchart shows the steps of this study in summary.

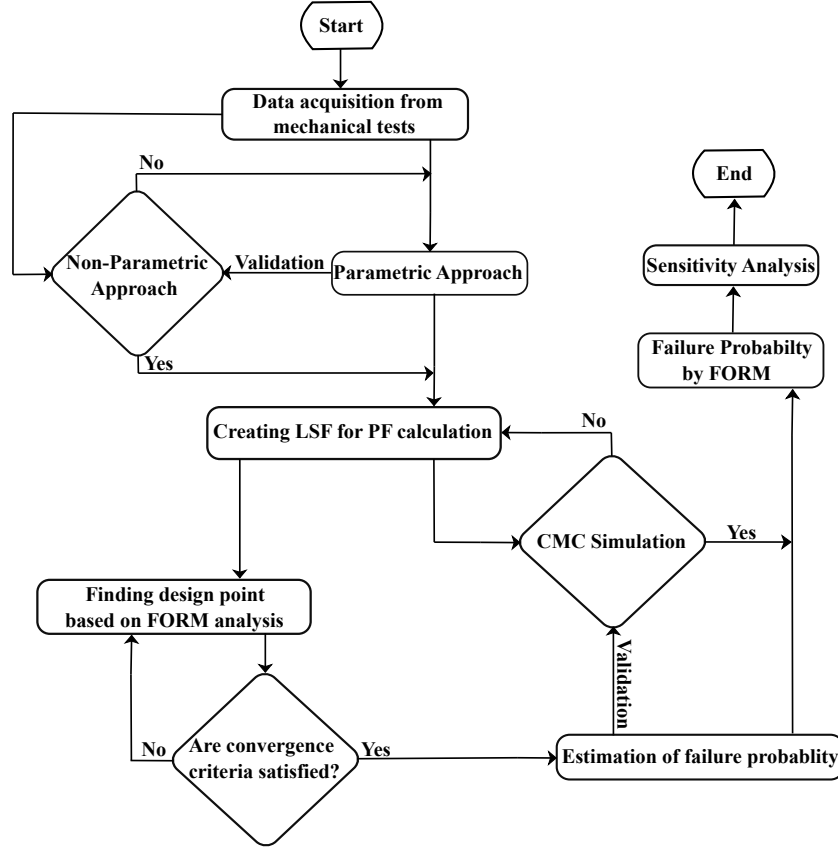


Figure 7.4. Flowchart of steps of conducted study

Sensitivity Analysis

Importance vector, γ , is used as a computational tool to determine the relative influence of the parameters in the failure probability function in the reliability analysis. Since now we can approximate the limit state function around the design point $G(\mathbf{x}) = \|\nabla G(\mathbf{x}^*)\| (\beta - \alpha^T \mathbf{x})$, variance of LSF, namely $var(G)$, can be written as follows

$$var(G) = \nabla G^T \Sigma_{xx} \nabla G = (-\|\nabla G\| \alpha)^T (-\|\nabla G\| \alpha) = \|\nabla G\|^2 (\alpha_1^2 + \alpha_2^2 + \dots + \alpha_n^2), \quad (7.36)$$

where Σ_{xx} is the covariance matrix. In Eq. 7.36, we define the contribution of each random variable in the variance of the limit state function through α_i^2 with higher values of $|\alpha_i|$ representing larger influence of their associated random variables. If $\alpha_i > 0$, the random variable is called the load

variable, and is called the resistance variable otherwise when $\alpha_i < 0$. So, whenever the FORM analysis is carried out to derive γ , one can determine the significance of random variables, which has the greatest interference in the probability of failure. To consider the correlation between the variables, the importance vector γ is defined as follows

$$\gamma = \frac{\alpha \mathbf{j}_{x,w}^* \mathbf{D}}{\|\alpha \mathbf{j}_{x,w}^* \mathbf{D}\|}, \quad (7.37)$$

where $\mathbf{j}_{x,w} = \mathbf{D}\mathbf{L}$. Here, \mathbf{D} is the derivation matrix in $\sigma = \mathbf{D}\mathbf{R}\mathbf{D}$ where \mathbf{R} is the correlation coefficient matrix, and \mathbf{L} is derived as the Cholesky factor of the upper triangle of \mathbf{R} , namely $\mathbf{L} = \text{chol}(\mathbf{R})$.

7.5 Results

7.5.1 Experimental Tests

A uni-axial test is implemented for three materials, silicon, polyurethane black, and Styrene-butadiene rubber. Four specimens were used to characterize each failure point used in the experimental data.

Our tests were mostly focused on uniaxial tensile tests performed on Dumbbell specimen with specifications given in ASTM D412- Die C and shown in Fig. 7.5.

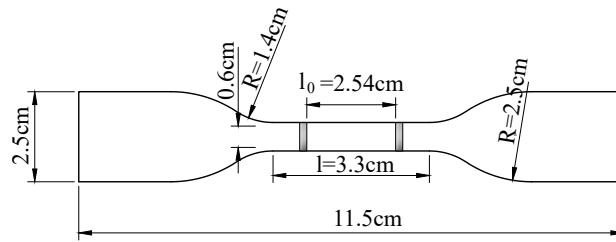


Figure 7.5. Detailed sample dimensions

Mechanical Test Quasi-static tensile tests were conducted on a uni-axial universal Testing Machine (*TestResources* 311 Series Frame). Samples were clamped between two grips and stretched at the rate of $50\text{mm}/\text{min}$ at room conditions to minimize the visco-elastic effects(i.e.

$22 \pm 2^{\circ}C$, $50 \pm 3\%RH$). Measurement is conducted using an external extensometer to avoid clamp slippage. In Fig. 7.6, stretch-stress curves are depicted for all samples and as illustrated, the samples failure were very close to each other in small deformation. As deformation increases, the evolution of defects in the samples leads to uncertainty in the material's response.

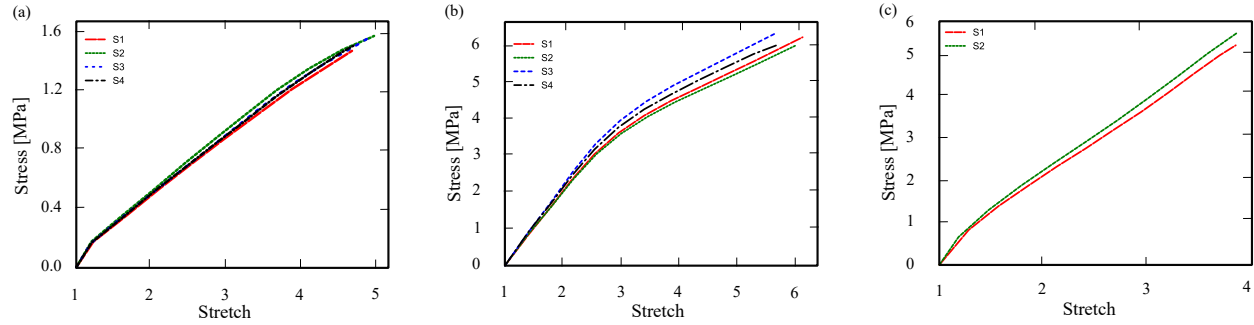


Figure 7.6. Stretch-Stress results of mechanical tests for a) Silicone, b) Polyurethane c) Styrene-butadiene rubber

Parametric Stochastic Constitutive Model Model calibration is conducted based on Bayesian regression to demonstrate UQ of Carroll model with respect to the behaviour of three elastomeric compounds, silicon, polyurethane, and styrene-butadiene rubber (SBR). MLE and MAP of the Carroll model were derived for three materials, while several plausible models of MAP are plotted in Figs. 7.7, 7.8, and 7.9 for polyurethane and Silicone, respectively. Similarly, table 7.1, 7.2, and 7.3 show the stochastic parameters for Silicone, Polyurethane, and Styrene-butadiene rubber.

Table 7.1. Statistical characteristics of Carroll model for Polyurethane

Parameters	Statistical distribution	Mean value	Standard deviation	Coefficient of Variation
W1	Normal	0.61025	0.01555	0.0255
W2	Normal	-5.4944e-7	0.9059e-7	0.1648
W3	Normal	0.09649	0.23623	2.4481

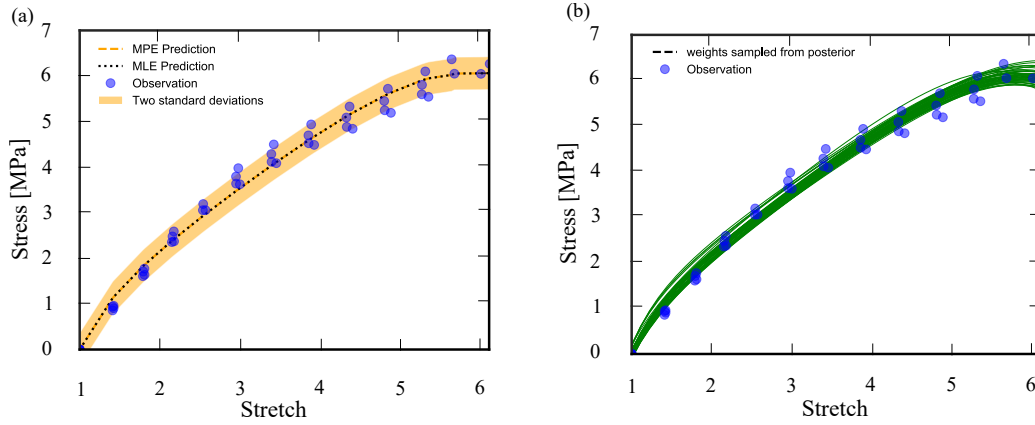


Figure 7.7. Model calibration of Carroll model for Polyurethane a) prediction b) plausible models

Table 7.2. Statistical characteristics of Carroll model for Silicone

Parameters	Statistical distribution	Mean value	Standard deviation	Coefficient of Variation
W1	Normal	0.173568	0.002315	0.013341
W2	Normal	-8.43e-8	3.492e-8	0.414199
W3	Normal	-0.206981	0.028986	0.140046

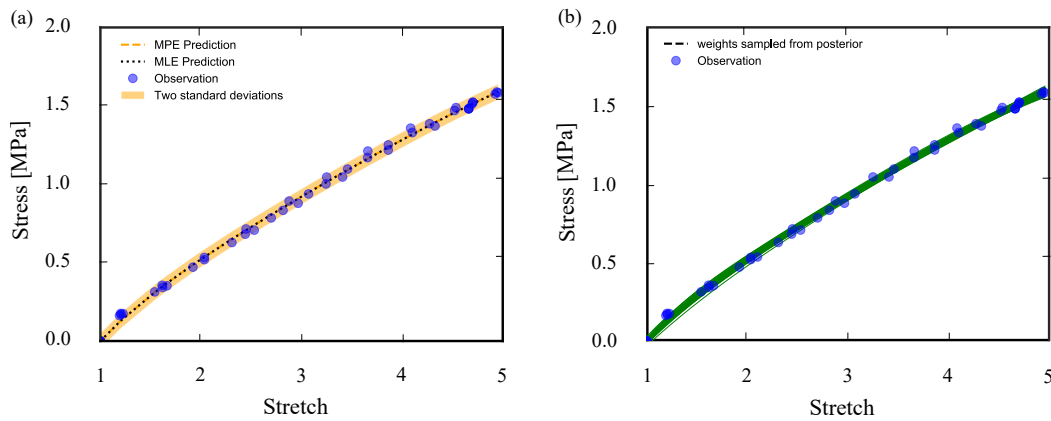


Figure 7.8. Model calibration of Carroll model for Silicone a) prediction b) plausible models

Table 7.3. Statistical characteristics of Carroll model for Styrene-butadiene rubber

Parameters	Statistical distribution	Mean value	Standard deviation	Coefficient of Variation
W1	Normal	0.671017	0.01242	0.01851
W2	Normal	3.5265e-6	1.567e-6	0.4443
W3	Normal	-0.3385	0.03127	0.09237

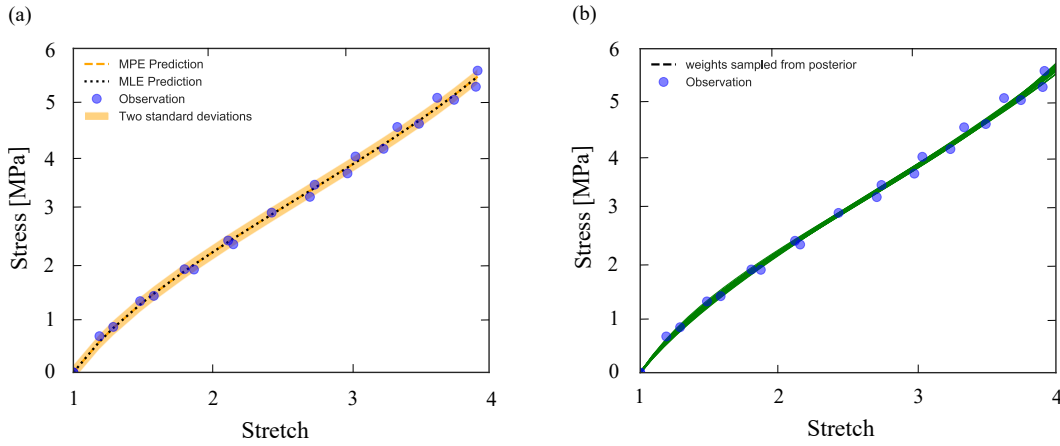


Figure 7.9. Model calibration of Carroll model for Styrene-butadiene rubber a) prediction b) plausible models

Non-Parametric Stochastic Constitutive Model To see the non-parametric model's performance, a GP analysis is conducted on these data sets to find hyper-parameters of the kernel in GP. We maximized log-likelihood based on L-BFGS method for two experimental data sets. Fig. 7.10, Fig. 7.11, 7.12 show the results for Polyurethane, Silicone, and Styrene-butadiene rubber respectively. Besides, several plausible models are plotted based on obtained hyperparameters. Data is more scatter in larger deformation due to the breakage of some samples and cumulative errors with stretch increasing. Note that we employed homoscedastic noise in the case study and this is the reason which initial stretch of curves have uncertainty. To make it zero, we can use heteroscedatic sparse Gaussian processes which Bessa et al. [285] employed to design a metamaterial and quantify

the uncertainty.

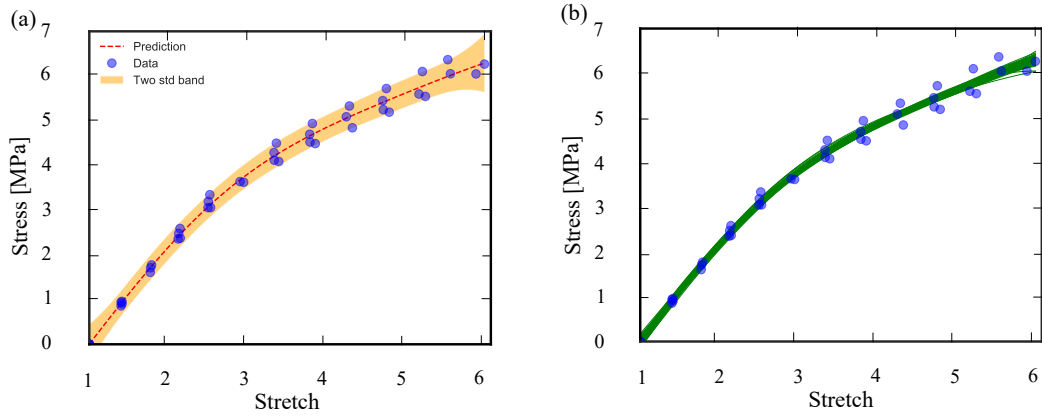


Figure 7.10. GP model for Polyurethane a) prediction b) plausible models

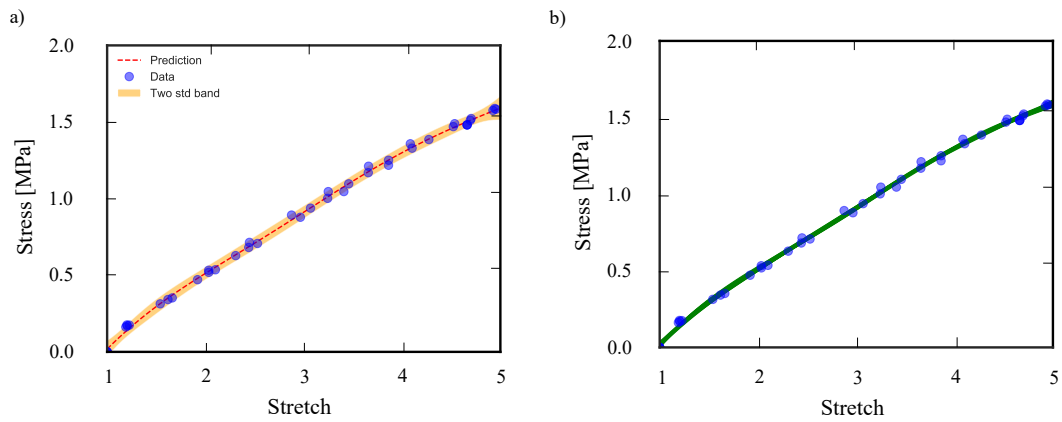


Figure 7.11. GP model for Silicone a) prediction b) plausible models

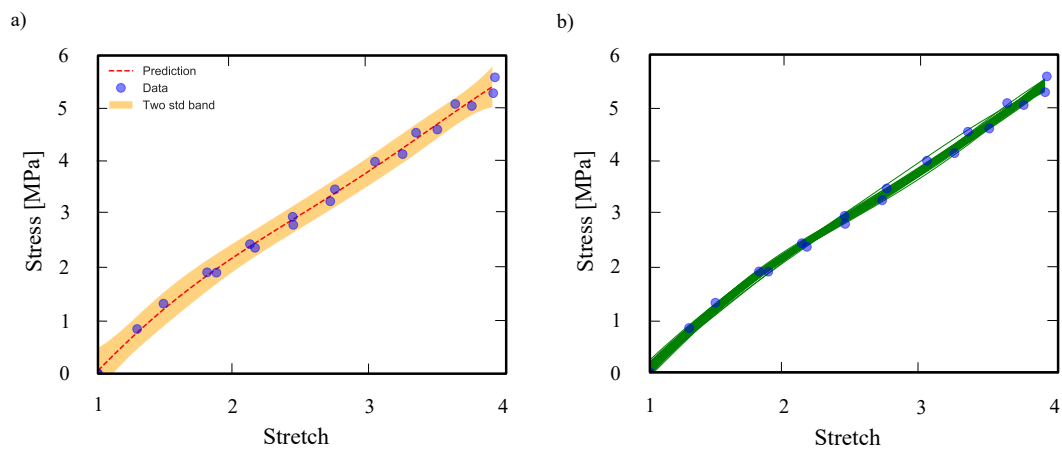


Figure 7.12. GP model for Styrene-butadiene rubber a) prediction b) plausible models

Table 7.4. Probability of failure for Polyurethane, Silicone, Styrene-butadiene based on FORM and CMC

Method	PUB ^a		DC ^b		SBR ^c	
	FORM	CMC	FORM	CMC	FORM	CMC
$P_f(\%)$	10.185	9.725	5.577	5.671	2.2903	2.3235
β	1.2710	1.2973	1.5912	1.5829	1.9971	1.9910

^a Polyurethane, ^b Silicone, ^c Styrene-butadiene

Probability of Failure For failure analysis, the first step is creating the limit state function $g(\mathbf{W})$.

Based on the previously derived stochastic constitutive model, $g(\mathbf{W})$ can be written as

$$g(\mathbf{W}) = \sigma_U - \left(2W_1 + 8W_2 \left(2\lambda^{-1} + \lambda^2 \right)^3 + W_3 \left(1 + 2\lambda^3 \right)^{-\frac{1}{2}} \right) \left(\lambda - \lambda^{-2} \right), \quad (7.38)$$

where we consider $\lambda = 5.861$ for Polyurethane predictions, $\lambda = 4.815$ for Silicone, and $\lambda = 3.91$ for Styrene-butadiene which are the mean of stretch in experimental datasets. Note that the selection of stretch for failure probability calculation depends on how much we stretch the material.

Failure distribution pattern for Polyurethane, Silicone, Styrene-butadiene can be best represented by $\sigma_U = \mathcal{N}(6.19, 0.16)$, $\sigma_U = \mathcal{N}(5.9, 0.237)$, and $\sigma_U = \mathcal{N}(5.45, 0.145)$ respectively. Those distributions were derived based on the data of four samples at failure points (i.e., a distribution analysis on failure points of four samples in each case). Table 7.4 shows the results of FORM analysis and CMC for Polyurethane, Silicone, Styrene-butadiene rubber. Also, Fig. 7.13, Fig. 7.14, and 7.15 Show the details of CMC simulation and distribution of $g(\mathbf{W})$ analysis for Polyurethane, Silicone, Styrene-butadiene rubber, respectively.

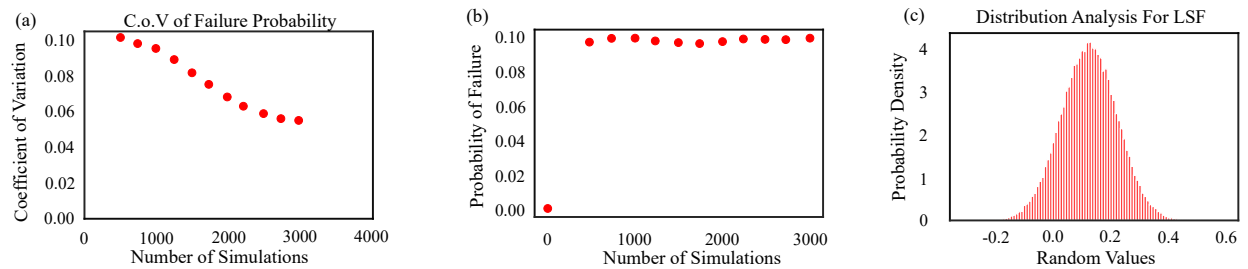


Figure 7.13. Polyurethane: a) coefficient of variation for failure probability respect to number of simulation b) probability of failure respect to number of simulation c) LSF distribution analysis

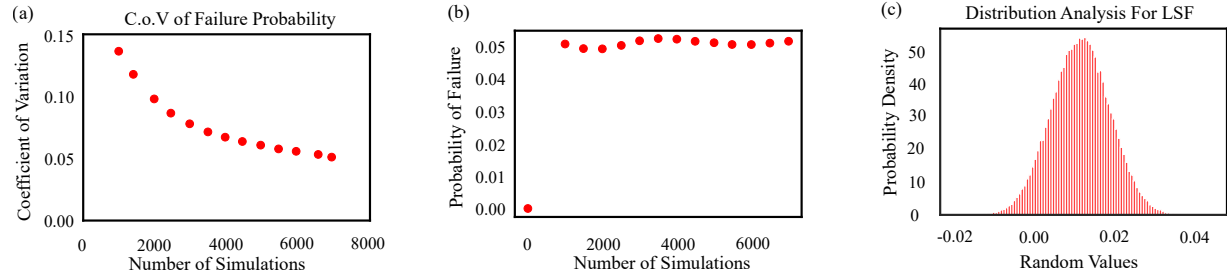


Figure 7.14. Silicone: a) coefficient of variation for failure probability respect to number of simulation b) probability of failure respect to number of simulation c) LSF distribution analysis

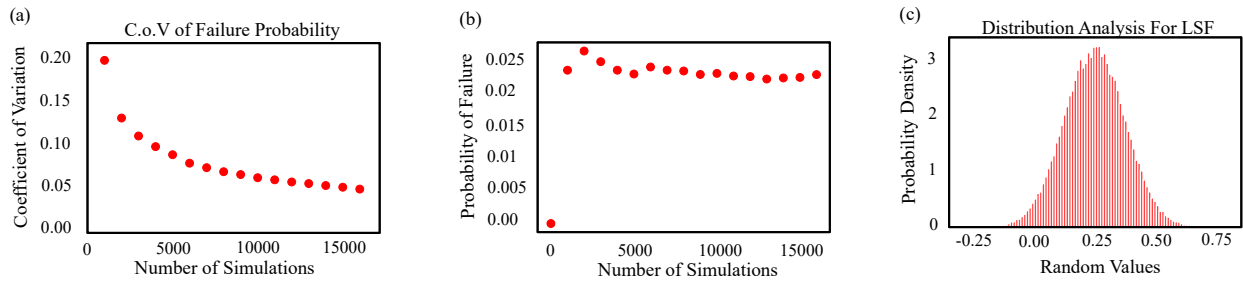


Figure 7.15. Styrene-butadiene: a) coefficient of variation for failure probability respect to number of simulation b) probability of failure respect to number of simulation c) LSF distribution analysis

Accordingly, the derived failure probability exhibits the probability of material failure at any specific stretch values. To show the importance of the random variables in failure probability, a sensitivity analysis has also been conducted, and the results for Polyurethane, Silicone, and Styrene-butadiene are shown in Fig. 7.16.

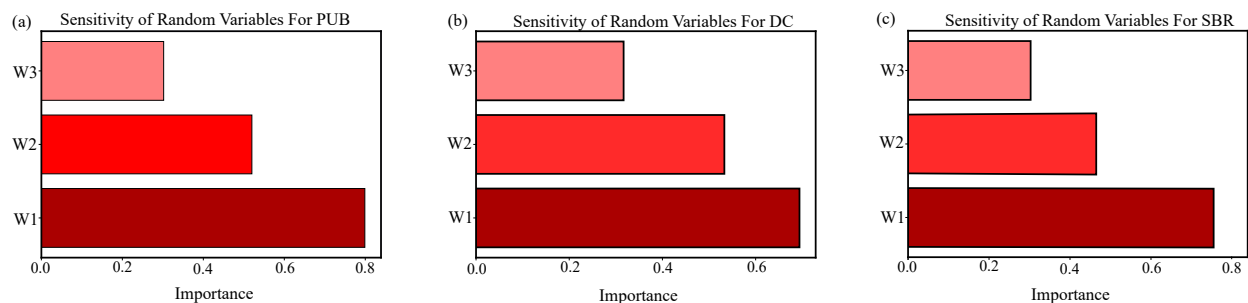


Figure 7.16. Importance analysis a) for Polyurethane b) for Silicone c) for Styrene-butadiene

7.6 Concluding remarks

This paper developed a Bayesian surrogate constitutive model to estimate failure probability of elastomers. First, a comprehensive uncertainty analysis was conducted and validated at multiple stage, including a parametric Bayesian inference on Carroll model which was calibrated based on two methods (MAP and MLE), a non-parametric Gaussian process which is based on squared exponential kernel. Both models were trained and validated with respect to two sets of our experiments on silicon- and polyurethane-based elastomers to demonstrate their capabilities in explaining uncertainty propagation. Next, For these data sets, failure probability analysis was performed using the First Order Reliability Method (FORM) by constructing a limit state function based on the stochastic constitutive model at the failure point. Crude Monte Carlo (CMC) simulation was used concurrently to estimate the limit state probabilities in order to determine the validity of adopting FORM. Finally, the importance of Carroll model parameters in predicting failure probability was demonstrated using sensitivity analysis. The developed framework is generic and can be implemented on any combination of data and constitutive model.

CHAPTER 8

SUMMARY AND FUTURE WORKS

The main goal of this research was to create a hybrid framework for the constitutive model of cross-linked polymers under extreme and regular environmental conditions. Each section of the dissertation is briefly summarized in this chapter. An introduction to cross-linked polymers and their applications was presented in the first part of this dissertation.

8.1 General Remarks

- In chapter 2, by embedding neural networks into a multi-scale model, a physics-informed data-driven constitutive model for cross-linked polymers is developed. Using current understanding of polymer science, continuum physics, and statistical mechanics, we proposed a systematic method to lower the order of the constitutive mapping. Our model can effectively represent various inelastic effects in material behavior, is much less data-dependent, has smaller dimensionality, and is interpretable, according to the results.
- In chapter 3, we developed a constitutive model for elastomers to capture the dependence of elastomer behavior on loading conditions such as strain rate and temperature, as well as compound morphology factors such as filler percentage and crosslink density. It is capable of considering the effects of loading conditions such as strain rate, temperature, and filler percentage in different deformation states, as well as enjoying a high training speed and accuracy even in complicated loading scenarios. It is applicable to a variety of soft materials, including soft robotics, soft digital materials (DMs), hydrogels and adhesives. This model has a distinct advantage over existing phenomenological models as it can capture strain rate

and temperature dependency in a much more comprehensive way.

- In chapter 4, we described a novel physics-informed hybrid framework to capture the relation between elastomeric network mechanics and environmental damage. The proposed model is used to describe the effect of single-mechanism aging, such as thermal-induced or hydrolytic aging, on the behavior of the material in this hybrid system. The model arises from polymer physics and an order reduction strategy ending to the constrained L-agents training. The polymer matrix was described by a cooperative multi-agents system, in which each agent is represented by a simple deep-learned CondNN that is super-constrained by laws derived from physics, thermodynamics, and continuum mechanics. The efficiency of the model was found satisfactory, and in some cases, excellent when compared with the experimental data.
- Chapter 5 introduced a novel physics-informed data-driven constitutive model to evaluate the combined effects of thermal aging and cyclic fatigue on the constitutive and failure behavior of cross-linked polymers. Our model, building upon recent models of thermal-oxidative aging and hydrolytic aging, was constructed on the premise of the complete independence of mechanical and environmental effects.
- In chapter 6, we employed Physics Informed Neural Networks (PINNs) to simulate the stiff and semi-stiff ODEs governing Pyrolysis and Ablation. Our engine is specifically tailored to calculate char formation and the degree of burning during the pyrolysis of crosslinked polymeric systems.
- Chapter 7 saw the development of a Bayesian surrogate constitutive model to estimate the failure probability of elastomers. After a comprehensive uncertainty analysis, failure probability analysis was conducted using the First Order Reliability Method (FORM).

8.2 Potential Future Research

Building upon the foundation laid in this dissertation, there are numerous avenues for further exploration and research in the realm of cross-linked polymers and their behavior under various

conditions. Some of the intriguing questions and potential research directions that arise from this study include:

- **Diffusion Limited Oxidation (DLO) Effects:** One of the pivotal phenomena in understanding the aging behavior of cross-linked polymers is Diffusion Limited Oxidation (DLO). Incorporating the effects of DLO into the proposed model can significantly enhance its predictive accuracy. DLO plays a crucial role in correlating accelerated aging tests with non-accelerated aging conditions. A deeper investigation into how DLO impacts the mechanical and chemical properties of cross-linked polymers, especially under varying environmental conditions, can provide invaluable insights. This research direction can help in bridging the gap between laboratory testing scenarios and real-world aging conditions, ensuring the reliability and longevity of polymer-based products.
- **Integration of Neural Network Models into FEM Frameworks:** Implementing neural network models, particularly physics-informed NN models like those developed in this work, into traditional Finite Element Method (FEM) frameworks presents a set of unique challenges. Firstly, the inherent differences between the deterministic nature of FEM and the probabilistic nature of neural networks can lead to complexities in model integration. Secondly, ensuring that the physics-informed constraints of the NN models are consistently upheld within the FEM environment is crucial, yet challenging. This is especially relevant when dealing with boundary conditions, material discontinuities, and non-linearities. Additionally, the computational overhead introduced by neural networks can strain the efficiency of FEM simulations, necessitating optimization strategies. Another challenge lies in the training of these integrated models; ensuring convergence and avoiding overfitting while maintaining the physical fidelity of the system can be intricate. Addressing these challenges can pave the way for more robust and accurate hybrid modeling approaches, combining the best of data-driven and physics-based methodologies.
- **Advancing Physics-Informed Neural Networks through Constraints:** The evolution of

physics-informed neural models necessitates the integration of background knowledge, which can manifest as physical laws, imprecise scientific knowledge, or even rough simulations that are only partly accurate. Two primary methods for this integration are the introduction of hard and soft constraints. Hard constraints are defined by amending the parameters formulations, and while significantly reducing the computational load, they introduce complexities in model development. They enforce strict adherence of parameters to physical laws or known behaviors, which can be challenging when dealing with imprecise or incomplete knowledge. On the other hand, soft constraints are defined as a fading terms in loss functions, and they are more flexible and can accommodate uncertainties, increase the computational load due to their probabilistic nature. However, they simplify the formulation by allowing for deviations within certain bounds. The major challenge lies in striking a balance between these two approaches. Determining when to employ hard constraints versus soft constraints, and understanding their implications on both the computational efficiency and the accuracy of the model, is crucial for the advancement of PINNs in real-world applications.

- **Material Design and Optimization:** Exploring new compounds or additives that can enhance the properties of cross-linked polymers to sustain certain servicelife condition, tailoring the compounds to make them more resilient to aging and environmental damage, can be a promising direction.

Outlook: AI in Material Science

The integration of artificial intelligence (AI) into material science presents a transformative opportunity to accelerate discoveries and optimize material properties. However, several barriers hinder seamless integration:

1. **Data Scarcity and Quality:** Material science often grapples with a lack of extensive, high-quality datasets. Experiments can be costly and yield limited data, making it challenging for AI models that thrive on vast datasets.

2. **Complexity and Interpretability:** Materials exhibit intricate behaviors influenced by numerous factors. While AI can predict these behaviors, understanding the rationale behind predictions is vital. The black-box nature of many AI models poses a challenge to their acceptance in the field.
3. **Physical Consistency and Generalization:** Ensuring AI models adhere to established physical laws is crucial. Additionally, materials phenomena span various scales, and models trained at one scale might not be effective at another, limiting their general applicability.
4. **Integration and Computational Costs:** Material science has a rich legacy of computational methods. Seamlessly integrating AI with these methods, especially given the computational intensity of deep learning models, remains a significant hurdle.

In this thesis, we have ventured into the intricate realm of material science, leveraging the power of AI, such as Deep neural network and machine learning, to simulate and predict behavior of polymers in different conditions. While the aforementioned efforts are a small step toward AI-driven digital simulation of materials, they also present a new path with significant opportunities to benefit from AI integration in material science. A full convergence of AI and material science promises to revolutionize our understanding and utilization of materials. As we move forward, the insights and methodologies presented in this work can serve as basic pillars, guiding future endeavors to navigate and surmount the barriers in this interdisciplinary domain. The journey ahead, though challenging, may lead to significant acceleration in material discoveries and advancements.

BIBLIOGRAPHY

- [1] C Ovalle Rodas, Fahmi Zaïri, Moussa Naït-Abdelaziz, and Pierre Charrier. Temperature and filler effects on the relaxed response of filled rubbers: Experimental observations on a carbon-filled sbr and constitutive modeling. *International Journal of Solids and Structures*, 58:309–321, 2015.
- [2] Roozbeh Dargazany, Vu Ngoc Khiêm, Uwe Navrath, and Mikhail Itskov. Network evolution model of anisotropic stress softening in filled rubber-like materials: Parameter identification and finite element implementation. *Journal of Mechanics of Materials and Structures*, 7(8):861–885, 2013.
- [3] Gabriel R Schleder, Antonio CM Padilha, Carlos Mera Acosta, Marcio Costa, and Adalberto Fazzio. From dft to machine learning: recent approaches to materials science—a review. *Journal of Physics: Materials*, 2(3):032001, 2019.
- [4] Maziar Raissi, Paris Perdikaris, and George E Karniadakis. Physics-informed neural networks: A deep learning framework for solving forward and inverse problems involving nonlinear partial differential equations. *Journal of Computational Physics*, 378:686–707, 2019.
- [5] Abhishek Panigrahi, Abhishek Shetty, and Navin Goyal. Effect of activation functions on the training of overparametrized neural nets. *arXiv preprint arXiv:1908.05660*, 2019.
- [6] Kurt Hornik, Maxwell Stinchcombe, and Halbert White. Multilayer feedforward networks are universal approximators. *Neural networks*, 2(5):359–366, 1989.
- [7] Visar Farhangi, Moses Karakouzian, and Marten Geertsema. Effect of micropiles on clean sand liquefaction risk based on cpt and spt. *Applied Sciences*, 10(9):3111, 2020.
- [8] Visar Farhangi and Moses Karakouzian. Effect of fiber reinforced polymer tubes filled with recycled materials and concrete on structural capacity of pile foundations. *Applied Sciences*, 10(5):1554, 2020.
- [9] Alborz Izadi and Rebecca J Anthony. A plasma-based gas-phase method for synthesis of gold nanoparticles. *Plasma Processes and Polymers*, 16(7):e1800212, 2019.
- [10] Mayank Sinha, Alborz Izadi, Rebecca Anthony, and Sara Roccabianca. A novel approach to finding mechanical properties of nanocrystal layers. *Nanoscale*, 11(15):7520–7526, 2019.
- [11] Alborz Izadi, Branton Toback, Mayank Sinha, Andrew Millar, Michael Bigelow, Sara Roccabianca, and Rebecca Anthony. Mechanical and optical properties of stretchable silicon nanocrystal/polydimethylsiloxane nanocomposites. *physica status solidi (a)*, 217(17):2000015, 2020.
- [12] Gilles Marckmann and Erwan Verron. Comparison of hyperelastic models for rubber-like materials. *Rubber chemistry and technology*, 79(5):835–858, 2006.

- [13] Paul Steinmann, Mokarram Hossain, and Gunnar Possart. Hyperelastic models for rubber-like materials: consistent tangent operators and suitability for treloar’s data. *Archive of Applied Mechanics*, 82(9):1183–1217, 2012.
- [14] Mohammad Shojaeifard, Sara Sheikhi, Majid Baniassadi, and Mostafa Baghani. On finite bending of visco-hyperelastic materials: A novel analytical solution and fem. *Acta Mechanica*, 231(8):3435–3450, 2020.
- [15] Mohammad Shojaeifard, Mostafa Baghani, and Hamid Shahsavari. Rutting investigation of asphalt pavement subjected to moving cyclic loads: an implicit viscoelastic–viscoplastic–viscodamage fe framework. *International Journal of Pavement Engineering*, 21(11):1393–1407, 2020.
- [16] Wing Kam Liu, George Karniakis, Shaoqiang Tang, and Julien Yvonnet. A computational mechanics special issue on: data-driven modeling and simulation—theory, methods, and applications, 2019.
- [17] Francisco J Montáns, Francisco Chinesta, Rafael Gómez-Bombarelli, and J Nathan Kutz. Data-driven modeling and learning in science and engineering. *Comptes Rendus Mécanique*, 347(11):845–855, 2019.
- [18] Xiaoxin Lu, Dimitris G Giovanis, Julien Yvonnet, Vissarion Papadopoulos, Fabrice Detrez, and Jinbo Bai. A data-driven computational homogenization method based on neural networks for the nonlinear anisotropic electrical response of graphene/polymer nanocomposites. *Computational Mechanics*, 64(2):307–321, 2019.
- [19] Guorong Chen, Tiange Li, Qijun Chen, Shaofei Ren, Chao Wang, and Shaofan Li. Application of deep learning neural network to identify collision load conditions based on permanent plastic deformation of shell structures. *Computational Mechanics*, 64(2):435–449, 2019.
- [20] Amin Vahidi-Moghaddam, Majid Mazouchi, and Hamidreza Modares. Memory-augmented system identification with finite-time convergence. *IEEE Control Systems Letters*, 5(2):571–576, 2020.
- [21] Aidin Tamhidi, Nicolas Kuehn, S Farid Ghahari, Ertugrul Taciroglu, and Yousef Bozorgnia. Conditioned simulation of ground motion time series using gaussian process regression. 2020.
- [22] Frederic E Bock, Roland C Aydin, Christian Johannes Cyron, Norbert Huber, Surya R Kalidindi, and Benjamin Klusemann. A review of the application of machine learning and data mining approaches in continuum materials mechanics. *Frontiers in Materials*, 6:110, 2019.
- [23] Trenton Kirchdoerfer and Michael Ortiz. Data-driven computational mechanics. *Computer Methods in Applied Mechanics and Engineering*, 304:81–101, 2016.
- [24] Lu Trong Khiem Nguyen and Marc-André Keip. A data-driven approach to nonlinear elasticity. *Computers & Structures*, 194:97–115, 2018.

- [25] Adrien Leygue, Michel Coret, Julien Réthoré, Laurent Stainier, and Erwan Verron. Data-based derivation of material response. *Computer Methods in Applied Mechanics and Engineering*, 331:184–196, 2018.
- [26] Laurent Stainier, Adrien Leygue, and Michael Ortiz. Model-free data-driven methods in mechanics: material data identification and solvers. *Computational Mechanics*, 64(2):381–393, 2019.
- [27] Yoshihiro Kanno. Mixed-integer programming formulation of a data-driven solver in computational elasticity. *Optimization Letters*, 13(7):1505–1514, 2019.
- [28] Piotr Breitkopf and Rajan Filomeno Coelho. *Multidisciplinary design optimization in computational mechanics*. John Wiley & Sons, 2013.
- [29] Víctor Jesús Amores, José María Benítez, and Francisco Javier Montáns. Average-chain behavior of isotropic incompressible polymers obtained from macroscopic experimental data. a simple structure-based wpiwyg model in julia language. *Advances in Engineering Software*, 130:41–57, 2019.
- [30] Rubén Ibanez, Emmanuelle Abisset-Chavanne, Jose Vicente Aguado, David Gonzalez, Elias Cueto, and Francisco Chinesta. A manifold learning approach to data-driven computational elasticity and inelasticity. *Archives of Computational Methods in Engineering*, 25(1):47–57, 2018.
- [31] Ruben Ibañez, Domenico Borzacchiello, Jose Vicente Aguado, Emmanuelle Abisset-Chavanne, Elías Cueto, Pierre Ladevèze, and Francisco Chinesta. Data-driven non-linear elasticity: constitutive manifold construction and problem discretization. *Computational Mechanics*, 60(5):813–826, 2017.
- [32] Víctor Jesús Amores, José María Benítez, and Francisco Javier Montáns. Data-driven, structure-based hyperelastic manifolds: A macro-micro-macro approach to reverse-engineer the chain behavior and perform efficient simulations of polymers. *Computers & Structures*, 231:106209, 2020.
- [33] Rubén Ibáñez, Emmanuelle Abisset-Chavanne, David González, Jean-Louis Duval, Elias Cueto, and Francisco Chinesta. Hybrid constitutive modeling: data-driven learning of corrections to plasticity models. *International Journal of Material Forming*, 12(4):717–725, 2019.
- [34] Marcos Latorre and Francisco J Montáns. Wpiwyg hyperelasticity without inversion formula: Application to passive ventricular myocardium. *Computers & Structures*, 185:47–58, 2017.
- [35] Mar Miñano and Francisco J Montáns. Wpiwyg damage mechanics for soft materials: a data-driven approach. *Archives of Computational Methods in Engineering*, 25(1):165–193, 2018.

- [36] Satyaki Bhattacharjee and Karel Matouš. A nonlinear manifold-based reduced order model for multiscale analysis of heterogeneous hyperelastic materials. *Journal of Computational Physics*, 313:635–653, 2016.
- [37] Felix Fritzen and Oliver Kunc. Two-stage data-driven homogenization for nonlinear solids using a reduced order model. *European Journal of Mechanics-A/Solids*, 69:201–220, 2018.
- [38] Denise Reimann, Kapil Chandra, Napat Vajragupta, Tobias Glasmachers, Philipp Junker, Alexander Hartmaier, et al. Modeling macroscopic material behavior with machine learning algorithms trained by micromechanical simulations. *Frontiers in Materials*, 6:181, 2019.
- [39] Kun Wang, WaiChing Sun, and Qiang Du. A cooperative game for automated learning of elasto-plasticity knowledge graphs and models with ai-guided experimentation. *Computational Mechanics*, 64(2):467–499, 2019.
- [40] Marcus Stoffel, Franz Bamer, and Bernd Markert. Neural network based constitutive modeling of nonlinear viscoplastic structural response. *Mechanics Research Communications*, 95:85–88, 2019.
- [41] Ivan Kopal, Ivan Labaj, Marta Harničárová, Jan Valíček, and Dušan Hrubý. Prediction of the tensile response of carbon black filled rubber blends by artificial neural network. *Polymers*, 10(6):644, 2018.
- [42] C Zopf and M Kaliske. Numerical characterisation of uncured elastomers by a neural network based approach. *Computers & Structures*, 182:504–525, 2017.
- [43] Ehsan Haghighat, Maziar Raissi, Adrian Moure, Hector Gomez, and Ruben Juanes. A deep learning framework for solution and discovery in solid mechanics: linear elasticity. *arXiv preprint arXiv:2003.02751*, 2020.
- [44] Kailai Xu, Alexandre M Tartakovsky, Jeff Burghardt, and Eric Darve. Inverse modeling of viscoelasticity materials using physics constrained learning. *arXiv preprint arXiv:2005.04384*, 2020.
- [45] Aref Ghaderi, Vahid Morovati, and Roozbeh Dargazany. A bayesian surrogate constitutive model to estimate failure probability of rubber-like materials. *arXiv preprint arXiv:2010.13241*, 2020.
- [46] Pouria Tooranjipour, Ramin Vatankhah, and Mohammad Mehdi Arefi. Prescribed performance adaptive fuzzy dynamic surface control of nonaffine time-varying delayed systems with unknown control directions and dead-zone input. *International Journal of Adaptive Control and Signal Processing*, 33(7):1134–1156, 2019.
- [47] Sungmoon Jung and Jamshid Ghaboussi. Neural network constitutive model for rate-dependent materials. *Computers & Structures*, 84(15-16):955–963, 2006.
- [48] Leonard Mullins. Softening of rubber by deformation. *Rubber chemistry and technology*, 42(1):339–362, 1969.

- [49] Amir Bahrololoumi, Vahid Morovati, Emad A Poshtan, and Roozbeh Dargazany. A multi-physics constitutive model to predict quasi-static behaviour: Hydrolytic aging in thin cross-linked polymers. *International Journal of Plasticity*, page 102676, 2020.
- [50] F Bueche. Molecular basis for the mullins effect. *Journal of Applied Polymer Science*, 4(10):107–114, 1960.
- [51] David E Hanson, Marilyn Hawley, Robert Houlton, Kiran Chitanvis, Philip Rae, E Bruce Orler, and Debra A Wroblewski. Stress softening experiments in silica-filled polydimethylsiloxane provide insight into a mechanism for the mullins effect. *Polymer*, 46(24):10989–10995, 2005.
- [52] Rubber Houwink. Slipping of molecules during the deformation of reinforced rubber. *Rubber Chemistry and Technology*, 29(3):888–893, 1956.
- [53] G Kraus, CW Childers, and KW Rollmann. Stress softening in carbon black-reinforced vulcanizates. strain rate and temperature effects. *Journal of Applied Polymer Science*, 10(2):229–244, 1966.
- [54] Marie Dalémat, Michel Coret, Adrien Leygue, and Erwan Verron. Measuring stress field without constitutive equation. *Mechanics of Materials*, 136:103087, 2019.
- [55] Clifford Truesdell. *The Elements of Continuum Mechanics: Lectures given in August-September 1965 for the Department of Mechanical and Aerospace Engineering Syracuse University Syracuse, New York*. Springer Science & Business Media, 2012.
- [56] Gerhard A Holzapfel, Thomas C Gasser, and Ray W Ogden. A new constitutive framework for arterial wall mechanics and a comparative study of material models. *Journal of elasticity and the physical science of solids*, 61(1-3):1–48, 2000.
- [57] Stefan Hartmann and Patrizio Neff. Polyconvexity of generalized polynomial-type hyperelastic strain energy functions for near-incompressibility. *International journal of solids and structures*, 40(11):2767–2791, 2003.
- [58] P Bažant and BH Oh. Efficient numerical integration on the surface of a sphere. *ZAMM-Journal of Applied Mathematics and Mechanics/Zeitschrift für Angewandte Mathematik und Mechanik*, 66(1):37–49, 1986.
- [59] Roozbeh Dargazany, Vu Ngoc Khiem, and Mikhail Itskov. A generalized network decomposition model for the quasi-static inelastic behavior of filled elastomers. *International Journal of Plasticity*, 63:94–109, 2014.
- [60] Julie Lambert-Diani and Christian Rey. New phenomenological behavior laws for rubbers and thermoplastic elastomers. *European Journal of Mechanics-A/Solids*, 18(6):1027–1043, 1999.
- [61] WV Mars and A Fatemi. Observations of the constitutive response and characterization of filled natural rubber under monotonic and cyclic multiaxial stress states. *J. Eng. Mater. Technol.*, 126(1):19–28, 2004.

- [62] Leslie Ronald George Treloar. *The physics of rubber elasticity*. Oxford University Press, USA, 1975.
- [63] P Heuillet and L Dugautier. Modélisation of the hyperélastic behavior of rubbers and thermoplastic, compact or cellular. *Mechanical Engineering of Rubbers and Thermoplastic Elastomers*, 1997.
- [64] Thanh-Tam Mai, Yoshihiro Morishita, and Kenji Urayama. Novel features of the mullins effect in filled elastomers revealed by stretching measurements in various geometries. *Soft matter*, 13(10):1966–1977, 2017.
- [65] C Miehe, Serdar Göktepe, and F Lulei. A micro-macro approach to rubber-like materials—part i: the non-affine micro-sphere model of rubber elasticity. *Journal of the Mechanics and Physics of Solids*, 52(11):2617–2660, 2004.
- [66] Vu Ngoc Khiêm and Mikhail Itskov. Analytical network-averaging of the tube model:: Rubber elasticity. *Journal of the Mechanics and Physics of Solids*, 95:254–269, 2016.
- [67] Ellen M Arruda and Mary C Boyce. A three-dimensional constitutive model for the large stretch behavior of rubber elastic materials. 1993.
- [68] Mikhail Itskov and Anna Knyazeva. A rubber elasticity and softening model based on chain length statistics. *International Journal of Solids and Structures*, 80:512–519, 2016.
- [69] Danming Zhong, Yuhai Xiang, Tenghao Yin, Honghui Yu, Shaoxing Qu, and Wei Yang. A physically-based damage model for soft elastomeric materials with anisotropic mullins effect. *International Journal of Solids and Structures*, 176:121–134, 2019.
- [70] Julie Diani, Mathias Brieu, and JM Vacherand. A damage directional constitutive model for mullins effect with permanent set and induced anisotropy. *European Journal of Mechanics-A/Solids*, 25(3):483–496, 2006.
- [71] Georges Ayoub, Fahmi Zaïri, Moussa Naït-Abdelaziz, Jean Michel Gloaguen, and G Kridli. A visco-hyperelastic damage model for cyclic stress-softening, hysteresis and permanent set in rubber using the network alteration theory. *International Journal of Plasticity*, 54:19–33, 2014.
- [72] Qiang Guo, Fahmi Zaïri, and Xinglin Guo. A thermo-viscoelastic-damage constitutive model for cyclically loaded rubbers. part ii: Experimental studies and parameter identification. *International Journal of Plasticity*, 101:58–73, 2018.
- [73] Revision Issued Annually. Astm standards. 1995.
- [74] Michael Kaliske and H Rothert. Formulation and implementation of three-dimensional viscoelasticity at small and finite strains. *Computational Mechanics*, 19(3):228–239, 1997.
- [75] Shan Tang, Ying Li, Hai Qiu, Hang Yang, Sourav Saha, Satyajit Mojumder, Wing Kam Liu, and Xu Guo. Map123-ep: A mechanistic-based data-driven approach for numerical elastoplastic analysis. *Computer Methods in Applied Mechanics and Engineering*, 364:112955, 2020.

- [76] Xin Liu, Su Tian, Fei Tao, and Wenbin Yu. A review of artificial neural networks in the constitutive modeling of composite materials. *Composites Part B: Engineering*, 224:109152, 2021.
- [77] Jingda Tang, Xing Chen, Yongmao Pei, and Daining Fang. Pseudoelasticity and nonideal mullins effect of nanocomposite hydrogels. *Journal of Applied Mechanics*, 83(11), 2016.
- [78] Aref Ghaderi, Vahid Morovati, and Roozbeh Dargazany. A physics-informed assembly of feed-forward neural network engines to predict inelasticity in cross-linked polymers. *Polymers*, 12(11):2628, 2020.
- [79] Xavier Glorot and Yoshua Bengio. Understanding the difficulty of training deep feedforward neural networks. In *Proceedings of the thirteenth international conference on artificial intelligence and statistics*, pages 249–256. JMLR Workshop and Conference Proceedings, 2010.
- [80] Kaiming He, Xiangyu Zhang, Shaoqing Ren, and Jian Sun. Delving deep into rectifiers: Surpassing human-level performance on imagenet classification. In *Proceedings of the IEEE international conference on computer vision*, pages 1026–1034, 2015.
- [81] Elias Wang, Atli Kosson, and Tong Mu. Deep action conditional neural network for frame prediction in atari games. Technical report, Technical Report, Stanford University, 2017.
- [82] Yani Ioannou, Duncan Robertson, Darko Zikic, Peter Kotschieder, Jamie Shotton, Matthew Brown, and Antonio Criminisi. Decision forests, convolutional networks and the models in-between. *arXiv preprint arXiv:1603.01250*, 2016.
- [83] AE Ehret, M Itskov, and H Schmid. Numerical integration on the sphere and its effect on the material symmetry of constitutive equations—a comparative study. *International journal for numerical methods in engineering*, 81(2):189–206, 2010.
- [84] AFMS Amin, A Lion, S Sekita, and Y Okui. Nonlinear dependence of viscosity in modeling the rate-dependent response of natural and high damping rubbers in compression and shear: Experimental identification and numerical verification. *International Journal of Plasticity*, 22(9):1610–1657, 2006.
- [85] Alexander Lion. A constitutive model for carbon black filled rubber: experimental investigations and mathematical representation. *Continuum Mechanics and Thermodynamics*, 8(3):153–169, 1996.
- [86] CM Roland, JN Twigg, Y Vu, and PH Mott. High strain rate mechanical behavior of polyurea. *Polymer*, 48(2):574–578, 2007.
- [87] Xintao Fu, Zepeng Wang, Lianxiang Ma, Zhaoxuan Zou, Qingling Zhang, and Yuxin Guan. Temperature-dependence of rubber hyperelasticity based on the eight-chain model. *Polymers*, 12(4):932, 2020.
- [88] J Diani and Patrick Le Tallec. A fully equilibrated microsphere model with damage for rubberlike materials. *Journal of the Mechanics and Physics of Solids*, 124:702–713, 2019.

- [89] Koichi Mayumi, Alba Marcellan, Guylaine Ducouret, Costantino Creton, and Tetsuharu Narita. Stress–strain relationship of highly stretchable dual cross-link gels: separability of strain and time effect. *ACS Macro Letters*, 2(12):1065–1068, 2013.
- [90] Mincong Liu, Jingyi Guo, Chung-Yuen Hui, Costantino Creton, Tetsuhara Narita, and Alan Zehnder. Time-temperature equivalence in a pva dual cross-link self-healing hydrogel. *Journal of Rheology*, 62(4):991–1000, 2018.
- [91] Yuhai Xiang, Danming Zhong, Peng Wang, Tenghao Yin, Haofei Zhou, Honghui Yu, Chinmay Baliga, Shaoxing Qu, and Wei Yang. A physically based visco-hyperelastic constitutive model for soft materials. *Journal of the Mechanics and Physics of Solids*, 128:208–218, 2019.
- [92] Roozbeh Dargazany and Mikhail Itskov. A network evolution model for the anisotropic mullins effect in carbon black filled rubbers. *International Journal of Solids and Structures*, 46(16):2967–2977, 2009.
- [93] Amir Bahrololoumi, Aref Ghaderi, Mamoon Shaafaey, and Roozbeh Dargazany. A micro-mechanical constitutive model to predict hygrothermal aging of cross-linked polymers. In *ASME International Mechanical Engineering Congress and Exposition*, volume 85680, page V012T12A039. American Society of Mechanical Engineers, 2021.
- [94] Mat Celina, Kenneth T Gillen, and RA Assink. Accelerated aging and lifetime prediction: Review of non-arrhenius behaviour due to two competing processes. *Polymer Degradation and stability*, 90(3):395–404, 2005.
- [95] M Nait Abdelaziz, Georges Ayoub, Xavier Colin, M Benhassine, and M Mouwakeh. New developments in fracture of rubbers: Predictive tools and influence of thermal aging. *International Journal of Solids and Structures*, 165:127–136, 2019.
- [96] Tesfaldet Mengistu and Richard J Pazur. The thermal oxidation of hydrogenated acrylonitrile-co-butadiene rubber from ambient to 150° c. *Polymer Degradation and Stability*, 188:109574, 2021.
- [97] Richard J Pazur and Ivan Petrov. The thermo-oxidation of isoprene containing copolymers of isobutylene: Activation energies and reactions from room temperature to 100° c. *Polymer Degradation and Stability*, 113:55–65, 2015.
- [98] Hamid Mohammadi and Roozbeh Dargazany. A micro-mechanical approach to model thermal induced aging in elastomers. *International Journal of Plasticity*, 118:1–16, 2019.
- [99] Hamid Mohammadi, Vahid Morovati, Emad Poshtan, and Roozbeh Dargazany. Understanding decay functions and their contribution in modeling of thermal-induced aging of cross-linked polymers. *Polymer Degradation and Stability*, page 109108, 2020.
- [100] Mamoon Shaafaey, Amir Bahrololoumi, Hamid Mohammadi, Sharif Alazhary, and Roozbeh Dargazany. Investigation of hygrothermal aging on the polyurethane-based (pub) adhesive: substantiating competition scenario between sub-aging thermo-oxidation and hydrolytic phenomena. *Journal of Polymer Research*, 28(12):1–25, 2021.

- [101] Amir Bahrololoumi, Vahid Morovati, Mamoon Shaafaey, and Roozbeh Dargazany. A multi-physics approach on modeling of hygrothermal aging and its effects on constitutive behavior of cross-linked polymers. *Journal of the Mechanics and Physics of Solids*, 156:104614, 2021.
- [102] A Lion and M Jöhrlitz. On the representation of chemical ageing of rubber in continuum mechanics. *International Journal of Solids and Structures*, 49(10):1227–1240, 2012.
- [103] Kenneth T Gillen, Robert Bernstein, and Mathew Celina. Non-arrhenius behavior for oxidative degradation of chlorosulfonated polyethylene materials. *Polymer degradation and stability*, 87(2):335–346, 2005.
- [104] Mathew C Celina. Review of polymer oxidation and its relationship with materials performance and lifetime prediction. *Polymer Degradation and Stability*, 98(12):2419–2429, 2013.
- [105] L Steinke, U Veltin, M Flamm, A Lion, and M Celina. Numerical analysis of the heterogeneous ageing of rubber products. *Constitutive Models for Rubber*, 7:155–160, 2011.
- [106] M Celina, J Wise, DK Ottesen, KT Gillen, and RL Clough. Oxidation profiles of thermally aged nitrile rubber. *Polymer degradation and stability*, 60(2-3):493–504, 1998.
- [107] John A Shaw, Alan S Jones, and Alan S Wineman. Chemorheological response of elastomers at elevated temperatures: experiments and simulations. *Journal of the Mechanics and Physics of Solids*, 53(12):2758–2793, 2005.
- [108] Bertrand Huneau, Jean-Benoît Le Cam, Yann Marco, and Erwan Verron. *Constitutive Models for Rubber XI: Proceedings of the 11th European Conference on Constitutive Models for Rubber (ECCMR 2019), June 25-27, 2019, Nantes, France*. CRC Press, 2019.
- [109] Man Zhang, Baozhong Sun, and Bohong Gu. Meso-structure ageing mechanism of 3-d braided composite’s compressive behaviors under accelerated thermo-oxidative ageing environment. *Mechanics of Materials*, 115:47–63, 2017.
- [110] Man Zhang, Baozhong Sun, and Bohong Gu. Experimental and numerical analyses of matrix shrinkage and compressive behavior of 3-d braided composite under thermo-oxidative ageing conditions. *Composite Structures*, 204:320–332, 2018.
- [111] Jiri Duchoslav, Christoph Unterweger, Roland Steinberger, Christian Fürst, and David Stifter. Investigation on the thermo-oxidative stability of carbon fiber sizings for application in thermoplastic composites. *Polymer Degradation and Stability*, 125:33–42, 2016.
- [112] C Slater, C Davis, and M Strangwood. Compression set of thermoplastic polyurethane under different thermal–mechanical–moisture conditions. *Polymer degradation and stability*, 96(12):2139–2144, 2011.
- [113] DF Farrar and RK Gillson. Hydrolytic degradation of polyglyconate b: the relationship between degradation time, strength and molecular weight. *Biomaterials*, 23(18):3905–3912, 2002.

- [114] AC Vieira, JC Vieira, JM Ferra, FD Magalhães, RM Guedes, and AT Marques. Mechanical study of pla–pcl fibers during in vitro degradation. *Journal of the mechanical behavior of biomedical materials*, 4(3):451–460, 2011.
- [115] Jalal El Yagoubi, Gilles Lubineau, Abderrazak Traidia, and Jacques Verdu. Monitoring and simulations of hydrolysis in epoxy matrix composites during hygrothermal aging. *Composites Part A: Applied Science and Manufacturing*, 68:184–192, 2015.
- [116] Daniel Pieniak, Krzysztof Przystupa, Agata Walczak, Agata M Niewczas, Aneta Krzyzak, Grzegorz Bartnik, Leszek Gil, and Paweł Lonkwc. Hydro-thermal fatigue of polymer matrix composite biomaterials. *Materials*, 12(22):3650, 2019.
- [117] Mitchell F Shockley and Anastasia H Muliana. Modeling temporal and spatial changes during hydrolytic degradation and erosion in biodegradable polymers. *Polymer Degradation and Stability*, 180:109298, 2020.
- [118] Xian Jun Loh, Suat Hong Goh, and Jun Li. Hydrolytic degradation and protein release studies of thermogelling polyurethane copolymers consisting of poly [(r)-3-hydroxybutyrate], poly (ethylene glycol), and poly (propylene glycol). *Biomaterials*, 28(28):4113–4123, 2007.
- [119] Michael Johlitz, Nico Diercks, and Alexander Lion. Thermo-oxidative ageing of elastomers: A modelling approach based on a finite strain theory. *International Journal of Plasticity*, 63:138–151, 2014.
- [120] Hyoung J Choi, Chul A Kim, Jeong-In Sohn, and Myung S Jhon. An exponential decay function for polymer degradation in turbulent drag reduction. *Polymer degradation and stability*, 69(3):341–346, 2000.
- [121] RW Hutson and CH Dowding. Joint asperity degradation during cyclic shear. In *International Journal of Rock Mechanics and Mining Sciences & Geomechanics Abstracts*, volume 27, pages 109–119. Elsevier, 1990.
- [122] Matthieu Bizeul, Christophe Bouvet, Jean-Jacques Barrau, and Rémy Cuenca. Influence of woven ply degradation on fatigue crack growth in thin notched composites under tensile loading. *International Journal of Fatigue*, 32(1):60–65, 2010.
- [123] T Ha-Anh and Toan Vu-Khanh. Prediction of mechanical properties of polychloroprene during thermo-oxidative aging. *Polymer testing*, 24(6):775–780, 2005.
- [124] Michael Johlitz. On the representation of ageing phenomena. *The Journal of Adhesion*, 88(7):620–648, 2012.
- [125] Hamid Mohammadi, Vahid Morovati, Abd-Elrahman Korayem, Emad Poshtan, and Roozbeh Dargazany. Constitutive modeling of elastomers during photo-and thermo-oxidative aging. *Polymer Degradation and Stability*, 191:109663, 2021.
- [126] Benedikt Dippel, Michael Johlitz, and Alexander Lion. Ageing of polymer bonds: a coupled chemomechanical modelling approach. *Continuum Mechanics and Thermodynamics*, 26(3):247–257, 2014.

- [127] Andre C Vieira, Rui M Guedes, and Volnei Tita. Damage-induced hydrolyses modelling of biodegradable polymers for tendons and ligaments repair. *Journal of biomechanics*, 48(12):3478–3485, 2015.
- [128] C Vieira, Rui M Guedes, and Volnei Tita. Constitutive modeling of biodegradable polymers: Hydrolytic degradation and time-dependent behavior. *International Journal of Solids and Structures*, 51(5):1164–1174, 2014.
- [129] Quentin Breche, Gregory Chagnon, Guilherme Machado, Benjamin Nottelet, Xavier Garric, Edouard Girard, and Denis Favier. A non-linear viscoelastic model to describe the mechanical behavior’s evolution of biodegradable polymers during hydrolytic degradation. *Polymer degradation and stability*, 131:145–156, 2016.
- [130] Julie Diani, Bruno Fayolle, and Pierre Gilormini. A review on the mullins effect. *European Polymer Journal*, 45(3):601–612, 2009.
- [131] Haixiao Wan, Ke Gao, Sai Li, Liquan Zhang, Xiaohui Wu, Xiaodong Wang, and Jun Liu. Chemical bond scission and physical slippage in the mullins effect and fatigue behavior of elastomers. *Macromolecules*, 52(11):4209–4221, 2019.
- [132] Bruno Musil, Michael Johlitz, and Alexander Lion. On the ageing behaviour of nbr: chemo-mechanical experiments, modelling and simulation of tension set. *Continuum Mechanics and Thermodynamics*, pages 1–17, 2018.
- [133] Mariacristina Gagliardi, Pietro Lenarda, and Marco Paggi. A reaction-diffusion formulation to simulate eva polymer degradation in environmental and accelerated ageing conditions. *Solar Energy Materials and Solar Cells*, 164:93–106, 2017.
- [134] Pellegrino Musto, Giuseppe Ragosta, Mario Abbate, and Gennaro Scarinzi. Photo-oxidation of high performance epoxy networks: correlation between the molecular mechanisms of degradation and the viscoelastic and mechanical response. *Macromolecules*, 41(15):5729–5743, 2008.
- [135] Yoichi Kodaera and Benjamin J McCoy. Distribution kinetics of radical mechanisms: reversible polymer decomposition. *AIChE journal*, 43(12):3205–3214, 1997.
- [136] Gottfried W Ehrenstein and Sonja Pongratz. *Beständigkeit von Kunststoffen*. Hanser München, 2007.
- [137] Jacques Verdu. *Oxydative ageing of polymers*. John Wiley & Sons, 2012.
- [138] Aref Ghaderi, Vahid Morovati, Amir Bahrololoumi, and Roozbeh Dargazany. A physics-informed neural network constitutive model for cross-linked polymers. In *ASME International Mechanical Engineering Congress and Exposition*, volume 84607, page V012T12A007. American Society of Mechanical Engineers, 2020.
- [139] Hüsniü Dal, Osman Gültekin, and Kemal Açıkgöz. An extended eight-chain model for hyperelastic and finite viscoelastic response of rubberlike materials: Theory, experiments and numerical aspects. *Journal of the Mechanics and Physics of Solids*, 145:104159, 2020.

- [140] P-Y Le Gac, Peter Davies, and Dominique Choqueuse. Evaluation of long term behaviour of polymers for offshore oil and gas applications. *Oil & Gas Science and Technology—Revue d'IFP Energies nouvelles*, 70(2):279–289, 2015.
- [141] A Stevenson. On the durability of rubber/metal bonds in seawater. *International Journal of Adhesion and adhesives*, 5(2):81–91, 1985.
- [142] WV Mars and A Fatemi. A phenomenological model for the effect of r ratio on fatigue of strain crystallizing rubbers. *Rubber chemistry and technology*, 76(5):1241–1258, 2003.
- [143] K Karapiperis, L Stainier, M Ortiz, and JE Andrade. Data-driven multiscale modeling in mechanics. *Journal of the Mechanics and Physics of Solids*, 147:104239, 2021.
- [144] Ari Frankel, Craig M Hamel, Dan Bolintineanu, Kevin Long, and Sharlotte Kramer. Machine learning constitutive models of elastomeric foams. *Computer Methods in Applied Mechanics and Engineering*, 391:114492, 2022.
- [145] Hüsni Dal, Kemal Açıkgoz, and Yashar Badienia. On the performance of isotropic hyperelastic constitutive models for rubber-like materials: A state of the art review. *Applied Mechanics Reviews*, 73(2):020802, 2021.
- [146] Ehsan Allahyari and Masoud Asgari. Fiber reinforcement characteristics of anisotropic dielectric elastomers: A constitutive modeling development. *Mechanics of Advanced Materials and Structures*, pages 1–15, 2021.
- [147] Réda Kadri, M Nait Abdelaziz, Bruno Fayolle, M Ben Hassine, and Jean-François Witz. A unified mechanical based approach to fracture properties estimates of rubbers subjected to aging. *International Journal of Solids and Structures*, 234:111305, 2022.
- [148] KY Volokh. Hyperelasticity with softening for modeling materials failure. *Journal of the Mechanics and Physics of Solids*, 55(10):2237–2264, 2007.
- [149] Kishore Ginjupalli, Gopal Venkat Shavi, Ranjith Kumar Averineni, Mahalinga Bhat, N Udupa, and P Nagaraja Upadhy. Poly (α -hydroxy acid) based polymers: A review on material and degradation aspects. *Polymer Degradation and Stability*, 144:520–535, 2017.
- [150] Hüsni Dal and Michael Kaliske. A micro-continuum-mechanical material model for failure of rubber-like materials: Application to ageing-induced fracturing. *Journal of the Mechanics and Physics of Solids*, 57(8):1340, August 2009.
- [151] M Naït-Abdelaziz, F Zaïri, Z Qu, A Hamdi, and N Aït Hocine. J integral as a fracture criterion of rubber-like materials using the intrinsic defect concept. *Mechanics of Materials*, 53:80–90, 2012.
- [152] Pooya Behroozinia, Reza Mirzaeifar, and Saied Taheri. A review of fatigue and fracture mechanics with a focus on rubber-based materials. *Proceedings of the Institution of Mechanical Engineers, Part L: Journal of Materials: Design and Applications*, 233(5):1005–1019, 2019.

- [153] Georges Ayoub, Moussa Nait-Abdelaziz, Fahmi Zaïri, Jean-Michel Gloaguen, and P Charrier. A continuum damage model for the high-cycle fatigue life prediction of styrene-butadiene rubber under multiaxial loading. *International Journal of Solids and Structures*, 48(18):2458–2466, 2011.
- [154] Bo Wang, Hongbing Lu, and Gyu-ho Kim. A damage model for the fatigue life of elastomeric materials. *Mechanics of Materials*, 34(8):475–483, 2002.
- [155] Ieuan Collins, Mokarram Hossain, Wulf Dettmer, and Ian Masters. Flexible membrane structures for wave energy harvesting: A review of the developments, materials and computational modelling approaches. *Renewable and Sustainable Energy Reviews*, 151:111478, 2021.
- [156] Chennakesava Kadapa, Zhanfeng Li, Mokarram Hossain, and Jiong Wang. On the advantages of mixed formulation and higher-order elements for computational morphoelasticity. *Journal of the Mechanics and Physics of Solids*, 148:104289, 2021.
- [157] Bruno Musil, Michael Johlitz, and Alexander Lion. On the ageing behaviour of nbr: chemo-mechanical experiments, modelling and simulation of tension set. *Continuum Mechanics and Thermodynamics*, 32(2):369–385, 2020.
- [158] Mariaenrica Frigione and Alvaro Rodríguez-Prieto. Can accelerated aging procedures predict the long term behavior of polymers exposed to different environments? *Polymers*, 13(16):2688, 2021.
- [159] Amina Dinari, Fahmi Zaïri, Makram Chaabane, Jewan Ismail, and Tarek Benameur. Thermo-oxidative stress relaxation in carbon-filled sbr. *Plastics, Rubber and Composites*, pages 1–16, 2021.
- [160] Jason Mulderrig, Bin Li, and Nikolaos Bouklas. Affine and non-affine microsphere models for chain scission in polydisperse elastomer networks. *Mechanics of Materials*, 160:103857, 2021.
- [161] Maha Zaghdoudi, Anja Kömmling, Matthias Jaunich, and Dietmar Wolff. Erroneous or arrhenius: A degradation rate-based model for epdm during homogeneous ageing. *Polymers*, 12(9):2152, 2020.
- [162] Shabnam Konica and Trisha Sain. A reaction-driven evolving network theory coupled with phase-field fracture to model polymer oxidative aging. *Journal of the Mechanics and Physics of Solids*, 150:104347, 2021.
- [163] Kenneth T Gillen and Hisaaki Kudoh. Synergism of radiation and temperature in the degradation of a silicone elastomer. *Polymer Degradation and Stability*, 181:109334, 2020.
- [164] Kenneth T Gillen. Importance of synergism for degradation of elastomers in combined radiation plus temperature environments. *Rubber Chemistry and Technology*, 93(1):121–141, 2020.

- [165] Kenneth T Gillen and Mathew C Celina. Issues with approaches for simulating aging of nuclear power plant cable materials. *Rubber Chemistry and Technology*, 2021.
- [166] Sarah Hettal, Sébastien Roland, Konsta Sipila, Harri Joki, and Xavier Colin. A new analytical model for predicting the radio-thermal oxidation kinetics and the lifetime of electric cable insulation in nuclear power plants. application to silane cross-linked polyethylene. *Polymer Degradation and Stability*, 185:109492, 2021.
- [167] Takato Ishida, Ryoma Kitagaki, Hideaki Hagihara, and Yogarajah Elakneswaran. Challenges in prediction of significant structural changes during photochemical “degelation” of acrylic-urethane network. *Polymer*, 186:122035, 2020.
- [168] T Šarac, N Quiévy, A Gusarov, and MJ Konstantinović. Influence of γ -irradiation and temperature on the mechanical properties of epdm cable insulation. *Radiation Physics and Chemistry*, 125:151–155, 2016.
- [169] Hui Fang, Jianguo Li, Hongbin Chen, Bo Liu, Wei Huang, Yilun Liu, and Tiejun Wang. Radiation induced degradation of silica reinforced silicone foam: Experiments and modeling. *Mechanics of Materials*, 105:148–156, 2017.
- [170] Shunping Yan, Dong Jia, Yong Yu, Luobin Wang, Yong Qiu, and Qiang Wan. Influence of γ -irradiation on mechanical behaviors of poly methyl-vinyl silicone rubber foams at different temperatures. *Mechanics of Materials*, 151:103639, 2020.
- [171] Dong Jia, Shunping Yan, Yunqiang Peng, Liming Wei, Luobin Wang, Yang Gao, Zhiming Hao, Yong Qiu, and Qiang Wan. Constitutive modeling of γ -irradiated silicone rubber foams under compression and shear loading. *Polymer Degradation and Stability*, 183:109410, 2021.
- [172] Rami Bouaziz, Komla Dela Ahose, Stéphane Lejeunes, Dominique Eyheramendy, and Franck Sosson. Characterization and modeling of filled rubber submitted to thermal aging. *International Journal of Solids and Structures*, 169:122–140, 2019.
- [173] Makram Chaabane, Ning Ding, and Fahmi Zaïri. An approach to assess the thermal aging effects on the coupling between inelasticity and network alteration in filled rubbers. *International Journal of Non-Linear Mechanics*, 136:103783, 2021.
- [174] Jannik Voges and Daniel Juhre. A phase field model for thermo-oxidative aging in cracked polymers. *PAMM*, 19(1):e201900384, 2019.
- [175] Roozbeh Dargazany and Weiyi Lu. Building super-dissipativity into hydrogels. *Nature Materials(submitted)*, 2018.
- [176] Aref Ghaderi, Vahid Morovati, Yang Chen, and Roozbeh Dargazany. A physics-informed multi-agents model to predict thermo-oxidative/hydrolytic aging of elastomers. *International Journal of Mechanical Sciences*, page 107236, 2022.
- [177] Vahid Morovati, Amir Bahrololoumi, and Roozbeh Dargazany. Fatigue-induced stress-softening in cross-linked multi-network elastomers: Effect of damage accumulation. *International Journal of Plasticity*, 142:102993, 2021.

- [178] Amir Bahrololoumi, Mamoon Shaafaey, Georges Ayoub, and Roozbeh Dargazany. Thermal aging coupled with cyclic fatigue in cross-linked polymers: Constitutive modeling & fe implementation. *International Journal of Solids and Structures*, page 111800, 2022.
- [179] Georges Ayoub, Moussa Naït-Abdelaziz, Fahmi Zaïri, Jean-Michel Gloaguen, and P Charrier. A continuum damage model for the high-cycle fatigue life prediction of styrene-butadiene rubber under multiaxial loading. *International Journal of Solids and Structures*, 48(18):2458–2466, 2011.
- [180] Maurizio Natali, Ivan Puri, Marco Rallini, Josè Kenny, and Luigi Torre. Ablation modeling of state of the art epdm based elastomeric heat shielding materials for solid rocket motors. *Computational Materials Science*, 111:460–480, 2016.
- [181] D Chronopoulos, M Ichchou, B Troclet, and O Bareille. Thermal effects on the sound transmission through aerospace composite structures. *Aerospace Science and Technology*, 30(1):192–199, 2013.
- [182] Shuheng Liao, Tianju Xue, Jihoon Jeong, Samantha Webster, Kornel Ehmann, and Jian Cao. Hybrid full-field thermal characterization of additive manufacturing processes using physics-informed neural networks with data. *arXiv preprint arXiv:2206.07756*, 2022.
- [183] Yu I Dimitrienko. Thermomechanical behaviour of composite materials and structures under high temperatures: 1. materials. *Composites Part A: Applied Science and Manufacturing*, 28(5):453–461, 1997.
- [184] Colonel Vijay Kumar and Balasubramanian Kandasubramanian. Advances in ablative composites of carbon based materials: A review. *Industrial & Engineering Chemistry Research*, 58(51):22663–22701, 2019.
- [185] Changsong Luo and Paul E DesJardin. Thermo-mechanical damage modeling of a glass–phenolic composite material. *Composites Science and Technology*, 67(7-8):1475–1488, 2007.
- [186] CHANGSONG Luo and J Lua. Thermo-mechanical damage modeling of polymer matrix composite structures in fire. *Fire Safety Science*, 10:1179–1192, 2011.
- [187] J Bo Henderson, J A Wiebelt, and MR Tant. A model for the thermal response of polymer composite materials with experimental verification. *Journal of composite materials*, 19(6):579–595, 1985.
- [188] JB Henderson and TE Wiecek. A mathematical model to predict the thermal response of decomposing, expanding polymer composites. *Journal of composite materials*, 21(4):373–393, 1987.
- [189] John Florio Jr, Jack B Henderson, Frederick L Test, and Ramamurthy Hariharan. A study of the effects of the assumption of local-thermal equilibrium on the overall thermally-induced response of a decomposing, glass-filled polymer composite. *International Journal of Heat and Mass Transfer*, 34(1):135–147, 1991.

- [190] RM Sullivan and NJ Salamon. A finite element method for the thermochemical decomposition of polymeric materials—i. theory. *International Journal of Engineering Science*, 30(4):431–441, 1992.
- [191] Roy Michael Sullivan. *A finite element model for thermochemically decomposing polymers*. The Pennsylvania State University, 1990.
- [192] AP Mouritz, S Feih, E Kandare, Z Mathys, AG Gibson, PE Des Jardin, SW Case, and BY Lattimer. Review of fire structural modelling of polymer composites. *Composites Part A: Applied Science and Manufacturing*, 40(12):1800–1814, 2009.
- [193] Y Carpier, B Vieille, A Coppalle, and Fabrice Barbe. About the tensile mechanical behaviour of carbon fibers fabrics reinforced thermoplastic composites under very high temperature conditions. *Composites Part B: Engineering*, 181:107586, 2020.
- [194] Stefanie Feih and AP Mouritz. Tensile properties of carbon fibres and carbon fibre–polymer composites in fire. *Composites Part A: Applied Science and Manufacturing*, 43(5):765–772, 2012.
- [195] Shengbo Shi, Jun Liang, Guochang Lin, and Guodong Fang. High temperature thermomechanical behavior of silica-phenolic composite exposed to heat flux environments. *Composites science and technology*, 87:204–209, 2013.
- [196] Aishwarya Kulkarni and Harshini Dasari. Current status of methods used in degradation of polymers: a review. In *MATEC Web of Conferences*, volume 144, page 02023. EDP Sciences, 2018.
- [197] Han Li, Nasidan Wang, Xuefei Han, Baoxin Fan, Zhenyu Feng, and Shijun Guo. Simulation of thermal behavior of glass fiber/phenolic composites exposed to heat flux on one side. *Materials*, 13(2):421, 2020.
- [198] CS Vatikiotis and D Salinas. Heat transfer in a fibrous composite with combustion. In *American Society of Mechanical Engineers and American Institute of Chemical Engineers, Joint National Heat Transfer Conference, Orlando, Fla*, page 1980, 1980.
- [199] Craig L Beyler and Marcelo M Hirschler. Thermal decomposition of polymers. *SFPE handbook of fire protection engineering*, 2(7), 2002.
- [200] Andrew Johnston, Pascal Hubert, Göran Fernlund, Reza Vaziri, and Anoush Poursartip. Process modeling of composite structures employing a virtual autoclave concept. *Science and Engineering of Composite Materials*, 5:235–252, 1996.
- [201] Nicolas Boyard. *Heat Transfer in Polymer Composite Materials: Forming Processes*. John Wiley & Sons, 2016.
- [202] Olek C Zienkiewicz, Robert L Taylor, and Jian Z Zhu. *The finite element method: its basis and fundamentals*. Elsevier, 2005.

- [203] Philippe Boisse, Bassem Zouari, and Alain Gasser. A mesoscopic approach for the simulation of woven fibre composite forming. *Composites science and technology*, 65(3-4):429–436, 2005.
- [204] Dmitrii Kochkov, Jamie A Smith, Ayya Alieva, Qing Wang, Michael P Brenner, and Stephan Hoyer. Machine learning–accelerated computational fluid dynamics. *Proceedings of the National Academy of Sciences*, 118(21), 2021.
- [205] Yuehaw Khoo, Jianfeng Lu, and Lexing Ying. Solving parametric pde problems with artificial neural networks. *European Journal of Applied Mathematics*, 32(3):421–435, 2021.
- [206] Leah Bar and Nir Sochen. Unsupervised deep learning algorithm for pde-based forward and inverse problems. *arXiv preprint arXiv:1904.05417*, 2019.
- [207] George Em Karniadakis, Ioannis G Kevrekidis, Lu Lu, Paris Perdikaris, Sifan Wang, and Liu Yang. Physics-informed machine learning. *Nature Reviews Physics*, 3(6):422–440, 2021.
- [208] Wenqian Chen, Qian Wang, Jan S Hesthaven, and Chuhua Zhang. Physics-informed machine learning for reduced-order modeling of nonlinear problems. *Journal of Computational Physics*, 446:110666, 2021.
- [209] Ehsan Haghighat, Maziar Raissi, Adrian Moure, Hector Gomez, and Ruben Juanes. A physics-informed deep learning framework for inversion and surrogate modeling in solid mechanics. *Computer Methods in Applied Mechanics and Engineering*, 379:113741, 2021.
- [210] Kaushik Bhattacharya, Bamdad Hosseini, Nikola B Kovachki, and Andrew M Stuart. Model reduction and neural networks for parametric pdes. *arXiv preprint arXiv:2005.03180*, 2020.
- [211] Apostolos F Psaros, Kenji Kawaguchi, and George Em Karniadakis. Meta-learning pinn loss functions. *arXiv preprint arXiv:2107.05544*, 2021.
- [212] Jan Niklas Fuhg, Christoph Böhm, Nikolaos Bouklas, Amelie Fau, Peter Wriggers, and Michele Marino. Model-data-driven constitutive responses: application to a multiscale computational framework. *International Journal of Engineering Science*, 167:103522, 2021.
- [213] Claresta Dennis and Brian Bojko. On the combustion of heterogeneous ap/htpb composite propellants: A review. *Fuel*, 254:115646, 2019.
- [214] Travis A Bogetti and John W Gillespie Jr. Process-induced stress and deformation in thick-section thermoset composite laminates. *Journal of composite materials*, 26(5):626–660, 1992.
- [215] Pietro Tadini, Nathan Grange, Khaled Chetehouna, Nicolas Gascoin, Samuel Senave, and Isabelle Reynaud. Thermal degradation analysis of innovative pekk-based carbon composites for high-temperature aeronautical components. *Aerospace Science and technology*, 65:106–116, 2017.

- [216] Sina Amini Niaki, Ehsan Haghighat, Trevor Campbell, Anoush Poursartip, and Reza Vaziri. Physics-informed neural network for modelling the thermochemical curing process of composite-tool systems during manufacture. *Computer Methods in Applied Mechanics and Engineering*, 384:113959, 2021.
- [217] AP Mouritz and AG Gibson. Modelling the thermal response of composites in fire. *Fire properties of polymer composite materials*, pages 133–161, 2006.
- [218] AP Mouritz, Z Mathys, and CP Gardiner. Thermomechanical modelling the fire properties of fibre–polymer composites. *Composites Part B: Engineering*, 35(6-8):467–474, 2004.
- [219] AG Gibson, PNH Wright, Y-S Wu, AP Mouritz, Z Mathys, and CP Gardiner. Modelling residual mechanical properties of polymer composites after fire. 32(2):81–90.
- [220] Navid Zobeiry and Keith D Humfeld. A physics-informed machine learning approach for solving heat transfer equation in advanced manufacturing and engineering applications. *Engineering Applications of Artificial Intelligence*, 101:104232, 2021.
- [221] Dmitry Yarotsky. Error bounds for approximations with deep relu networks. *Neural Networks*, 94:103–114, 2017.
- [222] Daniel S Berman, Anna L Buczak, Jeffrey S Chavis, and Cherita L Corbett. A survey of deep learning methods for cyber security. *Information*, 10(4):122, 2019.
- [223] Umair bin Waheed, Ehsan Haghighat, Tariq Alkhalifah, Chao Song, and Qi Hao. Pin-neik: Eikonal solution using physics-informed neural networks. *Computers & Geosciences*, 155:104833, 2021.
- [224] Ehsan Haghighat and Ruben Juanes. Sciann: A keras/tensorflow wrapper for scientific computations and physics-informed deep learning using artificial neural networks. 373:113552.
- [225] Luning Sun, Han Gao, Shaowu Pan, and Jian-Xun Wang. Surrogate modeling for fluid flows based on physics-constrained deep learning without simulation data. *Computer Methods in Applied Mechanics and Engineering*, 361:112732, 2020.
- [226] Ömer Faruk Ertuğrul. A novel type of activation function in artificial neural networks: Trained activation function. *Neural Networks*, 99:148–157, 2018.
- [227] Siddhartha Mishra and Roberto Molinaro. Estimates on the generalization error of physics-informed neural networks for approximating a class of inverse problems for pdes. *IMA Journal of Numerical Analysis*, 2021.
- [228] Aditi Krishnapriyan, Amir Gholami, Shandian Zhe, Robert Kirby, and Michael W Mahoney. Characterizing possible failure modes in physics-informed neural networks. *Advances in Neural Information Processing Systems*, 34, 2021.
- [229] Sifan Wang, Xinling Yu, and Paris Perdikaris. When and why pinns fail to train: A neural tangent kernel perspective. *Journal of Computational Physics*, 449:110768, 2022.

- [230] Jerome Bolte and Edouard Pauwels. A mathematical model for automatic differentiation in machine learning. *Advances in Neural Information Processing Systems*, 33:10809–10819, 2020.
- [231] Rizwan Ul Haq, Syed Saqib Shah, Ebrahim A Algehyne, and Iskander Tlili. Heat transfer analysis of water based swcnts through parallel fins enclosed by square cavity. *International Communications in Heat and Mass Transfer*, 119:104797, 2020.
- [232] Guofei Pang, Lu Lu, and George Em Karniadakis. fpinns: Fractional physics-informed neural networks. *SIAM Journal on Scientific Computing*, 41(4):A2603–A2626, 2019.
- [233] Dougal Maclaurin, David Duvenaud, and Ryan Adams. Gradient-based hyperparameter optimization through reversible learning. In *International conference on machine learning*, pages 2113–2122. PMLR, 2015.
- [234] Qiming Zhu, Zeliang Liu, and Jinhui Yan. Machine learning for metal additive manufacturing: Predicting temperature and melt pool fluid dynamics using physics-informed neural networks. *Computational Mechanics*, 67(2):619–635, 2021.
- [235] Sebastian Bock and Martin Weiß. A proof of local convergence for the adam optimizer. In *2019 International Joint Conference on Neural Networks (IJCNN)*, pages 1–8. IEEE, 2019.
- [236] Quanhui Zhu and Jiang Yang. A local deep learning method for solving high order partial differential equations. *arXiv preprint arXiv:2103.08915*, 2021.
- [237] Tianhe Yu, Saurabh Kumar, Abhishek Gupta, Sergey Levine, Karol Hausman, and Chelsea Finn. Gradient surgery for multi-task learning. *Advances in Neural Information Processing Systems*, 33:5824–5836, 2020.
- [238] Bahador Bahmani and WaiChing Sun. Training multi-objective/multi-task collocation physics-informed neural network with student/teachers transfer learnings. *arXiv preprint arXiv:2107.11496*, 2021.
- [239] R Timothy Marler and Jasbir S Arora. The weighted sum method for multi-objective optimization: new insights. *Structural and multidisciplinary optimization*, 41(6):853–862, 2010.
- [240] Sifan Wang, Yujun Teng, and Paris Perdikaris. Understanding and mitigating gradient pathologies in physics-informed neural networks. *arXiv preprint arXiv:2001.04536*, 2020.
- [241] Kun Xi, Jiang Li, Mengfei Guo, and Yang Liu. Redeposition and densification of pyrolysis products of polymer composites in char layer. *Polymer Degradation and Stability*, 166:238–247, 2019.
- [242] Soren Pirk, Michal Jarzabek, Torsten Hädrich, Dominik L Michels, and Wojciech Palubicki. Interactive wood combustion for botanical tree models. *ACM Transactions on Graphics (TOG)*, 36(6):1–12, 2017.

- [243] DK Shen, MX Fang, ZY Luo, and KF Cen. Modeling pyrolysis of wet wood under external heat flux. *Fire Safety Journal*, 42(3):210–217, 2007.
- [244] Melvin Mooney. A theory of large elastic deformation. *Journal of applied physics*, 11(9):582–592, 1940.
- [245] Raymond William Ogden. Large deformation isotropic elasticity—on the correlation of theory and experiment for incompressible rubberlike solids. *Proceedings of the Royal Society of London. A. Mathematical and Physical Sciences*, 326(1567):565–584, 1972.
- [246] Pejman Honarmandi. *Materials Design Under Bayesian Uncertainty Quantification*. PhD thesis, 2019.
- [247] Lixiong Cao, Jie Liu, Ling Xie, Chao Jiang, and Rengui Bi. Non-probabilistic polygonal convex set model for structural uncertainty quantification. *Applied Mathematical Modelling*, 89:504–518.
- [248] Qiang Yang, Songhe Meng, Hua Jin, Weihua Xie, and Xinghong Zhang. Multi-fidelity uncertainty quantification method with application to nonlinear structural response analysis. *Applied Mathematical Modelling*, 75:853–864, 2019.
- [249] S Pouresmaeeli, SA Fazelzadeh, E Ghavanloo, and P Marzocca. Uncertainty propagation in vibrational characteristics of functionally graded carbon nanotube-reinforced composite shell panels. *International Journal of Mechanical Sciences*, 149:549–558, 2018.
- [250] Roberto Rocchetta, Matteo Broggi, and Edoardo Patelli. Do we have enough data? robust reliability via uncertainty quantification. *Applied Mathematical Modelling*, 54:710–721, 2018.
- [251] AR Ghanipour, E Ghavanloo, SA Fazelzadeh, and S Pouresmaeeli. Uncertainty propagation in the buckling behavior of few-layer graphene sheets. *Microsystem Technologies*, 24(2):1167–1177, 2018.
- [252] RSI Rivlin. Large elastic deformations of isotropic materials. i. fundamental concepts. *Philosophical Transactions of the Royal Society of London. Series A, Mathematical and Physical Sciences*, 240(822):459–490, 1948.
- [253] Sandeep Madireddy, Bhargava Sista, and Kumar Vemaganti. A bayesian approach to selecting hyperelastic constitutive models of soft tissue. *Computer Methods in Applied Mechanics and Engineering*, 291:102–122, 2015.
- [254] Patrick T Brewick and Kirubel Teferra. Uncertainty quantification for constitutive model calibration of brain tissue. *Journal of the mechanical behavior of biomedical materials*, 85:237–255, 2018.
- [255] Danielle Fitt, Hayley Wyatt, Thomas E Woolley, and L Angela Mihai. Uncertainty quantification of elastic material responses: testing, stochastic calibration and bayesian model selection. *Mechanics of Soft Materials*, 1(1):13, 2019.

- [256] Marcin Kamiński and Bernd Lauke. Probabilistic and stochastic aspects of rubber hyperelasticity. *Meccanica*, 53(9):2363–2378, 2018.
- [257] Kirubel Teferra and Patrick T Brewick. A bayesian model calibration framework to evaluate brain tissue characterization experiments. *Computer Methods in Applied Mechanics and Engineering*, 357:112604, 2019.
- [258] L Orta and FM Bartlett. Reliability analysis of concrete deck overlays. *Structural Safety*, 56:30–38, 2015.
- [259] N Dimitrov, RD Bitsche, and JP Blasques. Spatial reliability analysis of a wind turbine blade cross section subjected to multi-axial extreme loading. *Structural Safety*, 66:27–37, 2017.
- [260] Mihir Mishra, Vahid Keshavarzzadeh, and Arash Noshadravan. Reliability-based lifecycle management for corroding pipelines. *Structural safety*, 76:1–14, 2019.
- [261] UA Khashaba, AA Aljinaidi, and MA Hamed. Fatigue and reliability analysis of nano-modified scarf adhesive joints in carbon fiber composites. *Composites Part B: Engineering*, 120:103–117, 2017.
- [262] MM Carroll. A strain energy function for vulcanized rubbers. *Journal of Elasticity*, 103(2):173–187, 2011.
- [263] L Angela Mihai, Thomas E Woolley, and Alain Goriely. Stochastic isotropic hyperelastic materials: constitutive calibration and model selection. *Proceedings of the Royal Society A: Mathematical, Physical and Engineering Sciences*, 474(2211):20170858, 2018.
- [264] George EP Box and George C Tiao. *Bayesian inference in statistical analysis*, volume 40. John Wiley & Sons, 2011.
- [265] Christian Robert. *The Bayesian choice: from decision-theoretic foundations to computational implementation*. Springer Science & Business Media, 2007.
- [266] James O Berger and José M Bernardo. On the development of the reference prior method. *Bayesian statistics*, 4(4):35–60, 1992.
- [267] Edwin T Jaynes. *Probability theory: The logic of science*. Cambridge university press, 2003.
- [268] J-P Vila, Véréne Wagner, and Pascal Neveu. Bayesian nonlinear model selection and neural networks: A conjugate prior approach. *IEEE Transactions on neural networks*, 11(2):265–278, 2000.
- [269] James O Berger, Luis R Pericchi, JK Ghosh, Tapas Samanta, Fulvio De Santis, JO Berger, and LR Pericchi. Objective bayesian methods for model selection: Introduction and comparison. *Lecture Notes-Monograph Series*, pages 135–207, 2001.
- [270] Robert H Berk. Limiting behavior of posterior distributions when the model is incorrect. *The Annals of Mathematical Statistics*, pages 51–58, 1966.

- [271] Michael E Tipping. Sparse bayesian learning and the relevance vector machine. *Journal of machine learning research*, 1(Jun):211–244, 2001.
- [272] Tao Chen and Elaine Martin. Bayesian linear regression and variable selection for spectroscopic calibration. *Analytica chimica acta*, 631(1):13–21, 2009.
- [273] Thomas L Burr. Bayesian inference: Parameter estimation and decisions, 2004.
- [274] Miguel A Bessa, R Bostanabad, Zeliang Liu, A Hu, Daniel W Apley, C Brinson, Wei Chen, and Wing Kam Liu. A framework for data-driven analysis of materials under uncertainty: Countering the curse of dimensionality. *Computer Methods in Applied Mechanics and Engineering*, 320:633–667, 2017.
- [275] Carl Edward Rasmussen. Gaussian processes in machine learning. In *Summer School on Machine Learning*, pages 63–71. Springer, 2003.
- [276] Robert J Adler. *The geometry of random fields*. SIAM, 2010.
- [277] Taeksang Lee, Ilias Bilonis, and Adrian Buganza Tepole. Propagation of uncertainty in the mechanical and biological response of growing tissues using multi-fidelity gaussian process regression. *Computer Methods in Applied Mechanics and Engineering*, 359:112724, 2020.
- [278] DG Lu, PY Song, YF Liu, and XH Yu. An extended first order reliability method based on generalized nataf transformation. *Safety, Reliability, Risk and Life-Cycle Performance of Structures and Infrastructures, Editors George Deodatis, Bruce R. Ellingwood, Dan M. Frangopol, CRC Press*, pages 1177–1184, 2014.
- [279] Régis Lebrun and Anne Dutfoy. Do rosenblatt and nataf isoprobabilistic transformations really differ? *Probabilistic Engineering Mechanics*, 24(4):577–584, 2009.
- [280] Michael Havbro Faber. Basics of structural reliability. *Swiss Federal Institute of Technology ETH, Zürich, Switzerland*, 2009.
- [281] Maurice Lemaire. *Structural reliability*. John Wiley & Sons, 2013.
- [282] TV Santosh, RK Saraf, AK Ghosh, and HS Kushwaha. Optimum step length selection rule in modified hl-rf method for structural reliability. *International Journal of Pressure Vessels and Piping*, 83(10):742–748, 2006.
- [283] SRd Santos, LC Mاتيoli, and AT Beck. New optimization algorithms for structural reliability analysis. *Computer Modeling in Engineering & Sciences(CMES)*, 83(1):23–55, 2012.
- [284] Yuan Xiukai, Zheng Zhenxuan, and Zhang Baoqiang. Augmented line sampling for approximation of failure probability function in reliability-based analysis. *Applied Mathematical Modelling*, 80:895–910, 2020.
- [285] Miguel A Bessa, Piotr Glowacki, and Michael Houlder. Bayesian machine learning in meta-material design: Fragile becomes supercompressible. *Advanced Materials*, 31(48):1904845, 2019.